

4. SITE 798¹

Shipboard Scientific Party²

HOLE 798A

Date occupied: 27 August 1989
Date departed: 28 August 1989
Time on hole: 20 hr, 1 min
Position: 37°03832'N, 134°79976'E
Bottom felt (rig floor; m, drill-pipe measurement): 914.2
Distance between rig floor and sea level (m): 11.1
Water depth (drill-pipe measurement from sea level, m): 903.1
Total depth (rig floor, m): 1057.5
Penetration (m): 143.3
Number of cores: 17
Total length of cored section (m): 143.3
Total core recovered (m): 148.3
Core recovery (%): 103
Oldest sediment cored:
Depth (mbsf): 143.0
Nature: siliceous-nannofossil ooze with clay
Age: Quaternary
Hard rock:
Depth (mbsf): 143.0
Nature: dolomite cemented siliceous ooze

HOLE 798B

Date occupied: 28 August 1989
Date departed: 30 August 1989
Time on hole: 2 days, 17 hr, 18 min
Position: 37°03848'N, 134°79961'E
Bottom felt (rig floor; m, drill-pipe measurement): 911.1
Distance between rig floor and sea level (m): 11.1
Water depth (drill-pipe measurement from sea level, m): 900.0
Total depth (rig floor, m): 1429.0
Penetration (m): 517.9
Number of cores: 54
Total length of cored section (m): 517.9
Total core recovered (m): 514.4
Core recovery (%): 99
Oldest sediment cored:
Depth (mbsf): 517.9
Nature: siliceous claystones
Age: early Pliocene

HOLE 798C

Date occupied: 31 August 1989
Date departed: 31 August 1989
Time on Hole: 14 hr, 10 min
Position: 37°03846'N, 134°07991'E
Bottom felt (rig floor; m, drill-pipe measurement): 911.2
Distance between rig floor and sea level (m): 11.1
Water depth (drill-pipe measurement from sea level, m): 900.1
Total depth (rig floor, m): 1031.3
Penetration (m): 120.1
Number of cores: 13
Total length of cored section (m): 120.1
Total core recovered (m): 132.1
Core recovery (%): 110
Oldest sediment cored:
Depth (mbsf): 120.1
Nature: clayey mixed sediment
Age: Quaternary

Principal results: Our prime objective at Site 798, located on Oki Ridge, was to obtain a Miocene to Holocene paleoceanographic reference section in pelagic-hemipelagic sediments deposited above the local calcium carbonate compensation depth (CCD). A secondary objective was to collect microbiologic samples using special sterile sampling techniques, with the aim of quantifying the role of bacteria in the diagenesis of marine sediments. The first objective was almost fully realized as we recovered an excellent late early Pliocene through Holocene sequence rich in siliceous and calcareous plankton. However, drilling was halted short of the Miocene at a depth of 517.9 mbsf because of abrupt increases in hydrocarbon gases in Hole 798B. In addition, we successfully obtained a series of whole-round samples for bacterial analysis from the sediment/water interface to 510 mbsf. Results at Site 798 are summarized as follows, and a stratigraphic summary is presented in Figure 1:

1. A 517.9-m-thick, late early Pliocene through Holocene sequence of diatomaceous and terrigenous clays, claystones, oozes, and volcanic ashes was recovered at Site 798. The age of this sequence was well established using siliceous microfossil and paleomagnetic datums. The average rate of sedimentation for the entire column is 120 m/m.y., emphasizing the expanded and high-resolution record presented by this sequence.

2. The Holocene through Pleistocene section at Site 798 is characterized by a visually striking series of cyclic lithofacies that involve the repeated appearance of decimeter- to meter-scale alternations between dark, laminated diatomaceous sediments and light-colored, clay-rich, bioturbated to homogeneous sediments. The rhythmic nature of Quaternary sedimentation also is expressed by natural gamma-ray logs through this interval. The organic-rich sediments of the laminated facies and the bioturbated and terrigenous-rich signature of the lighter-colored lithofacies suggest that these couplets are the product of rhythmic late Pliocene to Quaternary paleoceanographic changes that involve major variations in surface productivity, oxygen levels of bottom water, and accumulation of terrigenous clays. Although diatom

¹ Ingle, J. C., Jr., Suyehiro, K., von Breyman, M. T., et al., 1990. *Proc. ODP, Init. Repts.*, 128: College Station, TX (Ocean Drilling Program).

² Shipboard Scientific Party is as given in the list of participants preceding the contents.

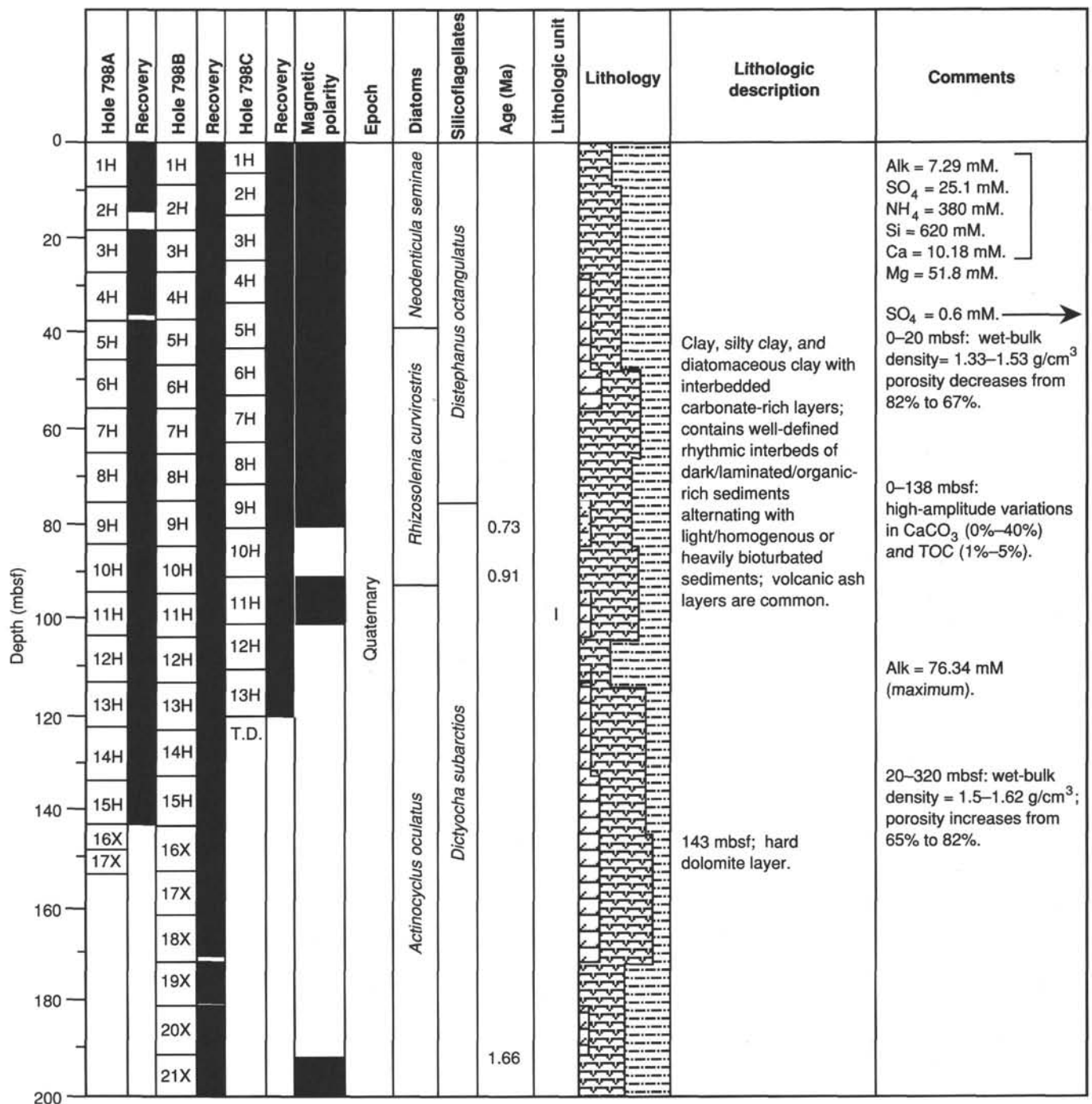


Figure 1. Summary diagram for Site 798.

abundance is generally high throughout the cyclic Quaternary deposits, preliminary analysis of accumulation rates at Site 798 indicates that a peak in biogenic silica flux (3 to 8 g opal/cm²/k.y.) occurred between 2.2 to 2.5 Ma at Site 798, correlative with a late Pliocene episode of high diatom productivity identified at other ODP sites in the Sea of Japan.

3. The older Pliocene portion of the column at Site 798 is marked by indurated siliceous claystones, less well-developed depositional cycles, very low carbonate values, and higher proportions of terrigenous sediment, including glauconitic and quartz turbidite sands. The change from coarse, terrigenous-rich, and carbonate-poor Pliocene sediments to diatomaceous and carbonate-rich, uppermost Pliocene and Pleistocene hemipelagic-pelagic sediments may reflect early Pleistocene uplift of Oki Ridge above

the CCD and basal conduits of turbidite sedimentation, and/or major variations in the position of the local CCD.

4. Well-preserved volcanic ash layers at Site 798 provide an unusually detailed and well-calibrated record of Pleistocene through Pliocene explosive volcanism. Variations in the petrology, thickness, and frequency of ashes suggest that the most likely origins of these deposits are the large acidic to intermediate to calc-alkaline volcanoes of the southwestern and northeastern Japan Arc. In fact, the cores recovered at Site 798 contain 113 discrete ash layers, many of which can be correlated with the three holes drilled at this site. Thicker ashes in the upper 100 m of the section correlate with prominent reflectors on 3.5-kHz seismic profiles across the Oki Ridge Basin. Combined use of the well-constrained sedimentation curve and spectral analysis of natural

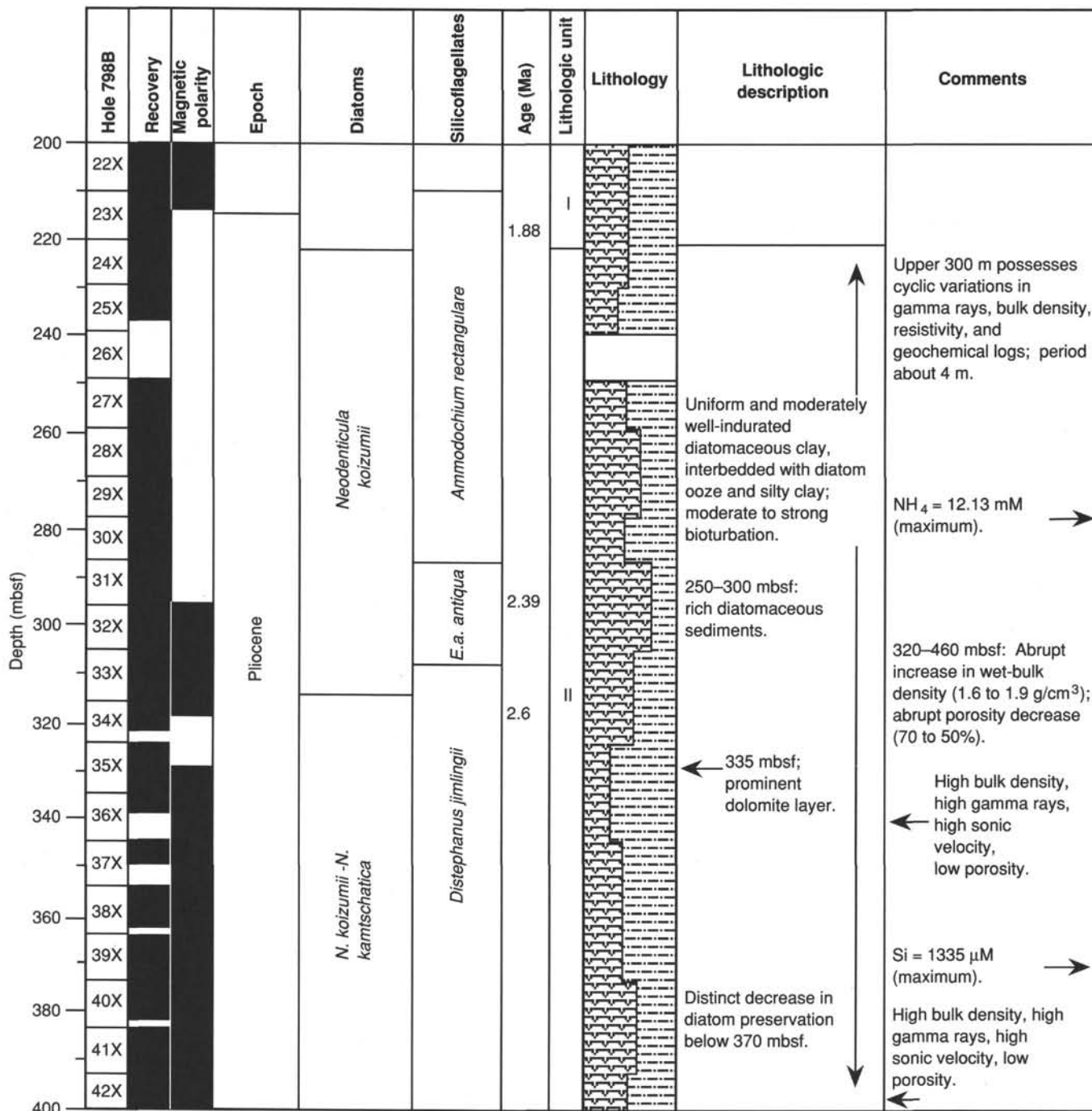


Figure 1 (continued).

gamma-ray logs that reflect the cyclic lithofacies at this site allowed us to assign each of the volcanic ashes an extrapolated age. A high potential also exists for correlation of the youngest ashes at Site 798 with the well-established sequence of explosive events in southern Japan during the last 10,000 yr.

Location and Approach

Site 798 is located in a small fault-bounded basin on top of Oki Ridge in the southeastern Sea of Japan at the original location approved as Site JS2. The site was confirmed by two *JOIDES Resolution* seismic lines. Line 128-1-A parallels Geological Survey of Japan seismic line GSJ-GH8604, originally used to locate proposed Site JS2. A beacon was dropped during the second

crossing of the site along *JOIDES Resolution* line 128-1-C, with the final drilling site adjusted to avoid a sharp depression in the sediment cover seen on the 3.5-kHz record immediately after the beacon drop.

Lithology

The sedimentary section cored in Holes 798A, 798B, and 798C consists of 517.9 m of late early Pliocene through Holocene, fine-grained, pelagic and hemipelagic, diatomaceous and terrigenous sediment that includes common volcanic ashes. Carbonate-rich sediments are restricted to the upper 220 m of the section, whereas well-preserved opaline sediments occur from the sediment/water interface to a depth of 400 mbsf. Glauconitic and quartz sands and indurated siliceous claystones form the lower-

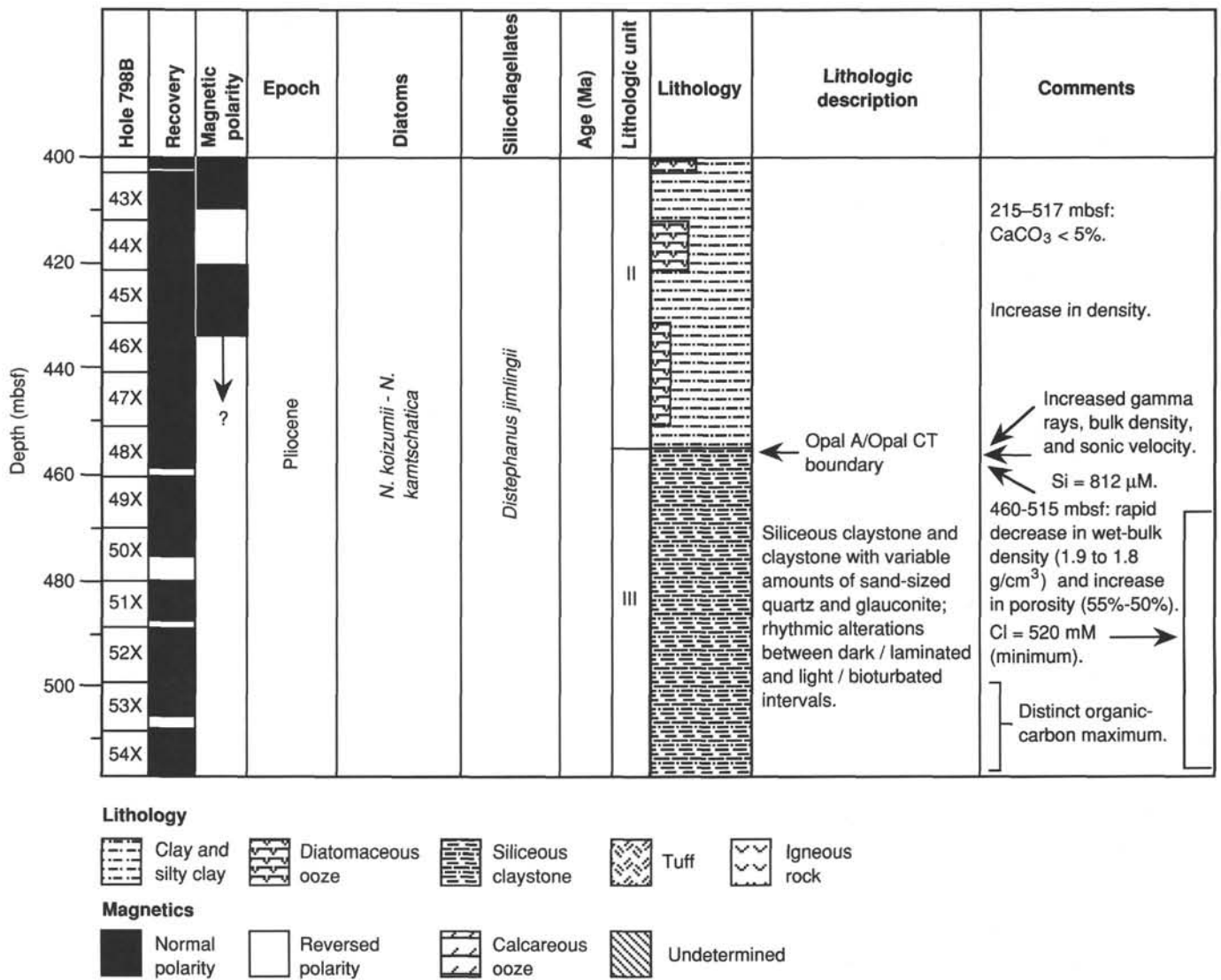


Figure 1 (continued).

most 60 m of the section. The sedimentary column at Site 798 was divided into three lithologic units based on composition, sedimentary structures, and mineralogy as follows:

1. Unit I (0-220 mbsf; latest Quaternary to latest Pliocene) is composed of clay, silty clay, diatomaceous clay, and diatom ooze, with common foraminifers and calcareous nannofossils. This unit displays well-defined decimeter- to meter-scale rhythmic interbeds of dark-colored, laminated sediments that alternate with light-colored, homogeneous to intensely bioturbated intervals. The darker laminated facies are enriched in diatoms, foraminifers, and organic matter relative to low abundances of these components in the lighter bioturbated facies. These distinctive cycles are present to a depth of 180 mbsf. Discrete volcanic ash layers ranging from 0.1 to 10 cm thick are common in the upper 170 m of Unit I.

2. Unit II (220-455 mbsf; late Pliocene) is made up of moderately indurated, diatomaceous clay interbedded with diatom ooze and silty clay. The carbonate content of this unit averages less than 4%. The well-defined, laminated/bioturbated cycles characterizing Unit I are absent in this unit, and most sediments are bioturbated. Volcanic ashes are restricted to the upper portion of Unit II.

3. Unit III (455-518 mbsf; late to late early Pliocene) is composed of siliceous claystone and claystone with glauconitic and quartz sands in the lower 30 m. A sharp decrease in preservation of biogenic silica in Unit III is accompanied by the first distinct occurrence of opal-CT. The rhythmic alterations of dark,

laminated sediments with colored bioturbated sediments common to Unit I reappear in Unit III, but with less clarity and with burrows distorted by compaction. Volcanic ashes up to 15 cm thick occur in the lower one-half of this unit.

Age and Sedimentation Rates

Sedimentation rates at Site 798 are well constrained by microfossil and paleomagnetic datums. Diatoms provide reliable biostratigraphic ages to a depth of 440 mbsf, and age-diagnostic silicoflagellates and ebridians are present to 334 mbsf. The siliceous microfossil data indicate a Holocene to late early Pliocene age range for the Site 798 sequence. The oldest diatoms recognized have been assigned to the top of the *Neodricula kamtschatica*-*N. koizumii* Zone, which is correlated with the top of the Gauss magnetic chron. Calcareous microfossils are best preserved and most abundant in Quaternary sediments, with age-diagnostic calcareous nannofossils present to 191 mbsf. Planktonic foraminifers are present to 249 mbsf, with isolated rare occurrences below this depth. Although the cool-water aspect of the planktonic foraminiferal assemblages at this site precludes the common occurrence of key low-latitude markers, analysis of the coiling ratios of *Neogloboquadrina pachyderma* probably will permit further biostratigraphic resolution of the upper Pliocene-Pleistocene section. A good paleomagnetic signature was recorded to a depth of 305 mbsf, with clear recognition of the Brunhes, Matuyama (including the

Jaramillo and Olduvai events), and the top of the Gauss chron. Shore-based processing of cores in the bottom of Hole 798B probably will provide further definition of the paleomagnetic record and will assist scientists in dating the base of this sequence. Applying combined microfossil and paleomagnetic age data yielded an average sedimentation rate of 120 m/m.y. for Site 798.

Inorganic Geochemistry

A total of 38 interstitial water samples were collected at Site 798. High-density sampling in the upper 100 m of this sequence allowed us to construct high-resolution profiles and to scrutinize closely the mechanisms of early diagenesis. The relatively high sedimentation rate, the high organic carbon accumulation, and the vigorous bacterial decomposition of organic matter at this site are responsible for the very high concentrations of organic metabolites recorded here, with alkalinity reaching 76 mM, ammonia 12 mM, and phosphate 290 μ M. These same processes are also responsible for marked sulphate depletion at 12 mbsf, with further decomposition of the organic matter proceeding by carbonate reduction and methanogenesis. The upper 50 m of the section is characterized by a decrease in calcium that is concurrent with high levels of alkalinity. Carbonate diagenesis in this highly alkaline setting clearly is responsible for the formation of the authigenic dolomites encountered between 143 and 335 mbsf, both in the form of small, disseminated crystals and in cemented horizons. The distribution of silica in these sediments has been governed primarily by the dissolution of biogenic siliceous components (mainly diatoms) above 425 mbsf and by silicification reactions at depth. The opal-A/opal-CT transition is signaled by a severe decrease in dissolved silica below 425 mbsf, with the first recorded appearance of opal-CT at 445 mbsf. The calcium, magnesium, and strontium distributions at the bottom of Hole 798B indicate the alteration of volcanic rocks known to be present at depth on Oki Ridge.

Organic Geochemistry

Variations in carbonate content allowed us to divide the Site 798 sequence into two intervals. Interval I (0–220 mbsf) corresponds to lithologic Unit I and is characterized by carbonate values ranging between 1% and 35%. Within this interval, shorter-term high-amplitude lithologic variations having high carbonate values are concentrated in the upper 140 m, whereas the lower part of Interval I (140–220 mbsf) displays values between 1% and 15%. Interval II (220–517 mbsf) corresponds to lithologic Units II and III and is characterized by very low carbonate values of less than 5%. The downhole distribution of total organic carbon (TOC) at Site 798 is characterized by predominantly high values that range from 1% to almost 6%, with the highest values recorded in Holocene through upper Pleistocene and lower upper Pliocene sediments. The distinctive dark/light depositional cycles present in the uppermost Pliocene through Quaternary portion of the section also are reflected by organic carbon values. The dark basal units of each cyclic couplet contain up to 5% organic carbon, whereas the light-colored upper units contain about 2%. Rock-Eval TOC data, hydrogen index values, and carbon/nitrogen ratios suggest that most of the organic matter in Site 798 sediments is a mixture of kerogen types II (marine origin) and III (terrigenous origin), with marine type II dominant. The organic carbon values at this site are distinctly higher than those recorded in "normal" open-ocean benthic environments and point to special conditions favoring high productivity and/or enhanced preservation during deposition. Combined sedimentologic and organic geochemical evidence within the more organic-rich portions of this sequence suggest that periods of high surface productivity alternated with phases of increased rates of preservation of organic matter under the influence of suboxic bottom water at the Oki Ridge site during the past 3.5 m.y.

Hydrocarbons

Elevated concentrations of ethane and propane occurred near 450 mbsf in Hole 798B, which resulted in sharp decreases in the C_1/C_2 and C_1/C_3 ratios. Significant amounts of *i*-butane and *n*-

butane also occurred at this latter depth and increased downhole to 517 mbsf. The combined hydrocarbon gas shows in Hole 798B caused us to halt drilling at 517.9 mbsf. The immature nature of the *in-situ* organic matter in Site 798 sediments indicates that these hydrocarbons probably migrated from other source rocks in this area.

Seismic Stratigraphy

Three seismic intervals above acoustic basement can be clearly recognized on all profiles in the immediate vicinity of Site 798, including (1) a thin stratified unit at the top of the section, (2) a middle unit characterized by several strong reflectors, and (3) a lower, less-stratified unit. The second or middle unit can be subdivided into three additional intervals, so that altogether five seismic intervals can be recognized at this site. The upper two intervals are continuous and undisturbed across the entire Oki Ridge basin, whereas the lower intervals include discontinuous reflectors and indistinct but important signs of deformation. The most prominent reflectors in all seismic profiles at this site represent thicker volcanic ashes and dolomitic horizons, as confirmed by correlations with the sonic velocity log and the synthetic seismic profile constructed for Site 798. Lithologic Units I and II correlate with seismic Intervals 1 through 4, and lithologic Unit III correlates with the upper portion of seismic Interval 5.

Heat Flow

We conducted two successful runs using the Barnes-Uyeda temperature probe down to 132.8 mbsf in Hole 798A and to 110.4 mbsf in Hole 798C. The combined readings for these two sets of measurements indicate an average temperature gradient of approximately 111°C/km for the uppermost 130 m at this site. The Lamont-Doherty Geological Observatory temperature logging tool (TLT) was run in all three holes at Site 798. The highest temperature measured with the TLT at the bottom of Hole 798B (517 mbsf) was 43°C, yielding a thermal gradient of 83°C/km. However, the time-temperature curves indicate that this temperature was not stabilized at the time of measurement and that the actual gradient may have been somewhat higher. Thus, the lower temperature gradient obtained from the TLT probably results from thermal disequilibrium, whereas the higher temperature gradients obtained with the Barnes/Uyeda tool may reflect a change in thermal conductivity of the drilled sediments. A previous measurement of heat flow in the Oki Ridge area in 1965 yielded a value of 98 mW/m².

Logging

Four successful logging runs were completed at Site 798, including (1) sonic/seismic stratigraphy, (2) formation microscanner, (3) lithoporosity/density, and (4) geochemistry. The quality of the logs obtained was generally excellent. In particular, the spectral gamma-ray (SGR) and the aluminum logs yielded an exceptionally clear and continuous record of the cyclic depositional history of upper Pliocene and Quaternary sediments. In fact, preliminary dating and spectral "tuning" of the cyclic gamma-ray log pattern using paleomagnetic datums suggest that the depositional cycles delineated by this log have a periodicity of about 40,000 yr. These records, together with analysis of the cyclic lithofacies patterns, geochemical variations, and microfaunal trends within this interval, portend reconstruction of a truly high-resolution paleoceanographic history at Site 798.

Microbiology

Whole-round samples (3–25 cm) for analysis of bacteria were successfully collected from APC and XCB cores between 0 and 510 mbsf in Hole 798B, with the upper portion of this hole dedicated to this task. Special techniques were used to prevent sample contamination including use of a sterile core cutter and flushing of cores using oxygen-free nitrogen. The aim of this sampling and analysis is to quantify the role of bacteria in

diagenesis of marine sediments by measuring variations in their activity and biomass with depth below the sediment/water interface. Laboratory studies will include direct bacterial counts and analysis of bacterial composition, activity, and lipids. Bacterial samples were offloaded from the ship three days after collection via a specially chartered vessel.

BACKGROUND AND SCIENTIFIC OBJECTIVES

Location and Bathymetry

Site 798 lies in the southeastern Sea of Japan, about 160 km north of the western coast of Honshu (Fig. 2). Specifically, the site is located in a small, sediment-filled graben on

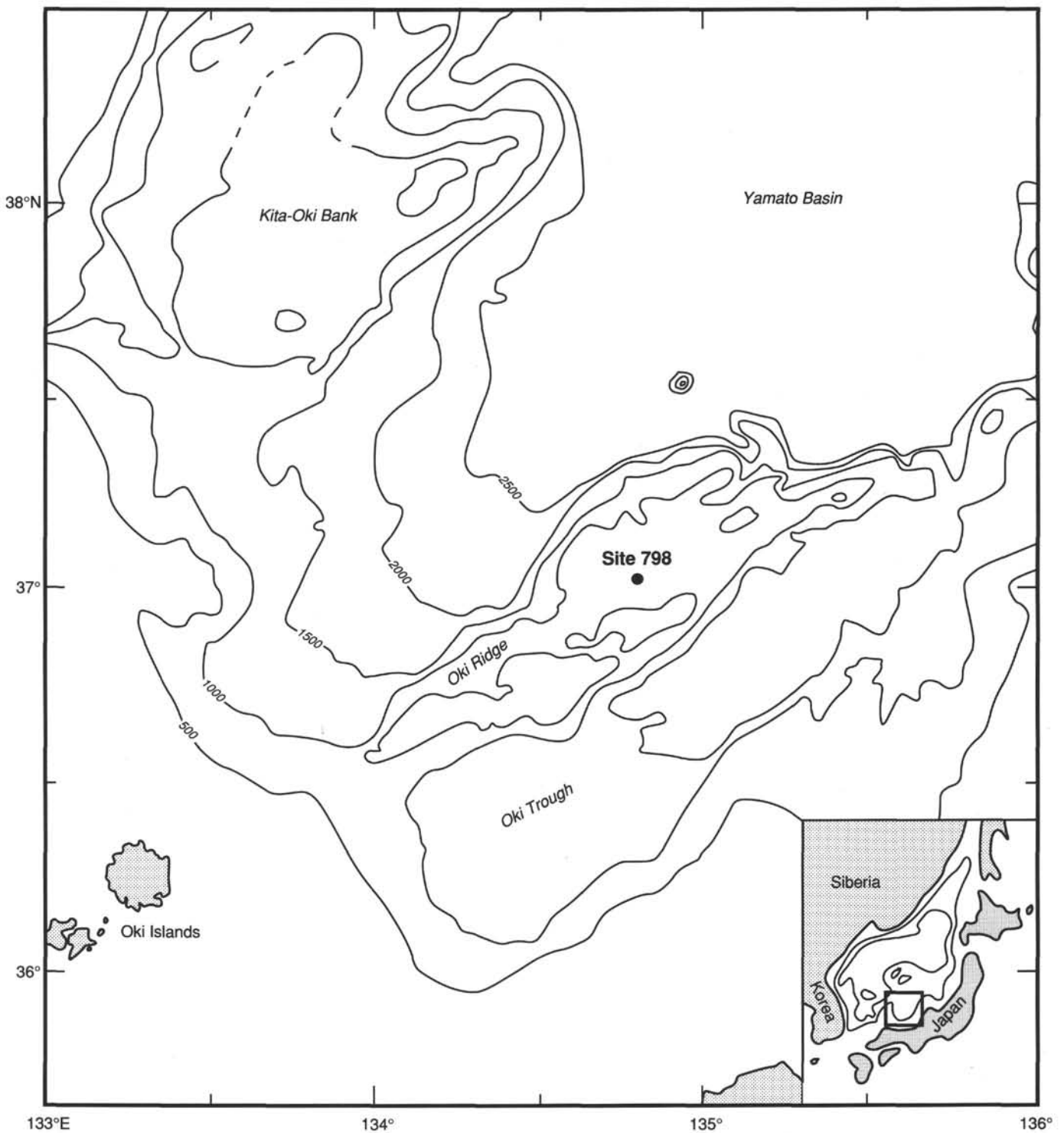


Figure 2. Location map of the area surrounding Site 798, showing site location and bathymetry. Contour interval is 500 m. Note location of the Oki Islands relative to Oki Ridge.

top of Oki Ridge at a water depth of 902 m. Oki Ridge is one of a series of northeast-southwest trending ridges and troughs that characterize the eastern and southern Sea of Japan. Oki Trough, Kita-Oki Bank, and Yamato Basin represent the ridges and troughs adjacent to Oki Ridge and Site 798 (Fig. 2). Although Kita-Oki Bank and the insular shelf around the Oki Islands have relatively flat surfaces, the top of Oki Ridge exhibits significant relief. The shallowest areas of the ridge are less than 300 m deep, with the floor of the ridge-top basin containing Site 798 at a water depth of about 902 m. The ridge as a whole exhibits a maximum relief of more than 2200 m, with the steep north flank of Oki Ridge meeting the abyssal plain of the Yamato Basin at a water depth of 2500 m (Fig. 2).

Oki Ridge is on geomorphic and structural strike from the Oki Islands, and the geology of these islands has special significance for any interpretation of the rocks forming the ridge. Oki Ridge also forms an effective sediment dam with respect to terrigenous debris that is shed westward from central Honshu, with Oki Trough forming a rapidly filling basin.

Crustal Structure

Interpretations of crustal structure in the general area of Site 798 are constrained by two sources of seismic refraction data. Older sonobuoy records reported by Ludwig et al. (1975) provide a deep seismic section across the north end of Oki Ridge, Yamato Basin, and the Yamato Seamount Chain (Fig. 3). More recent data derived from a detailed survey using an ocean bottom seismometer (OBS) array in the Yamato Basin and Oki Trough (Hirata et al., 1987, 1989) provide a series of *P*-wave profiles surrounding the northern half of Oki Ridge (Figs. 4 and 5).

Mantle velocities beneath the Yamato Basin range from 7.6 to 8.3 km/s, with the crust/mantle boundary or Moho identified at depths between 11 to 12 km below the seafloor (Figs. 3 and 5). This crustal thickness is intermediate between typical oceanic crust (5–10 km) and continental crust (<30 km). The increasing depth of the boundary between crustal "layer 3" and "layer 2" beneath Oki Ridge, Oki Trough, and the adjacent insular shelf off Honshu implies that the depth of the underlying Moho and crustal thickness increase abruptly beneath the Japanese arc.

Crustal structure above the Moho in the Oki Ridge area is defined by velocities of 6.7 to 7.4 km/s marking "layer 3" between depths of 6.5 and 8 km. Overlying "layer 2" has a thickness in this area of about 5 km and velocities between 3.8 to 5.7 km/s. This latter envelope of vertical and horizontal velocities is indicative of the layered volcanic rock and volcanoclastic sediments thought to form the bulk of the younger acoustic basement rock beneath Oki Ridge (Tamaki et al., 1981; Kobayashi, 1985).

"Layer 1" exhibits velocities of 1.5 to 2.1 km/s (Figs. 3 and 5) and is assumed to represent unconsolidated and semiconsolidated sediments. *P*-wave traveltimes indicate that this layer is up to 2.5 km thick in the northern Oki Trough, but only 1 km thick in that portion of the Yamato Basin immediately outboard of Oki Ridge and Oki Trough, reflecting the rapid accumulation of sediments trapped east of Oki Ridge.

Heat Flow

Measured heat-flow values in the area surrounding Site 798 range from 68 to 137 mW/m², with a questionable value of 53 mW/m² measured on the north flank of Oki Ridge (Fig. 6). A single heat-flow station directly on top of Oki Ridge about 40 km north of Site 798 yielded a value of 98 mW/m². The average

heat-flow value measured in the ridge, basin, and shelf areas surrounding Site 798 is 91 mW/m². The average value for four stations located on Kita-Oki Bank and Oki Ridge is 79 mW/m², which is significantly lower than the average value of 97 mW/m² in the Yamato Basin (M. Yamano, pers. comm., 1989).

Magnetics and Gravity

Magnetic anomalies in the area of Site 798 form an east-west pattern of mixed high-amplitude and relatively long wave-length anomalies and low-amplitude, high-frequency anomalies (Fig. 7) typical of ridge and bank areas (Isezaki, 1986). The profile passing nearest Site 798 exhibits peak-to-peak amplitudes of 250 nT and a wave length of 60 km immediately adjacent to the site. The mixed character of this anomaly pattern probably is a response to the rapid change from the deep floor of the Yamato Basin to the abruptly shallower depths of Oki Ridge, which in turn reflects differences in crustal thickness beneath these two features.

Free-air gravity anomalies on Oki Ridge and in the vicinity of Site 798 range from 0 to more than 60 mgals (Fig. 8). In fact, the general pattern of anomalies in this area essentially mimics the topography of the northwest-southeast trending Oki Ridge. Anomaly values of -20 mgals or less characterize the Yamato Basin and Oki Trough, with contours of the highest values clearly outlining the shallower portions of Oki Ridge (Fig. 8). Presumably, this pattern is a reflection of the differences in depth to basement, with lower values coincident with the basinal areas that contain the thickest sedimentary sequences.

Basement Rocks

Rock dredge sites in the area of Oki Ridge are shown in Figure 4, along with the locations of radiometrically dated igneous rocks that were collected from Oki Island and dredged from Kita-Oki Bank, as described by Honza (1979), Yuasa et al. (1979), Kaneoka (1986), and Tamaki (1988). Basement rock-types recovered in various dredge hauls in this area include Mesozoic granite and gneiss and Tertiary (Miocene?) volcanic rocks.

The oldest firmly dated rocks thought to represent basement in the Oki Ridge area are present on the Oki Islands due southwest along strike from Oki Ridge (Fig. 4). Granite exposed on these islands yielded a Jurassic potassium/argon biotite age of 169 to 165 Ma (Tamaki, 1988). In addition, gneiss exposed on these islands has been assigned to the Hida group of metamorphic rocks thought to represent pre-Silurian sediments metamorphosed during Permian to Jurassic time. Significantly, *in-situ* granite dredged from Kita-Oki Bank also was determined to be Jurassic in age (Tamaki, unpubl. potassium-argon date of 141.6 Ma, 1988), although it yielded a somewhat younger age than the Oki Island granites (Fig. 4).

Rounded cobbles of granite and gneiss (probably representing the same rocks as those exposed on the Oki Islands) were recovered in Dredges D264 and D267 on the south flank and on top of Oki Ridge (Fig. 4). These rocks clearly experienced transport from their source areas and may represent material that was redeposited during Pleistocene lowstands of sea level prior to the erosional or tectonic separation of Oki Ridge from the adjacent insular shelf area.

Volcanic rocks dredged on and around Oki Ridge (Fig. 4) and thought to be *in-situ* include rhyolitic welded tuff, tuffaceous breccia, andesite, pillow basalt, and dolerite (Yuasa et al., 1979). Although none of these rocks have been dated, their compositions are similar to the lower Miocene andesitic and rhyolitic rocks of the so-called "Green Tuff" units that constitute ubiquitous synrift flows and deposits at

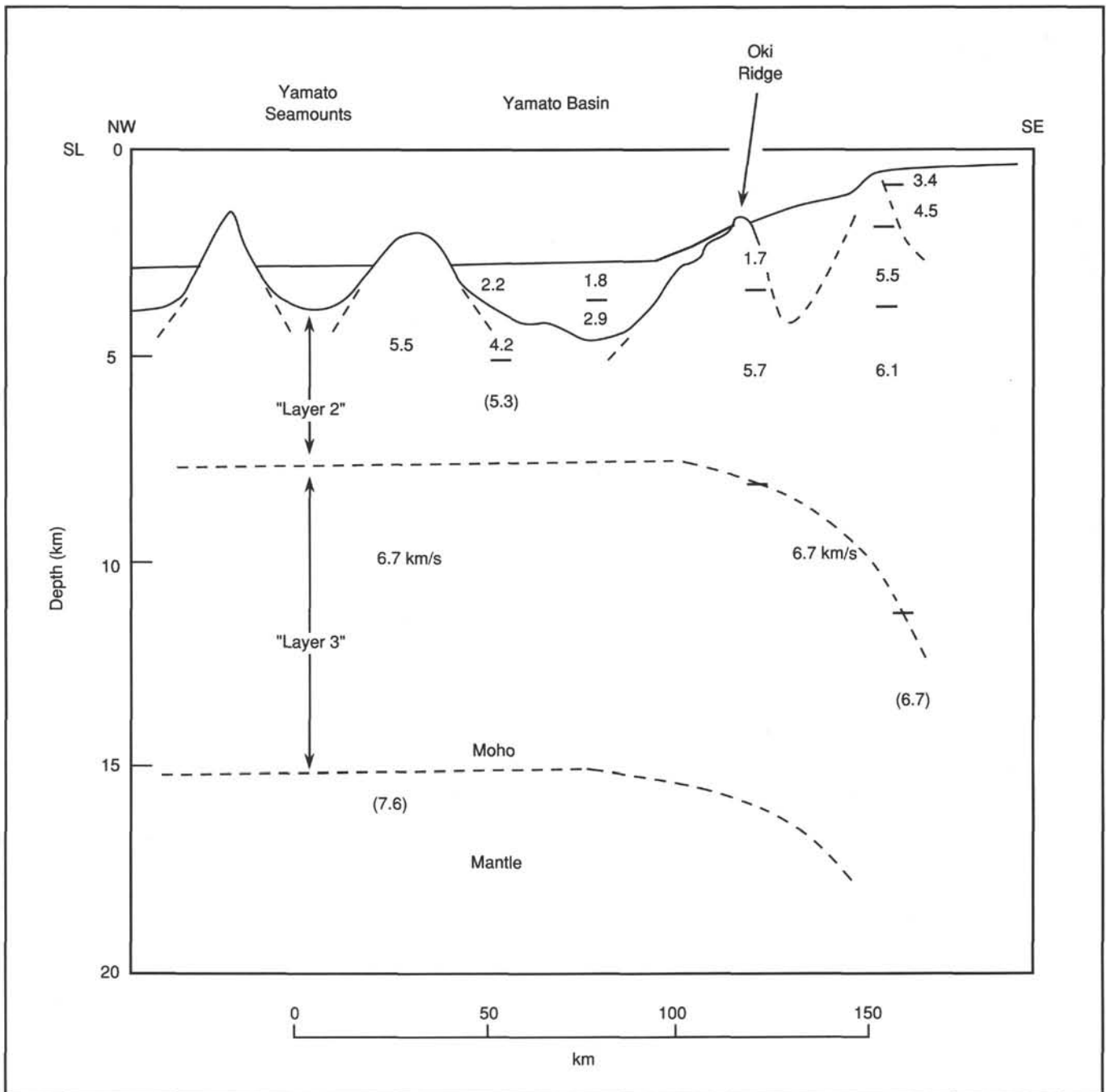


Figure 3. Crustal section based on seismic refraction data in the eastern Yamato Basin, Oki Ridge, and the insular shelf of Honshu, Japan. This figure represents a portion of NW-SE profile A-B presented by Ludwig et al. (1975).

the base of Neogene sequences that are widely exposed in western Honshu (Geological Survey of Japan, 1982). Kobayashi (1985) noted that in many areas of the Sea of Japan, P-wave velocities common to "layer 2" may represent the widespread occurrence of "Green Tuff" units at depth. However, Tamaki et al. (1981) took a more conservative view and simply noted the presence of undifferentiated volcanic rocks on and beneath Oki Ridge, based on their analysis of dredge hauls and seismic reflection data. In this context, it is important to note that lower Miocene "Green Tuff" formations occur on the Oki Islands (Geological Survey of Japan, 1982). In addition, correlative "Green

Tuff" units are present at the base of the Neogene sequence in the Himi area of Honshu, located to the southeast of Oki Ridge (Morozumi and Koizumi, 1981).

In summary, the oldest and closest *in-situ* basement rocks to Site 798 are Jurassic granites and gneisses on the Oki Islands, and these rock types may form a portion of the basement beneath Oki Ridge, as they do on Kita-Oki Bank, Yamato Rise, and along the adjacent coast of Honshu. Undated volcanic rocks dredged on Oki Ridge include lithologies common to lower Miocene "Green Tuff" units also exposed along strike on the Oki Islands, and these rocks probably constitute the bulk of the shallow basement and "layer 2" beneath Oki Ridge.

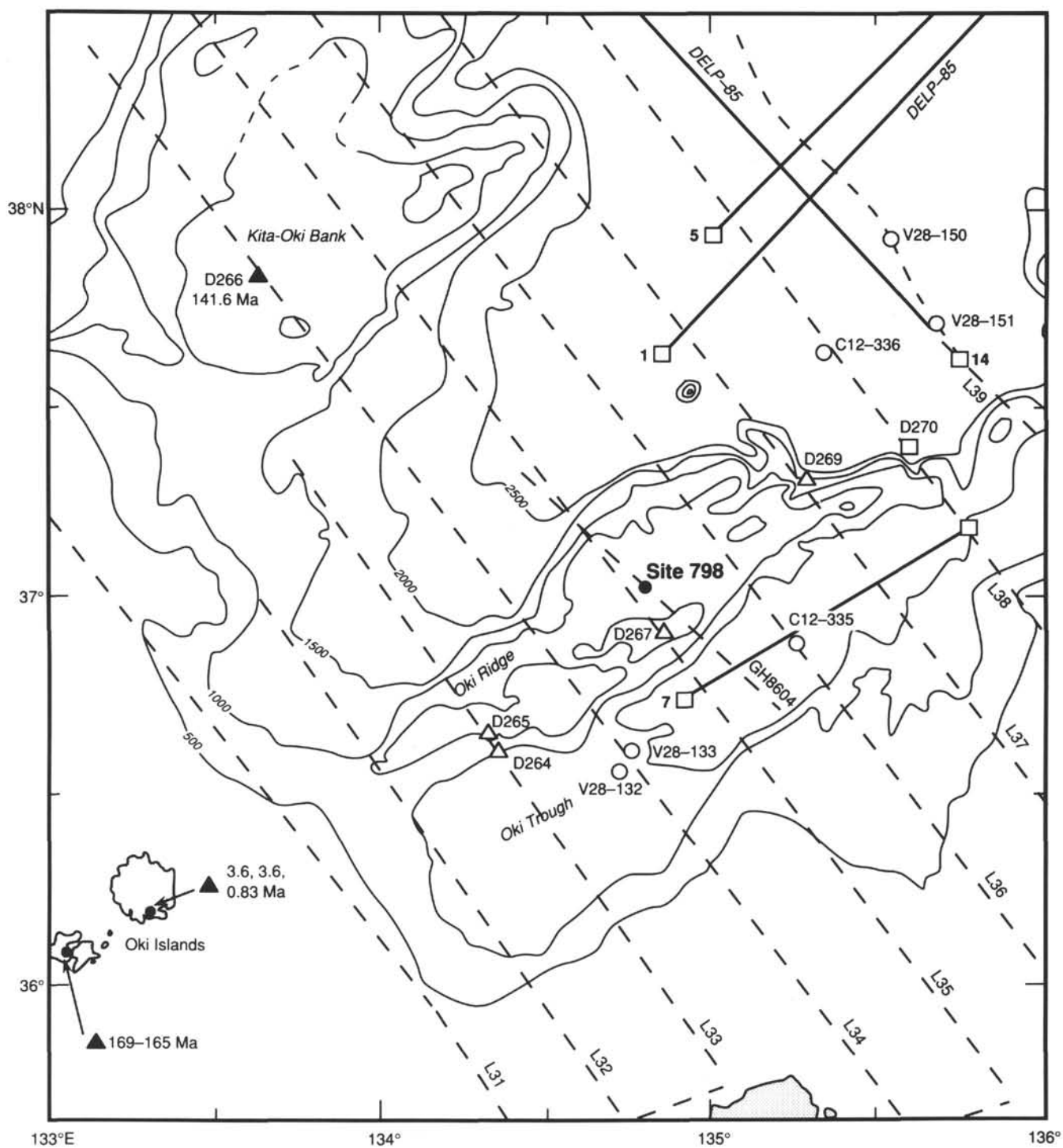


Figure 4. Location map of seismic reflection profiles, seismic refraction profiles and stations, rock dredges, and radiometrically dated rocks on Kita Oki Bank and the Oki Islands, in the vicinity of Oki Ridge. Dashed lines L31 to L39 represent Geological Survey of Japan seismic reflection profiles (Tamaki, 1988). Open circles represent seismic refraction sonobuoy stations and solid lines represent two-ship refraction profiles (1, 5, 7; Murauchi, 1966) and OBS-array profiles (*DELP-85*; Hirata et al., 1987). Open triangles mark the position of rock dredges described by Yuasa et al. (1979) and filled triangles represent the locations of radiometrically dated granite dredged from Kita Oki Bank (Tamaki, 1988) and radiometrically dated granite and volcanic rocks from the Oki Islands.

Finally, sedimentary rocks dredged from Oki Ridge (Dredges D264, D267, and D269; Fig. 4) include sandstones, shaley siltstone, and hard shale typical of lithologies characterizing middle to upper Miocene marine formations that overlie the lower Miocene synrift "Green Tuff" units along the eastern and southern margins of the Sea of Japan. These

rocks are typified by the middle to upper Miocene Nakanami, Sugata, and Inazumi formations that are exposed on the Noto Peninsula to the southeast of Oki Ridge, with correlative units exposed on the Oki Islands. Thus, middle to upper Miocene hard shales and siltstones probably overlie volcanic units on some areas of Oki Ridge, as also was noted by Tamaki (1988).

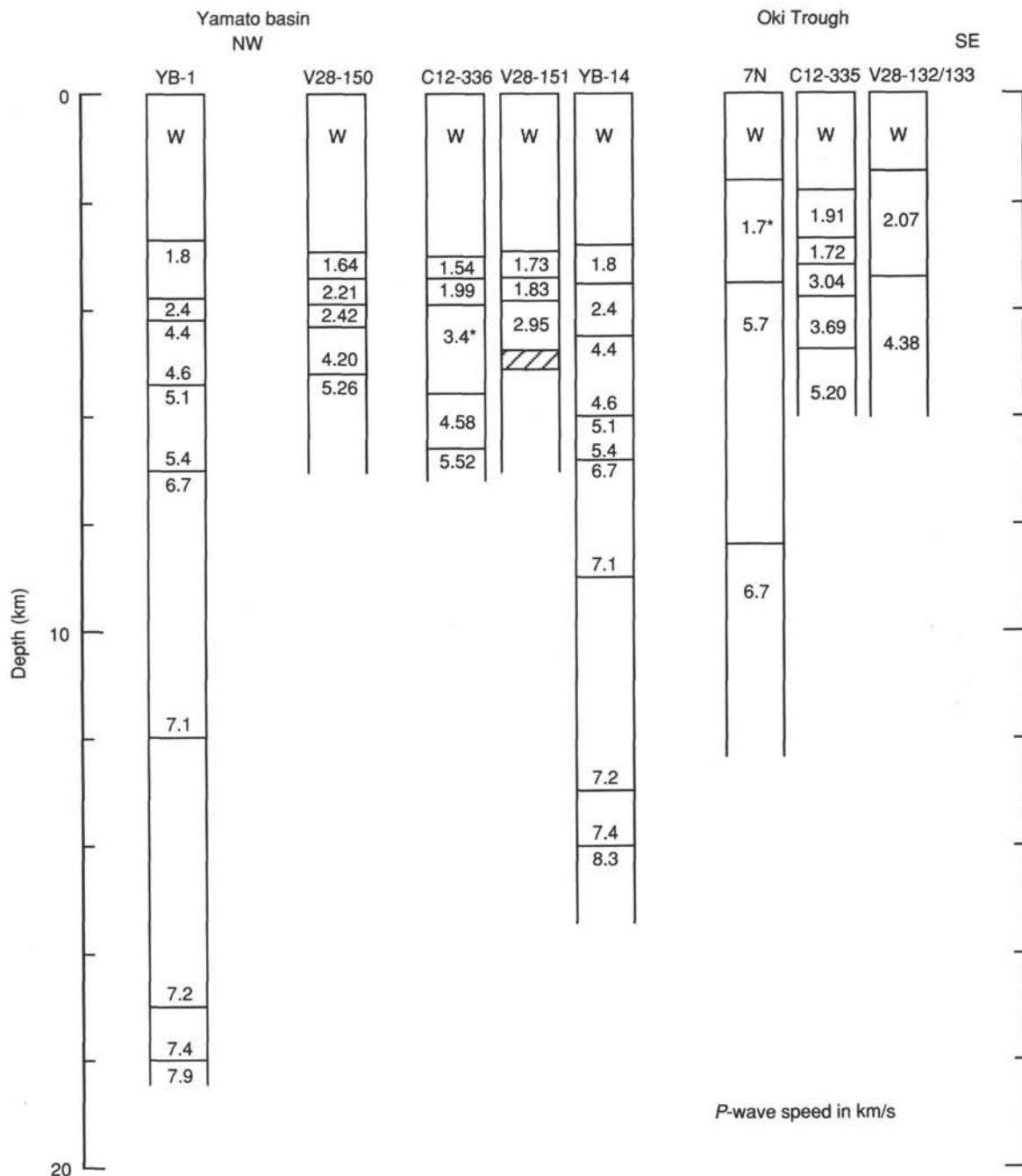


Figure 5. Seismic refraction profiles beneath the Yamato Basin and Oki Trough. Figure from Ludwig et al. (1975) and Hirata et al. (1987). See Figure 4 for locations of these stations.

Tectonic Setting

The structure beneath Site 798 and the Oki Ridge is typical of many ridges and banks that form the borderland-style topography of the eastern and southern Sea of Japan (Tamaki, 1988). Seismic reflection profiles across these features, including the Yamato Rise and Kita-Oki Bank, illustrate that these structures involve northeast-southwest trending folds and faults in acoustic basement units (Figs. 9 and 10). Steep normal faults demark the sides of the Oki Trough and adjacent Oki Ridge, with similar faults bounding the sediment-filled basins to the east beneath the insular shelf of Honshu and to

the west in the Yamato Basin (Fig. 10). The results of drilling at DSDP Site 302 on the northern flank of the Yamato Rise (Karig, Ingle, et al., 1975), dredge hauls from Yamato Rise and other highs, interpretation of seismic refraction and reflection profiles, and the well-dated stratigraphies of Neogene basins exposed along the eastern margin of the Sea of Japan collectively indicate that the extensional fault system that cuts acoustic basement units throughout this area was initiated in early Miocene time, during the initial rifting of the Sea of Japan. Subsequent subsidence of the Neogene basins formed during this process probably was accommodated along these same faults. Later compressional deformation of basin

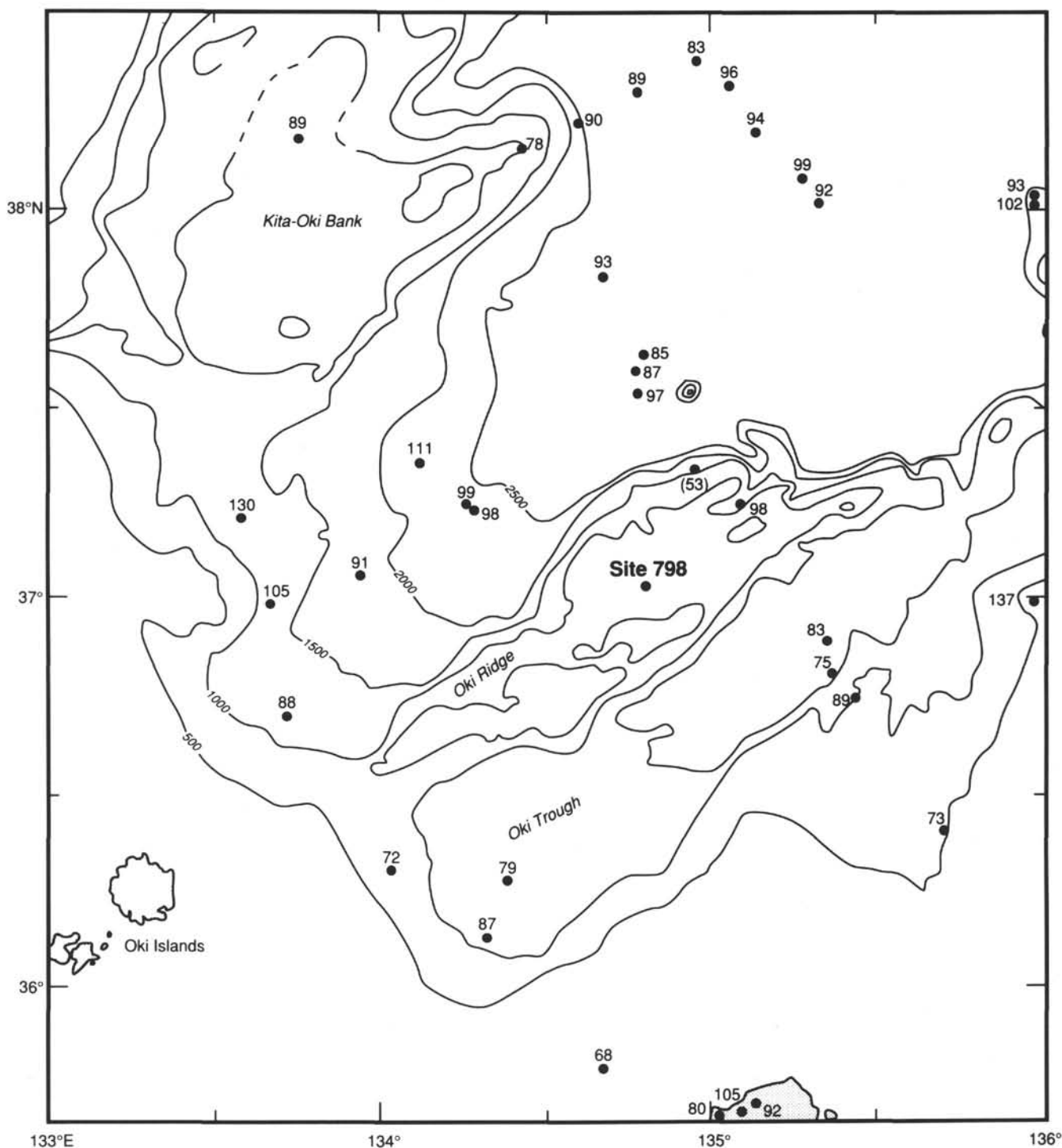


Figure 6. Heat flow measurements in the vicinity of Site 798, as compiled by Yamano (pers. comm., 1989).

fills is expressed by a widespread unconformity between lower Pleistocene and older units and overlying upper Pleistocene and Holocene sediments in many areas of the eastern Sea of Japan (Ishiwada et al., 1984).

Site 798 is located in a small graben on top of Oki Ridge, while seismic profiles demonstrate that acoustic basement lies structurally above and flanking the younger basin fill as a result of faulting (Figs. 9 and 10). The youngest unconsolidated and semiconsolidated sediments in this basin seem little disturbed, except for subsidence resulting from compaction. Alternatively,

a poorly reflecting unit below the youngest sediments and above acoustic basement appears to be structurally deformed.

Sedimentation

The sedimentary deposits filling the small basin atop Oki Ridge where Site 798 is located are approximately 710 m thick (Fig. 10). Three seismic intervals are apparent above acoustic basement in this sequence, including (1) a shallow, moderately well-stratified unit, (2) a middle, less well-stratified unit, and (3) a poorly reflecting lower unit that exhibits evidence of

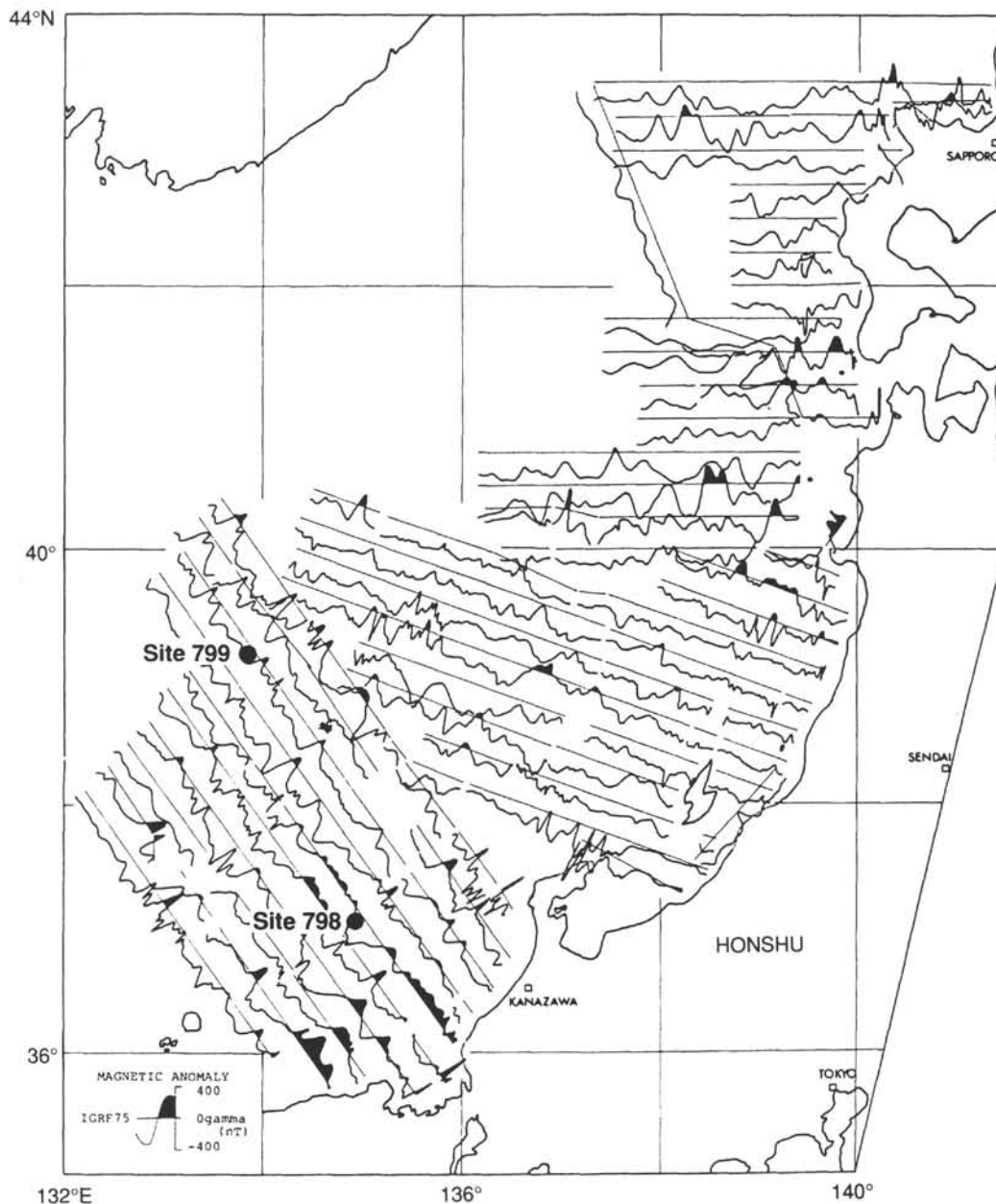


Figure 7. Magnetic anomaly profiles in the area of Site 798. Map from Honza (1979).

deformation (see "Seismic Stratigraphy" section, this chapter). Prior to drilling, the upper two units were thought to represent Pleistocene and Pliocene hemipelagic and pelagic sediments and the lowermost unit possible Miocene strata. Acoustic basement was assumed to represent volcanic and volcanoclastic rock following Honza (1979) and Tamaki (1988).

Objectives

Paleoceanographic History

Our primary objective at Site 798 was to obtain a Miocene to Holocene paleoceanographic reference section in sediment thought to have been deposited above the local CCD. Previous piston-core studies and deep-sea drilling in the Sea of Japan demonstrate that this sea has apparently had an unusually shallow CCD (at about 2000–1500 m) during various phases of its late Neogene evolution (Ujiie and Ichikura, 1973;

Ingle, 1975a; Ichikura and Ujiie, 1976; Arai et al., 1981; Matoba, 1983), resulting in carbonate-poor sediments that contain few or no calcareous microfossils essential for isotopic and faunal analysis of water mass and climatic history. Consequently, a site in relatively shallow water, located on a structurally isolated high above 1500 m, was sought to obtain a carbonate-rich sequence undiluted by coarse gravity flow sediments common to basinal areas. The small, sediment-filled basin located on top of Oki Ridge at Site 798 was considered ideal in this respect. The seismic character of the sediment column at this site suggested the presence of a Miocene to Holocene pelagic-hemipelagic sequence that would provide a high-resolution paleontologic, isotopic, and sedimentologic record of (1) surface and intermediate water history, including variations in productivity, dissolved oxygen, and shallow excursions of the CCD; (2) anoxic to oxic

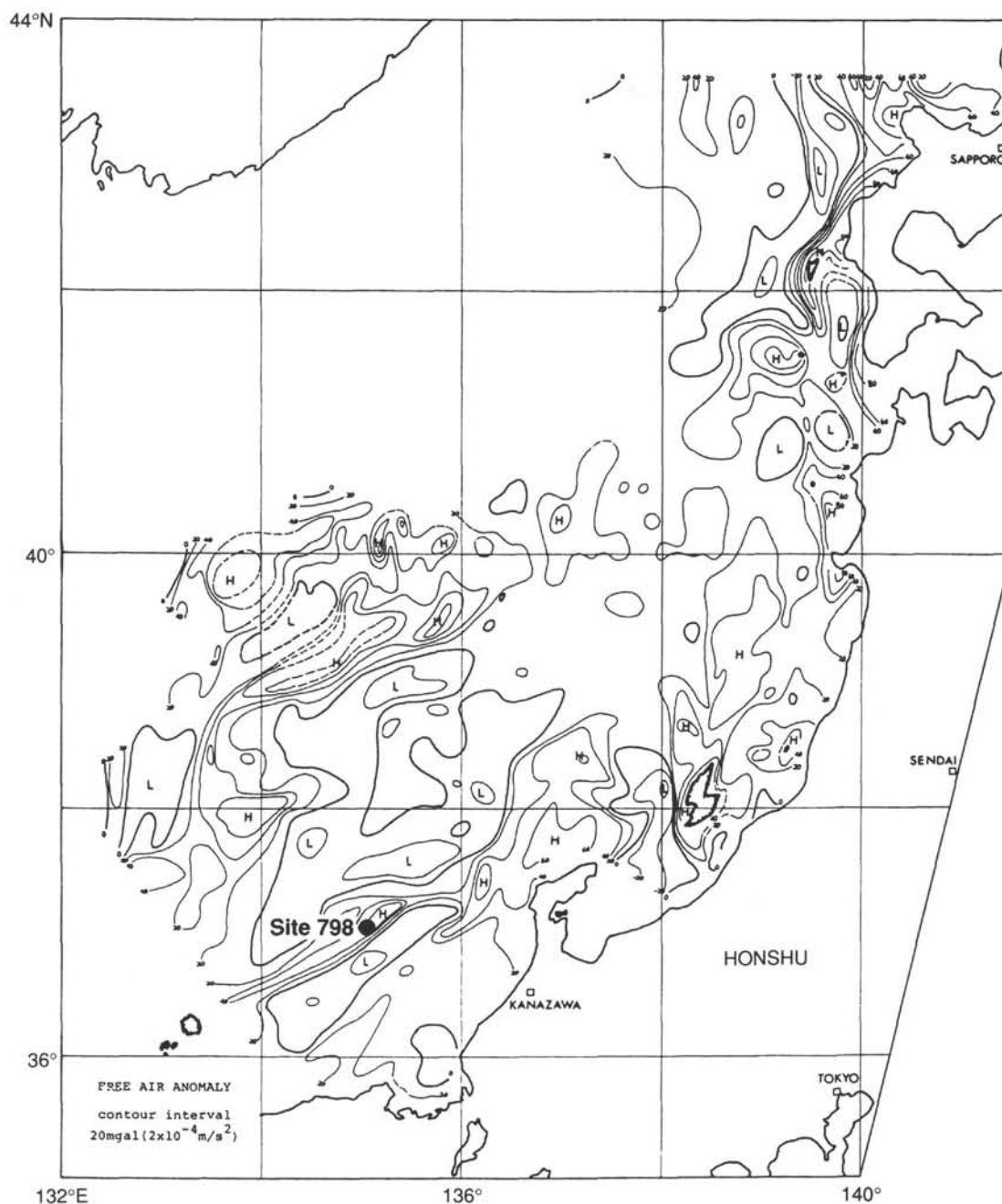


Figure 8. Map of free-air gravity anomalies in the vicinity of Site 798. Contour interval is 10 mgals. Map from Honza (1979).

episodes in basin history known to have occurred during Miocene, Pliocene, and Pleistocene time (Ingle, 1975; Matoba, 1983); and (3) faunal and sedimentary responses to extremes in water-mass character and circulation thought to have accompanied the episodic tectonic and eustatic isolation of the Sea of Japan from the open Pacific Ocean (Matoba, 1983; Burckle and Akiba, 1977).

Bacterial Studies

In addition to paleoceanographic objectives, special collection of bacterial samples from the upper portion of the sediment column was planned for Site 798, with one of three holes to be dedicated for this task. The goal of this unusual study was to quantify the role of bacteria in diagenetic

processes at increasing depths below the sediment/water interface. We considered that Site 798 was an ideal setting for this study because of its high potential for recovery of a sedimentary record of high-amplitude variations in productivity, anoxia, and the resulting organic-rich facies.

OPERATIONS

Pusan to Site 798

The *JOIDES Resolution* departed Pusan, Korea, with the first anchor up at 0920UTC, 25 August 1989. Site 798 (proposed Site JS2) is located 296 nmi east-northeast of Pusan; the transit required 30.5 hr at an average speed of 9.7 kt. A positioning beacon was dropped at 0545UTC, 27 August, after

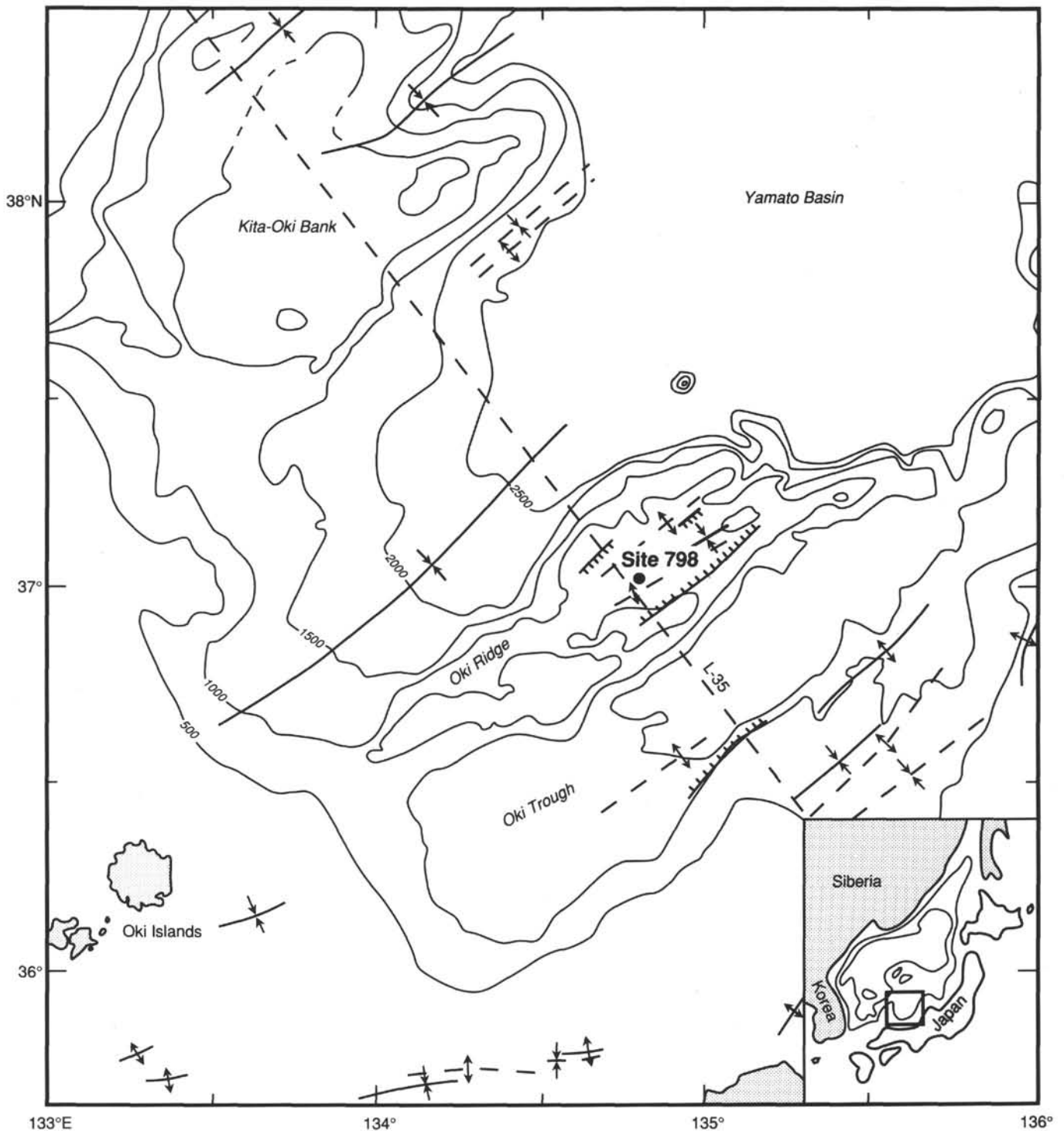


Figure 9. Tectonic map of the area surrounding Site 798 showing recognized faults and fold axes and the location of seismic reflection profile L-35 (shown in Fig. 10). Structural features are from Tamaki et al. (1981). Bathymetric contour interval is 500 m.

a 35-nmi preliminary survey of the site at an average speed of 6.1 kt.

Hole 798A

Hole 798A was spudded at 0523UTC, 27 August 1989, at a depth of 903.1 m below sea level (bsl). From Core 128-798A-1H we recovered 9.3 m of sediment (Table 1); it was accepted as a mud-line core. Based on subsequent mud-line drill-pipe

measurements at Holes 798B and 798C, we estimate that the top of Core 128-798-1H is actually 1.5 m below the mud line. Continuous APC cores were taken to a depth of 142.5 mbsf. Recovery was good (Table 1), and values higher than 100% result from surface expansion of the gaseous sediments. Heat flow was measured every other core after Core 128-798-4H. A multishot camera was deployed to measure core orientation for all APC cores, starting with Core 128-798-5H.

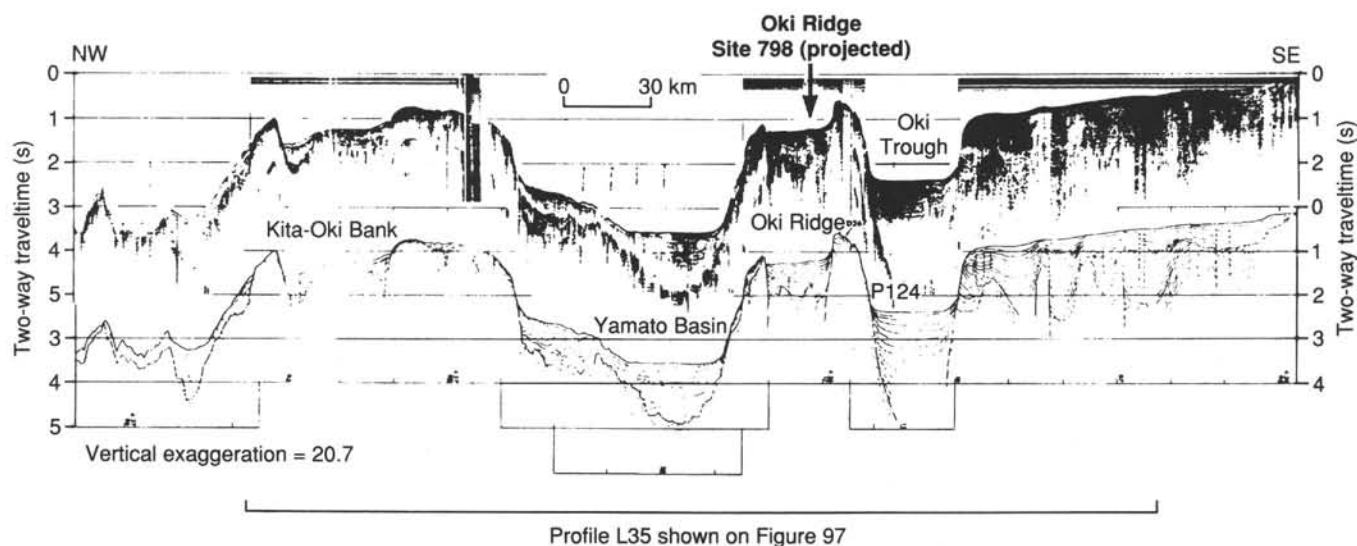


Figure 10. NW-SE single-channel seismic reflection profile L-35 across Oki Ridge and the eastern Yamato Basin from Tamaki (1988). Location of this profile is shown in Figure 9.

Table 1. Coring summary, Hole 798A.

Core number	Date (Aug. 1989)	Time (UTC)	Depth (mbsf)	Length cored (m)	Length recovered (m)	Recovery (%)	Age
1H	27	0530	0–9.3	9.3	9.29	99.9	Quaternary
2H	27	0600	9.3–18.3	9.0	5.08	56.4	
3H	27	0620	18.3–27.3	9.0	8.84	98.2	
4H	27	0645	27.3–36.7	9.4	7.41	78.8	
5H	27	0830	36.7–46.2	9.5	10.27	108.1	
6H	27	0910	46.2–55.7	9.5	9.99	105.0	
7H	27	1040	55.7–65.3	9.6	11.39	118.6	
8H	27	1105	65.3–74.8	9.5	10.54	110.9	
9H	27	1235	74.8–84.4	9.6	10.37	108.0	
10H	27	1305	84.4–94.1	9.7	10.85	111.8	
11H	27	1425	94.1–103.8	9.7	10.20	105.1	
12H	27	1500	103.8–113.4	9.6	11.14	116.0	
13H	27	1650	113.4–123.1	9.7	10.13	104.4	
14H	27	1725	123.1–132.8	9.7	10.73	110.6	
15H	27	1910	132.8–142.5	9.7	11.67	120.3	
16X	27	2030	142.5–143.0	0.5	0.00	0.0	Quaternary
17X	27	2205	143.0–143.3	0.3	0.37	120.0	
Coring totals				143.3	148.27	103.5	

We could not penetrate the hard formation encountered at 142.5 mbsf using the APC, and therefore decided to begin XBC operations with Core 128-798-16X. Cores 128-798-16X and 128-798-17X were taken to a depth of 143.3 mbsf; however, poor recovery (Table 1) and a poor rate of penetration (0.8 m in 60 min) with the poly-diamond compact bit (PDC) in the hard layer, later identified as a dolomite concretion (see "Lithostratigraphy" section, this chapter), resulted in a decision to terminate the hole. The bit cleared the rotary at 0124UTC, 28 August.

A severe tropical depression (Roger) came within 90 nmi of the site on 27 August, with heavy rain, winds of up to 42 kt, and 14-ft swells; however, operations continued without incident.

Hole 798B

The ship was moved 20 m north, and Hole 798B was spudded at 0542UTC, 28 August. Core 128-798-1H was shot 3 m shallower than the first core in Hole 798A to assure our recovery of the mud line. Continuous APC cores were taken to 142.6 mbsf (Table 2). As in Hole 798A, a recovery greater

than 100% results from expansion of gaseous sediments. Cores 128-798A-16X to 128-798A-54X were taken with the XCB to a depth of 517.9 mbsf. These cores were gaseous, causing sediment expansion with extrusion of material from both ends of the core barrel. In some cases, core bits were blown off during removal.

As it is standard practice, hydrocarbon gases were measured by both vacutainer and headspace analysis. Elevated concentrations of hydrocarbons (C_2 to C_5) were detected below 490 mbsf (see "Organic Geochemistry" section, this chapter). A rapid decrease in the methane to ethane (C_1/C_2) ratio, and an increase in concentrations of butane to propane were recorded at 510 mbsf. The C_1/C_2 values were anomalously low, given the estimated temperature in the hole (G. Claypool, written comm., 1989), indicating a possible thermogenic gas migration. Therefore, we decided to terminate drilling on the basis of the JOIDES Pollution Prevention and Safety Panel guidelines.

After a short trip to condition the hole, we displaced the hole with 2% KCl mud, and the drill pipe was pulled to 86

Table 2. Coring summary, Hole 798B.

Core number	Date (Aug. 1989)	Time (UTC)	Depth (mbsf)	Length cored (m)	Length recovered (m)	Recovery (%)	Age
1H	28	0450	0-9.4	9.4	9.43	100.0	Quaternary
2H	28	0510	9.4-18.4	9.0	9.41	104.0	
3H	28	0535	18.4-27.4	9.0	9.94	110.0	
4H	28	0550	27.4-36.8	9.4	10.27	109.2	
5H	28	0610	36.8-46.3	9.5	9.98	105.0	
6H	28	0640	46.3-55.8	9.5	11.19	117.8	
7H	28	0700	55.8-65.4	9.6	11.50	119.8	
8H	28	0720	65.4-74.9	9.5	11.10	116.8	
9H	28	0735	74.9-84.5	9.6	11.27	117.4	
10H	28	0755	84.5-94.2	9.7	10.27	105.9	
11H	28	0815	94.2-103.9	9.7	10.27	105.9	
12H	28	0840	103.9-113.5	9.6	10.89	113.4	
13H	28	0905	113.5-123.2	9.7	11.33	116.8	
14H	28	0925	123.2-132.9	9.7	11.41	117.6	
15H	28	0940	132.9-142.6	9.7	11.48	118.3	
16X	28	1025	142.6-152.3	9.7	9.83	101.0	
17X	28	1045	152.3-161.9	9.6	10.13	105.5	
18X	28	1115	161.9-171.6	9.7	9.29	95.8	
19X	28	1140	171.6-181.3	9.7	9.16	94.4	
20X	28	1210	181.3-191.0	9.7	11.79	121.5	
21X	28	1235	191.0-200.6	9.6	9.59	99.9	
22X	28	1305	200.6-210.3	9.7	11.88	122.5	Quaternary Pliocene
23X	28	1330	210.3-220.0	9.7	11.55	119.1	
24X	28	1355	220.0-229.7	9.7	9.93	102.0	
25X	28	1414	229.7-239.3	9.6	7.71	80.3	
26X	28	1435	239.3-249.0	9.7	0.00	0.0	
27X	28	1515	249.0-258.7	9.7	9.80	101.0	
28X	28	1550	258.7-268.3	9.6	11.21	116.8	
29X	28	1620	268.3-277.2	8.9	11.11	124.8	
30X	28	1655	277.2-286.4	9.2	9.18	99.8	
31X	28	1725	286.4-296.0	9.6	10.57	110.1	
32X	28	1755	296.0-305.7	9.7	11.94	123.1	
33X	28	1835	305.7-315.3	9.6	10.14	105.6	
34X	28	1905	315.3-325.0	9.7	6.77	69.8	
35X	28	1955	325.0-334.6	9.6	9.47	98.6	
36X	28	2035	334.6-344.3	9.7	3.50	36.1	
37X	28	2110	344.3-353.9	9.6	3.93	40.9	
38X	28	2150	353.9-363.6	9.7	8.64	89.1	
39X	28	2220	363.6-373.2	9.6	9.39	97.8	
40X	28	2255	373.2-382.9	9.7	7.85	80.9	
41X	28	2335	382.9-392.5	9.6	9.88	103.0	
42X	29	0015	392.5-402.2	9.7	9.33	96.2	
43X	29	0055	402.2-411.8	9.6	8.40	87.5	Pliocene
44X	29	0140	411.8-421.5	9.7	10.45	107.7	
45X	29	0220	421.5-431.1	9.6	12.63	131.5	
46X	29	0315	431.1-440.8	9.7	9.90	102.0	
47X	29	0400	440.8-450.4	9.6	9.71	101.0	Pliocene (?)
48X	29	0535	450.4-460.1	9.7	8.66	89.3	
49X	29	0635	460.1-469.7	9.6	9.92	103.0	
50X	29	0810	469.7-479.4	9.7	4.85	50.0	
51X	29	0940	479.4-489.0	9.6	9.00	93.7	
52X	29	1110	489.0-498.7	9.7	9.82	101.0	
53X	29	1300	498.7-508.3	9.6	6.87	71.5	
54X	29	1530	508.3-517.9	9.6	10.90	113.5	
Coring totals				517.9	514.42	99.3	

mbsf. A complete suite of four Schlumberger logs was run in good hole conditions. These logs consisted of the seismic stratigraphy, formation microscanner (FMS), lithoporosity, and geochemical tool combinations. In addition, the Lamont-Doherty TLT was attached to the base of each of the Schlumberger tool strings. These tool strings and their applications are described in the "Explanatory Notes" (this volume), and the results are discussed in the "Downhole Measurements" section (this chapter). After the logs were completed, the bit was pulled out of the hole., clearing the seafloor at 2300UTC, 30 August, and thus ending Hole 798B.

Hole 798C

The *JOIDES Resolution* was offset 20 m north, and Hole 798C was spudded at 0030UTC, 31 August, in water 900.1

mbsl. Continuous APC Cores 128-798C-1H to 128-798C-13H were taken to a depth of 120.1 mbsf (Table 3). Heat flow was measured every other core after Core 128-798C-4H. Our scientific objectives were considered complete, and the bit was pulled to the seafloor at 1150UTC, 31 August. The *JOIDES Resolution* departed Hole 798C at 1500UTC, 31 August 1989.

LITHOSTRATIGRAPHY

Introduction

The sedimentary sequence recovered at Site 798 consists of 514 m of clay, silty clay, diatomaceous clay to diatom ooze, foraminifer- and nannofossil-bearing biosiliceous sediments, and siliceous claystone (Fig. 11, backpocket figure). Frequently,

Table 3. Coring summary, Hole 798C.

Core number	Date (Aug. 1989)	Time (UTC)	Depth (mbsf)	Length cored (m)	Length recovered (m)	Recovery (%)	Age
1H	31	0040	0–6.3	6.3	6.33	100.0	Quaternary
2H	31	0100	6.3–15.3	9.0	9.85	109.0	
3H	31	0125	15.3–24.3	9.0	9.94	110.0	
4H	31	0145	24.3–33.7	9.4	10.27	109.2	
5H	31	0310	33.7–43.2	9.5	11.04	116.2	
6H	31	0335	43.2–52.7	9.5	10.33	108.7	
7H	31	0450	52.7–62.3	9.6	10.19	106.1	
8H	31	0510	62.3–71.8	9.5	11.27	118.6	
9H	31	0645	71.8–81.4	9.6	10.16	105.8	
10H	31	0700	81.4–91.1	9.7	11.20	115.4	
11H	31	0825	91.1–100.8	9.7	10.35	106.7	
12H	31	0850	100.8–110.4	9.6	10.83	112.8	
13H	31	1020	110.4–120.1	9.7	10.32	106.4	
Coring totals				120.1	132.08	110.0	

these units are interbedded with volcanic ash layers. Carbonate-rich sections are restricted to the upper 220 m of the sediment column, whereas well-preserved opaline sediments occur throughout the core to a depth of approximately 400 mbsf. Indurated siliceous claystones that contain up to 18% opal-CT, as well as varying amounts of glauconite and quartz sand, form the lowermost 60 m of the sequence. Authigenic dolomite nodules were observed at depths of 143 and 344 mbsf. The age of the sedimentary succession ranges from late Quaternary to late early Pliocene. No major hiatuses have been identified.

Three holes were drilled at Site 798 (Table 1; "Operations" section, this chapter). Acoustic basement was not reached. Holes 798A and 798C were drilled using the APC piston core to depths of 143.3 and 120.1 mbsf, respectively. Hole 798B was drilled using a combination of APC and XCB techniques to 517.9 mbsf. The upper part of Hole 798B was extensively sampled for the shipboard microbiology program, hence Cores 128-798B-1H through 128-798-13H were visually described by shipboard sedimentologists, but were not sampled for smear-slide description. Our lithostratigraphic summary is derived from a composite of all three holes. We have divided the sedimentary sequence at Site 798 into three lithologic units on the basis of composition, sedimentary structures, and mineralogy.

Unit I

Cores 128-798A-1H through 128-798A-17X, 128-798B-1H through 128-798B-23X-, Core 128-798C-1H through Section 128-798C-13H-CC; depth, 0–220 mbsf.

Unit I is 220 m thick and is composed predominantly of clay, silty clay, and diatomaceous clay and is characterized by the common occurrence of foraminifers and calcareous nanofossils. The predominant sedimentary packaging consists of well-defined rhythmic interbeds of dark gray to dark olive gray laminated sediments, alternating with light gray to greenish gray homogeneous or heavily bioturbated intervals. The darker, laminated sediments are enriched in diatoms, foraminifers, and organic carbon relative to the overlying bioturbated portions. Laminated/bioturbated sequences are present throughout Unit I to a depth of 180 mbsf and occur at scales of several centimeters to several meters. Volcanic ash layers ranging from 1 mm to 10 cm thick are common in the upper 170 m of Unit I.

The upper 20 m of Unit I is composed of clay, silty clay, and diatomaceous clay and is noticeably enriched in siliciclastic material, compared with the remainder of Unit I. Quartz grains are the dominant silt-sized component. Laminated/

bioturbated sequences become prominent within several meters of the top of the cores.

The remainder of Unit I is made up of mainly clay, diatomaceous clay, and diatom ooze with calcareous interbeds. Foraminifers and calcareous nanofossils are well-preserved and carbonate contents average 10% to 15%, with peak values of 37% (see "Organic Geochemistry" section, this chapter). Foraminifers are the most abundant calcareous component within diatom oozes, while calcareous nanofossils are most abundant in 10- to 50-cm-thick bioturbated and light-colored clay-rich intervals. Sediment layers enriched in foraminifers and calcareous nanofossils occur are most common between 40 and 140 mbsf (Fig. 12; "Organic Geochemistry" section, this chapter) and decrease downhole toward the Unit I/Unit II boundary at 220 mbsf. Diagenetic carbonates also are present in Unit I, with silt-sized euhedral rhombs of authigenic dolomite or calcite observed as shallow as 75 mbsf and a well-lithified, 37-cm-thick dolomite cemented horizon at 143 mbsf in Section 128-798A-17X-CC.

Preservation of siliceous microfossils is excellent throughout this unit. In some samples, visually estimated diatom contents exceed 50%. Radiolarians, sponge spicules, and silicoflagellates are also present in minor amounts.

Light bioturbated and dark laminated sediment sequences are evident within the top 142 m of Unit I. Their frequency and definition decreases below 142 mbsf. Volcanic ash layers are most abundant within this unit, particularly between 50 and 90 mbsf, where there is an average of five ash horizons per core (Table 4).

Based on paleomagnetic and biostratigraphic datums (see "Sediment Accumulation Rates" section, this chapter), the age span of Unit I is from the latest Quaternary to 1.88 Ma, with an average sedimentation rate of 117 m/m.y. (8.8 g/cm²/k.y.).

Unit II

Sections 128-798B-24X-1 through 128-798B-48X-4; depth, 220–455 mbsf.

Unit II is composed of uniform and moderately indurated diatomaceous clay interbedded with diatom ooze and silty clay. Calcareous components are either absent or poorly preserved, and carbonate contents average less than 4% (see "Organic Geochemistry" section, this chapter). Well-defined laminated/bioturbated cycles are absent; most of the Unit II sediments are faintly to extensively bioturbated. Diatoms are well preserved in the upper part of Unit II, while the most

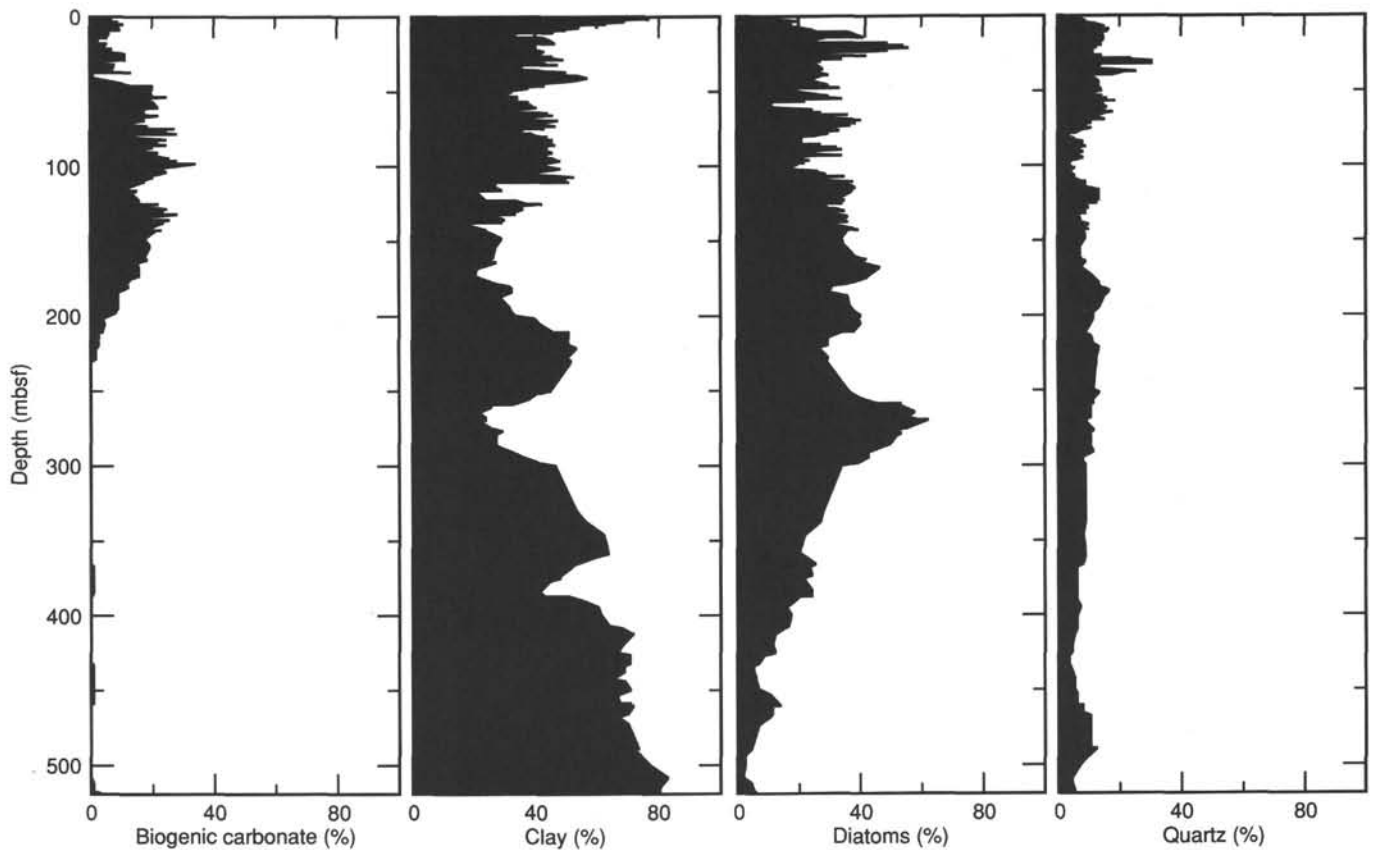


Figure 12. Estimated percentages of biogenic carbonate, diatoms, quartz, and clay vs. depth from smear slide observations of dominant lithologies in Holes 798A, 798B, and 798C. Data are presented as a 7-point moving average.

diatomaceous sediments (>50%) observed at Site 798 occur between 250 and 300 mbsf (Fig. 12). Diatom preservation estimated from smear slides decreases dramatically below Core 128-798B-39X (373 mbsf), coincident with the dissolved silica maxima in pore waters (see "Inorganic Geochemistry" section, this chapter). Biosiliceous sediments occur at the base of Unit II, but are characterized by an increasing ratio of sponge spicules to diatoms. Authigenic carbonate minerals are relatively rare in Unit II; however, small dolomite nodules approximately 3 to 4 cm in diameter were recovered at 334.4 mbsf in Section 128-798B-35X-CC and at 334.9 mbsf in Section 128-798B-36X-1.

The age of the base of Unit II is not well constrained by paleomagnetic or biostratigraphic datums, but is probably late Pliocene. The oldest datum (2.6 Ma) at 325 mbsf (see "Sediment Accumulation Rates" section, this chapter) yields an average sedimentation rate of 146 m/m.y. ($10.1 \text{ g/cm}^2/\text{k.y.}$) for the upper part of Unit II.

Unit III

Sections 128-798B-48X-4 through 128-798B-54X-CC; depth, 455–517.3 mbsf.

Unit III consists mainly of siliceous claystone and claystone, with variable amounts of sand-sized glauconite and quartz. The upper boundary of Unit III coincides with a sharp decrease in preservation of biogenic silica and the first distinct occurrence of opal-CT (Fig. 13). This boundary also corresponds to an abrupt increase in wet-bulk density and a decrease in porosity (see "Physical Properties" section, this chapter), as sediment lithification is enhanced by diagenetic transformation of opal-A to opal-CT. Unit III is also charac-

terized by rhythmic alternations between dark, laminated sediments and lighter-colored, bioturbated intervals, similar to the sequences observed in Unit I. At several intervals, burrows appear to be flattened as a result of sediment compaction. Near the base of the hole from 481 to 483 mbsf in Core 128-798B-51X, there are several coarse quartz sand layers. Glauconite sands were observed in four discrete layers that range from 5 to 20 cm thick and as isolated pockets between 489 and 492 mbsf in Sections 128-798B-51X-CC and 128-798B-52X-1 (Fig. 14). The age of the base of Unit III is most likely late early Pliocene.

Rhythmic Dark/Laminated and Light/Bioturbated Sequences at Site 798

Rhythmically alternating dark/light sedimentary couplets are prominent in sediments collected using the APC at Site 798 (Figs. 15 and 16). The characteristic color banding results from the presence of decimeter- to meter-scale cyclic alternations between dark, laminated and/or massive diatomaceous sediments enriched in foraminifers, and light-colored, clay-rich, bioturbated and/or massive sediments. Here, we provide a preliminary description and interpretation of the origin of these sedimentary rhythms.

Rhythmically alternating dark/light sequences are most clearly evident in APC-recovered sediments, particularly in the upper 45 m of Unit I, and appear in a less regular and prominent fashion downhole to 142 mbsf of Unit I. Below this depth, observations are obscured by drilling disturbance associated with the change from APC to XCB recovery. Nevertheless, rhythmic dark/light variations are present in some portions of the disturbed sediments downhole to Core 128-

Table 4. Ash layers at Site 798.

Layer number	Hole	Thickness (cm)	Lithologic type	Glass (%)	Petrographic type	Depth (mbsf)	Age (k.y.)
1	C	0.2	H		A	3.10	28.6
2	C	5.0	G		A	3.80	35.1
3	A, B, C	1.0	G	80	A	4.80	44.3
4	C	0.1	H	60	A	12.20	112.6
5	C	0.3	H		A	16.85	155.5
6	B, C	1.0	H		B	17.10	157.8
7	B, C	0.5	H	60	B	22.20	204.9
8	A, C	2.5	G	80	A	26.90	248.3
9	A	1.0	G	60	A	31.20	287.9
10	A, B, C	0.2	H	60	A	31.80	293.5
11	A, C	0.1	H	50	A	31.90	294.4
12	A, B	0.3	H	50	A	32.05	295.8
13	A, B, C	6.0	G	90	A	34.40	317.5
14	C	0.1	H		B	37.00	341.5
15	B, C	0.3	H		A	37.35	344.7
16	B, C	0.2	H		B	37.70	347.9
17	C	0.1	H		B	37.80	348.8
18	B, C	0.1	H		A	38.80	358.1
19	B, C	0.1	H		A	40.40	372.8
20	B, C	0.1	H		A	40.80	376.5
21	A, C	0.2	H		A	45.80	422.7
22	A, B, C	4.0	G	95	A	46.00	424.5
23	B, C	0.1	H		B	46.10	425.4
24	A, C	0.1	H	95	B	47.40	437.4
25	A, C	0.1	H	95	B	47.50	438.4
26	A	0.1	H	95	B	47.70	440.2
27	C	0.5	H		A	48.90	451.3
28	A, B, C	0.1	H	65	B	51.00	470.7
29	B	0.5	H		B	52.50	484.5
30	A, C	0.1	H	55	B	54.90	506.7
31	C	0.1	H		B	54.95	507.1
32	A, C	4.0	T	80	A	55.05	508.0
33	A, C	0.3	H		B	55.15	509.0
34	A, C	0.1	H		B	55.35	510.8
35	A, C	0.1	H	65	A	55.50	512.2
36	B, C	0.6	H		A	56.40	520.5
37	C	3.5	G	90	A	56.60	522.4
38	B, C	5.5	G	70	A	56.70	523.3
39	C	0.1	H		B	57.00	526.0
40	A, C	0.1	H	60	A	57.10	527.0
41	C	0.1	H	50	A	57.20	527.9
42	B, C	0.1	H	60	A	57.30	528.8
43	B, C	3.5	G	90	A	57.35	529.3
44	C	3.5	G	65	A	57.40	529.7
45	C	0.2	H		A	57.50	530.7
46	C	0.8	H	65	A	57.60	531.6
47	C	0.1	H	70	A	59.50	549.1
48	A, B	2.0	G	95	A	61.70	569.4
49	A	0.2	H		A	62.50	576.8
50	A, B, C	4.0	G	60	A	64.50	595.3
51	A, C	1.0	G		A	64.65	596.6
52	A, C	0.8	H	80	A	64.90	598.9
53	A	0.5	H		A	65.20	601.7
54	B, C	0.2	H		B	65.60	605.4
55	B	0.1	H		B	65.80	607.3
56	B	0.1	H		B	69.70	643.2
57	A, B, C	0.1	H		B	71.40	658.9
58	B, C	0.1	H		B	71.55	660.3
59	A, B, C	4.0	G	60	A	73.40	677.4
60	A, B, C	0.3	H	70	A	73.50	678.3
61	B, C	0.3	H		A	78.20	721.7
62	B, C	0.3	H		A	78.50	724.5
63	B, C	2.0	G		A	78.70	726.3
64	C	0.2	H		A	79.15	730.5
65	C	0.2	H		B	79.30	731.8
66	C	2.0	G		B	79.40	732.8
67	C	0.7	H		A	79.50	733.7
68	B, C	0.3	H		A	80.90	746.6
69	A, B, C	0.4	H		B	84.20	777.1
70	A, B, C	0.2	H		B	85.20	786.3
71	C	0.1	H	95	A	92.25	934.6
72	A, C	0.3	H		A	92.40	937.6
73	A, C	2.0	G	90	A	93.30	953.8
74	A, C	0.3	H	70	B	93.45	956.8
75	B, C	10.0	T		A	95.10	982.0
76	C	0.1	H	50	A	98.30	1008.0
77	A, C	0.1	H	50	B	103.80	1041.5

Table 4 (continued).

Layer number	Hole	Thickness (cm)	Lithologic type	Glass (%)	Petrographic type	Depth (mbsf)	Age (k.y.)
78	A, C	0.1	H		B	103.90	1042.8
79	C	0.1	H		B	104.80	1049.0
80	C	0.1	H	90	A	105.00	1050.5
81	C	0.2	H		A	105.80	1057.0
82	C	0.1	H		A	112.20	1109.0
83	A, C	0.2	H	90	A	112.90	1114.5
84	B, C	0.1	H		B	113.90	1122.0
85	A	0.2	H	95	A	114.90	1129.0
86	A,B,C	0.5	H	90	A	115.20	1131.0
87	B	0.1	H		A	119.40	1161.0
88	B	0.1	H		A	119.50	1162.0
89	B	0.1	H		A	119.90	1164.5
90	B	0.1	H		A	120.00	1165.0
91	B	0.1	H		A	120.35	1168.0
92	B	0.1	H		A	122.20	1181.0
93	A, B	1.0	H	95	A	124.40	1197.0
94	A	0.5	H	92	A	124.70	1199.0
95	A, B	0.3	H	90	A	125.00	1201.0
96	A	0.6	H		A	125.40	1204.0
97	A, B	0.3	H		A	125.90	1208.0
98	B	3.0	G	95	A	135.30	1287.0
99	A, B	0.2	H	95	A	140.40	1323.0
100	A, B	0.8	H	85	A	140.75	1324.5
101	A	0.5	H	95	A	140.80	1325.0
102	B	0.7	H	95	A	175.60	1535.0
103	B	1.5	G	90	A	176.80	1545.0
104	B	5.0	G	98	A	282.10	2370.0
105	B	2.0	G		A	404.60	3449.0
106	B	15.0	TT	97	A	414.00	3527.0
107	B	15.0	TT	65	A	425.80	3625.0
108	B	1.5	TT		A	429.20	3653.0
109	B	11.0	TT		A	435.50	3705.0
110	B	5.0	TT		A	439.80	3741.0
111	B	1.0	H		B	441.20	3752.0
112	B	2.5	G		B	441.30	3753.0
113	B	3.0	G	99	A	465.60	3954.0

Lithologic types: H = homogeneous, G = graded, T = heterogeneous, TT = turbidite. Petrographic types: A = acid, B = basic.

798B-19X (180 mbsf). The lowermost sediments within Unit I and throughout Unit II (180–455 mbsf) are uniformly bioturbated clays and diatomaceous clays, and observed dark/light sequences are restricted to short intervals (e.g., within Sections 128-798B-23X-7, at 218 mbsf, and 128-798B-30X-6, at 286 mbsf). Regular dark/laminated-light/bioturbated sequences appear again below 475 mbsf, within Unit III.

Thicknesses of the dark/light couplets are variable and range from several centimeters to several meters in the sediments of Unit I; in Unit III, sequence thicknesses vary on a decimeter scale.

The dark/light sequences consist predominantly of diatomaceous oozes and clays with diatoms; the relative proportion of biogenic silica vs. terrigenous clay is the first-order source of compositional variability. In addition, calcareous sediments, such as nanofossil clays and clays with nanofossils, are also distinctive components in some sections (e.g., Sections 128-798C-4H-4, at 0–33 cm (29 mbsf); Section 128-798C-5H-7, at 59–126 cm (41 mbsf)). In Unit III, the dark/light sequences are preserved in moderately well-indurated siliceous claystones.

Although some variability was observed in thickness and bulk composition, the internal arrangement of sedimentary and biogenic structures and the vertical lithologic variation within these dark/light sequences are remarkably constant (Table 5; Fig. 17); these are summarized as follows:

1. The base of the dark interval is generally well defined, and in a few cases, distinctively sharp, possessing millimeter-

scale irregularities. However, in most cases, evidence for erosional truncation is absent. In some cases, the lower boundary is gradational (e.g., Sections 128-798C-1H-2, at 75–90 cm (2.25 mbsf) and 128-798C-3H-6, at 85–105 cm (23.3 mbsf)).

2. The dark interval itself is either thinly to thickly laminated and finely bedded (laminae range from 1 mm to 2 cm thick) or massive. If both stratification types are present, the massive interval is often superimposed on the laminated interval. Individual laminae are composed of rhythmic dark/light couplets, which range from 3 to 15 mm thick. These fine laminae generally possess a sharp base—a dark, diatomaceous, lower sublayer that grades upward into a light, clay-rich upper sublayer. In this fashion, fine-scale rhythmic lamination mirrors the overall rhythmic bedding on a millimeter scale. Locally, thin laminae (1.5 mm thick) occur; these are matrix-poor and highly enriched in foraminifers or sponge spicules (e.g., Sections 128-798C-7H-3, at 13–16 cm (55.8 mbsf) and 128-798C-9H-5 at 135–136 cm (79 mbsf)). In general, the dark intervals are enriched in foraminifers and diatoms, and impoverished in clays, relative to the superjacent light intervals. Moreover, the dark intervals are enriched in organic matter, whereas the organic matter contents in the light intervals are considerably lower (see “Organic Geochemistry” section, this chapter).

3. The transition from the dark laminated and/or massive interval upward into the light-colored, clay-rich interval is commonly gradational; however, in most cases, this interface is partly to extensively reworked by burrowing, which pene-

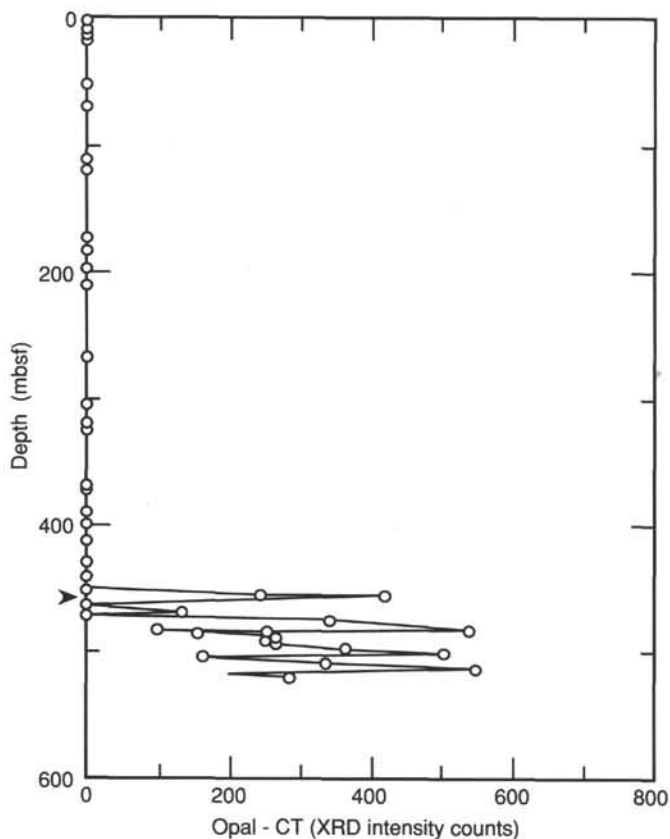


Figure 13. Opal-CT peak intensity counts from X-ray diffraction vs. depth for samples from Site 798. Arrow indicates first occurrence of Opal-CT.

trates downward into the dark sediments (maximum penetration depth observed is approximately 20 cm). The burrows commonly measure 2 to 4 mm in diameter, are characterized by downward-directed bifurcations, and are filled in with light-colored and clay-rich sediment similar to that of the overlying light-colored interval. These distinctive burrows are interpreted as *Chondrites* (Fig. 18).

In approximately one-third of all sequences (visual estimation), *Chondrites* burrows are crosscut by larger, subhorizontal to vertical, unidentified infaunal deposit feeding burrows (maximum diameter is 2 cm; some resemble *Planolites*), which generally penetrate more deeply downward into the laminated sediments (up to 30 cm or more; Figs. 19 and 20). *Chondrites* is generally interpreted as an indicator of anoxic pore waters and dysaerobic bottom waters (Bromley and Ekdale, 1984; Savdra and Bottjer, 1986); the larger, unidentified burrows may indicate better oxygenated bottom waters, and it is possible that the tiering of large burrows resulted from higher oxygenation levels in the bottom waters. In other cases, the upper portions of the *Chondrites* burrowed clay-rich sediment appear to lack bioturbation; here, the sediments may reflect a decrease in quality of the infaunal habitat (possibly low oxygen levels?) and consequent exclusion of *Chondrites*.

Dark/light rhythms within lithologic Unit III are somewhat different from those observed in Unit I. They are characterized by dark, finely laminated, siliceous claystones, interbedded with less darkly colored, thoroughly bioturbated, siliceous claystones (Fig. 21). The lower boundary of the dark intervals is either gradational or sharp; commonly, it is

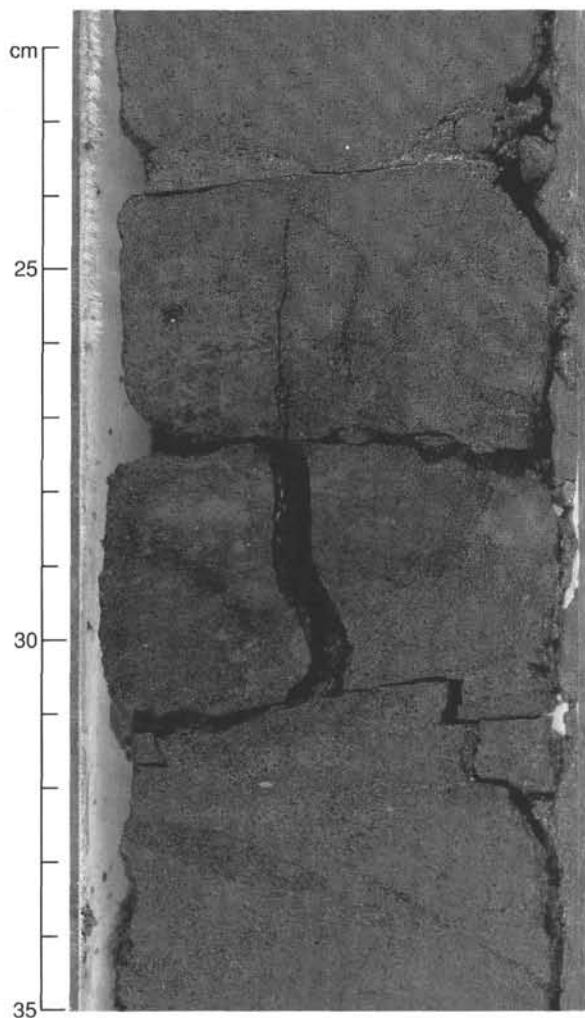


Figure 14. Glauconite-rich interval in lithologic Unit III. Dispersion of the glauconite particles results from extensive bioturbation (Section 128-798B-52X-1).

disrupted by bioturbation. The lower boundary of the light intervals is transitional and mostly obliterated by bioturbation. Light intervals contain scattered sand-sized glauconite grains, whereas the dark intervals are commonly glauconite-barren.

The prominent dark/light sedimentary rhythms observed in Pleistocene sediments at Site 798 may correlate to similar rhythms, described from other localities in the Sea of Japan (e.g., Ichikura and Ujiie, 1976; Tamaki, Pisciotto, et al., in press). The dark-colored sediments are enriched in organic matter, lack syndepositional burrowing infauna, and preserve their original stratification. This may document the presence of oxygen-depleted bottom waters during their formation, which prevented the colonization of burrowing macrofauna and enhanced preservation of organic matter. The lower portions of the light-colored intervals are thoroughly burrowed, and the observed tiering of burrows may indicate progressive oxygenation of bottom waters in some cases.

Sedimentary Structures

Soft-Sediment Deformation Features

Several features that could be related to syndepositional or late depositional events were encountered, especially in Hole

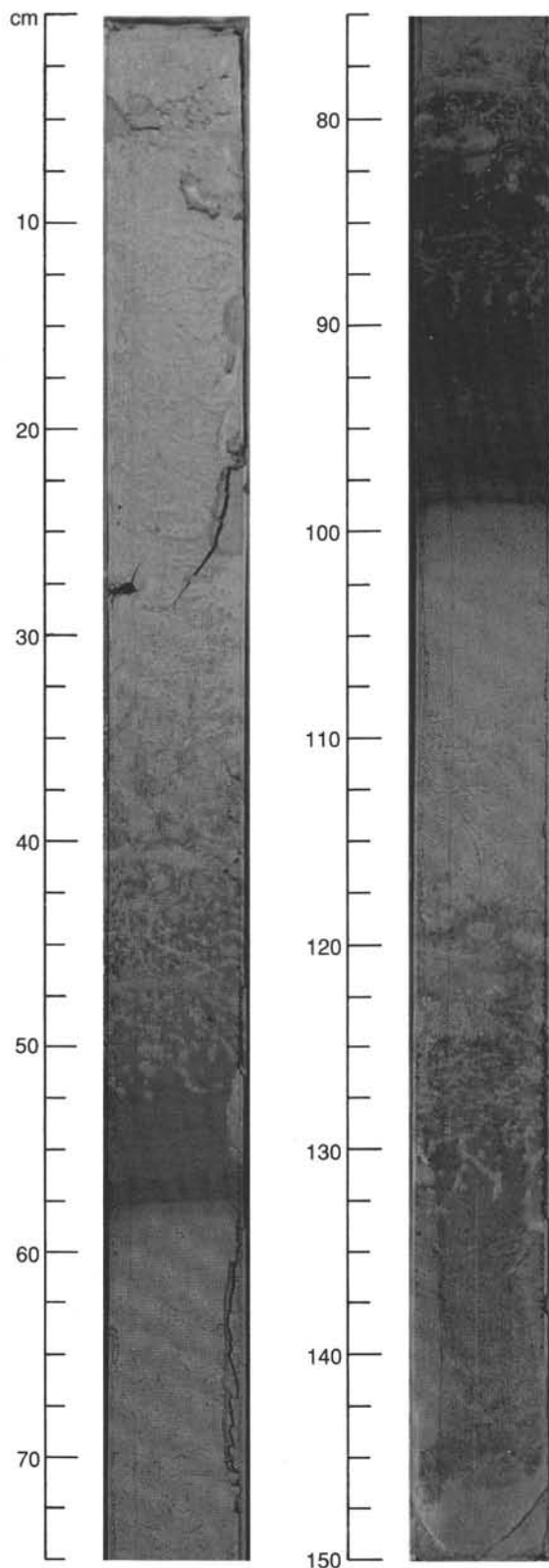


Figure 15. Rhythmic dark/light sequences in lithologic Unit I (Section 128-798A-1H-4). Note the sharp lower boundaries of the black intervals and the burrowed upper parts of the dark intervals (by *Chondrites*, and larger burrows).

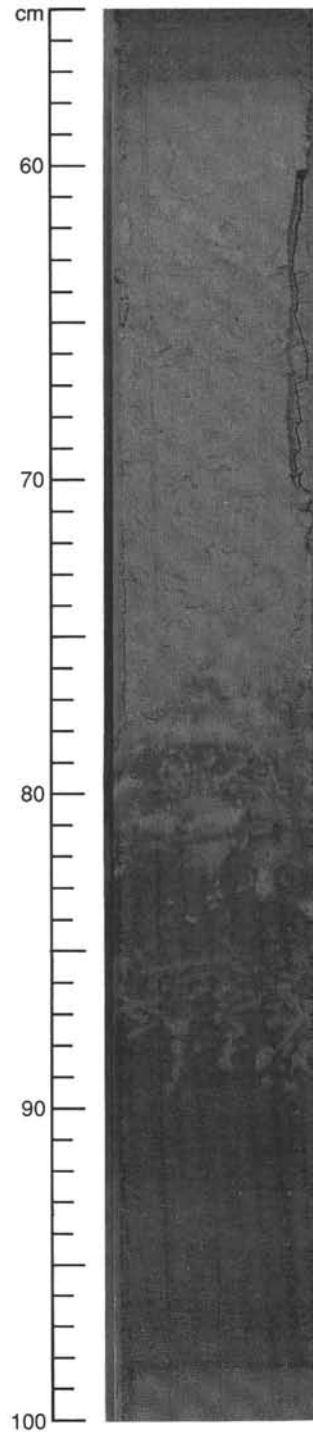


Figure 16. Close-up of a dark/light sequence, Section 128-798A-1H-4, 55-100 cm.

798A, and to a lesser extent in Hole 798C. These features consist of local irregular nonplanar and nonhorizontal lithologic boundaries and slumplike folding that was accompanied by stratal disruption. Some slumplike deformation probably results from drilling disturbance (see "Explanatory Notes" chapter, this volume).

Irregular lithologic boundaries are documented in Section 128-798A-7H-1. At the interval from 32 to 40 cm (about 56 mbsf), a piece of light olive gray clay is bounded at the bottom and to the right by a dark gray layer, while it is bounded at the

Table 5. Summary of properties of rhythmic sedimentary couplets, Site 798.

Color	Sedimentary structures	Composition	Total organic carbon ^a	Carbonate content ^a
"Dark"	Laminated or massive	Diatomaceous; foraminifer-rich laminations, ± nannofossil-enriched.	4%–5%	1%–30%
"Light"	Massive and structureless. Bioturbation is common (<i>Chondrites</i> , ± <i>Planolites</i>)	Clay-rich with diatoms; foraminifers very sparse	2%–3%	1%–30%

^aBased on limited analyses; see "Organic Geochemistry" section, this chapter.

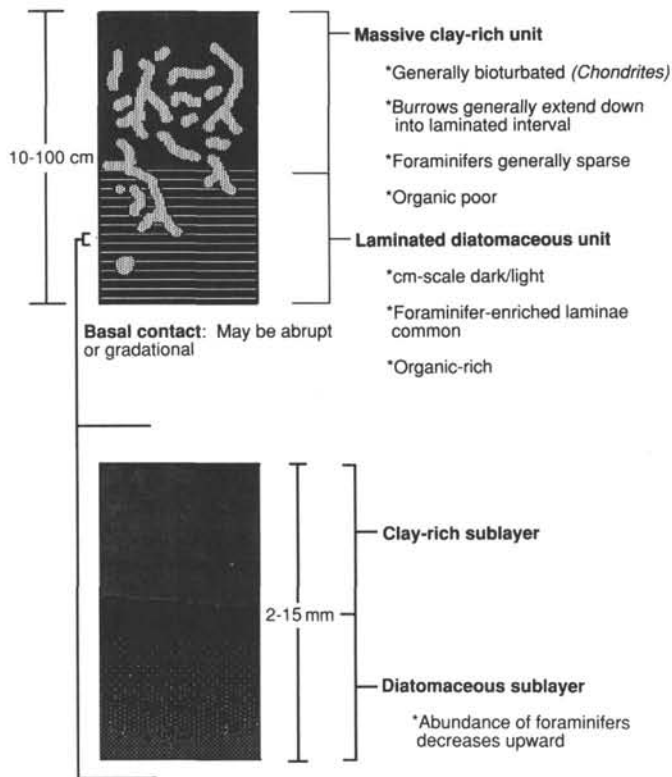


Figure 17. Schematic overview of a typical dark/light bedding sequence.

top by a darker olive gray clay having a faint horizontal basal contact (Fig. 22). At 42 cm, horizontal bedding can also be seen. This structure, with no symmetry with respect to the core axis, appears to be natural and probably results from slump deformation or a gliding phenomenon prior to deposition of the upper clay. The counterpart of this example may be the case of Section 128-798A-7H-1 at 77–79 cm (56.50 mbsf), where the clayey level is separated from the overlying darker biosiliceous clay by an irregular boundary (Fig. 23). Local nonhorizontal lithologic boundaries also occur in Sections 128-798A-9H-2 at 45 cm, 128-798A-9H-3 at 80 cm, and 128-798C-9H-5 at 131–138 cm (Fig. 24).

Brittle Features: Veins and Faults

A dozen brittle fractures of vein-type or unambiguous microfaults were observed from 38 mbsf to the bottom of Hole

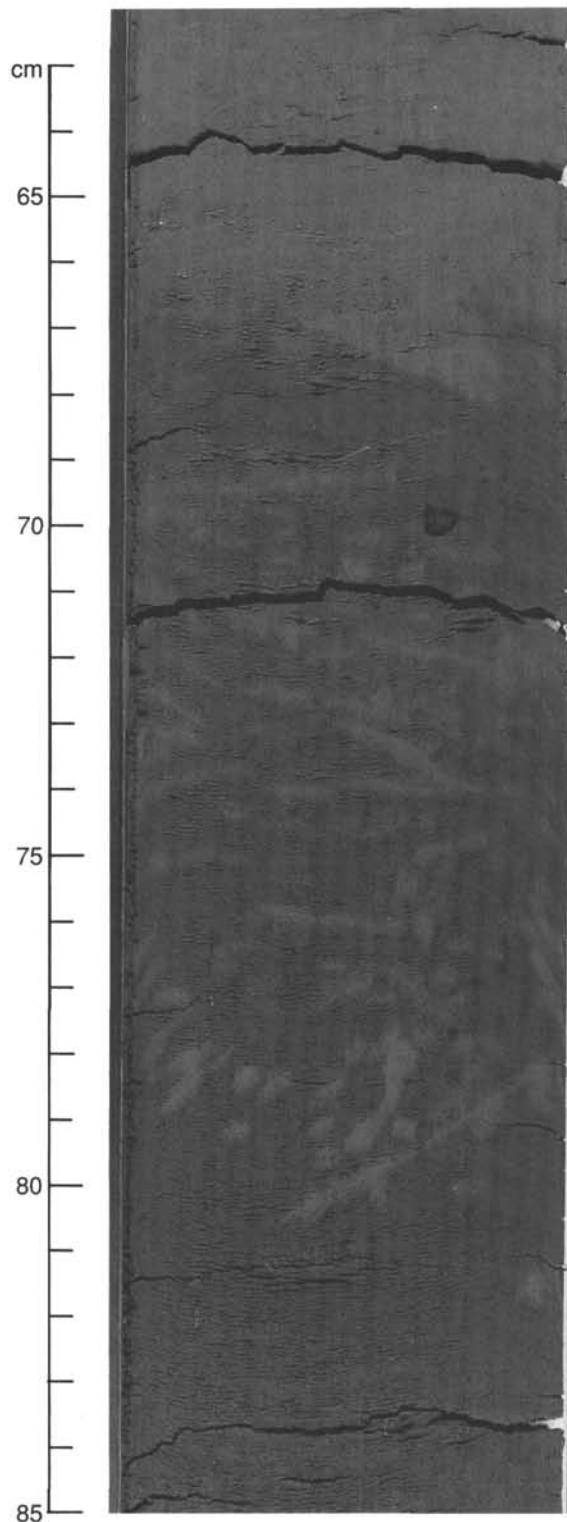


Figure 18. *Chondrites* burrows penetrate a dark-colored, diatomaceous interval. Burrows are filled with light-colored, clay-rich sediments similar to the overlying light-colored unit (Unit I, Section 128-798A-3H-6).

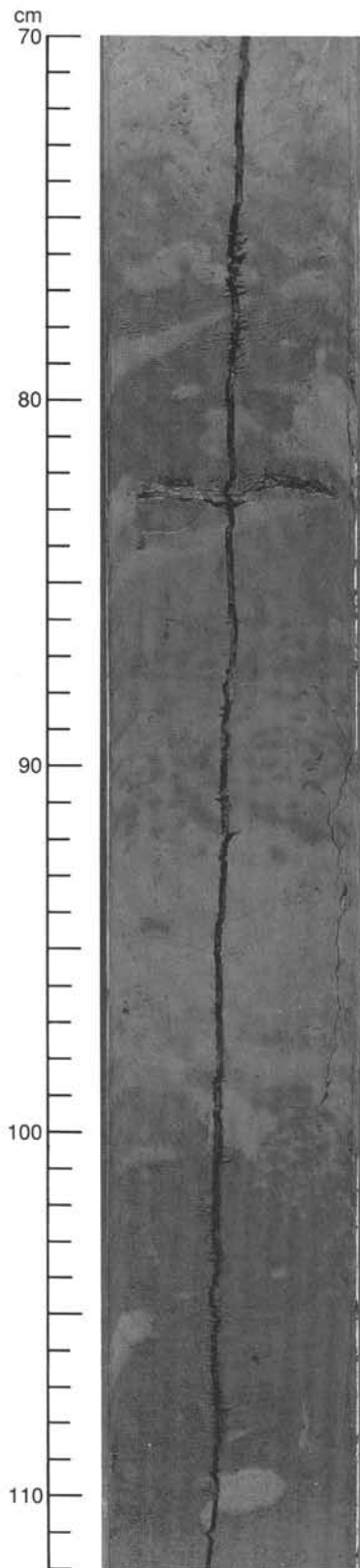


Figure 19. Three burrowed horizons marking interfaces of dark/light intervals. Note the presence of *Planolites*-like, subhorizontal burrows in the upper and lower horizons. Note also the presence of *Chondrites* in the light-colored sediments of the middle horizon, infilled by darker sediments (a typical configuration in dark/light intervals; Unit I, Section 128-798A-3H-2).

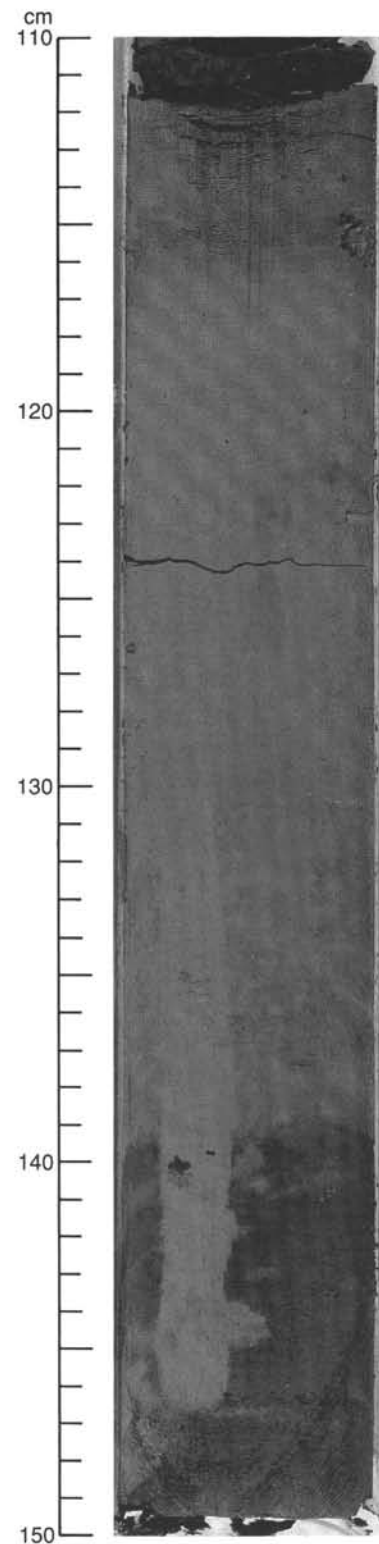


Figure 20. Tiering of burrows: small *Chondrites* burrows are intersected by a prominent vertical burrow, piping down into a dark, crudely laminated interval (Unit I, Section 128-798B-4H-1).

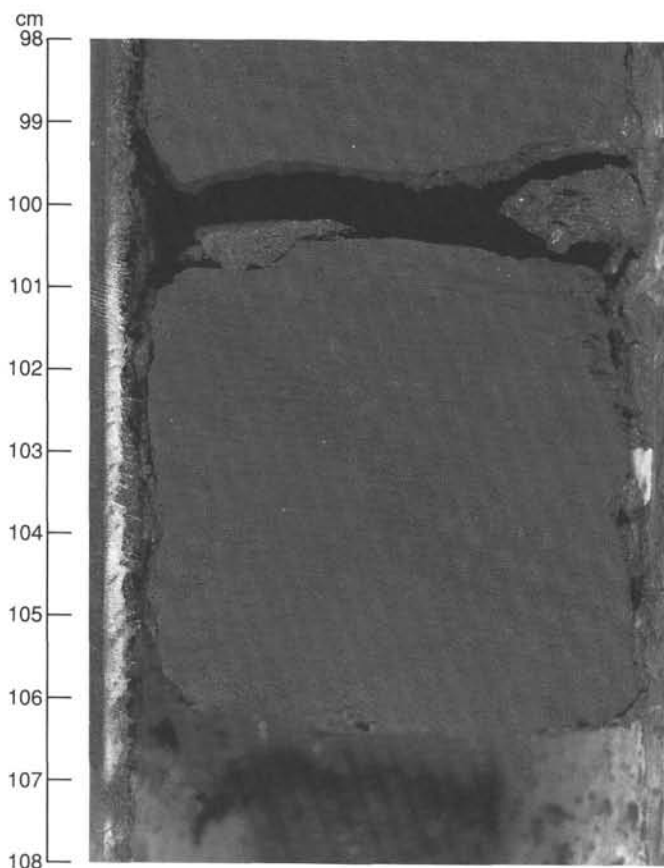


Figure 21. Burrowed interval in Unit III, Section 128-798B-51X-6. Note the general horizontal alignment of burrows, the tiering of *Chondrites* in larger burrows (*Planolites?*), and the prominent horizontal burrow with internal "spreiten" (probably *Teichichnus*).

798B (517.9 mbsf). These cluster in the lower part, but some are present in shallower levels.

A typical array of medium-sized dark veins (4 cm long), mainly parallel, sometimes branching, is present in Section 128-798B-53X-1 at 110–117 cm (Fig. 25). These are similar to the examples described in forearc regions (Carson et al., 1982; Lundberg and Moore, 1986) and in the hemipelagites of the Nankai Trench (Lundberg and Karig, 1986). The dark filling is probably composed of *in-situ* sediment. Along individual veins, with apparent dips of at least 65° to 70° (section is nonorthogonal to strike), a slight offset (less than 1 mm) of lamination beds is sometimes visible. Usually normal fault-slip movement is indicated, as has been observed at other sites (Lundberg and Moore, 1986). The bulk geometry of the array is a band parallel to bedding. The most likely interpretation is early bedding-parallel extension (Lundberg and Moore, 1986; Knipe, 1986), with the fractures providing dewatering channels. The *en-echelon* pattern also suggests a set of tension gashes related to a bedding parallel shear from gliding.

Other solitary veins of slightly larger size, steeply dipping, are present in Sections 128-798A-15H-3 at 47–65 cm and 128-798B-43X-4 at 55–61 cm (Fig. 26), 128-798B-50X-1 at 40–50 cm (Fig. 27) at about 136.4, 407.3, and 470.1 mbsf, respectively. These veins do not exhibit any macroscopically measurable offset, although the curvilinear one present in Section 128-798B-50X-1, similar to the "pseudoveins" of the Nankai Trench hemipelagites, seems to crosscut and bound a burrow. In Section 128-798B-50X-2 at 80–90 cm (Fig. 28), a similar vein exhibits millimeter-scale normal offset. Some

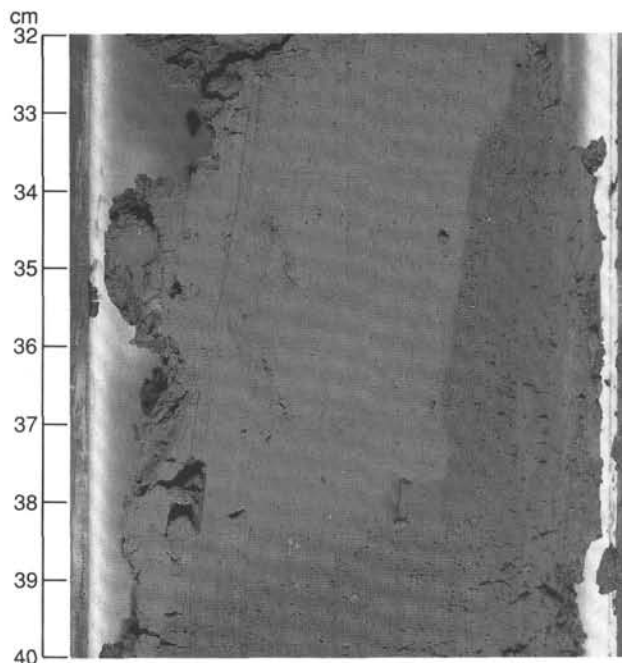


Figure 22. Irregular, nonhorizontal lithologic boundary in Section 128-798A-7H-1 at 32 to 40 cm.

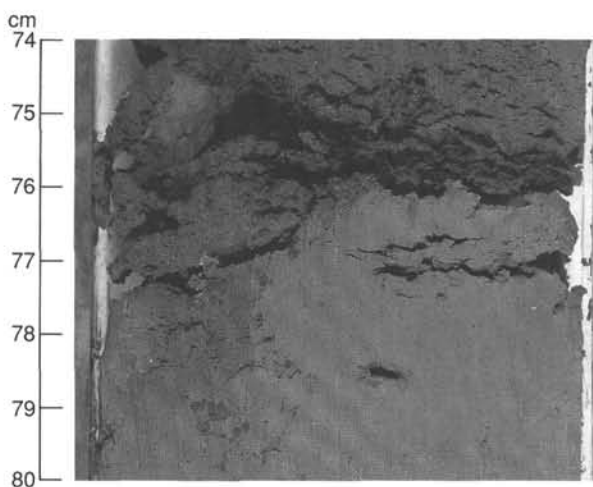


Figure 23. Disturbed, irregular lithologic boundary in Section 128-798A-7H-1 at 74 to 80 cm.

dark "veins," which have a gentle apparent dip (in the core splitting section), are probably healed normal faults, as shown in Sections 128-798B-49X-2 at 26–30 cm (Fig. 29) and at 125–142 cm (Fig. 30) at about 462 and 463 mbsf.

A long white vein occurs in Section 128-798A-5H-1 at 118–150 cm (38 mbsf) in Quaternary diatomaceous sediments (Fig. 31). The vein-filling material may be volcanic ash. This crack is evidence of brittle failure of diatomaceous clay, probably under layer parallel extension, in a shallow environment, and probably, under high fluid pressure. This can be related to the high fluid content and high porosity measured at that depth (see "Physical Properties" section, this chapter) under the load of the overlying pile.

In summary, some brittle features, interpreted as extensional structures, are noticeable at this site, especially between 400 and 517 mbsf, in the Pliocene. Similar vein structures have so far been described mainly in forearcs, with the

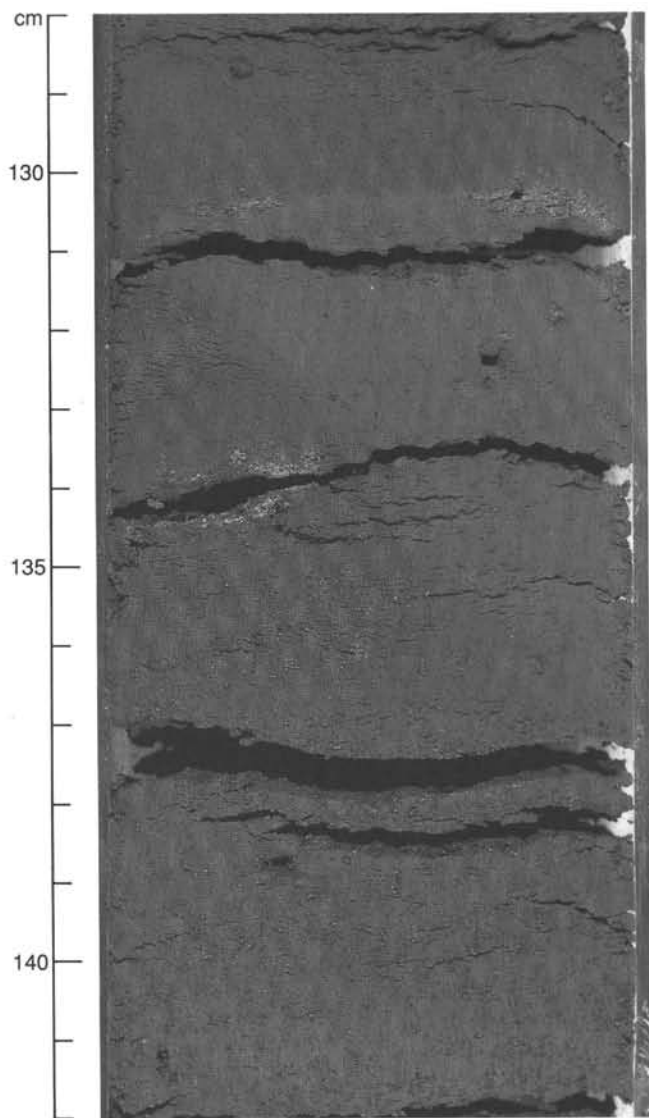


Figure 24. Nonhorizontal lithologic boundary in Section 128-798C-9H-5 at 128 to 142 cm. This dip was probably set before deposition of the upper layer, which shows a horizontal basal boundary.

exception of the Nankai Trough. Their occurrence in another setting is notable. At Site 798, we did not observe any evidence of compression, either in relation to the Holocene compressional deformation in the eastern Sea of Japan (Nakamura, 1983; Lallemand et al., 1985; Jolivet, 1986; Tamaki, 1988) or in the Izu collision on the Pacific coast of Japan (Matsuda, 1978; Huchon and Angelier, 1987), nor in the Pliocene strata, in relation to the Tanzawa collision that affected central Japan in the early Pliocene (Niitsuma and Matsuda, 1985; Huchon and Angelier, 1987; Charvet and Fabbri, 1987).

Gravitational Compaction Structures

Incipient fissility first appears within some drilling biscuits in Section 128-798B-43X-1 at 20–43 cm (Fig. 32), at 422.2 mbsf, where parting surfaces have been opened by core splitting. This feature is frequent from Core 128-798-51X (479.4 mbsf) down to the bottom of Hole 798B (518 mbsf). In the last cores, especially in Core 128-798-54X, the compaction effect is marked by a conspicuous flattening of bioturbation features, leading to a pseudolamination aspect. However,

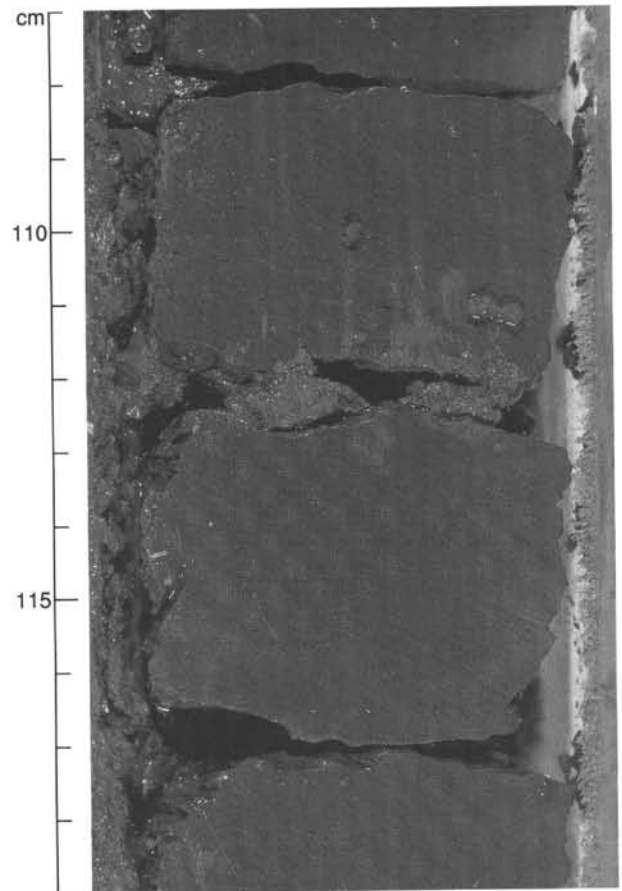


Figure 25. Vein array in Section 128-798B-53X-1 at 107 to 119 cm. Notice the *en-echelon* pattern and the slight offsets, mostly normal.

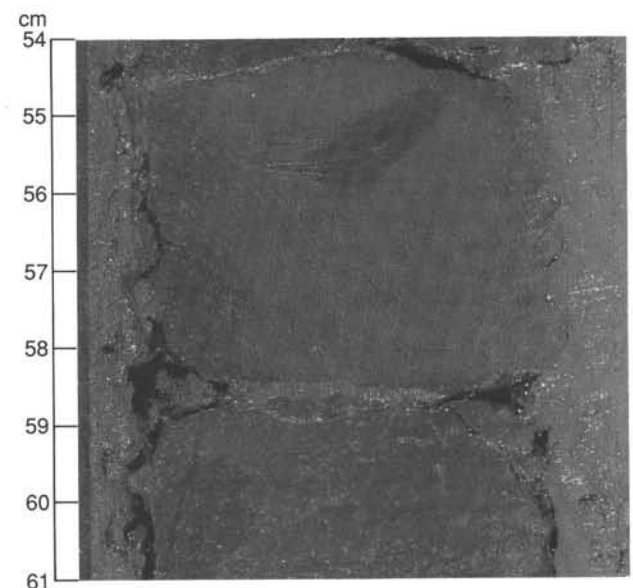


Figure 26. Dark vein in Section 128-798B-43X-4 at 54 to 61 cm.

the first appearance of fissility is late, compared with the late Pliocene hemipelagites of the Nankai Trough (Kagami et al., 1986; Lundberg and Karig, 1986). The reasons probably include the high porosity and fluid content observed at Site 798 down to its bottom and then a high pore pressure that reduced the effective stress.

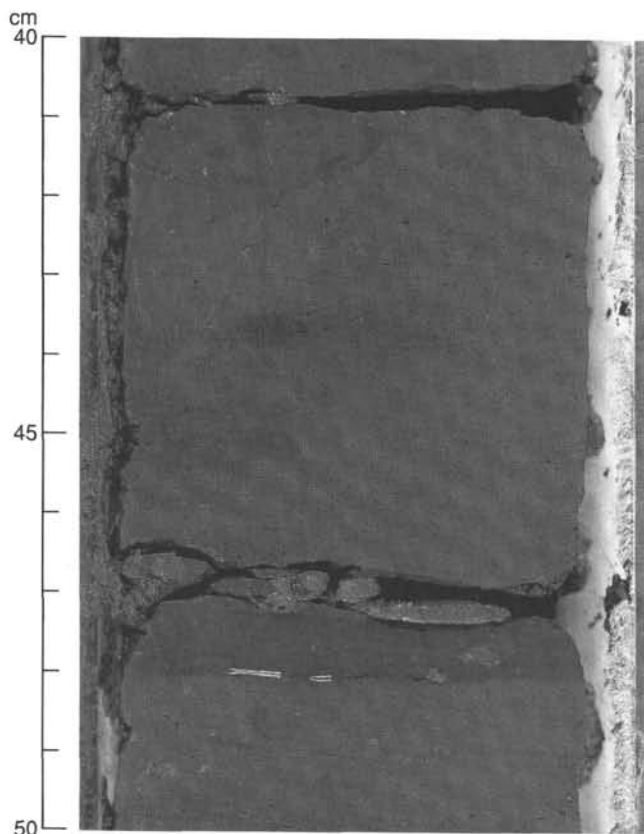


Figure 27. Curvilinear dark vein in Section 128-798B-50X-1 at 40 to 50 cm.

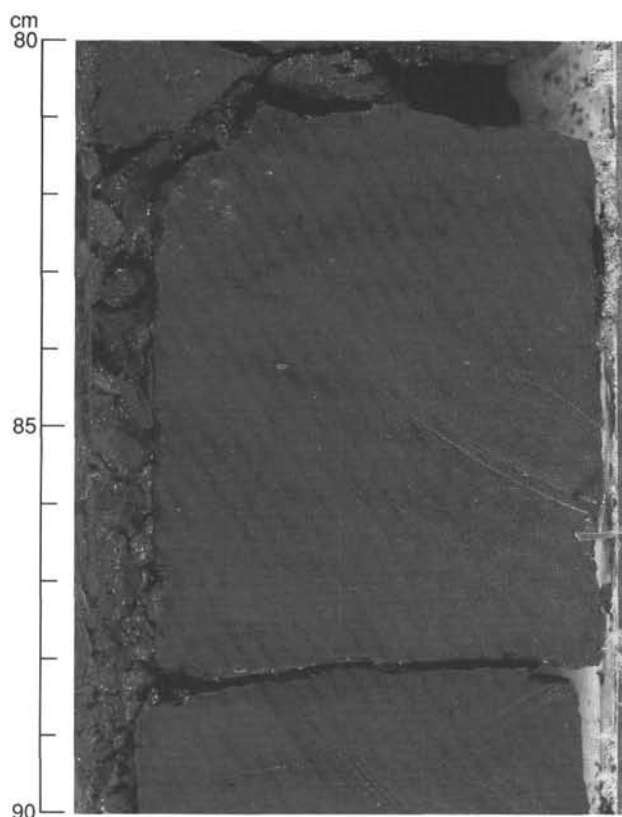


Figure 28. Curvilinear vein in Section 128-798B-50X-2 at 80 to 90 cm. Notice the small normal offset of a black lamination near the top.

Authigenic Carbonates

Authigenic carbonates are comparatively sparse at Site 798; megascopic dolomite concretions were encountered at only three horizons. This observation is in accord with the fact that pH values decrease from 7.5 at the sediment/water interface to about 7.1 at 400 mbsf (see "Inorganic Geochemistry" section, this chapter). Such unfavorable chemical conditions probably were created by the rapid rate of sedimentation and extremely high concentration of methane in the sediments (see "Organic Geochemistry" section, this chapter).

Authigenic carbonates at Site 798 occur as (1) disseminated rhombs, (2) pieces of nodules, and (3) a thick, hard, dolomite-cemented layer. Smear-slide observation revealed that 1 to 5 vol% disseminated, authigenic, carbonate rhombs occur in biogenic carbonate-bearing sediments of the upper part of lithologic Unit I (5–85 mbsf) and terrigenous matter-rich sediments of the lower part of Unit II and between 383 and 504 mbsf in Unit III. The lower part of Unit I and the upper part of Unit II are mostly carbonate-free with the exceptional dolomite concretion.

X-ray diffraction (XRD) analysis identified minor amounts of dolomite in three un lithified ooze and claystone samples (128-798B-20X-2, 40 cm; 128-798B-51X-4, 43 cm; 128-798B-53X-1, 1 cm) from 49 samples that were randomly selected throughout the cores of Hole 798B. Strong calcite peaks appear in all the samples from Unit I, as expected from the abundance of biogenic carbonates. However, no calcite was detected in samples from Units II and III. The amounts of disseminated carbonates may be under the detection limit of

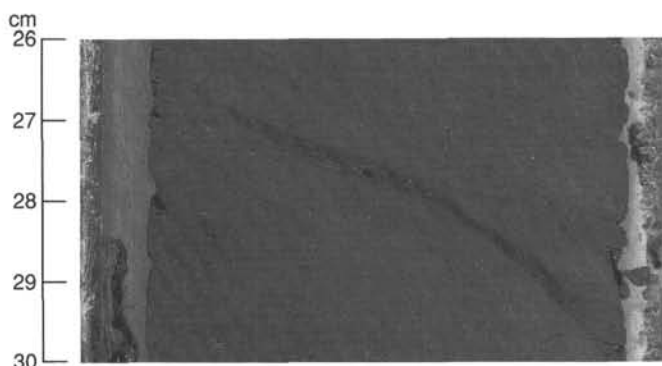


Figure 29. Healed fracture, probably normal fault, in Section 128-798-49X-2 at 26 to 30 cm.

the shipboard XRD system, and/or the authigenic carbonate at Site 798 might be dolomite. Shore-based studies will resolve this matter.

Portions of dolomite concretions were found in Samples 128-798B-35X-CC, 23–28 cm, and 128-798B-36X-1, 25–27 cm, at approximately 335 mbsf. These dolomites are olive gray to gray (5Y 4/2 to 5Y 5/1) and occur in moderately disturbed diatomaceous clay, or within an intensively disturbed drilling biscuit. They are considered to have been broken during drilling. A boundary between the dark- and light-colored parts observed in these dolomites is sharp. This color change in a broken concretion may represent a zoned structure within the original single concretion, or alternatively, it may be large burrow.

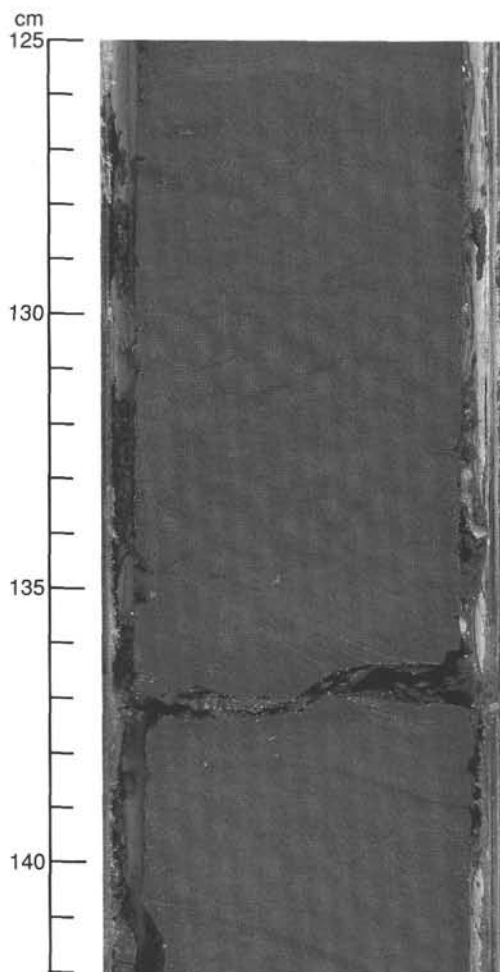


Figure 30. Apparent gently dipping oblique sections of healed fractures in Section 128-798B-49X-2 at 125 to 142 cm.

A hard dolomite layer was encountered in Section 128-798A-17H-CC at 0 to 33 cm (approximately 143 mbsf) in the lower part of Unit I. The dolomite layer, 33 cm thick, is dark gray to pale yellow (5Y 7/3 to 5Y 7/2) and is well lithified. The top surface is partly covered by 1 to 2 mm thick dark gray (5Y 4/2) diatomaceous ooze, whereas the bottom is broken and marked by a fresh fracture surface (Fig. 33). The true thickness of the layer is considered to be greater than the recovered length. The dolomite layer contains an abundance of *Chondrites* and *Planolites* burrows and is moderately mottled, suggesting that this layer was formed after the burrowing and mottling.

Under the microscope, this layer is tightly cemented by finely crystallized anhedral dolomite of 0.002 to 0.01 mm in diameter, with trace amounts of framboidal pyrite (Fig. 34). Well-preserved diatoms and sponge spicules are common, and foraminifers are rare. Calcareous nanofossils were not observed. Calcite was not detected by XRD analysis, probably because biogenic calcite has been replaced by dolomite. This thick dolomite layer was not encountered in Hole 798B, which was drilled only 20 m away from Hole 798A. This implies that the dolomite layer is not an extensive bed, but actually lensoid in shape, thinning out toward Hole 798B.

The rate of sedimentation of the sediments immediately surrounding the dolomite layer is 160 m/m.y., whereas the

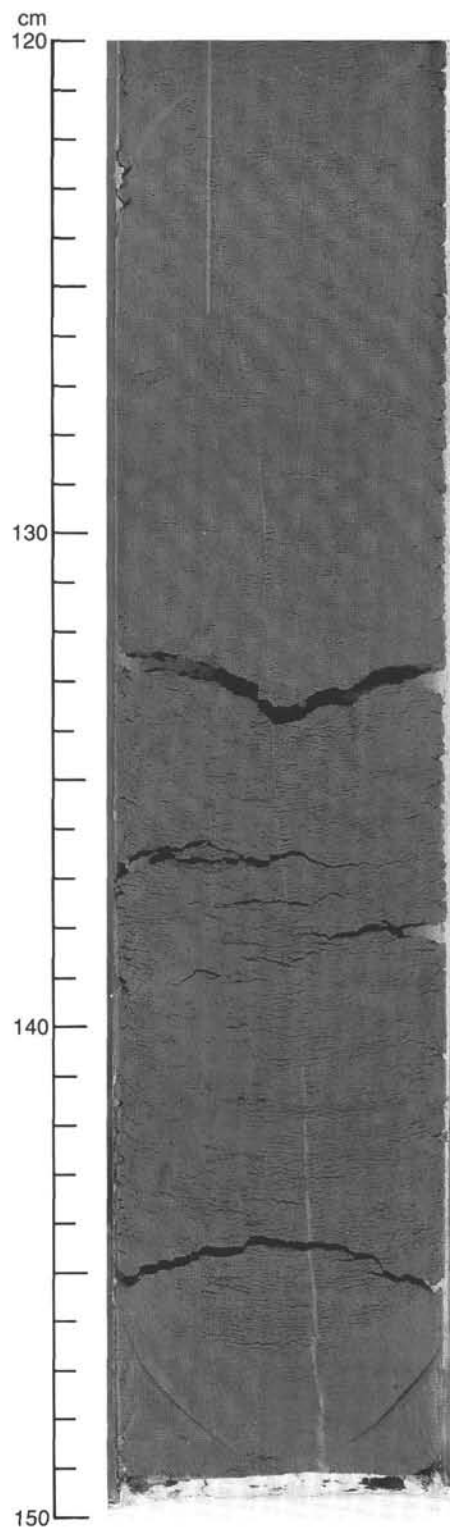


Figure 31. White vein in Section 128-798A-5H-1 at 120 to 150 cm.

sedimentation rate of the overlying sediments is less, approximately 45 to 122 m/m.y. (see "Sediment Accumulation Rates" section, this chapter). This decrease in rate of sedimentation might have contributed to the formation of a thick dolomite layer at this horizon, as has been documented by Raiswell (1987).

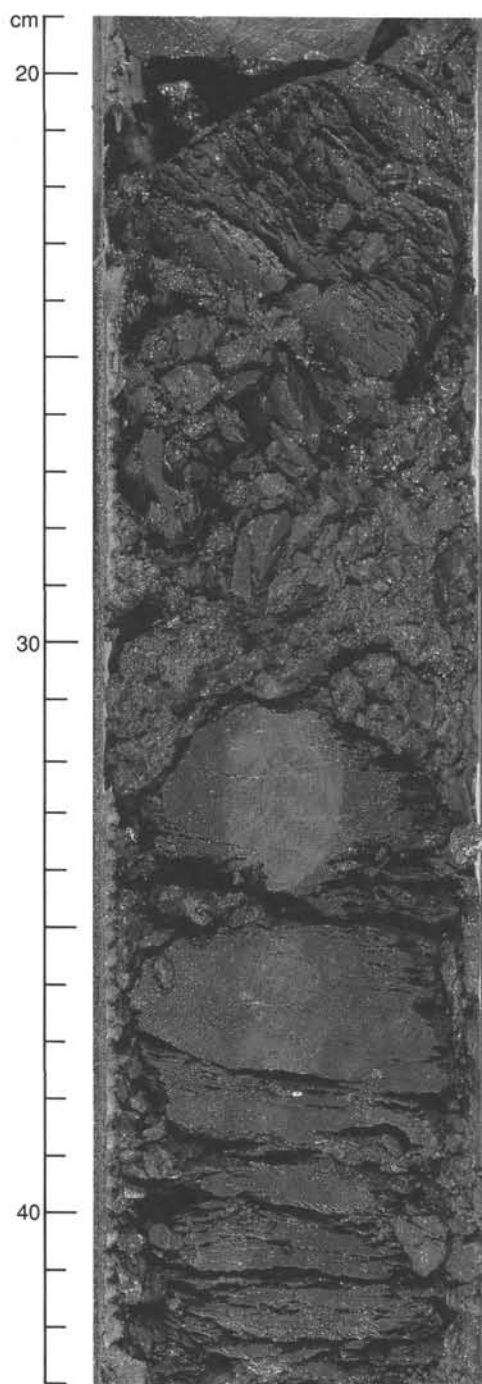


Figure 32. First appearance of fissility in Section 128-798B-43X-1 at 20 to 43 cm.

Silica Diagenesis

The transformation from opal-A to opal-CT occurs in Site 798 sediments at about 450 mbsf. The shallowest dissolution of siliceous microfossils was noted at about 380 mbsf, and the shallowest distinct opal-CT peak was noted in X-ray diffractograms at about 455 mbsf (Fig. 13). No abrupt lithologic boundary is apparent, but many gradual changes related to silica diagenesis occur, including (1) the disappearance of silicoflagellates below 450 mbsf (Core 128-798B-47X); (2) increasing fragmentation of diatom debris from 380

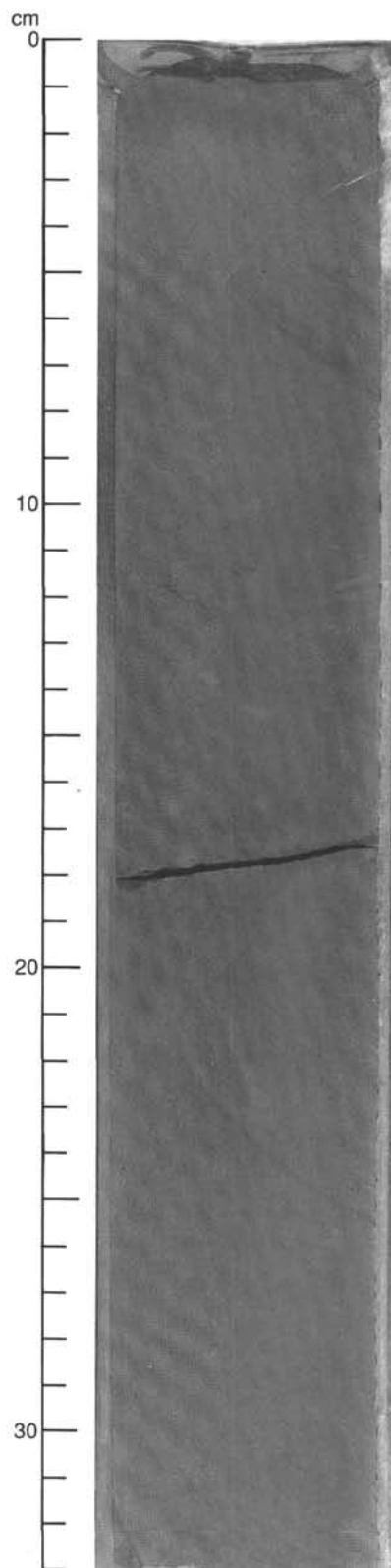


Figure 33. Well-lithified dolomite bed (1–33 cm) having sharp top boundary, with the host diatom ooze and drilling-fractured surface at the bottom (Section 128-798A-17X-CC at 0 to 33 cm). Note thin planar laminations in the upper part (1–13 cm) and *Chondrites* and *Planolites* burrows in the lower part (13–33 cm) of the bed. According to logging data, this dolomite bed is at least 1 m thick.

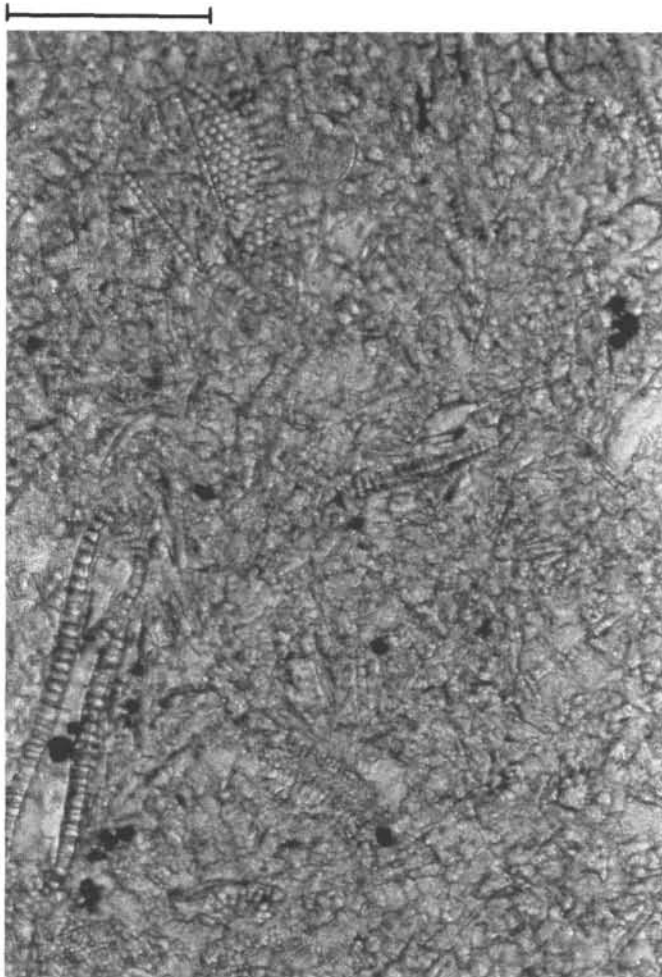


Figure 34. Photomicrograph of well-lithified dolomite bed (Sample 128-798A-17X-CC, 15–17 cm) in diatom ooze. Well-preserved diatoms are tightly cemented by anhedral, finely crystalline dolomite. Scale bar is 0.01 mm.

to 450 mbsf, and its virtual disappearance below 470 mbsf; (3) an increase of 1.4 to 1.8 g/cm³ in wet-bulk density between 300 and 500 mbsf (see “Physical Properties” section, this chapter); (4) a decrease in dissolved SiO₂ in interstitial water from 1300 to 800 μM between 370 and 500 mbsf, with silica precipitation indicated in the interval between 450 and 500 mbsf (see “Inorganic Chemistry” section, this chapter).

The lack of an abrupt lithologic change probably results from the generally low abundance of biogenic silica in sediments in the interval from 400 to 500 mbsf, as suggested by smear slide data (Fig. 12) and the aluminum log (see “Downhole Measurements” section, this chapter). The abundance of biogenic silica was estimated from X-ray fluorescence (XRF) analysis of six sediment samples. Two samples well above the diagenetic boundary were analyzed from Core 128-798B-34X—one was identified as rich in biogenic silica (in Sample 128-798B-34X-2, 83–88 cm), the second identified as having sparse biogenic silica (<5%) by smear-[008c]slide analysis (in Sample 128-798B-34X-CC, 23–25 cm). Based on a maximum of 5% biogenic silica in the latter sample, the ratio of SiO₂ to Al₂O₃ in the remainder of the sediment is 3.00. Assuming a constant detrital fraction, values of the abundance of biogenic silica were calculated

for the remaining samples, which average 3% to 8% in the samples from Cores 128-798B-41X and 128-798B-44X, and 13% to 18% in the samples from Cores 128-798B-48X and 128-798B-51X (Table 6).

The estimated minimum temperature at 450 mbsf is about 38°C (see “Downhole Measurements” section, this chapter). The equilibrium temperature might be 10°C or more higher (Byrne et al., 1987), but preliminary estimates suggest values of 5° to 6°C, placing the true transformation temperature at about 42° to 43°C in rocks having about 15% silica. This value is in good agreement with previous estimates for the transformation in a non-uplifted Pliocene sequence offshore California (Keller and Isaacs, 1985).

Volcanic Ash and Tephrochronology

The three holes cored at Site 798 contain 113 discrete ash layers. These correspond to 113 successive volcanic events that have been preserved in the sedimentary record dating from early Pliocene to Holocene. All but 12 of the layers in the deeper part of Hole 798B were correlated among two or three holes, within their ranges of overlapping depths. In addition, numerous pockets or pods of ash occur. Some of these are remnants of eroded or disturbed ash layers, and others are burrows filled with ash.

By definition, an ash layer contains at least 60% of volcanoclastic material (lithic, vitric, crystal). It is difficult to estimate the proportion of volcanic material accumulated in discrete ash layers relative to that which is scattered in the sediment. In some cores, which are rich in ash beds, the proportion of dispersed glass may reach 50%. Likewise, under the same conditions of deposition, the cores or sections where ash beds are scarce are also poor in dispersed glass fragments. At Site 798, except for the lower part of Hole 798B where slumping has occurred, the rate of sedimentation was reasonably steady at about 120 m/m.y.; thus, variations in the abundance of discrete ash layers are evidence for pulses of volcanism. Therefore, the number of layers can be used to estimate the chronologic evolution of nearby explosive volcanic activity.

Significant features of these 113 discrete ash layers are given in Table 4.

Petrographic Aspects of Discrete Ash Layers

Composition

Typically, the ash layers contain a glass fraction and a crystal fraction. No lithic fragments were recognized in smear slides, and the volcanic products are pyroclastic, not hydroclastic. The volcanoclastic material may be mixed with terrigenous or biogenic sediments and authigenic minerals, but these usually constitute no more than 30% of the total.

The glass fraction consists of glass shards (sh), bubble wall fragments, and micropumices or microscoria. The vesicles of the micropumices are elongated to tubular; they are more spherical in the microscoria.

The crystal fraction consists of fragments or euhedral crystals of quartz, alkali feldspar, plagioclase, biotite, amphibole, clinopyroxene, and orthopyroxene. Scarce magnetite may be present. The proportion of crystals ranges from 5% to 30%. Two kinds of ash beds can be distinguished on the basis of their glass/crystal ratios: crystal-rich with 15% to 30% crystals, and glass-rich with 5% to 15% crystals.

The average grain size of most of the ash layers is a silt. Some layers are a coarser volcanic sand with subrounded fragments (e.g., layer 107 in Table 4). Others contain very fine particles that range from fine silt to clay size.

Table 6. Major oxides measured by X-ray fluorescence in Site 798 sediments.

Core 128-798B: Interval (cm):	34X-2 83-88	34X-CC 23-25	41X-5 60-65	44X-3 40-45	48X-5 97-99	51X-4 108-110
SiO ₂	75.40	64.05	66.12	66.25	70.13	69.97
TiO ₂	0.47	0.72	0.72	0.58	0.67	0.69
Al ₂ O ₃	13.78	19.71	19.32	19.47	17.51	17.40
Fe ₂ O ₃	4.19	6.07	7.15	6.17	6.18	5.78
MnO	0.04	0.05	0.04	0.05	0.05	0.05
MgO	1.57	2.46	2.55	2.43	2.48	2.25
CaO	0.55	0.76	0.66	0.46	0.54	0.86
Na ₂ O	3.48	3.03	2.69	2.51	2.20	2.12
K ₂ O	2.73	3.72	3.41	3.88	2.74	3.06
P ₂ O ₅	0.08	0.11	0.11	0.08	0.07	0.11
Total	102.29	100.68	102.78	101.87	102.58	102.28
Biosilica	31%-41%	0%-5%	3%-8%	3%-8%	13%-18%	13%-18%

Note: Biosilica was calculated on the basis of a range of 0% to 5% biogenic silica in Sample 128-798B-34X-CC, 23-25 cm, and by assuming a constant ratio of silicon:aluminum in the detrital fraction of all samples.

Petrochemical Distinction

Acidic glass is colorless, and basic glass is pale brown to brown. Acidic magmas are the more viscous of the two; they generate a higher proportion of explosive products, which are commonly widespread and produce discrete layers. Tubular micropumices are typical products of explosive acidic activity. Moreover, the mineralogy, such as the proportion of quartz and alkali feldspar vs. plagioclase and ferro-magnesian minerals, is characteristic of the chemical composition of the parent magma.

As a first approximation, acidic layers are white to gray owing to their high glass/crystal ratio, and basic layers are dark gray to brownish black. This color distinction was used as a primary means of sorting all of the ash layers into two groups for tephrochronological purposes (see below); the layers are listed as "A" for acidic and "B" for basic, under "Petrographic Group" in Table 4. About 72% of the ash layers are "acidic."

More detailed observations of smear slides permitted classification of ashes into three groups:

1. Acidic: contains shards, bubble wall fragments, and tubular micropumices. The latter can constitute 30% to 50% of the glass material. The glass is colorless. Crystals are quartz and alkali feldspar. Plagioclase, clinopyroxene, biotite, and/or amphibole are subordinate; orthopyroxene may be present.

2. Intermediate: Shards and bubble-wall fragments predominate. Tubular micropumices are scarce. The glass is always colorless. Plagioclase may be abundant compared to quartz and alkali feldspar. Clinopyroxene, biotite, and/or amphibole are abundant. Orthopyroxene is rare.

3. Basic: some shards and bubble wall fragments are colorless, but most are pale brown to brown. Tubular micropumices are absent. Scarce microscoria appear in some layers. There are variable amounts of plagioclase, clinopyroxene, biotite, and/or amphibole.

The presence of orthopyroxene indicates a calc-alkaline magmatic signature. In the absence of this mineral, the magmatic origin may be tholeiitic, calc-alkaline, or alkaline.

We tried to obtain a pure glass fraction of some samples for shipboard XRF analyses. However, the available equipment did not permit a concentration of glass of sufficient purity for petrogenetically reliable results. A not negligible amount of minerals remained, which precluded a correct analysis of the

glass for the most significant trace elements, such as rare earth elements, niobium, strontium, zirconium, and yttrium. In addition, the quantity of material was insufficient to prepare glass disks for XRF analyses of major elements and pressed-powder pellets for analyses of trace elements. These will be done post-cruise by inductively coupled plasma analysis.

Alteration

Hydration of deep-sea volcanic glass may reach 5% to 8% without optically perceptible alteration, even if the chemical composition is somewhat modified with the addition of water and leaching of some elements (Poulet et al., 1985a, 1985b). Beyond 10% hydration, smectite formation occurs, producing such minerals as beidellite and celadonite. Lithification in Hole 798B begins in Core 128-798B-40X at 373 mbsf, and yet all the volcanic glasses seem to be "fresh" down to the deepest encountered ash layer, which is present in Core 128-798B-49X at 460 mbsf. A pyroclastic lithified gravel with fresh glass occurs in Core 128-798B-51X. Scattered ash fragments in sediment, always "fresh," were recognized in the deepest cores. Even in Section 128-798B-54X-7 at 516 mbsf, colorless and angular shards are included in an ash-bearing claystone.

Sedimentary Aspects

The grain size of volcanic ash beds is related to (1) distance from the volcanic source, (2) the sedimentary process, and (3) post-sedimentary reworking. The layers range from very thin (0.2 mm) to very thick (30 cm). Graded bedding is obvious in the medium and thick layers. This bedding is generally normal, and the upper part commonly consists of well-sorted glass shards and micropumices. The base is sharp. In contrast, the top is more or less mixed with fine sediment. The thickest layers are always made of reworked material in turbidity flows.

Two different sedimentary aspects have been considered: normal underwater sedimentation and syndimentary to post-sedimentary processes.

Normal sedimentation

The tephra layers are classified into three types of normal sedimentation, given as H, G, and T under "Lithologic Type" in Table 4, as follows:

1. Type H, homogeneous layers (Fig. 35): the volcanic material has no macroscopic evidence of sorting. It is homogeneous in grain-size range and vitric/crystal composition.

The very thin to thin ash beds (0.2–5 mm) are typically of this type, as are almost all of the basic layers, although some of the latter may be thick (e.g., layer 6). In addition, many glass-rich white and gray layers (e.g., layers 4, 62, and 80) are homogeneous. One acidic layer of this type, layer 93, is abnormally thick (1 cm) in Hole 798A. The same layer is thin (0.1 cm) in Hole 798B and is absent in Hole 798C; thus, a local accumulation has been inferred. Rarely, homogeneous layers reach 1 cm thick, with a sharp base and top, and may correspond to the lower part of a graded layer (type G), of which the upper part has been eroded.

Homogeneous layers are products of a single volcanic event over a short period of time, in the case of acidic layers, or are products of very distant eruptions. In the latter case, the homogeneity is produced by winnowing during aerial transport.

2. Type G, graded layers (Figs. 35 and 36): normal graded bedding is obvious in the layer as a consequence of sorting of the volcanic material as it sinks from the surface. This gradation is distinguished by variation in grain size, as well as by the color variation related to the glass/crystal ratio. The lower part is coarser, darker, and crystal-rich. The upper part is finer, lighter, and glass-rich.

Grading is usually found in acidic deposits that exhibit a gray to light gray or light gray to white color variation. The white parts may contain 98% glass shards and micropumice. Thickness ranges from 0.5 to 4 cm, with some rare, very thick

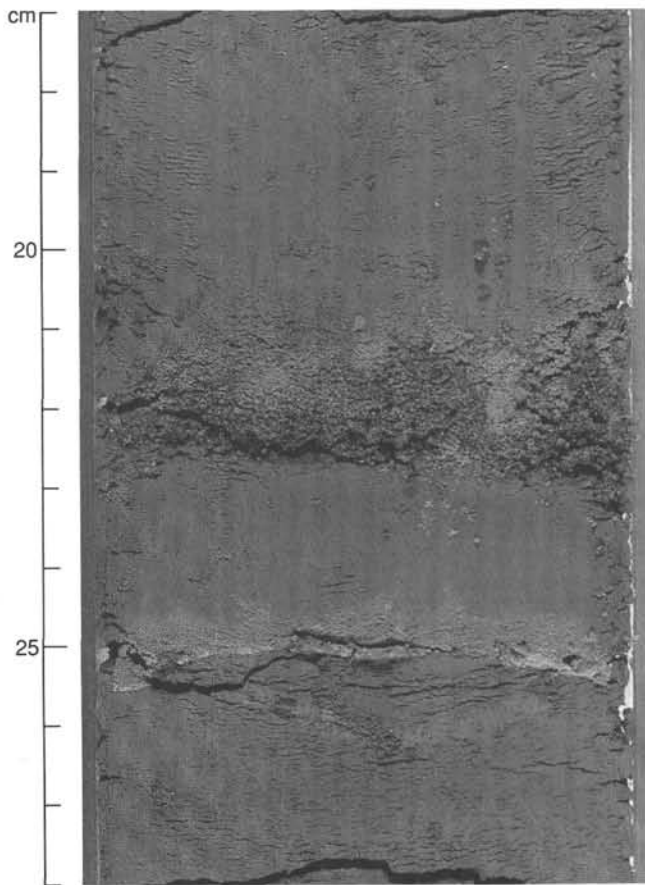


Figure 35. Homogeneous acidic ash layer 60 (25 cm) and graded, coarse-grained acidic layer 59 with crystal-rich lower part (21–22.5 cm); Section 128-798A-8H-5 at 17–28 cm. See Table 4 for layer numbers.

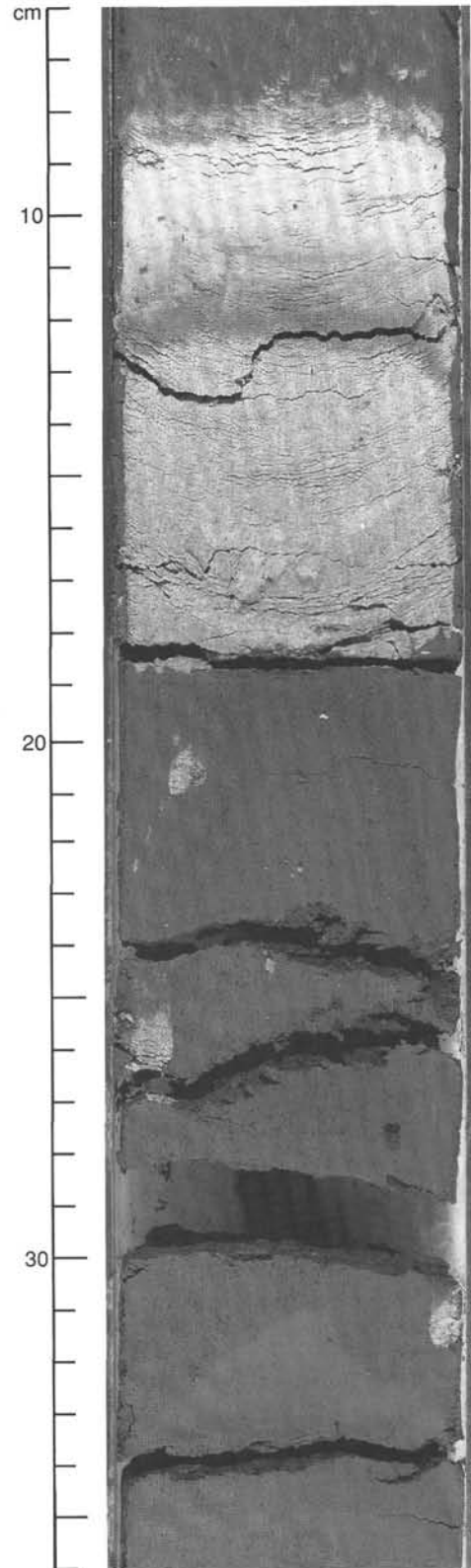


Figure 36. Graded layers (medium-grained) and 37 (fine-grained), separated by a fine-grained sedimentary bed. Note the burrows filled with the layer 38 material; Section 128-798C-7H-4 at 6 to 36 cm.

beds (5.5–6 cm). Only a few dark layers exhibit evidence of grading (e.g., layer 66).

Two adjacent layers, 38 and 37, are good examples of the graded type (Fig. 36). The sharp base of layer 38 is at 56.70 mbsf. This layer is 5.5 cm thick, normally graded, and medium to light gray. The top is slightly mixed with light green sediment. Subsequently, only 0.5 cm above, a new white ash was deposited that is 3.5 cm thick and weakly graded. The estimated time lapse between the two eruptions is 30 to 70 yr.

Graded layers are related to single- or close-spaced eruptions of the same volcanic origin. This eruptive activity was of strombolian to plinian or ultraplinian type.

3. Type T, heterogeneous layers (Fig. 37): different parts of the ash layer have different compositions (vitric and mineralogical) that exhibit different colors and ranges in grain size with or without graded bedding. This type of layer ranges from 4 to 10 cm thick. Type TT, heterogeneous layers produced by turbidite activity, are described next.

The heterogeneity in type T is a consequence either of complex volcanic activity from a single volcano or cluster of volcanoes, or of results from the superposition of products of different but close-spaced eruptions from different volcanoes. Two examples of the former were recognized in layers 32 (Fig. 37) and 75. Above a sharp base, there is 3 or 5 mm of very fine ash, which is rich in glass shards. This is overlain by 3 cm of weakly graded (layer 32) or 9.7 cm of well-graded (layer 75) vitric-crystal bed of medium gray to light gray. At the top, mixed sediments indicate a normal contact. In the absence of chemical analyses, the characteristics of these glass fragments indicate that the two superimposed beds came from the same source. The eruption would have begun with an explosive extrusion of the cooled upper part of the magma column, which frequently happens in pelean and plinian eruptions, and would have continued with the extrusion of new fresh magma.

Synsedimentary to Post-Sedimentary Processes

Three processes have modified the sedimentology of the primary deposit: bioturbation, erosion, and turbidity flow or slump.

1. Bioturbation is the most obvious mechanism for the modification and local destruction of ash layers as many layers have a disturbed upper part with admixed sediments and burrows. Also, there commonly occurs an accumulation of ash pods that clearly correspond to burrows of the *Chondrites* type that are filled with volcanic material from an overlying ash layer. This is evident for the wholly reworked layer 103; its volcanic constituents fill many burrows beneath the layer. Where only “*Chondrites* ash pods” were observed at a given level, we inferred that the mother ash-bed had been totally mined. Such occurrences are not listed in Table 4.

2. Erosion by deep-sea currents may entirely rework an ash deposit or may only remove the upper part. The latter happened to layer 44, which has been overlain at an oblique sharp unconformity by layer 43.

3. Turbidity flows and slumps: Four conspicuous classical turbidites (lithologic type TT in Table 4) and one slump were observed in Cores 128-798B-44X, 128-798B-45X, and 128-798B-46X, and in Core 128-798C-7H. In such cases, the measured thickness of a layer in the core has been arbitrarily reduced by 50% in Table 4 as an estimate of its original true thickness.

These turbidity flows have accumulated reworked volcanic material from original ash layers that were probably less thick. Layer 106 exhibits an almost complete turbidite sequence

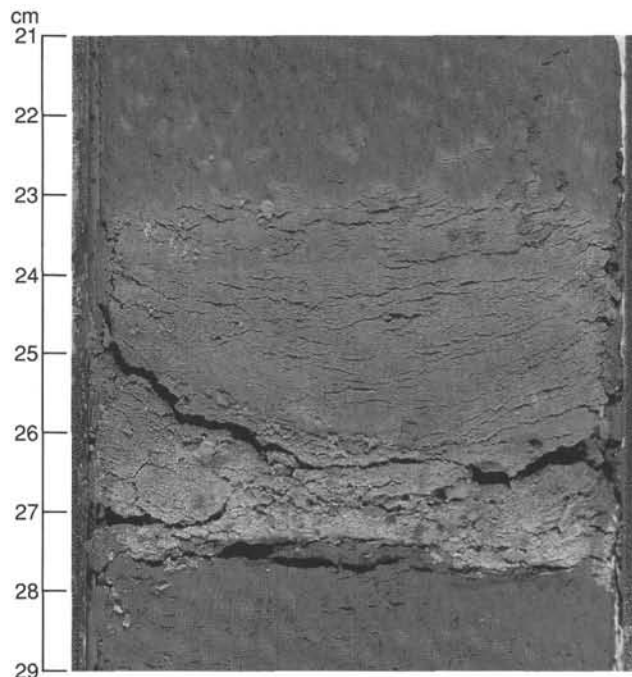


Figure 37. Heterogeneous acidic layer 32 (Table 4). The 5-mm lower part is a fine glass-rich ash. The part above is graded, medium- to fine-grained; Section 128-798C-7H-3 at 21 to 29 cm.

(Fig. 38). The measured thicknesses from the base to the top are (1) 15 cm of coarse-grained bed load, (2) 12 cm of laminated beds, and (3) 5 cm of fine-grained suspension material. This suggests a proximal position.

The slumped part of Section 128-798C-7H-4 has affected 26 cm of clayey mixed sediment including, in the middle part, a 2-mm-thick ash layer (45) and, at the top, a 3.5-cm ash layer (44; Fig. 39). The distortion caused by slumping of layer 45 and the adjacent sediment is readily distinguished from that caused by drilling. Layer 45 has not been reworked, but the top of layer 44 is missing and must have been eroded.

Tephrochronology

Correlation of Ash Layers

The number and thickness of the ash layers may be used to estimate the chronologic evolution of nearby volcanic activity. The ash record in the three holes is good to 143 mbsf, where sediments are dated from late-early Pliocene. The top of the sedimentary column has been dated as Holocene without greater precision. No hiatuses in sedimentation were recognized, but some ash layers may have been removed by bioturbation. The lower part of Hole 798B below 143 mbsf contains considerably fewer preserved ashes and ends at 518 mbsf in claystone. Here, the tephra record is less satisfactory.

Geophysical and logging data help provide a more complete record. The shipboard 3.5-Khz sub-bottom profiler registered all ash-layers that are >2-cm-thick, from the seafloor to 80–100 mbsf (Fig. 40). Ten discrete ash layers or groups of ash layers were recognized and correlate well with the layers in the cores. FMS logging in Hole 798B registered resistive ash beds from 85 mbsf (below casing bottom) to 517 mbsf (see “Downhole Measurements” section, this chapter), which is within 1 m of the bottom of the hole.

By adjusting the ash-layer sequences in each drill hole relative to one another, as well as the lithologic units, and by

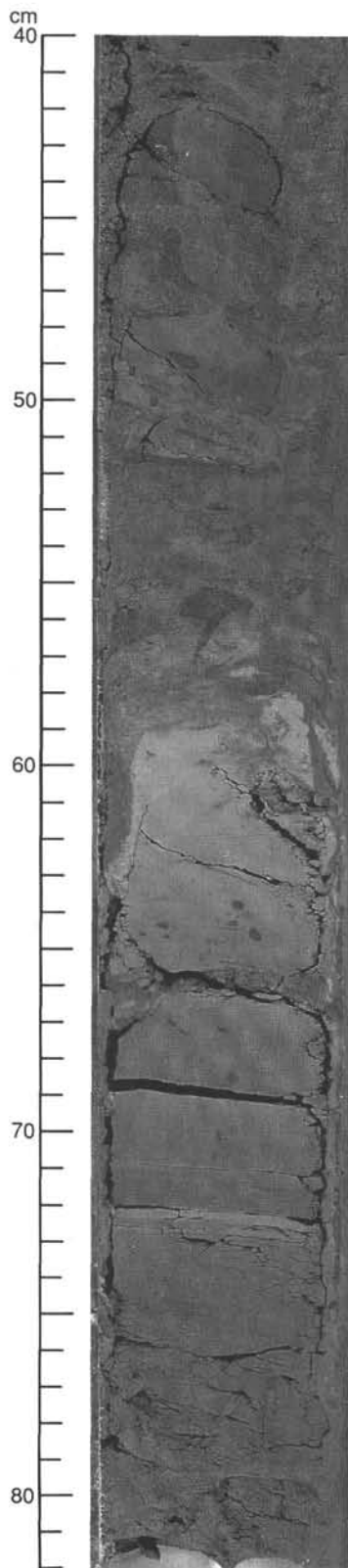


Figure 38. Turbidity flow of a volcanoclastic deposit, layer 106 (Table 4). Lower part (below 76 cm): coarse-grained bed load; middle part (76–64 cm): laminated beds; upper part (64–59 cm): glass-rich, fine-grained suspension top level; Section 128-798B-44X-2 at 40 to 82 cm.

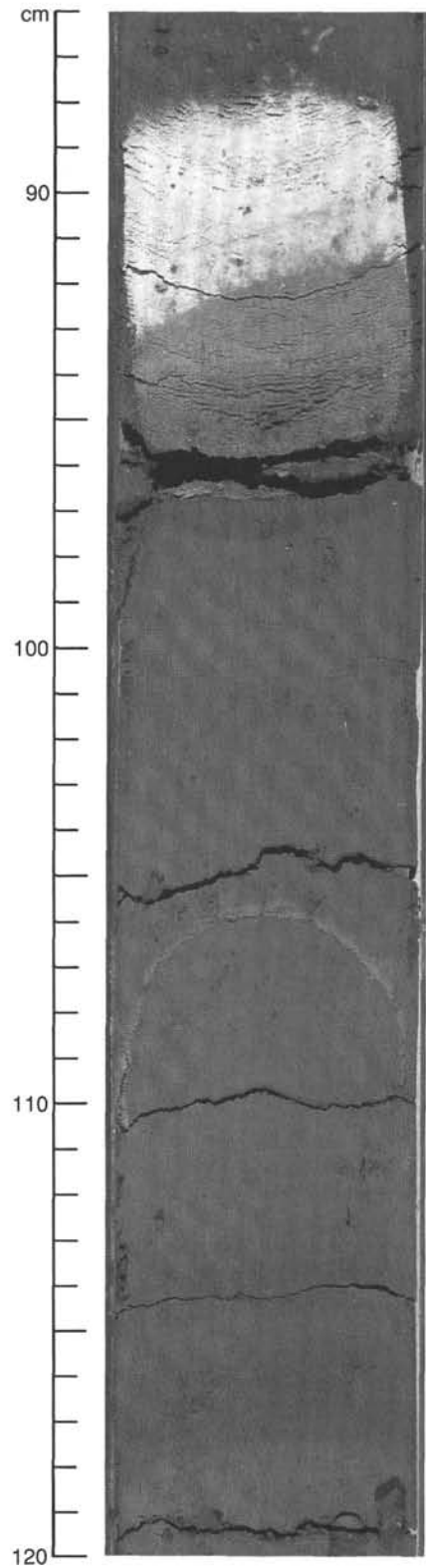


Figure 39. Slumped sediments, including a thin ash layer (45) in the middle part and a thick medium-grained ash layer (44) at the top. Note the eroded oblique truncation of this layer, which is overlain by a new, white, and fine-grained ash layer (43); Section 128-798C-7H-4 at 86 to 120 cm.

3.5-kHz Record

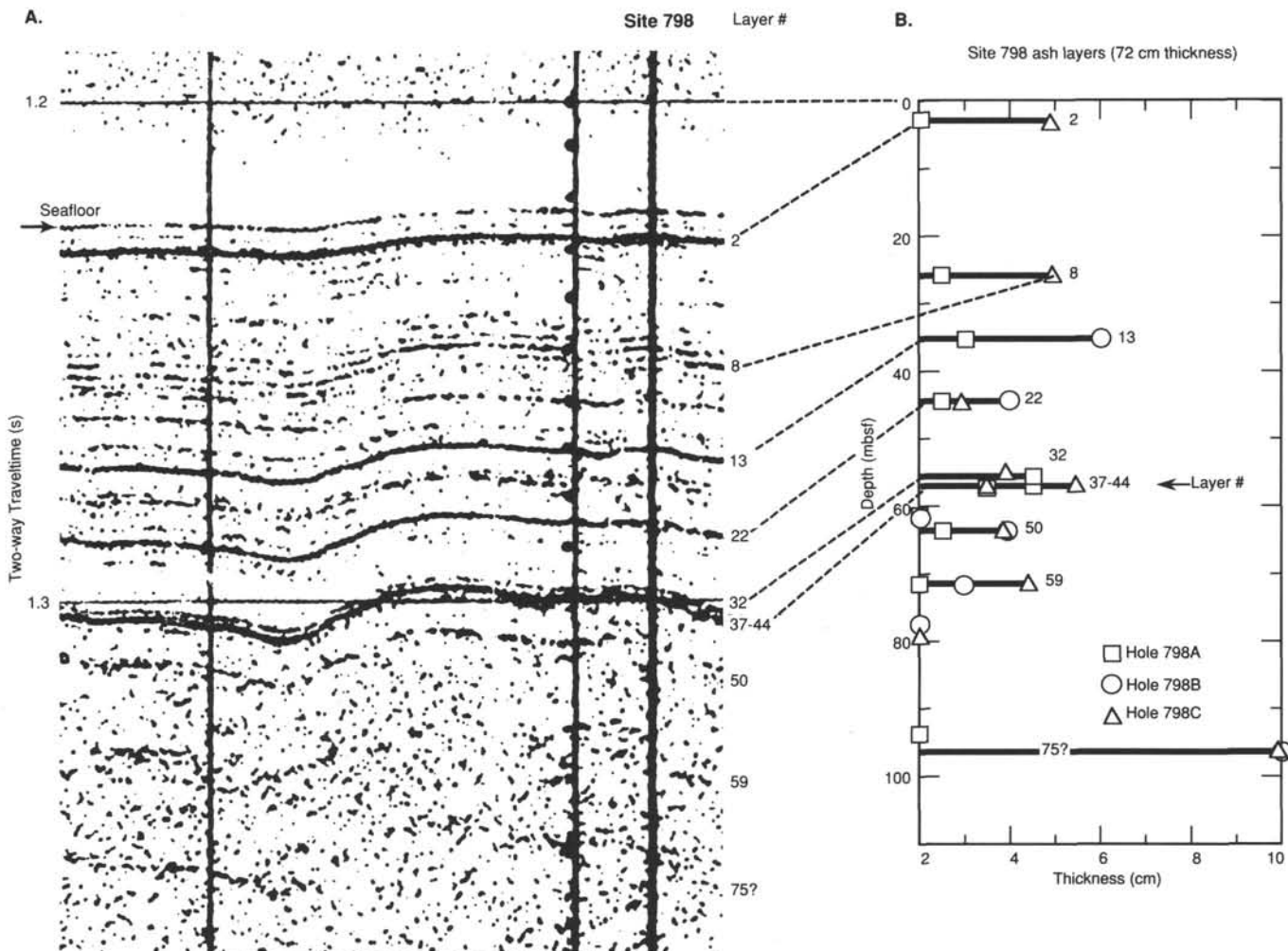


Figure 40. Correlation of ash layers greater than 2 cm thick in drill core with reflectors in the 3.5-kHz sub-bottom profile at Site 798. These ashes are clearly visible in the 3.5-kHz record to 65 m and vaguely visible to 100 m.

determining some tephra markers (e.g., thick, graded layer 50), 12% of the ash layers were correlated in all the three holes, 46% in two holes, and 42% in only one hole. The depths given in Table 4 are relative to Hole 798B, for which estimates of the mud line range from ± 0.1 m (G. Pollard, pers. comm., 1989) and which was taken as 0 mbsf.

Estimated Ages

Ages for each of the 113 ash layers in Table 4 were estimated from their depths below seafloor by means of a best-fit model that was constructed from the shipboard paleomagnetic dates and natural gamma-ray logs (Fig. 41). Depths were corrected for core expansion (due to gas pressure) and loss by multiplying the interval in a given core by 100 times the reciprocal of the percentage of recovery. The depth at the top of each core was assumed to be a fixed and known value (from drilling records). This effectively distributed the gain/loss in core length evenly over the total length of that particular core. Age information was handled in two ways. Cyclical variation in sediments, as revealed in the gamma-ray logs, has been "tuned" to Earth's 41,000-yr Milankovitch obliquity cycle in relation to shipboard paleomagnetic data to give a best-estimate of ages between 90 and 298 mbsf (see "Downhole Measurements" section, this chapter). The precision is estimated as $\pm 3\%$. Outside of this

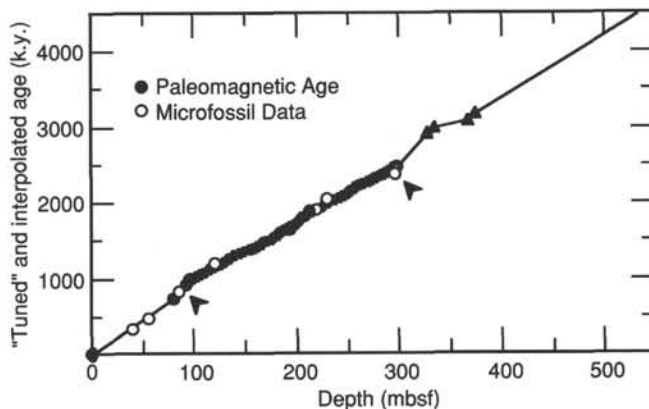


Figure 41. Model used to estimate the ages of ashes at Site 798. Wavy line is from natural gamma-ray log "tuned" to Earth's 41-k.y. obliquity cycle and initially pinned at paleomagnetic points. Other segments are linear interpolations between fixed paleomagnetic points. The fossil data were not used. See text for details.

interval, linear regression lines were constructed between adjacent paleomagnetic fixes as far back in time as the Mammoth/Gauss transition, and between zero age at the present seafloor and the Brunhes/Matuyama transition. The shipboard microfossil data were not used for the individual segments in Figure 41. Beyond the top of the Mammoth, a linear regression ($R^2 = 0.997$, forced through 0 yr at 0 mbsf) of all the paleomagnetic and microfossil data was used (Fig. 42).

Record of Volcanic Activity

Figure 43 presents variations of the number of ash layers and their thicknesses as a function of time. These are related to the volume and importance of the explosive activity. Major changes in volcanic activity led to the recognition of five different phases. These are numbered from Present to Pliocene time as V1 to V5 to allow for the later addition of older records, but are described in chronological sequence, starting with the oldest.

1. V5: A first important episode occurred between 4.0 and 3.5 Ma. There are nine thick ash beds of coarse material that must have originated from nearby and very important explosive volcanoes. As only Hole 798B reaches this time level and significant sedimentary modifications have affected these tephra deposits, it is highly probable that many thin ash beds were entirely reworked and are not discernable.

2. V4: After a depositional gap of important discrete ash layers, moderate activity has been registered from 2.4 to 1.3 Ma. Ash layers are scarce (6), but volcanic material has been dispersed in the sediments. The FMS detected several apparent ash layers in this interval that were not recovered in the core.

3. V3: Volcanic activity increased dramatically from 1.3 to 0.9 Ma, with numerous (28), mostly thin layers. There is one thick layer of type T (layer 75, 10 cm).

4. V2: A major volcanic pulse took place between 0.9 and 0.3 Ma, with a great number (58) of different types of ash layers. The paroxysmal explosive activity occurred between 0.7 and 0.55 Ma.

5. V1: Since 0.3 Ma, volcanic activity has been moderate, with about the same diversity of products as in V2.

There is no correlation between the thickness and the number of ash layers. The accumulated thickness of the ashes results from both the number of tephra deposits (i.e., the number of eruptions) and the magnitude and proximity of the eruptions, which are randomly distributed.

Some interesting features are apparent when the number of basic and acidic layers are examined as a function of time (Fig. 44). The late-early Pliocene volcanism (V5) is both acidic and basic. The low number of layers and the expected poor preservation of thin beds because of slumping precludes further interpretation. However, the presence of two thick basic or intermediate ash deposits indicates the proximity of nonevolved and onshore volcanoes. Late Pliocene and early Pleistocene time are devoid of basic products. Only acidic ashes (V4) were deposited. This may be explained either by a quiescence of the volcanic (and tectonic) activity, or by submergence of the volcanic arc. In the latter case, only the most important explosive and acidic eruptions could have provided a widespread blanket of ash. The V4 ash layers are essentially glass-rich and of plinian to ultraplinian type. Moreover, there is an unusual abundance of floated pumices, several millimeters to 1 cm in size, scattered in the sediments and even accumulated in pseudolayers, as at 175.8 mbsf. These observations support the second explanation that the volcanic arc was submergent during V4. In early Pleistocene time (V3), basic products were scarce, and acidic layers were

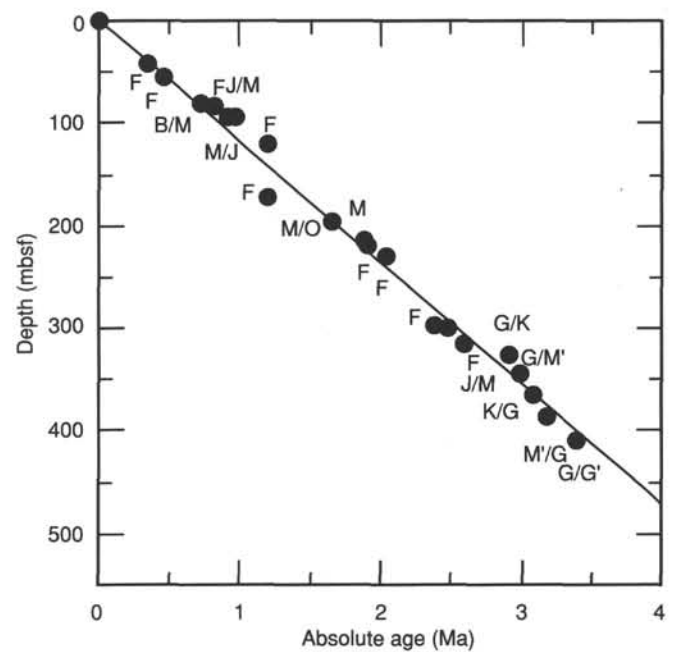


Figure 42. Least-squares linear fit to the paleomagnetic and microfossil data used to obtain estimated ages of ash layers greater than 3.18 Ma. B = Brunhes, F = microfossils, G = Gauss, G' = Gilbert, J = Jaramillo, K = Kaena, M = Matuyama, and M' = Mammoth. See text for details.

mainly of type H, indicating a distal origin from distant volcanoes. The single, thick, type T layer obviously originated from a nearby large volcano. The Pleistocene paroxysmal event (V2) indicates a major volcano-tectonic pulse and the activation of all the volcanic areas, supplying their various products. The Japan Arc must have been emergent at this time. The late Pleistocene to Holocene volcanism (V1) may be a prolongation of V2, with the same volcanic sources, but the activity is clearly weaker.

Possible Origin of the Volcanic Material

All volcanic materials recovered at Site 798 are air-fall pyroclastites. At present, the prevailing wind directions are north to south in winter and south to north in summer, but they are variable during the spring and fall. Therefore, significant quantities of tephra may have come from explosive activity all around Site 798, and from distances of at least 500 km and possibly as far away as 1000 km, or even 2000 km for ultraplinian explosions.

The most likely origins are the large acidic to intermediate and calc-alkaline volcanoes of the southwestern Japan Arc (Izu, Kyushu) at a distance of 250 to 800 km and the northeastern Japan Arc (Tohoku) at a distance of 500 to 900 km. The nearby alkaline volcanic islands of the Sea of Japan, Oki-Dogo (at 170 km) and Ulleung-Do (at 360 km), which have produced trachytic extrusions, are also good candidates. The Pliocene-Pleistocene Korean volcanoes were not explosive. Some northeastern Chinese volcanoes have produced widespread ashes (e.g., Baegdusan), but they are probably too far from Site 798 for their ashes to be evident.

The thickness of the ash is a function of the distance of transport. A frequency plot of the thickness of the ash layer is shown in Figure 45. The thinnest layers are numerous and mainly basic to intermediate in composition. They obviously originated from the Japan Arc. Many of the thin and fine-grained acidic layers may have had a more distant origin (e.g.,

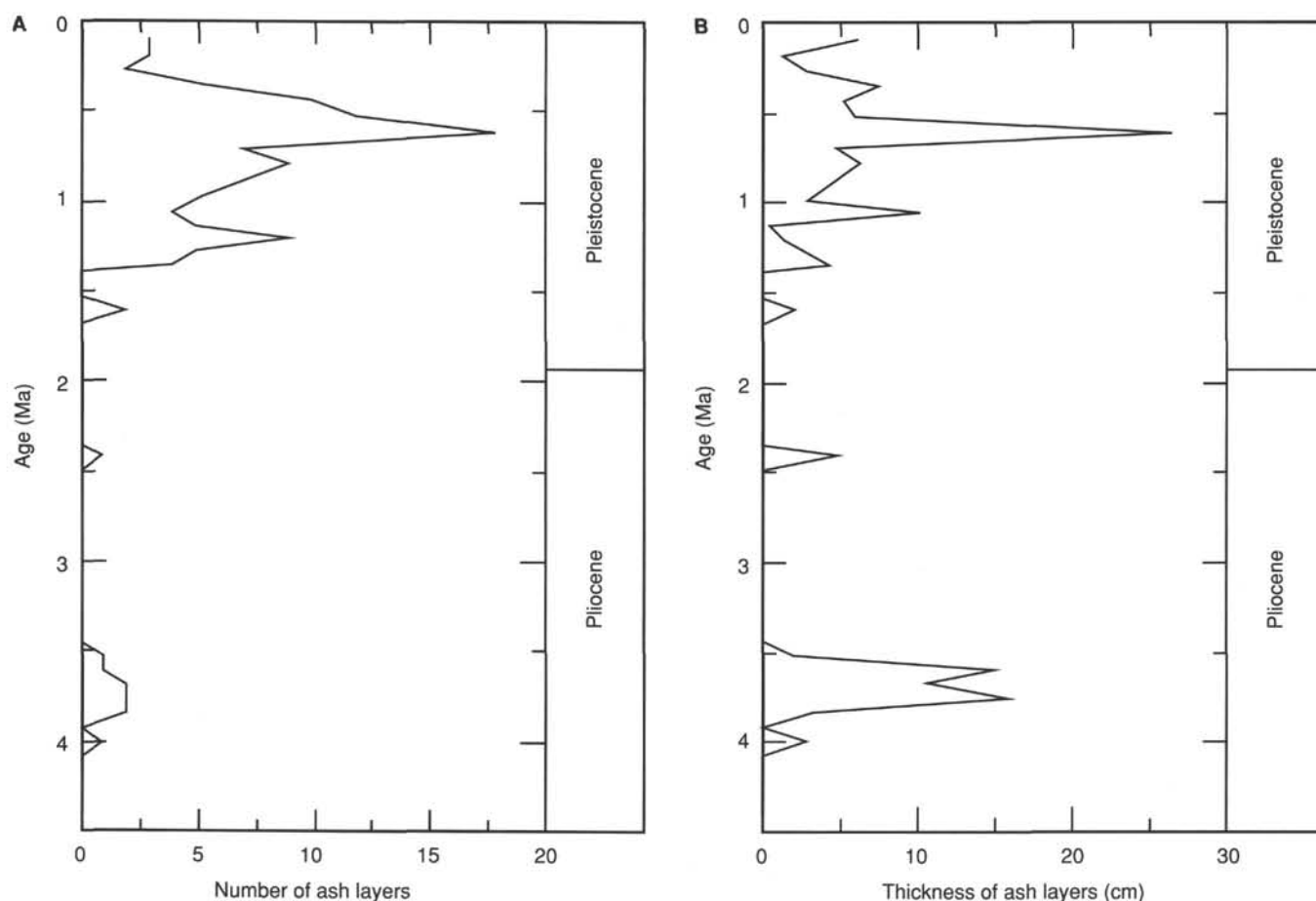


Figure 43. Frequency plots of number (A) and thickness (B) of ash layers at Site 798 as a function of estimated age from Figure 41. Data are from Table 4. The Pleistocene/Pliocene boundary is at 1.88 Ma.

Kyushu-Ryuku or northeastern Japan). The medium-thick layers are of medium silt size or of coarse silt to sand size; all the different sources are probable. The thickest layers generally include coarse elements; they must have come from the larger explosive acidic volcanoes, such as Aso, Aira, and Kikai.

Five tephra markers have been identified in the southern part of the Sea of Japan (Machida, 1981; Machida and Arai, 1981; Kobayashi, 1985). These are as follows:

1. Kikai-Akahoya (K-Ah), from south Kyushu: 6,300 yr B.P.; this deposit has been found only in the southeasternmost Sea of Japan.
2. Ulleung-Oki, from Ulleung: 9,300 yr B.P.
3. Aira-Tn (AT), from southern Kyushu: 21,000 to 22,000 yr B.P.
4. Yamato, from Ulleung: 25,000 to 35,000 yr B.P.
5. Aso-4, from the Aso volcano: 80,000 yr B.P.

In addition to these recognized markers, explosive tephritic activity from Ulleung Island has been dated at 0.29 ± 0.07 Ma (Poulet and Lee, 1988).

One can make some tentative assignments to the known tephra markers from the age data in Table 4, but note that these ages are probably overestimated in the uppermost part of the section because of the absence of significant compaction. Layers 1 and 2 are either Aira-Tn and/or Yamato. Aira-Tn is calc-alkaline, whereas Yamato is alkaline; thus, these may be distinguished by post-cruise chemical analyses.

Layer 3 is probably Yamato. Layers 8 through 18 are candidates for the 0.29-Ma Ulleung event.

Depositional History

With an average sedimentation rate of 121 m/m.y. (see "Sediment Accumulation Rates" section, this chapter), the depositional sequence recovered at Site 798 provides a high-resolution record of late early Pliocene through Holocene paleoceanographic and tectonic events in the southeastern Sea of Japan. The oldest sediments recovered at Site 798 are rich in terrigenous detritus and contain both glauconite and quartz sands. Although intense bioturbation has disrupted the primary sedimentary structures within these layers, the well-rounded nature of the glauconite grains, their association with quartz sands, and their occurrence in sequential thick beds suggests an allochthonous origin.

The modern Oki Ridge receives relatively little coarse terrigenous detritus because it is isolated from the margins of the Sea of Japan by a series of deep basins (see "Background and Scientific Objectives" section, this chapter). The terrigenous-rich and sandy character of the base of lithologic Unit III suggests that these sediments were deposited prior to significant uplift of the present-day Oki Ridge. The absence of sand layers, the decreasing clay content, and the increasing diatom content from 450 to 250 mbsf are consistent with increasing isolation from coastal siliciclastic sources and perhaps reflect the late Pliocene/early Pleistocene uplift of the Oki Ridge.

Although the precise uplift history of the Oki Ridge is not yet known, there is abundant evidence for late Pliocene-early

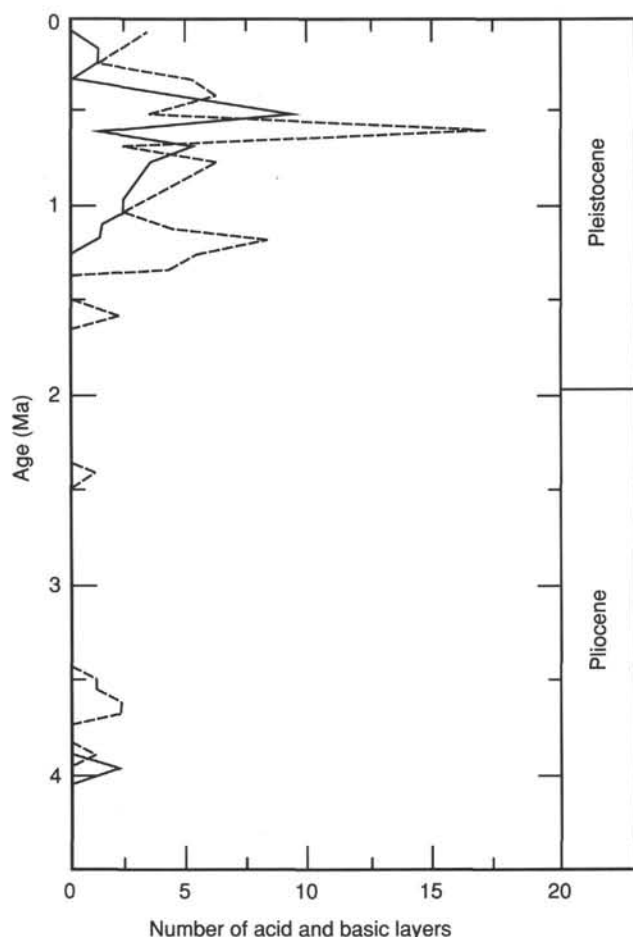


Figure 44. Frequency plots of number of acid (dotted line) and basic layers (solid line) at Site 798 as a function of estimated age. Data are from Table 4.

Pleistocene deformation and flexure in the southern and eastern Sea of Japan. Along the Oga Peninsula, Sado Island, and the Himi area of the Noto Peninsula, western Honshu, Miocene through Pliocene basinal to shelf/slope or neritic marine sediments were uplifted and deformed during the early Pleistocene (Taisuke and Matoba, 1976; Ingle, 1975b, 1981; Morozumi and Koizumi, 1981). Offshore seismic profiles suggest the presence of deformed Pliocene sediments beneath a thin drape of Quaternary units within 50 km of Site 798 (Tamaki, 1988). The collective evidence suggests widespread deformation in the eastern and southern Sea of Japan, beginning about 2 Ma. This event was marked by a widespread unconformity observed in onshore stratigraphic sections and offshore seismic profiles (Ingle, 1975b; Ishiwada et al., 1984). Although no hiatus was observed at Site 798, the sedimentary succession can be interpreted to be the result of late Pliocene/early Pleistocene uplift of the Oki Ridge.

Carbonate deposition at Site 798 began about 1.9 Ma (220 mbsf), perhaps as the result of emergence of the Oki Ridge above the early Pleistocene CCD. Ichikura and Ujiie (1976) suggested a depth range of 1500 to 2100 m for the modern CCD in the Sea of Japan and attributed its shallow depth to a combination of low temperatures and salinities of the bottom waters. It is unlikely that the CCD has been significantly deeper during the late Neogene. The carbonate content of upper Miocene through Quaternary sediments in the deep basins of the Sea of Japan (Sites 794 through 797, water depths

of 2570 to 3300 m, Tamaki, Pisciotto, Allan, et al., in press) is generally less than 1%, and foraminiferal preservation is poor, indicating deposition below the CCD (Tamaki, Pisciotto, Allan, et al., in press).

Diatoms are a significant component (10%–50%) of the upper 350 m of the sedimentary sequence at Site 798, indicating highly productive surface waters. The highest concentration of diatoms occurs between 250 and 300 mbsf (Fig. 12), from approximately 2.2 to 2.5 Ma. This was also a period of high sedimentation rates (as much as 210 m/m.y.; see "Sediment Accumulation Rates" section, this chapter). Based on smear-slide and XRF data (Fig. 12 and Table 6) and sediment accumulation rates, we estimate that peak biogenic silica fluxes of roughly 3 to 8 g opal/cm²/k.y. occurred at Site 798 during the late Pliocene. Although this estimate is semiquantitative, we note that this opal accumulation rate is similar to those reported for the modern mud lens along the Peru margin, one of the world's most highly productive coastal upwelling systems (DeMaster, 1979; Scheidegger and Krissek, 1983). Late Pliocene high productivity events also were noted at other Sea of Japan sites cored during Leg 127 (Tamaki, Pisciotto, Allan, et al., in press).

Diatom content and sediment accumulation rates decreased slightly during the Pleistocene, indicating lower productivity in surface waters. The frequency of volcanic events, as recorded by ash layers, increased between about 0.4 and 1.2 Ma, with a peak at 0.6 Ma. The sediments above 100 mbsf (younger than 1 Ma) have decreasing amounts of biogenic carbonate, lower diatom content, and increased and more variable amounts of quartz and clay. Fine-scale variations in these parameters may well record glacial/interglacial, as well as higher frequency, cycles in the Sea of Japan. The most prominent high-frequency cycles evident at Site 798 are the dark/light laminated to bioturbated couplets that became common after about 1.5 Ma and were most clearly developed during the last 0.4 Ma. These cycles reflect rhythmic paleoceanographic changes during the Pleistocene. Rhythmic changes in bottom-water oxygen levels probably contributed to cyclic interbedding of laminated/organic-rich vs. bioturbated/organic-poor sediments. Changes in the relative richness of biosiliceous and biocalcareous components have been attributed to changes in productivity and/or preservation of these components, as well as to differing degrees of dilution of the biogenic components by terrigenous clays. Further elucidation awaits more detailed study of the Site 798 cores.

BIOSTRATIGRAPHY

Introduction

Microfossils occur with variable abundance and preservation states throughout Holes 798A, 798B, and 798C. In general, calcareous microfossils are most abundant and best preserved in Quaternary sediments. For reasons that are not entirely clear, calcareous microfossils exhibit the best preservation in Hole 798B. Siliceous microfossils occur throughout the section, with the exception of Sections 128-798B-50X-CC to 128-798B-54X-CC, where they are absent. The best biosiliceous preservation in the Quaternary sequence occurs in laminated sediments, whereas the poorest preservation occurs in clay-rich sediments.

Diatoms were best used in this site to zone the late Pliocene through Quaternary, although calcareous nannofossils and silicoflagellate/ebridian datum levels also proved useful. The paucity of carbonate made it difficult for us to use calcareous nannofossils or foraminifers below the Quaternary. It seems likely that with more closely spaced samples, one will be able to use changes in coiling ratios of *Neogloboquadrina pachy-*

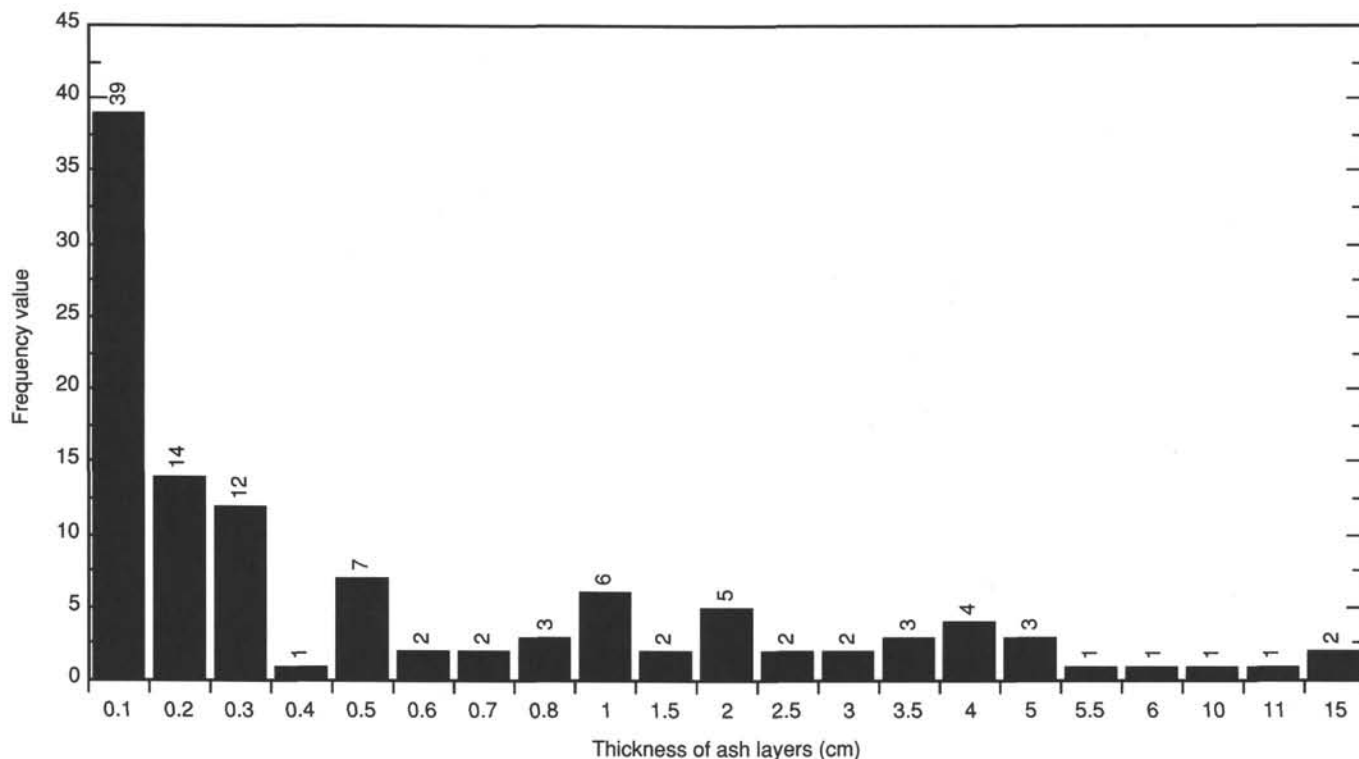


Figure 45. Frequency of occurrence of ash layers of different thicknesses at Site 798. Data are from Table 4.

derma to zone the late Quaternary into glacial/interglacial intervals. Diatom datum levels appear to be consistent with those described for Leg 127 and for the north Pacific (Koizumi and Tanimura, 1985). All microfossil data are summarized in Table 7, which includes paleomagnetic reversal boundaries (see "Paleomagnetism" section, this chapter). Biostratigraphic data are summarized in Figure 46.

Diatoms

On the basis of diatom biostratigraphy, drilling at this site penetrated to the middle Pliocene. Diatoms are generally present throughout much of the section, sometimes in considerable abundance; only near the bottom of Hole 798B do they disappear completely from the sediment.

Sections 128-798A-1H-CC through 128-798A-5H-1, 38 cm, contain few to common diatoms (Table 8), and have been assigned to the *Neodenticula seminae* Zone. The assemblage is typical for a branch of the Kuroshio Current and includes, besides the named taxon, *Thalassiothrix nitzschioides*, *T. nitzschioides* var. *parva*, *Coscinodiscus marginatus*, *C. radiatus*, *Pseudoeunotia doliolus*, and *Paralia sulcata*. Sections 128-798A-5H at 38cm, through 128-798A-10H-CC contain common to abundant, moderately to well-preserved diatoms that belong to the *Rhizosolenia curvirostris* Zone. The top of this zone is defined by the last occurrence of the nominate taxon and the base by the last occurrence of *Actinocyclus oculatus*. Within the lower part of this zone, we observed the last appearance of the silicoflagellate *Mesocena elliptica*. In the equatorial Pacific, this last appearance has been noted between the top of the Jaramillo subchron and the base of the Brunhes chron (Hays et al., 1969). Diatom species found in this zone include *P. doliolus*, *N. seminae*, *Thalassiosira lineata*, *Rhizosolenia hebetata*, *C. excentricus* and *T. nitzschioides* and varieties.

The top of the *A. oculatus* Zone is defined by the last appearance of the nominate taxon. In Hole 798A, this species

is scattered and occurs rarely. In some instances, we did not find it at all, but the samples were still assigned to that zone on the strength of stratigraphic position. The *A. oculatus* Zone extends from Sample 128-798A-10H-CC to the base of the hole (128-798A-16H-CC) and contains few to common, poor to moderately well-preserved diatoms. Besides the nominate taxon, the assemblage in this interval includes *N. seminae*, *R. curvirostris*, *C. radiatus*, *C. excentricus*, *T. nitzschioides* and varieties, and *P. sulcata*.

Drilling at Hole 798B penetrated into the middle Pliocene (the lower part of the Gauss magnetic chron). Samples 128-798B-1H-CC through 128-798B-5H-CC are in the *N. seminae* Zone (late Quaternary). There are few to common diatoms in this zone, and they are generally moderately well preserved. Besides the nominate taxon, species include *T. nitzschioides* and varieties, *C. marginatus*, *C. excentricus*, *T. oestrupii*, and *P. sulcata*. Although an open-ocean marine environment is indicated by this assemblage, *P. sulcata* also is present, sometimes in chains, and frequently *Cocconeis* sp. and *Cyclotella* cf. *C. striata* are encountered. The early late Quaternary *R. curvirostris* Zone occurs in Samples 128-798-6H-CC through 128-798B-9H-CC. Here, the diatoms are few to common and are generally moderately well preserved. Besides the nominate taxon, species include *T. nitzschioides* and varieties, *N. seminae*, *C. marginatus*, *P. sulcata*, *T. oestrupii*, and *Cyclotella* cf. *C. striata*. In the lower part of this zone, we encountered the last appearance of *M. elliptica*, indicating that we had passed into the Matuyama chron.

The underlying *A. oculatus* Zone extends from Sample 128-798B-10H-CC to 128-798B-23X-CC. Diatoms are few to abundant through this interval, and preservation ranges from moderately well preserved to good. At some levels, the nominate taxon was not observed, but the sample was still assigned to this zone on the basis of stratigraphic position. Species observed within this zone include *T. nitzschioides*, *Coscinodiscus obscurus*, *N. seminae*, *R. curvirostris*, *C.*

Table 7. Biostratigraphic data for Site 798, including paleomagnetic reversal boundaries.

Core, section, interval (cm)	Depth (mbsf)	Planktonic foraminifers	Calcareous nanofossils	Diatoms	Silicoflagellates/ Ebridians	<i>N. pachyderma</i>		Paleo- magnetics	Age (Ma)
						(dextral)	(sinistral)		
798A-1H	0-9.4					8	65		
798A-2H	9.4-18.4					13	15		
798A-3H	18.4-27.4					1	24		
798A-4H	27.4-36.8					35	22		
798A-5H-2, 100	40.8-40.8			LAD <i>R. curvi</i> .					0.34
798A-5H	36.8-46.3					3	8		
798A-6H	46.3-55.8		LAD <i>P. lacunosa</i>			3	56		0.46
798A-7H	55.8-65.4					3	39		
798A-8H	65.4-74.9					1	34		
798A-9H-4, 95	80.34-80.34				LAD <i>M. ellip.</i>			B/M boundary	0.73
798A-9H	74.9-84.5	Coil.dir. 8/9				1	7		0.82
798A-10H-5, 95	92.95-92.95							M/J boundary	0.91
798A-10H-8, 105	93.75-93.75							J/M boundary	0.98
798A-10H	84.5-94.2					12	53		
798A-11H	94.2-103.9					21	55		
798A-13H-4, 103	113.5-120.48		LAD <i>H. sellii</i>						1.2
798A-13H	113.5-123.2					31	3		
798A-14H	123.2-132.9					1	0		
798B-15H	132.9-142.6					2	6		
798B-16H	142.6-152.3					2	0		
798B-18X	161.9-171.6					4	2		
798B-19X	171.6-181.3					16	2		
798B-20X	181.3-191					13	4		
798B-21X-2, 63	194.63-194.63							M/O boundary	1.66
798B-21X	191-200.6					2	3		
798B-22X	200.6-210.3					1	1		
798B-23X-2, 138	214.68-214.68							O/M boundary	1.88
798B-23X	210.3-220			LAD <i>E. antiqua</i>		1	0		1.9
798B-24X	220-229.7				LAD <i>A. rect.</i>	1	1		2.04
798B-25X	229.7-239.3					11	15		
798B-26X	239.3-249					2	4		
798B-27X	249-258.7					4	2		
798B-31X	286.4-296				LAD <i>Ebr. a.a.</i>				2.39
798B-32X-1, 113	298.63-298.63							M/G boundary	2.47
798B-32X	296-305.7								
798B-33X	305.7-315.3								
798B-34X	315.3-325			LAD <i>N. kamts.</i>	LAD <i>D. jimlingii</i>				2.6

Note: Reversal boundaries are included for completion (see "Paleomagnetism" section, this chapter). Unless specified, all samples were taken from core-catchers.

marginatus, *C. excentricus*, *A. senarius*, *Nitzschia reinholdii*, *P. doliolus*, *T. oestrupii*, and *P. sulcata*. The base of this zone was identified with some difficulty. It is approximately below the Pliocene/Pleistocene boundary and is defined by the last appearance of *Neodenticula koizumii*.

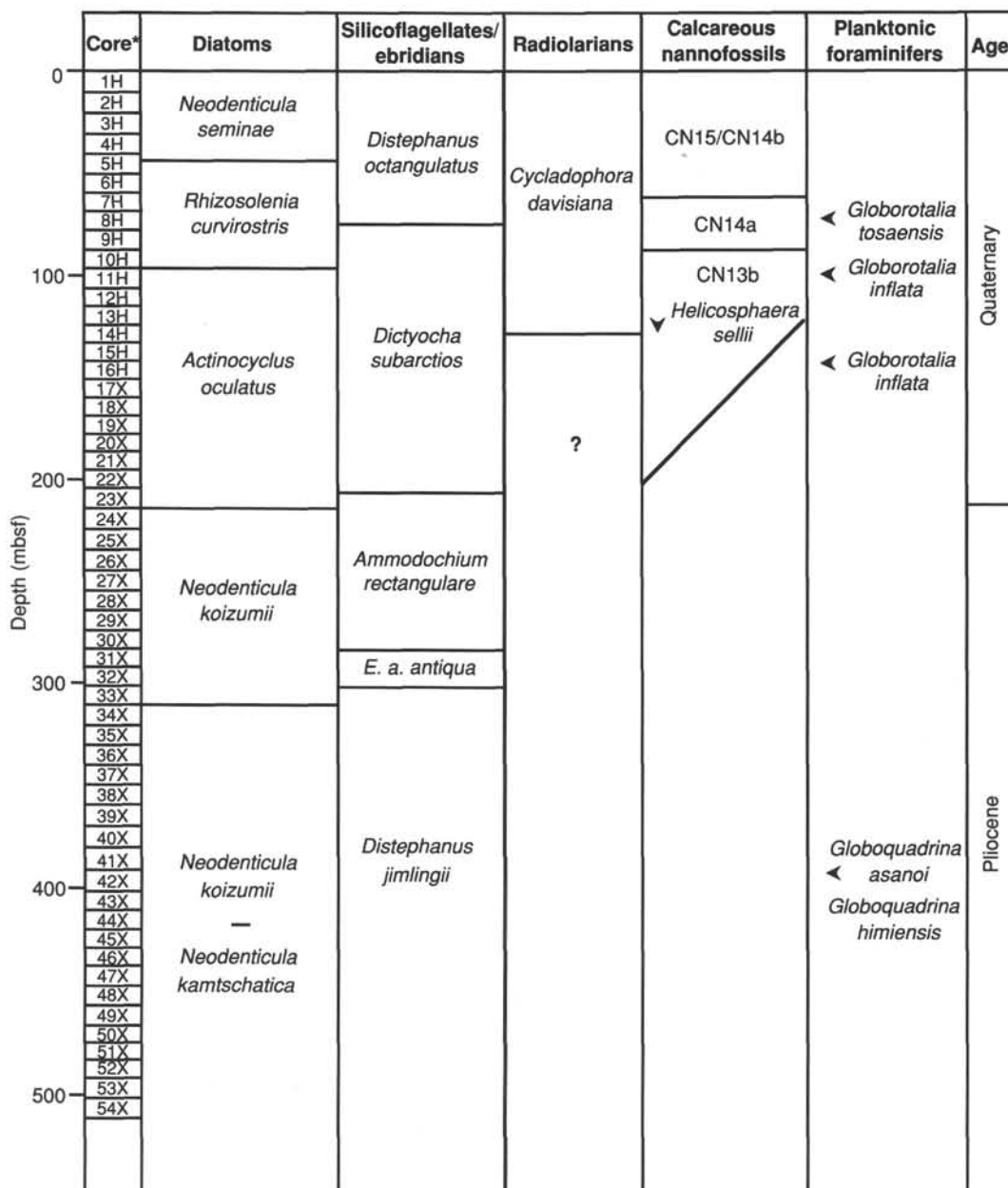
This last appearance defines the top of the underlying *N. koizumii* Zone. In some cases, the nominate taxon was not observed, but the sample was placed in this zone because of stratigraphic position. The diatoms range from common to abundant in this interval, but tend to be more abundant than in any of the overlying intervals. Preservation is moderate to good. The diatom *T. nitzschoides* is especially abundant in this zone. This form is found most abundantly in upwelling areas and in regions where salinity is below the ocean average. The species is found in surface sediments beneath the Peru/Chile Current, where surface seawater temperatures are on the order of 18° to 20°C. It also is found in transitional waters where surface-water temperatures are on the order of 12°C.

Sample 128-798B-27X-CC contains abundant *C. marginatus*. This species is most common in transitional waters. Besides these forms, we also find the following species in this zone: *R. curvirostris*, *N. seminae*, *R. hebetata*, *A. oculus*, *N. reinholdii*, *C. curvatulus*, *T. oestrupii*, and *Thalassiosira antiqua*.

The top of the *Neodenticula kamtschatica*-*N. koizumii* Zone, defined by the last occurrence of *N. kamtschatica*, occurs in Sample 128-798B-34X-CC. The last appearance of this species, which occurs near the top of the Gauss magnetic

chron (Koizumi and Tanimura, 1985), is a well-known datum in the North Pacific. As such it may be used to identify paleoenvironmental and paleoclimatic events that are known to have occurred in the late Gauss and early Matuyama chrons (see, for example, Shackleton and Opdyke, 1977; Prell, 1985; Shackleton et al., 1984). Diatoms range from rare to abundant in this zone, and preservation ranges from poor to good. Unlike the overlying zone, the *D. kamtschatica*-*N. koizumii* Zone does not feature abundant *T. nitzschoides* or *C. marginatus*. Rather, when diatoms are abundant, the assemblage tends to be more diverse. Species found in this zone include *T. nitzschoides*, *N. koizumii*, *C. curvatulus*, *A. oculus*, *C. marginatus*, *A. senarius*, *N. reinholdii*, *P. sulcata*, *R. styliformis*, *T. oestrupii*, *Coscinodiscus* cf. *C. pustulatus*, and *R. curvirostris*. Preservation decreases between Samples 128-798B-47X-CC and 128-798B-49X-CC, so that in the latter sample, diatoms are rare and preservation is poor. The only species observed in this latter sample was *T. nitzschoides*. Samples from 128-798B-50X-CC through 128-798B-54X-CC contain no diatoms.

Samples 128-798C-1H-CC through 128-798C-4H-CC belong to the *N. seminae* Zone. Diatoms are few to common in abundance, and preservation generally ranges from poor to moderate. In this hole, we were able to recover the mud line and to examine the diatoms in surface sediments. Samples from the sediment/water interface contain abundant, well-preserved diatoms of Holocene age. In composition and preservation, the diatoms are not unlike those found in other



*Composite summary of Holes 798A, 798B, and 798C

◀ Indicates position of cited species

▼ Last appearance datum

Figure 46. Correlation chart showing microfossil zones relative to depth and time.

surface samples around this site (L. Burckle, unpubl. notes). Diatoms found in this zone include *T. nitzschioides* and varieties, *C. marginatus*, *Thalassiosira decipiens*, *T. oestrupii*, and *Asteromphalous robustus*.

Samples 128-798C-5H-CC through 128-798C-9H-CC belong to the *R. curvirostris* Zone. In the lower part of this zone, we observed the silicoflagellate *M. elliptica*, indicating that we have passed through the Brunhes/Matuyama chron boundary. Diatoms are generally common to abundant, and preservation ranges from moderate to good. Diatoms found in the zone include *T. nitzschioides* and varieties, *N. seminae*, *P. doliolus* and *P. sulcata*. Samples 128-798C-10H-CC through 128-798C-13H-CC belong to the *A. oculatus* Zone. Diatoms are gener-

ally common to abundant, and preservation is moderate to good. Species found within this zone include *P. doliolus*, *R. styliiformis*, *N. seminae*, *C. marginatus*, *T. nitzschioides*, *T. oestrupii*, *C. excentricus*, and *R. curvirostris*.

Radiolarians

Moderately well-preserved radiolarians were observed in most of the samples examined from Site 798. However, their low abundance and the absence of any age indicators widely recognized in North Pacific late Neogene sequences preclude any attempt at zonation beyond the top of the *Cycladophora davisiana* Zone, which covers the Quaternary (Samples 128-798A-1H-CC to 128-798A-15H-CC; 128-798B-1H-CC to 128-

798B-20X-CC; 128-798C-1H-CC to 128-798C-13H-CC). Although the last appearance datum (LAD) of *Saccospyris conithorax* was recognized in Samples 128-798A-12H-CC and 128-798C-11H-CC, which may serve as a datum level, it will require verification from later sites. Similarly, the LAD of *Botryostrobus acquiloni* in Sample 128-798C-31X-CC and *Thecosphaera japonica* in Sample 128-798C-47X-CC will need additional confirmation. Radiolarians were absent from Samples 128-798B-48X-CC through 128-798B-54X-CC.

The radiolarian assemblage recovered from subsurface samples of Site 798 is low in species diversity and consists mainly of cold water elements as reported previously (Ling, 1975a). However, the occurrence of modern warm-to-temperate forms, such as *Euchitonia furcata*, *Euchitonia* spp., and *Tetrapyle octacantha*, in Samples 128-798A-3H-CC and 128-798A-4H-CC (27.3–36.7 mbsf) suggests the presence of a short warm interval at this site during the Quaternary. This short, late Pleistocene, warm interval can be traced along the eastern Sea of Japan, because among the four sites drilled during the DSDP Leg 31 cruise (Sites 299 through 302), only Site 299 from the northeast Yamato Basin yielded the typical modern warm water species, e.g. *Amphirrhopalum ypsiron*, *Euchitonia furcata*, and *Spongater tetras teras* from similar depths, 28.5 to 38 mbsf.

Silicoflagellates and Ebridians

Most samples examined from Site 798 contained moderately well-preserved silicoflagellates and/or ebridians, except for Sections 128-798B-48X-CC to 128-798B-54X-CC, which were barren of these groups.

In general, the previously proposed zonal scheme from the Sea of Japan based on the results of DSDP Leg 31 (Ling, 1975b) is applicable at this site. Zones are as follows:

Zone	Age
<i>Distephanus octangulatus</i>	Quaternary to middle Pleistocene
<i>Dictyochoa subarctios</i>	early Pleistocene
<i>Ammodoichium rectangulare</i>	late Pliocene
<i>Ebriopsis antiqua antiqua</i> (= <i>Ebriopsis antiqua</i> , without spine)	middle Pliocene
<i>Distephanus jimlingii</i> (= <i>Cannopilus hemisphericus</i>)	early Pliocene

The LAD of *Dictyochoa subarctios* was observed in Sample 128-798A-9A-CC, indicating that the top of the *D. subarctios* Zone (with the overlying section being assigned to the *Distephanus octangulatus* Zone) continues to the bottom of the hole (Sample 128-798A-15H-CC).

Samples were examined from Section 128-798B-14H-CC to the bottom of the hole, but, as stated earlier, the bottom seven cores were barren of these microfossils. The LAD of *Ammodoichium rectangulare* was encountered in Sample 128-798B-23X-CC, marking the upper limit for the zone of the named species and indicating the Pliocene/Pleistocene boundary (see discussion below). The LAD of *Ebriopsis antiqua antiqua* was recognized in Sample 128-798B-31X-CC, where the top of the *E. antiqua antiqua* Zone is drawn. Finally, the LAD of *Distephanus jimlingii* was observed in Sample 128-798B-33X-CC, indicating the top of the zone of the named species. The zone extends downward to the last silicoflagellate-bearing sample of the hole (128-798B-47X-CC).

The LAD of *Dictyochoa subarctios* was observed in Sample 128-798C-10H-CC, indicating the top of the *D. subarctios* Zone, with the overlying section assigned to the *Distephanus octangulatus* zone. *Dictyochoa subarctios* occurs down to the deepest sample of the hole (128-798C-13H-CC), indicating that

this part of the section is still in the *Dictyochoa subarctios* Zone.

In comparing the occurrence of these microfossils from Site 798 on Oki Ridge with occurrences reported from other areas of the North Pacific, the following new data have emerged after cross-correlation with the results of shipboard magnetostratigraphy:

1. The LAD of *Dictyochoa subarctios* was formerly thought to occur slightly above the Brunhes/Matsuyama chron boundary of ca. 0.7 Ma in the North Pacific (Ling, 1970). However, this datum is slightly older at Site 798, occurring between the Brunhes Chron and the Jaramillo Subchron at ca. 0.9 Ma;
2. The LAD of *Ammodoichium rectangulare* is placed at the beginning of Olduvai Subchron, ca. 1.88 Ma, thus confirming it as an index form for the Pliocene/Pleistocene boundary, as suggested previously (Ling, 1975b);
3. The LAD of *Ebriopsis antiqua antiqua* is thought to mark the top of the middle Pliocene. Based on analysis at Site 798, this event occurs within Core 128-798B-31X, and is slightly above the Matuyama/Gauss chron boundary (ca. 2.48 Ma).
4. The LAD of *Distephanus jimlingii* was thought to define the early/middle Pliocene boundary. However, this datum level has been recognized in the late Pliocene *Denticulopsis seminae* var. *fossilis*/*D. kamtschatica* (diatom) Zone in the Northwest Pacific, which is near the top of the Gauss Chron of ca. 2.6 Ma (Barron, 1980). The datum level from Site 798 seems to agree with the age from the Northwest Pacific.

Calcareous Nannofossils

Calcareous nannofossils are present in all three holes drilled at Site 798 on the Oki Ridge. With a few exceptions, descriptions of the nannofossils from each core are from core-catcher samples only. Hole 798B provided the most complete and highest quality recovery from the top of the section, where coccoliths were also the most numerous and best preserved. In general, the nannofossils recovered at this site are poorly preserved and exhibit a high degree of etching/dissolution (Table 8).

Because of the poor degree of preservation, nannofossils from Sample 128-798A-1H-1, 2 cm, to Sample 128-798A-6H-CC can be assigned only to the late Quaternary nannofossil Zones CN15 or CN14b. Within this interval, the nannofossils exhibit intense dissolution. It is difficult to distinguish consistently *Emiliania huxleyi* from poorly preserved species of *Gephyrocapsa* and *Reticulofenestra*, which also are present within this interval. This interval also contains *G. caribbeanica*, *G. oceanica*, *Coccolithus pelagicus*, *Coccolithus streckerii*, and *E. cf. huxleyi* in abundances of few to common. Many of the *Gephyrocapsa* species in this interval exhibit evidence of "I"-shaped elements in the distal shield, which may result from dissolution. Many of these same species have most of their central area bridge dissolved, making for further difficulty in species identification. *Calcidiscus leptoporus*, *Helicosphaera carteri*, and *Braarudosphaera bigelowii* occur within this interval in abundances ranging from barren to few. Sample 128-798A-7H-CC is barren.

The LAD of *Pseudoemiliania lacunosa* defines the top of middle to early Quaternary Subzone CN14a, and may be found in Sample 128-798A-8H-6, 109 cm. Samples 128-798A-8H-6, 109 cm, through 128-798A-10H-1, 47 cm, can be placed within Subzone CN14a. Species common to abundant in this interval include *G. oceanica*, *Gephyrocapsa sinuosa*, *Gephyrocapsa aperta*, *C. streckerii*, and *C. pelagicus*. Species few to common within this interval are *P. lacunosa*, *G. caribbeanica*, *B. bigelowii*, *C. leptoporus*, and *Gephyro-*

Table 8. Abundance and preservation of microfossils from Site 798.

Core number	Diatoms		Radiolarians		Silicoflagellates		Calcareous nannofossils		Planktonic foraminifers		Benthic foraminifers	
	Abundance	Preservation	Abundance	Preservation	Abundance	Preservation	Abundance	Preservation	Abundance	Preservation	Abundance	Preservation
128-798A-1H	C	G	R	M	R	M	F	M	A	M-G	A	G
2H	F	M	R	M	B		B		F	M	C	M
3H	F	M	R	M	R	M	F	P	F-C	M	F	P
4H	C	M	R	M	R	M	C	M	F-C	M	A	M
5H	C	M	R	M	R	M	B		A	G	A	M
6H	C	M	R	M	B		F	P	A	M-G	R	M
7H	F	M	R	M	B		B		R-F	P	C	M
8H	C	M	R	M	R	M	C	M	F-C	M	C	G
9H	F-C	M	R	M	F	M	A	M	A	G	R	M
10H	F	M	B	M	R	M	C	P	C	M	F	M
11H	C	M	R	M	R	M	F	P	A	M-G	C	M
12H	F-C	M	F	M	F	M	B		B		R	P
13H	C	M	R	M	F	M	A	M	A	P-M	F	M
14H	F	P	R	M	R	M	B		R	G	R	P
15H	F	P	R	M	F	M	B		R	M-G	R	P
128-798B-1H	C	M					F	P	A	G		
2H	C	M					F	P	C	M		
3H	F	M					C	M	C	G		
4H	C	M					F	P	F	M		
5H	C	M					B		R	M		
6H	A	G					B		A	M		
7H	F	P-M					C	M	A	G		
8H	F	P-M					C	M	A	G		
9H	C	M					C	M	A	G		
10H	A	M					F	P	F	G		
11H	F-C	G					F	P	F	G		
12H	C	M					R	P	C	G		
13H	A	M-G					B		R	G		
14H	F	P	R	M	R	M	F	P	F	G	A	G
15H	C	M	R	M	C	M	F	P	R	M	C	M
16X	C	M	R	M	C	M	C	P	R	M-G	R	M
17X	A	M	R	M	F	M	F	P	F	M	R	M
18X	C	P-M	R	M	F	M	F	P	R-F	G	C	M
19X	F	P-M	R	M	B		F	P	C	M-G	C	M
20X	C	M	R	M	F	M	F	P	F	M-G	C	M
21X	C-A	M	R	M	F	M	F	P	R	M-G	F	M
22X	C-A	M	B		B		F	P	R	G	R	M
23X	C	M	R	M	F	M	R	P	R	M	R	P
24X	C	M	R	M	F	M	B		R	M	R	P
25X	F-C	M	F	M	R	M	F	P	R	G	R	M
26X	A	G	R	M	A	G	F		R	G	R	
27X	A	G	R	M	R	M	B		R	G	B	
28X	A	G	R	M	R	M	B		B		R	
29X	NS		NS		NS		NS		NS		NS	
30X	F-C	M	R	M	R	M	B		B		B	
31X	A	G	R	M	F	M	B		B		B	
32X	A	G	R	M	F	M	B		B		B	
33X	C-A	M	R	M	F	M	B		B		R	P
34X	F-C	M	B		B		R	P	B		B	
35X	F	P	R	M	F	M	C	P	R	M	R	P
36X	F	P-M	R	M	F	M	B		B		R	P
37X	C-A	M	B		R	M	B		B		B	
38X	C-A	M	R	M	F	M	B		B		R	P
39X	C-A	M	R	M	R	M	B		B		B	
40X	A	M	R	M	R	M	B		B		B	
41X	F-C	M	R	M	R	M	B		B		B	
42X	B		R	M	R	M	B		R	P-M	R	P
43X	F	P	R	M	R	M	B		B		B	
44X	R	P	R	M	R	M	B		B		B	
45X	C-A	M	R	M	R	M	B		B		B	
46X	F	P	R	M	R	M	B		B		B	
47X	F	P-M	R	M	R	M	B		B		B	
48X	R	P	B		B		B		B		B	
49X	R	P	B		B		B		B		R	P
50X	B		B		B		B		B		R	P
51X	B		B		B		B		B		R	P
52X	B		B		B		B		B		B	
53X	NS		NS		NS		NS		NS		NS	
54X	B		B		B		B		B		R	P
128-798C-1H	A	M	R	M	B	M	C	M	A	G	F	M
2H	F	P	R	M	B		B		A	M	C	P
3H	C	M	F	M	R	M	F	P	A	M-G	A	M
4H	F	P-M	F	M	R	M	C	P	C-A	G	C	M
5H	A	M-G	R	M	R	M	C	P	A	M	C	M
6H	C-A	M	R	M	R	M	F	P	A	M	F	P
7H	C	M	R	M	R	M	B		F	P	C	M
8H	F	P-M	R	M	R	M	A	M	A	G	F	M
9H	F	M	R	M	A	M	A	M	A	G	R	P
10H	C	M	B		A	M	B		R-F	P	R	P
11H	C-A	M	F	M	C	M	B		R	M-G	R	P
12H	C-A	M	R	M	A	M	B		R	M	R	P
13H	C	M	R	M	F	M	R	P	R	M	C	P

Information is based on core-catcher samples. A = abundant, C = common, R = rare, and B = barren. G = good, M = moderate, and P = poor. NS = no sample.

capsa parallela. Large reticulofenestrids are also common to abundant throughout this interval. Samples from Cores 128-798A-8H through 128-798A-11H contain *C. pelagicus* and *B. bigelowii* in abundances on an order of magnitude higher than samples from farther up the section, and down the section, nannofossils are particularly abundant in Section 128-798A-9H-CC.

The first occurrence of *G. oceanica* in Sample 128-798A-11H-3, 90 cm, defines the top of early Quaternary Subzone CN13b. The base of this zone is impossible to distinguish due to the extremely poor preservation of the carbonate fossils down the section and because only 17 cores were recovered from this hole. However, paleomagnetic data from this site may limit the depth to which this zone can extend; the basal Matuyama/Olduvai boundary occurs in Core 128-798B-23X. Samples 128-798B-12H-1, 68 cm, and 128-798B-13H-2, 135 cm, contain an impoverished, poorly preserved assemblage of *B. bigelowii*, *C. pelagicus*, *P. lacunosa*, *G. sinuosa*, *H. carteri*, and *G. caribbeanica*, in abundances of common to few.

The LAD of *H. sellii* defines the top of Gartner's (1977) *H. sellii* Zone and lie within Subzone CN3b. The last occurrence of *H. sellii* in Hole 798A is found in Sample 128-798A-13H-4, 103 cm, and lies within Subzone CN13b. Within this sample, and in Sample 128-798A-14H-6, 110 cm, *H. sellii*, *C. leptoporus*, and *Pontosphaera* sp. occur in abundances of rare to few. Sample 128-798A-15H-2, 125 cm, contains very poorly preserved nannofossils, of which only *H. sellii*, *C. pelagicus*, and *P. lacunosa* are identifiable.

Samples 128-798A-15H-CC, 128-798A-16X-CC, and 128-798A-17X-CC (bottom of Hole 798A) are barren. Preservation within Hole 798A is dominated by periods of intense dissolution. All samples within this hole exhibit moderate to poor preservation, with the degree of preservation generally decreasing down the section.

Hole 798B provided the most complete recovery and highest quality section at Site 798. As with Hole 798A, the nannofossils in Hole 798B exhibit a high degree of dissolution and are poorly preserved, making the boundary between nannofossil Zones CN15 and CN14 impossible to select without the aid of an electron microscope. Consequently, core-catcher samples from Cores 128-798B-1H through 128-798B-4H have been assigned to Zone CN15 or Subzone CN14b. The core-catcher sample from Core 128-798B-5H is barren of nannofossils. Species of nannofossils within these samples reflect the same assemblages, abundances, and preservation as in Hole 798A for the same interval.

The last occurrence of *P. lacunosa* occurs in Sample 128-798B-6H-5, 114 cm. Thus, Subzone CN14a can be recognized from this level down the section until the first occurrence of *G. oceanica* in Sample 128-798B-9H-CC. Species of nannofossils present in this interval reflect the same assemblages, abundances, and preservation as in Hole 798A for the same interval.

The interval below Sample 128-798B-9H-CC through at least Sample 128-798B-18X-CC may be assigned to the early Quaternary nannofossil Subzone CN13b. The last occurrence of *Helicosphaera sellii* was observed in Sample 128-798B-18X-CC. From Hole 798A, however, this datum was recognized in Core 128-798A-13H. Core-catcher samples from Cores 128-798B-13H to 128-798B-18X contain poorly preserved assemblages of nannofossils; thus, it is not surprising that the first *H. sellii* specimen was not seen higher up the section. In Hole 798A many more samples were looked at within this interval. The base of Subzone CN13b cannot be determined because the FAD of *G. caribbeanica* was not observed. However, because the basal Matuyama/Olduvai

boundary was found in Core 128-798B-23X, Zone CN13 may not extend below that level.

Nannofossils were observed in the core-catcher samples of Cores 128-798B-26X and 128-798B-35X, but their degree of preservation is so poor that even species identification is impossible. Samples 128-798B-27X-CC through 128-798B-34X-CC and Samples 128-798B-36X-CC through 128-798B-54X-CC are barren.

Thirteen cores were drilled in Hole 798C. All 13 cores reflect the same late Quaternary assemblages found in Holes 798A and 798B. However, it is interesting to note here that *P. lacunosa* was not observed in any of the core-catcher samples from this hole. Of course, this does not mean that the *P. lacunosa* datum was not reached at this hole. In Holes 798A and 798B, *P. lacunosa* was present in only few to rare abundances. With only a limited number of samples available from the core catchers, coupled with the sporadic occurrences of any of the above listed species of nannofossils throughout each of the three holes, it is not surprising that a zonal marker might be overlooked or not be present within a core because of long sampling intervals and extremely poor carbonate preservation. Consequently, one can only say that Samples 128-798C-1H-CC through 128-798C-9H-CC have nannofossil assemblages that are characteristic of those found in Holes 798A and 798B in Zone CN15/Subzone CN14b.

Calcareous Nannofossil Summary and Some Paleooceanographic Considerations

The calcareous nannofossils observed at Site 798 occur consistently in all cores from the top of the section down to the Pliocene/Pleistocene boundary. Within this interval almost all assemblages seem to have been deposited within the paleo-lysocline. From this boundary, calcareous nannofossils are scattered only farther down the section, and then only in a highly dissolved state of preservation, possibly resulting from *in-situ* diagenetic alteration. The observed nannofossil assemblages at this site may be representative of truly pelagic conditions. Both the diatom and the planktonic foraminiferal assemblages observed within the lower Quaternary sequence are dominated by relatively warm-water assemblages. The absence of discoasters or sphenoliths (which are generally considered to be warm-water indicators) in the nannofossil assemblages in the Pliocene, however, is evidence that these waters may not have been warm enough to support them. However, within the late Pleistocene Brunhes Chron, the planktonic foraminiferal assemblages are generally indicative of colder water. Warm-water diatoms and foraminiferal assemblages may represent periods of time when a portion of the warm-water Kuroshio Current was directed northward through the Tsushima Strait into the Sea of Japan, while cold-water assemblages reflect periods of time when the Sea of Japan was somewhat isolated from the Pacific Ocean from the south because of lowered sea levels. The decrease in sea levels occurred in response to late Pleistocene glacial cycles that restricted the northward flow of a branch of the Kuroshio Current through the Tsushima Strait. The barren or extremely poorly preserved nannofossil assemblages observed throughout the Pleistocene at this site may be attributed to a fluctuating lysocline that operated in response to glacial to interglacial changes and subsequent changes in Sea of Japan chemistry. Changes in lysocline depth would indicate changes in the carbonate ion concentration in the deep water layer, which in turn can be related to the flux rate of calcite. The rate of mixing in the Sea of Japan may have been higher during glacial periods, as would the rate of carbon influx from nearby rivers, increasing the amount of biogenic calcite that was transported

to the ocean bottom. Further shore-based study will be required to assess the amount of calcite in these sediments. A comparison of the results with oxygen and carbon isotope data from the planktonic foraminifers would permit further assessment of the extent of calcite dissolution between glacial and interglacial changes.

Planktonic Foraminifers

The planktonic foraminiferal assemblages found in core-catcher samples from Holes 798A, 798B, and 798C exhibit variable levels of preservation and abundance (Tables 7 and 8). Samples 128-798A-1H-CC through 128-798A-15H-CC and 128-798B-1H-CC through 128-798B-267-CC, as well as 128-798C-1H-CC through 128-798C-13H-CC contain rare to abundant planktonic foraminifers. Below this level, only two samples (128-798B-35X-CC and 128-798B-42X-CC) contain rare specimens. Generally, preservation of planktonic foraminifers from this site ranges from poor to good. Sample 128-798A-5H-CC exhibits very good preservation. In this sample, delicate forms (such as *Globigerinita uvula* and *Globigerina quinqueloba*) constitute more than 50% of the assemblages. In diatom-rich sediments, foraminifers sometimes exhibit exceptional preservation. The only specimens of *Globorotalia inflata* (a relatively delicate form) were found within dense masses of diatoms in Samples 128-798B-11H-CC, 128-798A-14H-CC, 128-798A-15H-CC, and 128-798B-16H-CC. This possibly resulted from quick burial of these tests because of a high sedimentation rate of diatoms. However, other factors, such as organic matter decomposition and oxygen content, can affect preservation of calcareous shells (Berger and Soutar, 1970).

In some samples, foraminifers show signs of dissolution. The calcite along sutures of some specimens from the top five cores of this site have dissolved, creating impressions of sutural apertures similar to the genus *Globigerinoides*. Sample 128-798A-9H-CC includes an almost monospecific assemblage of *Globigerina bulloides* (s.l.). It is possible that this assemblage formed by preferential preservation, i.e., by winnowing. Examination of various cores revealed that specimens of this group occur throughout the cores at this site. In one location two small cavities were found to be filled with volcanic ash and *G. bulloides* (s.l.), respectively. This supports the possibility of preferential separation of these tests. However, similar monospecific assemblages were found in DSDP Site 173 (off northern California) at various intervals in the Pliocene and Pleistocene and may represent blooms of *G. bulloides* that were associated with periods of vigorous upwelling (J. Ingle, pers. comm., 1989). A combination of both winnowing and plankton blooms may have occurred at Site 798.

The core-catcher samples from Site 798 range in age from early late Pliocene through Pleistocene, based on diatoms, nannofossils, silicoflagellates, and magnetostratigraphy (Table 7). Few age-diagnostic species of planktonic foraminifers occur in the assemblages recovered. *G. inflata* (Samples 128-798B-11H-CC, 128-798A-14H-CC, 128-798A-15H-CC, and 128-798B-16-CC), *Globorotalia tosaensis* (Sample 128-798B-9H-CC), *Globoquadrina asanoi*, and *Globoquadrina himiensis* (Sample 128-798B-42X-CC) were observed. These latter species are among important Quaternary markers of Lagoe and Thompson (1988) and Maiya et al. (1976). However, scattered occurrences of these taxa did not permit recognition of first or last occurrence datums. The dominant species in these assemblages include *G. bulloides* (s.l.), *Globigerina quinqueloba*, *Globigerinita glutinata*, *Globigerinita uvula*, and *Neogloboquadrina pachyderma*. This is typical of Pliocene and Pleistocene subarctic to cool-temperate assem-

blages in the North Pacific. Some accessory species (other than the age-diagnostic forms mentioned above) are present in the core-catcher samples from Site 798. These include *Globigerina decoraperta*, *Globigerina falconensis*, *Globigerinoides obliquus*, *Globorotalia praeinflata*, and *Neogloboquadrina dutertrei*. A number of minor species also were tentatively identified, including *G. cf. decoraperta*, *G. cf. falconensis*, *G. cf. asanoi*, *Globorotalia cf. crassiformis*, *Globorotalia cf. puncticulata*, *G. cf. inflata*, *N. cf. dutertrei*, *Neogloboquadrina cf. humerosa*, and *Neogloboquadrina cf. kagaensis*. No major differences were noted among the assemblages of Holes 798A, 798B and 798C; however, age-diagnostic forms were recovered mainly from Hole 798B. This suggests better preservation at this hole.

Analyses of changes in the coiling direction of *N. pachyderma* have previously revealed Pliocene and Pleistocene trends that allow for correlation with well-calibrated datums in the North Pacific (Ingle, 1977; Ujiie and Ichikura, 1973; Lagoe and Thompson, 1988). Lagoe and Thompson (1988) established standard coiling direction (CD) intervals for *N. pachyderma*. Here, preliminary quantitative analysis (Fig. 47) permits approximation of the boundary between Lagoe and Thompson's (1988) standard intervals, CD8 and CD9 (Brunhes/Matuyama = B/M boundary), to near the base of Cores 128-798A-9H and 128-798C-9H, allowing us to separate the early from late Pleistocene or Zone N22 (Table 7). A quantitative study was not conducted for Cores 128-798B-1H through 128-798B-15H; however, the only occurrence of *G. tosaensis* in Sample 128-798B-9H-CC suggests the proximity of the B/M boundary.

The changes in coiling direction of *Neogloboquadrina pachyderma* are assumed to record fluctuations in surface temperature. The mixed dextral/sinistral and dominantly dextral intervals represent times when the Tsushima Current, a branch of the Kuroshio Current, had a stronger influence in the Sea of Japan. The presence of *Globigerinoides obliquus* (Sample 128-798B-9H-CC), which is a tropical to warm-temperate taxon, serves as additional evidence for the increased influence of the Tsushima Current. Further recognition of CD intervals of Lagoe and Thompson (1988) within the

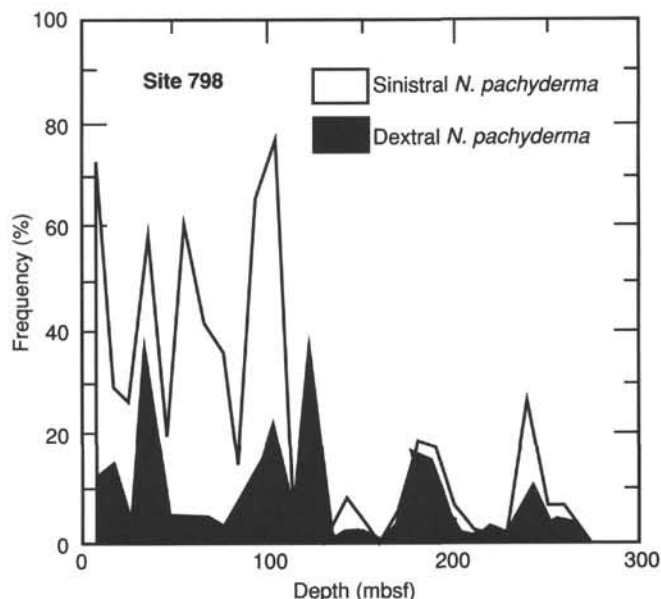


Figure 47. Dextral and sinistral *N. pachyderma*, plotted as an area graph showing the number of sinistral and dextral specimens in the core-catcher samples from Holes 798A and 798B (Data from Table 7).

Brunhes and Matuyama chronozones will be possible after quantitative study of additional samples.

Benthic Foraminifers

Benthic foraminifers are present in all samples examined in Holes 798A and 798C, except in Sample 128-798A-17X-CC. These are also present in the upper to middle parts of Hole 798B. Abundance and preservation vary. Assemblages in these samples are characterized by the dominance of *Bolivina pacifica*, *Uvigerina* spp. (*U. akitaensis* + *U. proboscidea*), *Angulogerina kokozuraensis*, *Cassidulina norcrossi*, *C. norvangi*, *Pseudoparrella takayanagii*, *Eilohedra nipponica*, and *Epistominella pulchella*. These species generally represent upper bathyal to middle bathyal depths (van Morkhoven et al., 1986).

Sediments from Sample 128-798B-27X-CC to the bottom of the hole (except Sample 128-798B-35X, CC) are mostly barren of calcareous foraminifers. Most washed residues in this interval contain siliceous microfossils that are associated with rare fragments of the agglutinated foraminifer, *Martinottiella communis*. Sediments in this interval have been interpreted to have been deposited below the local CCD.

In some samples (128-798A-6H-CC, 128-798A-10H-CC, 128-798B-3H-CC, 128-798C-1H-CC, 128-798C-8H-CC, and 128-798C-9H-CC), where species diversity is low, an increase in relative abundance of *Bolivina pacifica* (more than 40% of the population) was observed. *B. pacifica* is associated with low oxygen environments in the eastern Pacific (Phleger and Soutar, 1973). The high abundance of *B. pacifica*, therefore, strongly suggests dysaerobic to anaerobic bottom conditions.

The fauna of Sample 128-798B-35X-CC is characterized by the occurrence of a so-called "Tertiary-type" population, an important element of the Pliocene-Pleistocene fauna in the Sea of Japan area (Matoba, 1984). The main constituents of the Tertiary-type population are *Martinottiella communis*, *Sphaeroidina bulloides*, *Oridorsalis umbonatus*, *Epistominella pulchella*, *Pullenia apertura*, and *Valvulineria sadonica*. Although these species still live in the northwest Pacific, they are absent from the present-day Sea of Japan. Matoba (1984) considered that the Tertiary-type population became extinct following a drastic change in the bottom environment during the late Pleistocene. The last occurrences of species typical of the Tertiary-type fauna, as observed in the sediments of Site 798, are as follows in ascending order:

Species	Section
<i>Martinottiella communis</i> :	128-798B-25X-CC
<i>Sphaeroidina bulloides</i> :	128-798B-21X-CC
<i>Oridorsalis umbonatus</i> :	128-798A-13X-CC; 128-798B-13X-CC
<i>Epistominella pulchella</i> :	128-798A-3H-CC; 128-798B-3H-CC; 128-798C-3H-CC
<i>Pullenia apertura</i> :	128-798A-2H-CC; 128-798B-2H-CC; 128-798C-2H-CC
<i>Valvulineria sadonica</i> :	128-798A-2H-CC; 128-798B-2H-CC; 128-798C-2H-CC

Alternatively, many species representative of the modern fauna in the Sea of Japan are not found in the ancient Tertiary-type fauna. For example, *Nonionella globosa* makes its initial appearance in Samples 128-798A-8H-CC, 128-798B-9H-CC, and 128-798C-8H-CC.

Paleoenvironment

We can identify three intervals of time when the paleoenvironment at Site 798 apparently changed. These are the late Pliocene, the Pliocene/Pleistocene boundary, and the middle

Pleistocene. During the time span recorded at this site, water depth generally ranged from middle to upper bathyal, although changes in abundance of benthic foraminifers exist that apparently reflect discrete changes in deep-water mass structure or in the circulation and/or productivity of the overlying waters. Specifically, variations in microfossils indicate that significant environmental changes occurred during the late Pliocene near the top of the Gauss Chron, the interval around the Pliocene/Pleistocene boundary, and the middle Pleistocene just before the Brunhes Chron. The middle Pliocene, prior to 2.4 Ma, is characterized by variable preservation and an abundance of diatoms, generally suggesting warm water. The late Pliocene (between approximately 2.4 Ma and the Pliocene/Pleistocene boundary) is characterized by an upwelling assemblage of diatoms dominated by *Thalassionema nitzschioides* and having a low foraminiferal content. We suggest that these conditions were induced by a decrease in eustatic sea level at approximately 2.4 Ma, caused by the initiation of continental ice build-up on Greenland and by ongoing tectonic uplift across the southern part of Honshu, resulting in the closing of the Tsushima Strait.

Sediment deposited in association with the Pliocene/Pleistocene boundary contains the first consistent occurrence of calcareous microfossils, although their preservation is sometimes marginal. At the same time, several warm-water diatom species appear, suggesting that the Tsushima Strait was again submergent and that a branch of the Kuroshio Current, the Tsushima Current, was flowing into the Sea of Japan. The lower Quaternary sediments are characterized by variable preservation and an abundance of diatoms, with warm-water species predominating. Rare warm-water species of planktonic foraminifers also are present, whereas the mixed nature of the coiling ratios of *Neogloboquadrina pachyderma* reflect continuous influx from the Pacific across the Tsushima Strait via the Tsushima Current. We observed changes in both diatom and planktonic foraminiferal abundance and preservation in upper Quaternary sediments, probably reflecting changes in productivity that were induced by glacial/interglacial oscillations. *N. pachyderma* becomes dominantly sinistral in the lower Brunhes Chron, indicating subarctic surface temperatures. We found no evidence of the complete isolation of the Sea of Japan from the Pacific, but our data do suggest at least constriction of the Tsushima Strait during glacial maxima.

PALEOMAGNETISM

Introduction

The main purpose of our paleomagnetic study at this site was to obtain a sequence of the polarity transitions to compare with microfossil data for dating the sediment column. In addition, a high sedimentation rate at this site and the stable nature of the magnetic remanence in the sediment cores will allow us to investigate the detailed variation of the geomagnetic field during the last few million years as a future study.

Experimental Procedure

Remanence of the whole-round archive halves of APC cores from Holes 798A, 798B, and 798C was measured at a 10-cm spacing using a 2G-Enterprise cryogenic magnetometer. Remanence of Cores 128-798A-1H to 128-798A-15H was observed at demagnetization steps of 0, 2, 5, and 10 mT. Cores 128-798B-8H to 128-798B-15H were processed at demagnetization levels of 0 and 10 mT. Cores 128-798C-1H to 128-798C-15H also were measured at the same demagnetization levels as those at Hole 798B. Pilot samples were taken with 7-cm³

plastic cubes from the working half of the cores, and their remanence properties were observed with a minispin spinner magnetometer at demagnetization steps up to 60 mT. These analyses indicate that the remanence of the sediments in APC cores is stable, with a median destructive field (MDF) of more than 20 mT and a single component of the magnetization after demagnetization of 5 mT. Hence, measurements were performed at a demagnetization level of 10 mT, representative of the remanence of the sediment samples.

Difficulty in whole-core measurements using the cryogenic magnetometer lies in the magnetic field disturbance around void spaces within each section of a core. The edges of the sediment at a void space cause disturbance of the magnetic field in the vicinity of the void, and the measurement at these positions gives spurious results. Therefore, during measurement, the intervals of voids and highly disturbed parts were recorded on separate sheets, and the observations at these positions were deleted from the data file after measurement. This procedure is important for obtaining reliable results from whole-core measurements.

After deleting spurious data points, we found that the variations of declination, inclination, and intensity of the magnetization were stable except for Cores 128-798A-8H, 128-798B-8H, and 128-798C-9H. In these cores, the low intensity, more than two orders of magnitude lower than the upper section, may be the cause of this dispersion, because intensity is comparable to the noise level of the cryogenic magnetometer.

The declination of magnetization is fairly constant within each core measured. Hence, it was possible to adjust the relative orientation of the cores so that the mean declination was near zero for the normal magnetic field by subtracting the mean values of the declination within each core. The amount of the rotation applied for the adjustment is listed in Table 9. The orientation of Cores 128-798A-5H to 128-798A-15H was measured during drilling and is listed in Table 10. Orientations obtained from remanence measurements are also shown in Table 10 for comparison. As is evident from this table, the direction of the cores is near the vertical direction. As for azimuth measurements, by allowing an ambiguity of 180°, both orientation measurements give consistent results within about 30°.

For XCB cores from Hole 798B (Cores 128-798B-16X to 128-798B-54X), whole-core measurements are probably useless because of the disturbance of the sediments during coring. Hence, we took discrete samples from the working half of each core and observed their remanence by using the cryogenic magnetometer. Because of the low intensity of these

Table 9. Amount of rotation used for adjusting declination at Site 798.

Core number	Hole 798A (degrees)	Hole 798B (degrees)	Hole 798C (degrees)
1H	-194.1		-204.4
2H	-220.4		-88.1
3H	-224.0		-341.9
4H	-91.8		-165.1
5H	-60.0		-119.0
6H	-108.8		-86.4
7H	-41.4		-335.7
8H	9.2	-11.8	-314.2
9H	69.4	10.3	-25.0
10H	-307.3	168.9	8.6
11H	74.1	94.5	-258.0
12H	13.2	39.9	63.8
13H	-122.1	-117.1	-74.0
14H	-49.7	-111.3	
15H	-25.1	15.3	

Table 10. Orientation found during coring at Hole 798A.

Core number	Inclination off vertical	Direction of inclination	Azimuth	180°+ rotation
5H	0.75	N5E	153	120.0
6H	1.0	N10W	78	71.2
7H	1.0	N20E	182	138.6
8H	1.2	N58E	236	189.2
9H	1.4	N50E	225	249.4
10H	1.66	N55E	254	232.7
11H	1.75	S36W	26	254.1
12H	1.75	N55W	7	193.2
13H	1.5	N45E	264	57.9
14H	2.0	N15E	75	130.3
15H	2.0	S75E	300	154.9

samples, measurements using the spinner magnetometer were difficult. Sampling frequency for the XCB samples was about one sample per section whenever relatively undisturbed sediments were found. Cores 128-798B-35X to 128-798B-45X were most seriously disturbed. The demagnetization steps for these discrete samples are 0, 2, 5, 10, 15, and 20 mT.

Results

Stratigraphic variations in declination, inclination, and intensity of the magnetization of the APC cores are shown in Figures 48, 49, and 50 for Holes 798A, 798B, and 798C, respectively. As evident from these figures, variations in direction and intensity correlate well with declination values adjusted core-by-core.

Figures 48 and 50 indicate that the declination and inclination in the upper 50 m of the section are stable around a mean value of 0° and 60°, respectively. The average intensity of the magnetization is about 10 mA/m, and this intensity varies around the mean value by about a factor of two. Comparison of the variation of the remanence intensity with the variation of the magnetic susceptibility (shown in Fig. 51) suggests that most of the variation in intensity is caused by changes in the concentration of the magnetic minerals in sediments, which may reflect a change in environment during sedimentation.

Correlation of variations in magnetic intensity in cores from Holes 798A and 798C allowed us to determine the offset depth between these two cores. Within the upper 50 m of the section, the minimum local intensity observed at 4 mbsf in Hole 798A was observed at 6 mbsf in Hole 798C. Hence, the offset at this depth has been estimated as about 2 m. The depth of this intensity minimum at the bottom part of the section is 44.5 and 47.0 mbsf for Holes 798A and 798C, respectively, suggesting an offset value of 2.5 m.

Three reversals are present in the middle section of all three holes. The direction of the magnetization is highly dispersive in the intervals of 66 to 76 mbsf in Hole 798A (Fig. 48B), 70 to 80 mbsf in Hole 798B (Fig. 49A), and 72 to 82 mbsf in Hole 798C (Fig. 50B). In this interval, the intensity of the remanence is low and has a mean value of about 0.1 mA/m. The main cause of this dispersion can be attributed to the low intensity of the magnetization, although the possibility of a variation of the actual magnetic field cannot be rejected. Because of the high-angular dispersion just above the polarity reversal, the depth of the reversal and the thickness of the transition zone cannot be determined precisely. This feature is most obvious in the variations of declination. However, the variation of the inclination suggests that the depth of the polarity boundaries occur at 75.5, 79.5, and 80.5 mbsf, in Holes 798A, 798B, and 798C, respectively. The transition can be identified as the Brunhes/Matuyama boundary.

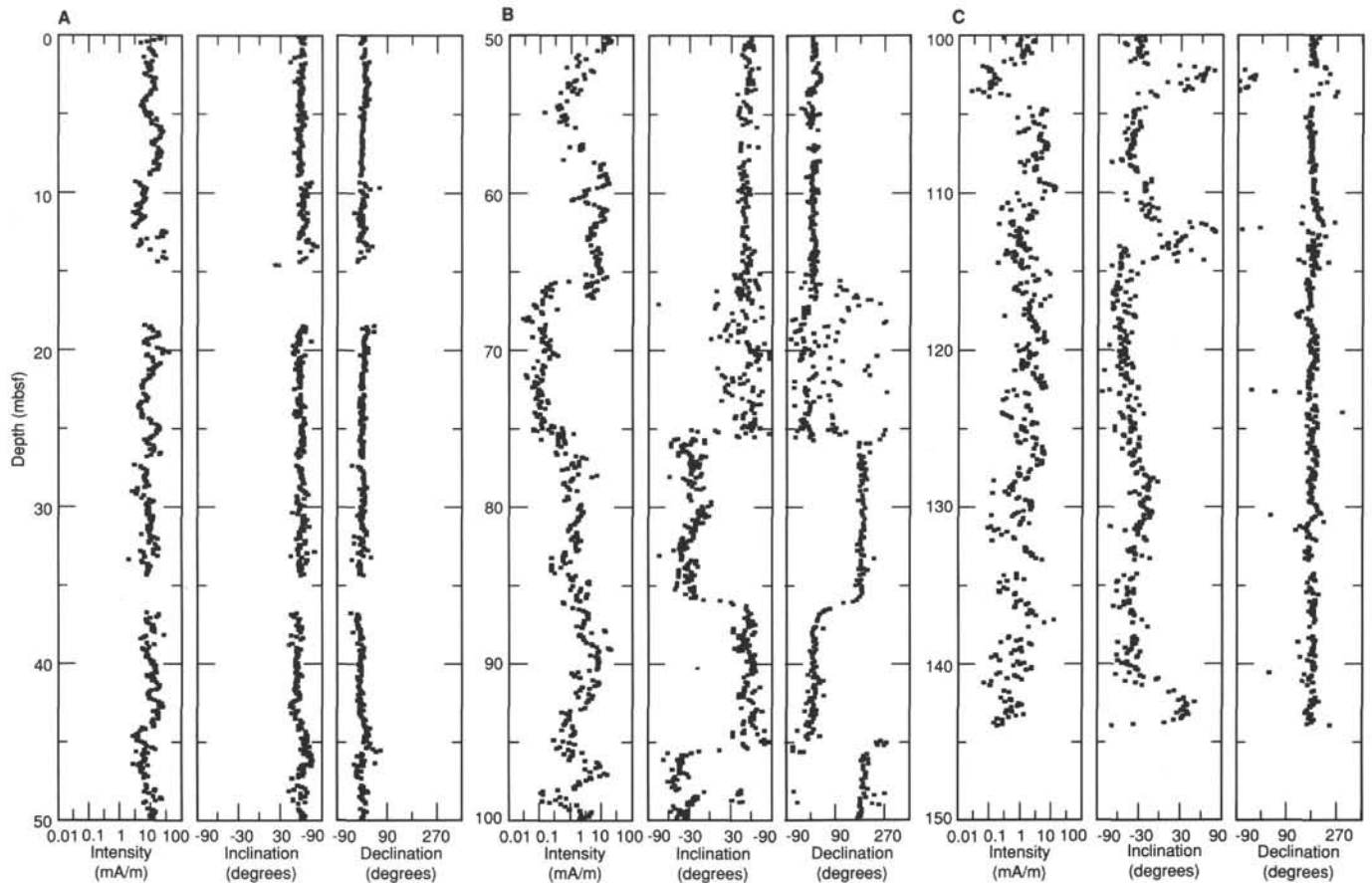


Figure 48. Plot of intensity, declination, and inclination, vs. depth for Hole 798A. Values after the demagnetization step of 10 mT have been plotted. A. 0 to 50 mbsf. B. 50 to 100 mbsf. C. 100 to 150 mbsf.

The Jaramillo normal event was clearly recorded in all three holes. The depth of this event is recorded from 86 to 95.5 mbsf in Hole 798A, 90 to 99.5 mbsf in Hole 798B, and 91 to 100.5 mbsf in Hole 798C. The offset depth of the two boundaries of the Jaramillo event is about 4 m between Holes 798A and 798B, and about 5 m between Holes 798A and 798C. Because both boundaries of the Jaramillo event correspond to the boundaries of the core in Hole 798C (the top boundary lies between Cores 128-798C-10H and 128-798C-11H, and the bottom boundary corresponds to the bottom of Core 128-798C-11H), the depth of the Jaramillo event boundaries in Hole 798C is ambiguous.

Systematic variations in intensity are present in the middle 50 m of the three holes. A low intensity interval, with a thickness of about 10 m just above the Brunhes/Matuyama boundary is observed in all three cores. Short wave-length disturbances may also be correlated among the holes.

Magnetization of the three cores indicates reversed polarity throughout the bottom 50 m of section (100 to 150 mbsf) in each hole. A dispersive zone about 2 m thick occurs approximately 5 m below the transition boundary in all three cores. This may reflect magnetic field disturbance during this period. However, the dispersion of the direction might be caused by the low intensity of the magnetization in this zone. Within the bottom section, the variation of the intensity in Hole 798B is somewhat different from other two holes. The reason is not clear at present.

Figures 52A and 52B present an extended view of the magnetic field reversal of the inclination; Figure 52A displays

the Brunhes/Matuyama transition, and Figure 52B exhibits the Jaramillo event. The sediment magnetization represents the smoothed version of the variation of the magnetic field because of the gradual acquisition of remanence during the consolidation process. These figures indicate that the transition at the Brunhes/Matuyama boundary is broad and encompasses about 2 m of section in the transition zone. On the other hand, the field transition on both sides of the Jaramillo event is sharp, and the thickness of the transition zone may be smaller than 50 cm. As mentioned previously, the nature of the field transition cannot be identified in Hole 798C because of the coincidence of the core boundaries with the polarity boundary.

An enlarged view of the Matuyama/Jaramillo transition is shown in Figure 52C to demonstrate the behavior of the inclination and declination during the transition recorded in Core 128-798A-10H. This transition is recorded in a sequence of thin, laminated sediments free of disturbance. Hence, the curves shown in Figure 52C probably reflect the true behavior of the geomagnetic field during the transition. Note that the transition zone in inclination is much narrower than that in declination. Assuming a constant sedimentation rate of 100 m/m.y., the time required for the transition is estimated as about 2,000 yr for the inclination and more than 5,000 yr for the declination. These observations are important for investigations of the origin of Earth's magnetic field.

Observed inclination and intensity for the discrete samples from XCB cores from the bottom part of Hole 798B (Cores 128-798B-16X to 128-798B-54X) are presented in Figure 53 as

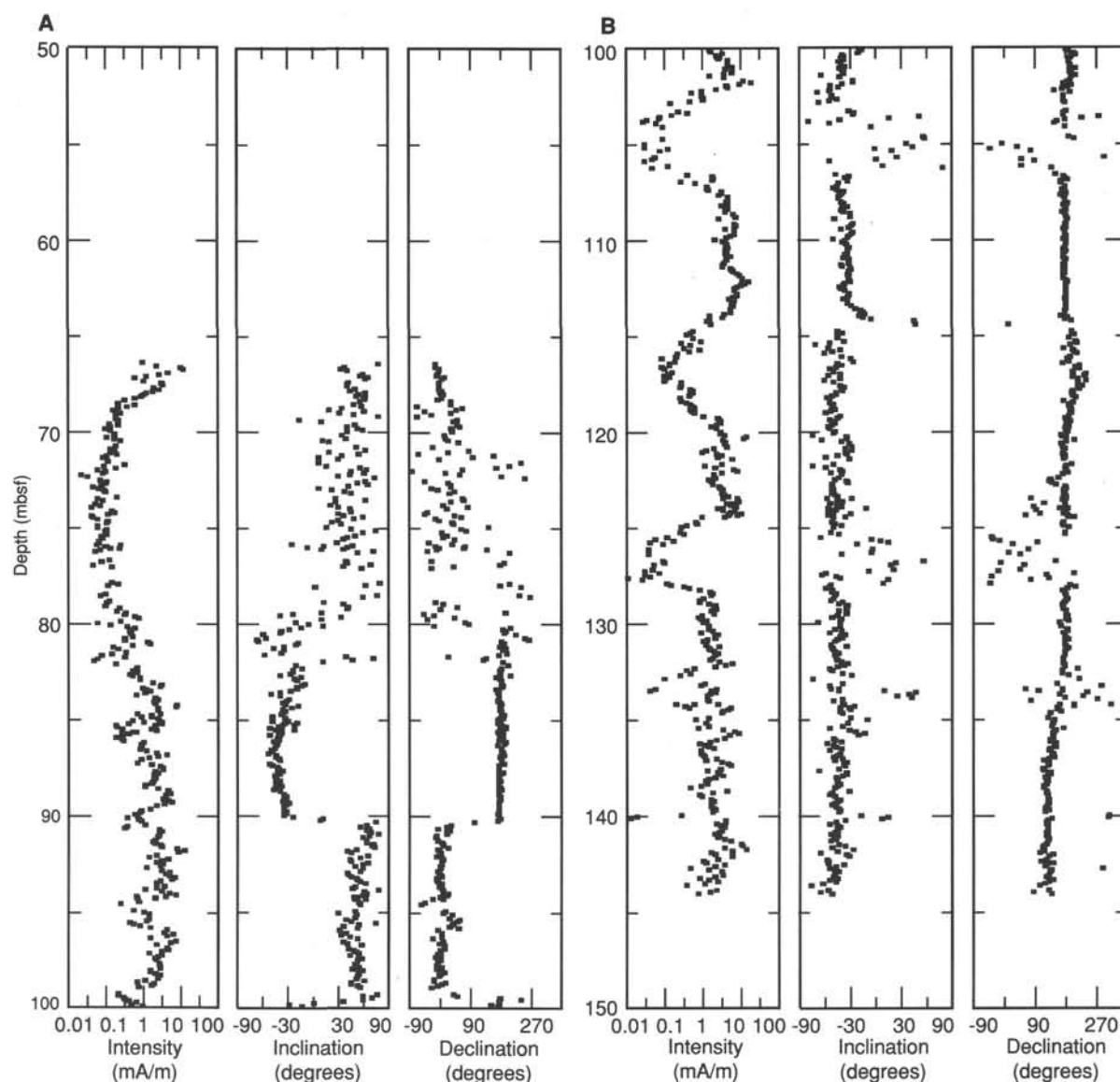


Figure 49. Plot of declination, inclination, and intensity vs. depth for Hole 798B. A. 50 to 100 mbsf. B. 100 to 150 mbsf.

a function of depth. Because of the possible rotation of the samples during coring, these declination data are not useful. In the figure, the normal polarity zone from 190 to 215 mbsf can be identified; the section below 300 mbsf also has a normal polarity. However, the zone below 300 mbsf exhibits rather dispersive directions, where the intensity of the magnetization is lower than in the upper part. Because of the dispersion, further work will be necessary to identify the polarity sequence in this zone.

Figures 54A and 54B show the behavior of magnetization during demagnetizations. Figure 54A illustrates consistent behavior of remanence, with the direction of magnetization hardly changed during the successive demagnetization steps. The Zijderfeld plot on the left of Figure 54A indicates that the remanence of this sample consists of one component. In contrast, Figure 54B represents an example of a "bad sample," where the direction of the magnetization varies significantly during demagnetization, suggesting several components of magnetization. It is difficult to obtain a stable direction from this sort of sample. This kind of variation during demagnetization is typical for highly anisotropic magnetic

minerals, such as pyrrhotite. Also note that the intensity of the former "good" sample is 6.90 mA/m, whereas that of the latter "bad" sample is 0.24 mA/m. This trend was observed throughout the XCB samples at Site 798; that is, high-intensity samples (higher than 1 mA/m) gave reliably stable directions, whereas low-intensity samples (lower than 1 mA/m) gave dispersive results. This can be explained if the sediment consists of two magnetic minerals, where one component has a high intensity of magnetization and good characteristics and the other has a low magnetization and ill-conditioned behavior. If the concentration of the former component is high, then the sediment magnetization shows good behavior, whereas if the latter component is dominant, the magnetization of the sediment exhibits poor behavior.

Considering this possibility, we tentatively decided to distinguish samples by the intensity of their magnetization. In Figure 55, variations of the inclination for the whole samples, with intensities greater than 0.5 mA/m, greater than 0.7 mA/m, and greater than 1.0 mA/m, are shown. Although there is no *a priori* criterion for the threshold value of the magnetization, we adopted the value of 0.7 mA/m for the threshold based on

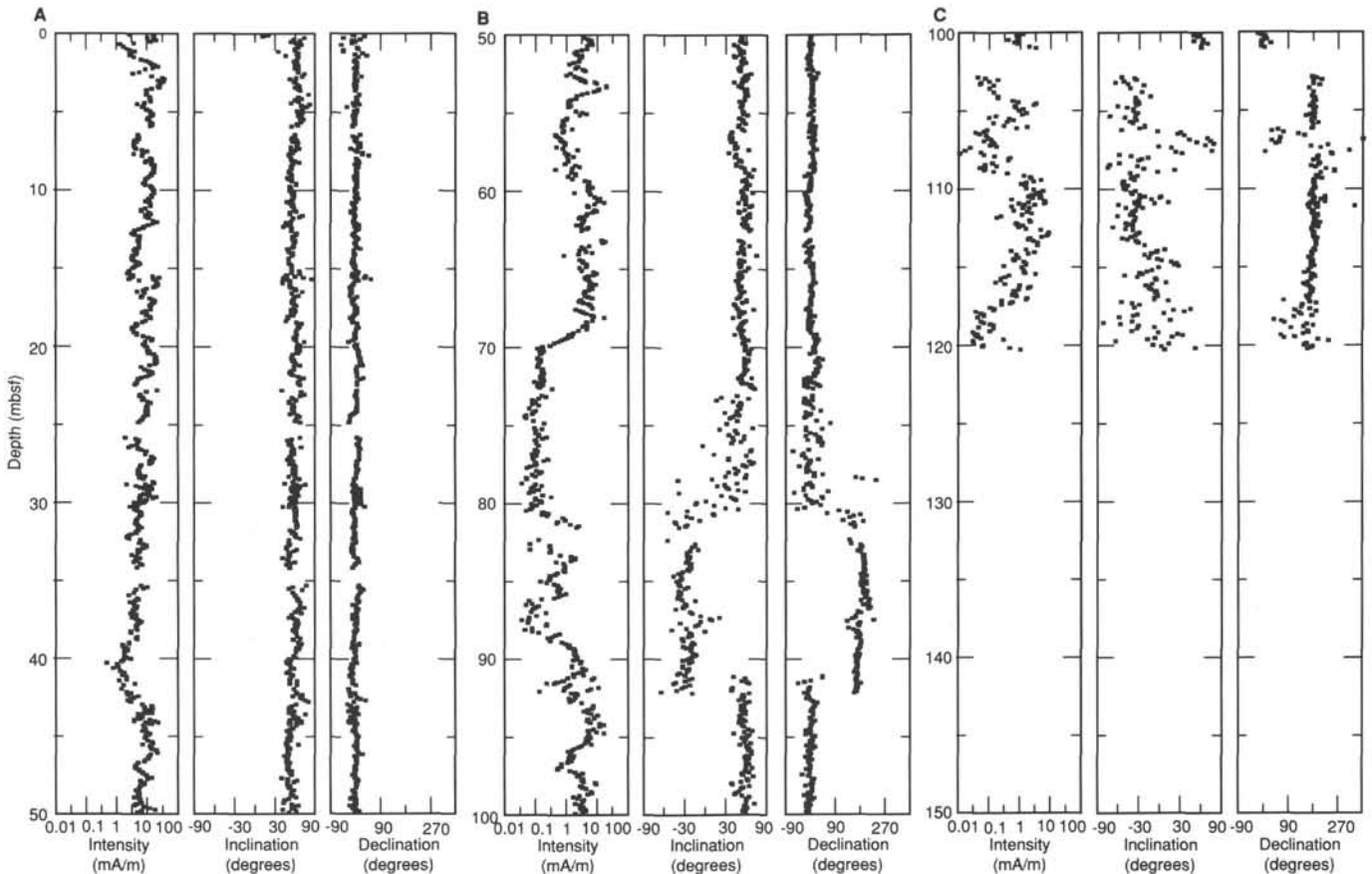


Figure 50. Plot of intensity, declination, and inclination, vs. depth for Hole 798C. A. 0 to 50 mbsf. B. 50 to 100 mbsf. C. 100 to 150 mbsf.

Figure 55 and the observations of the demagnetization characteristics of all the samples from XCB cores of Hole 798B.

Figure 56 presents the final polarity sequence, as based on the above criterion. In this plot, each polarity period was specified only when two or more successive samples exhibited the same polarity. Considering the quality of the data, the normal event identified at a depth of about 200 mbsf, which corresponds to the Olduvai event, and the boundary between the Matuyama and Gauss chrons at a depth of 290 mbsf have been reliably determined, whereas the two reversal events in the Gauss Chron are unreliable.

Discussion

The polarity-depth relationship obtained from our paleomagnetic study for the APC cores is summarized in Figure 57, which also includes the polarity time scale by Berggren et al. (1985). The depths of the Brunhes/Matuyama boundary and the Jaramillo event nearly coincide in Holes 798B and 798C, whereas the boundaries in Hole 798A were observed at a depth about 4 m shallower. Because this offset value is constant throughout all three holes, it cannot be attributed to the differences in sedimentation rates among these cores. Therefore, we infer that the top several meters of sediment are missing in Hole 798A. Holes 798A and 798C were terminated just below the Jaramillo event, whereas Hole 798B extends to a depth of more than 500 mbsf. The entire view of the polarity sequence is shown in Figure 58. In Hole 798B, the normal event observed at about 200 mbsf and the reverse to normal transition at about 300 mbsf can be identified as the Olduvai event and the boundary between the Matuyama and Gauss chrons, respectively. However, data at depths below 300 mbsf

are not considered reliable. If we assume that the sedimentation rate is constant throughout the Hole 798B section, we might expect a reversed zone at about 400 mbsf having a thickness of approximately 50 m. This reversed zone could not be identified from the present XCB cores from Hole 798B. Because results from the bottom 50-m section of Hole 798B are reliable, and because these indicate normal polarities, we should conclude that the bottom of Hole 798B is still in the Gauss Chron. Numerical values of the depths of the boundaries are listed in Figure 59 for convenience.

An age-vs.-depth relationship in Hole 798B is presented in Figure 60 using Berggren et al.'s (1985) time scale, where a straight line fitted by the least-squares method also is shown. As is evident from this figure, the depths of the Brunhes/Matuyama, Matuyama/Jaramillo, Jaramillo/Matuyama, Matuyama/Olduvai, Olduvai/Matuyama, and Matuyama/Gauss transitions plot in a straight line, whereas the points, tentatively assumed as the boundaries of the two reverse events (Kaena and Mammoth) are slightly offset from the line. The gradient of the fitted line gives a high sedimentation rate that exceeds 120 m/m.y. This sedimentation rate seems to have been constant for at least the last 2.5 m.y.

Summary

At Site 798, we conducted a paleomagnetic study for cores from Holes 798A, 798B, and 798C. The results for APC cores from all three holes indicate a clear sequence of polarity changes for the last 1 m.y. Results from XCB cores in Hole 798B also revealed polarity changes that correspond to the Olduvai event and the Matuyama/Gauss transition, although the bottom 200-m section of Hole 798B gave rather dispersive results because of its unstable remanence properties and

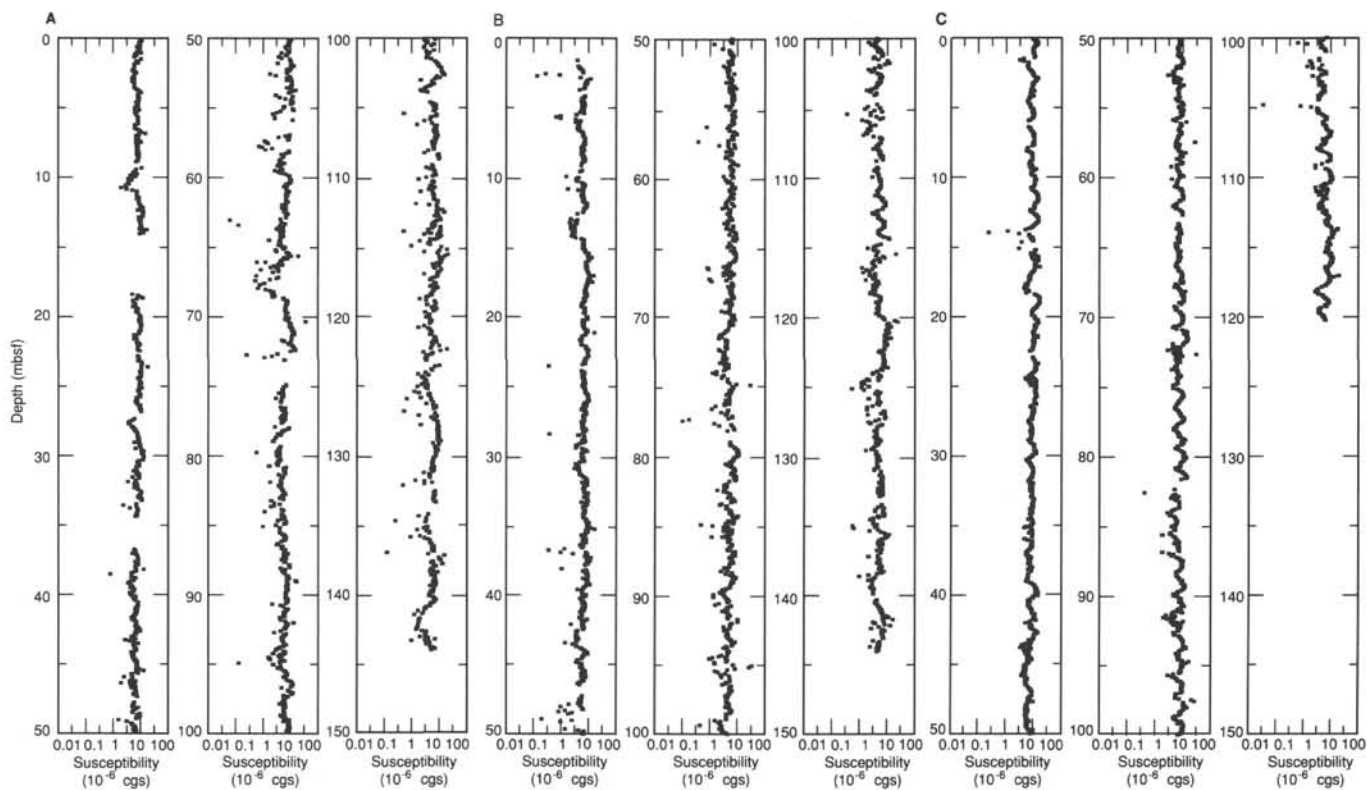


Figure 51. Plot of magnetic susceptibility vs. depth for Site 798. A. Hole 798A. B. Hole 798B. C. Hole 798C.

possible disturbances during coring. The sedimentation rate estimated from the identified boundaries is higher than 120 m/m.y., at least in the last 2.5 m.y.

SEDIMENT ACCUMULATION RATES

Estimates of sedimentation rates for Site 798 are based upon magnetic reversal stratigraphy and stratigraphic positions of biostratigraphic datums that were recognized at this site. These data include six magnetic reversals, three diatom datums, one calcareous nannofossil datum, and three silicoflagellate datums (Table 11). Although no radiolarian or foraminiferal datums were recognized in this section, these groups were still useful for verifying the stratigraphy. Sedimentation rates for 11 intervals were calculated from relationship of age vs. depth (Table 7; Fig. 61). In addition, we calculated the sediment accumulation rate ($\text{g}/\text{cm}^2/\text{k.y.}$) using the average dry-bulk density for each interval (see "Physical Properties" section, this chapter). These accumulation rates tend to agree well with sedimentation rates, but differences between the two values increase with depth, probably because of increased compaction.

Sedimentation rates at Site 798 range from less than 45 to 216 m/m.y., with an average rate of 121 m/m.y. Rates tend to be anomalously high when datum levels are far apart, and anomalously low when they are close together. There are two possible sources of error (or uncertainty) when constructing these curves. One is dictated by the fact that in defining levels of microfossil datums, we generally examined only core-catcher samples. These samples were usually about 9 to 10 m apart. The second source of error deals with the age assignments given to levels of microfossil datums. These were generally based upon sedimentation rates from a known absolute age datum (usually a magnetic reversal). Such data assume a constant sedimentation rate, which is almost never the case.

Given the above considerations, we noted higher rates in the Pliocene, and rates closer to the overall average in the Quaternary, particularly in the late Quaternary. The sedimentation rate for this upper Quaternary, rhythmically interbedded diatom ooze and diatomaceous clay, which includes high amounts of volcanic ash, is on the order of 120 m/m.y. Rates of sedimentation in pre-upper Pliocene portions of the Site 798 sequence are more variable, possibly because of compaction and differences in the influx of biogenic and nonbiogenic detritus.

INORGANIC GEOCHEMISTRY

This section summarizes the results of shipboard analysis of dissolved constituents in the interstitial water of sediments recovered from Site 798. Detailed sampling of pore fluids allowed us to obtain high-resolution profiles in the upper 100 mbsf. Distributions of dissolved manganese, sulfate, alkalinity, ammonium, and phosphate in this interval reflect bacterial decomposition of organic matter. The high rate of organic carbon accumulation at this site has resulted in sulfate depletion at about 10 mbsf. Carbonate diagenesis in this highly alkaline environment has led to the formation of authigenic dolomites between 143 and 335 mbsf (see "Lithostratigraphy" section, this chapter), with the consequent removal of calcium and magnesium from these pore fluids. The opal-A/opal-CT transition is accompanied by a marked decrease in dissolved silica below 425 mbsf. The distributions of calcium, magnesium, and strontium in the deepest sections of this site indicate an influence of basaltic basement alteration reactions.

Sample Handling and Analytical Techniques

A total of 38 interstitial water (IW) samples were collected at Site 798, with high-density sampling in the upper 100 mbsf. Standard ODP squeezing techniques were used for removing water samples (see "Explanatory Notes" chapter, this vol-

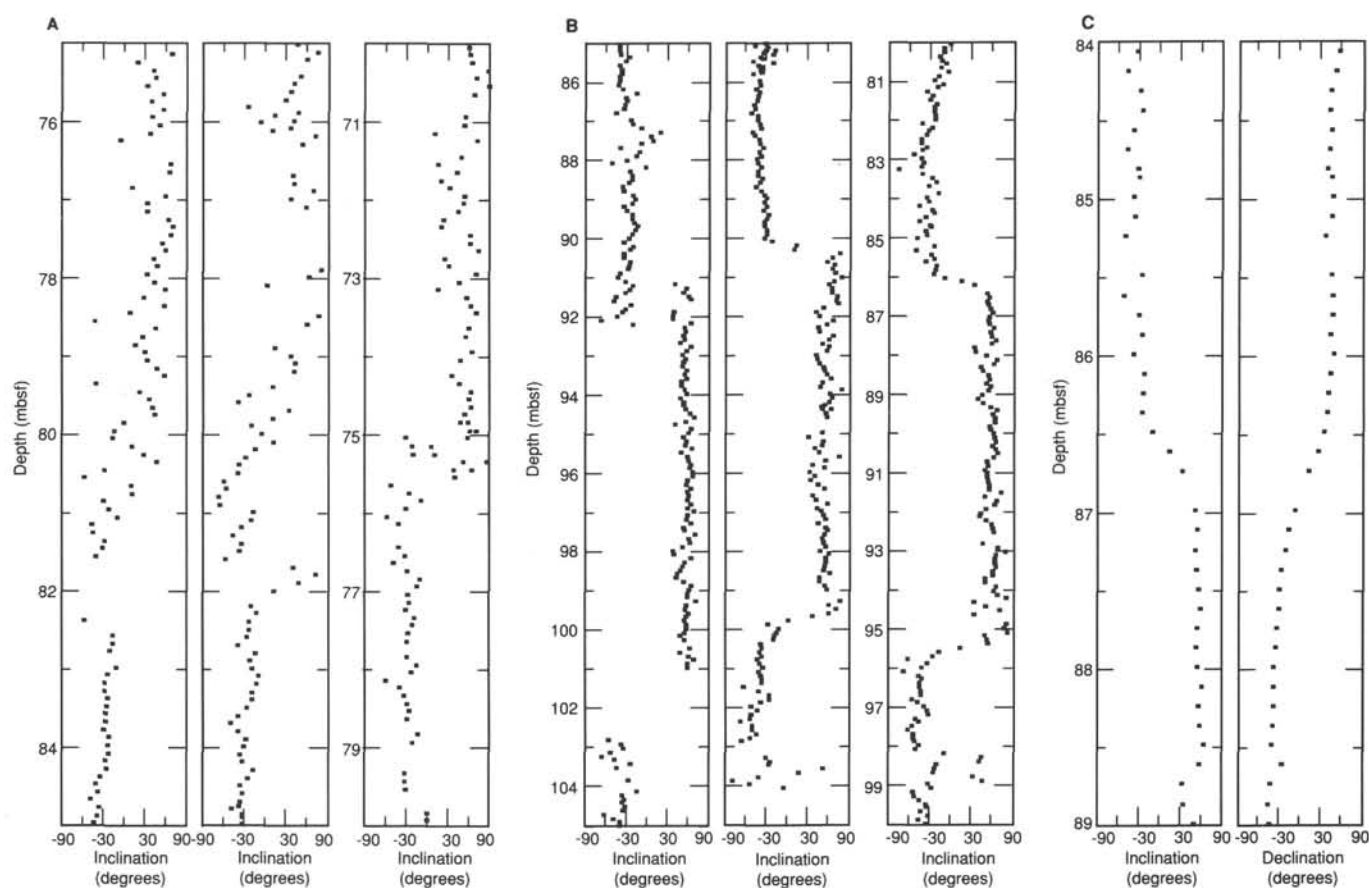


Figure 52. Comparison of the variations of inclination as a function of depth for Holes 798A, 798B, and 798C. A. Around the Brunhes-Matuyama boundary. B. Around the Jaramillo normal event. C. Example of the variation of the inclination and declination during the Matuyama-Jaramillo transition recorded in Core 128-798A-10H.

ume). Shipboard pore-water analyses were performed using the procedures described by Gieskes and Peretsman (1986); the analysis of cations by atomic absorption spectroscopy is discussed in the "Explanatory Notes" (this volume). Results are presented in Table 12.

Salinity and Chloride

The distributions of salinity and chloride are shown in Figure 62. The variation in salinity largely reflects a net change in the sum of concentrations of major dissolved ions; the increase in salinity in the upper 100 mbsf reflects the progressive addition of metabolites from the decomposition of organic matter. The observed decrease in salinity in the deeper sections of this site may be attributed to the loss of chloride, magnesium and potassium from solution. A decrease in the chloride content of pore fluids with depth has been observed at several other ODP sites. The dissociation of gas clathrates and the subsequent release of water may dilute the pore fluids. Even though high levels of methane were recorded at this site (see "Organic Geochemistry" section, this chapter), the zone of stability for the formation of clathrate occurs above the depth where low values of chloride were observed, and therefore this is not a plausible cause for the observed low chlorinity values in the deeper sections of this site. An ultrafiltration mechanism during the flow of pore fluids across clay membranes has resulted in a separation of ions from the interstitial water, which might have led to the observed low levels of chloride at this site. Such a mechanism has been suggested by Hanshaw and

Coplen (1973) and Marine and Fritz (1981) to explain the low chloride patterns observed in the interstitial fluids of the Barbados ridge complex (Masche, Moore, et al., 1988) and was thought to be partially responsible for the anomalously low chloride contents observed in the Peru margin (Suess, von Huene, et al., 1988). Dilution of pore waters by upward diffusion and/or advection of fresh water was proposed to explain the low chloride contents of pore fluids in the Oman margin (Prell, Niituma, et al., 1989). Possible sources of low-chlorinity pore fluids include (1) migration of fresh water along porous volcanoclastic units from the Oki Islands and (2) diffusion from formation waters trapped following episodes of subaerial exposure. A release of chemically bound water at depth from clays (von Huene and Lee, 1982) might also be responsible for the observed anomaly in the chlorinity profile.

Manganese and Sulfate

The high sampling resolution in the upper sections of Hole 798B permits detailed examination of the mechanisms of degradation of organic matter during early diagenesis. The distributions of manganese and sulfate are shown in Figures 63A and 63B. The decrease in manganese concentrations in the upper 5 m, accompanied by sulfate utilization, nicely illustrates the sequential pathways of bacterially mediated oxidation of organic carbon in marine sediments. Figure 63B also includes results of the distributions of methane in the upper 50 mbsf, which shows that the decomposition of organic carbon below the sulfate reduction zone proceeds by carbon-

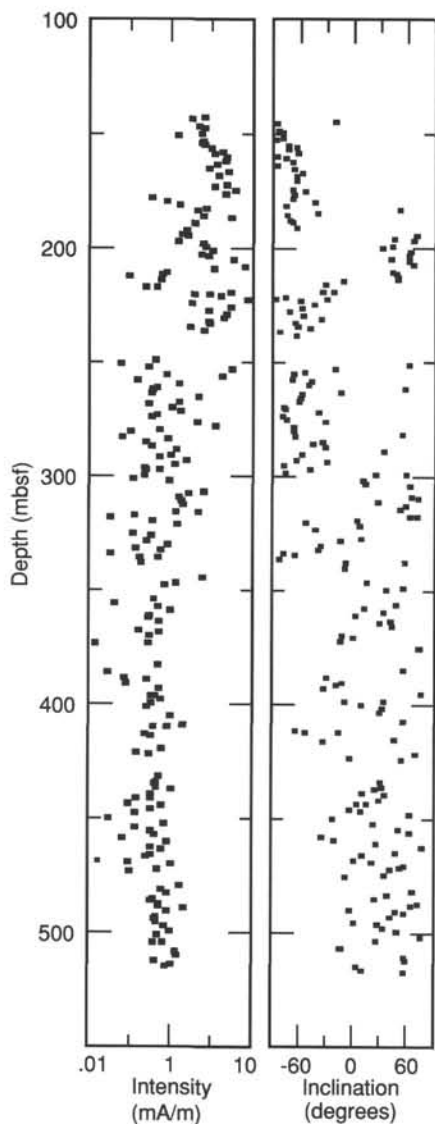


Figure 53. Plot of inclination and intensity vs. depth for the XCB section of Hole 798B.

ate reduction and methanogenesis (see "Organic Geochemistry" section, this chapter).

Alkalinity, Phosphate, and Ammonium

Alkalinity at this site increases to a maximum value of 76 mM at 109 mbsf (Fig. 64). This increase in alkalinity is the result of the production of bicarbonate during bacterial degradation of organic matter primarily by sulfate reduction. Below 109 mbsf, the decrease in alkalinity results from a combination of processes that include carbonate reduction and precipitation of authigenic carbonates.

Dissolved ammonium and phosphate also are metabolic products of the decomposition of organic carbon, and therefore it is not surprising to observe an increase in their concentrations in the upper sections of the hole (Fig. 64). Because phosphate is preferentially released during the degradation of organic matter, the phosphate maximum occurs at a shallower depth than the ammonium maximum (Balzer, 1984). The decrease in the concentration of ammonium below 300 mbsf is probably the result of ion exchange reactions on the surfaces of clay minerals (Rosenfeld, 1979) and the subsequent incorporation into clay-mineral interlayers (Wlotzka,

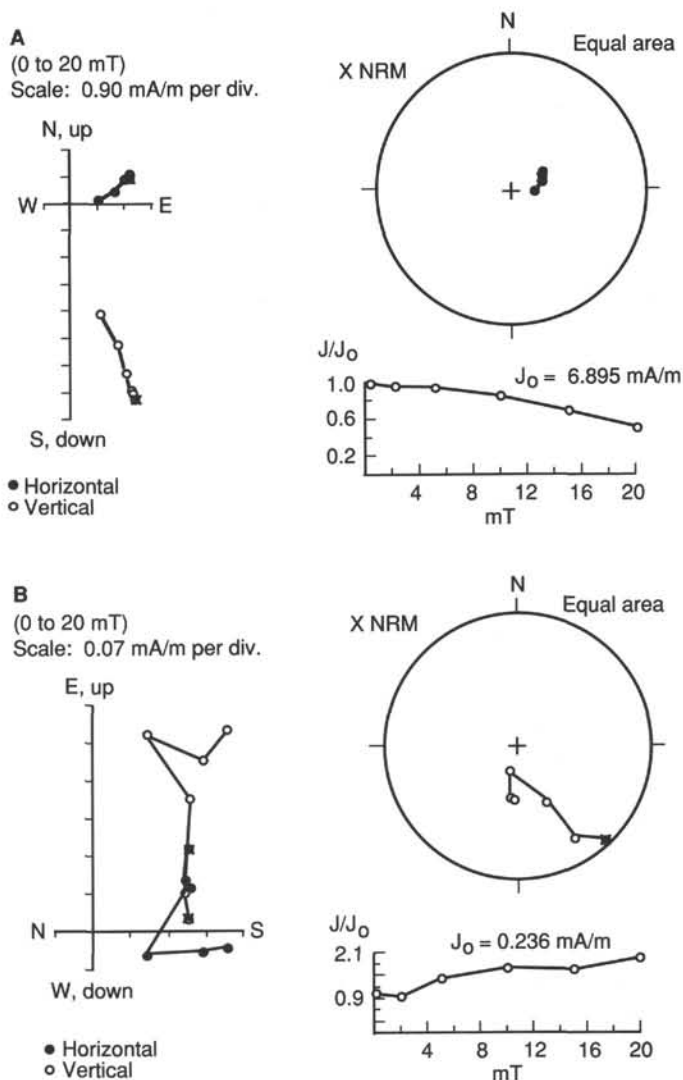


Figure 54. Zijderveld plot (left), equal area projection (right top), and intensity plot (right bottom) of the demagnetization curves. A. Sample 128-798B-22X-4, 22 cm. B. Sample 128-798B-35X-5, 46 cm.

1972). The decrease in phosphate below 70 mbsf suggests a diagenetic uptake of dissolved phosphate into sedimentary mineral phases.

Calcium, Magnesium, and Strontium

Profiles of calcium, magnesium, and strontium for Site 798 are shown in Figure 65; these result from diagenetic reactions in the sediment column, as well as an overprint of basalt alteration reactions that occur at greater depths.

The upper 50 m of this section is characterized by a decrease in calcium concurrent with high levels of alkalinity. Figure 66A indicates an alkalinity deficit from the 2:1 stoichiometric relationship between this component and sulfate, indicating removal of bicarbonate ions from solution. The linear relationship between the increase in alkalinity and the removal of calcium (Fig. 66B) indicates that calcium is being consumed by carbonate precipitation. In the upper 50 mbsf, the distribution of magnesium shows an increase with depth (Fig. 65). The maximum in the magnesium distribution found at this site has been observed almost ubiquitously in anoxic environments, and it is thought to result from the desorption of magnesium from solid phases in rapidly accumulating

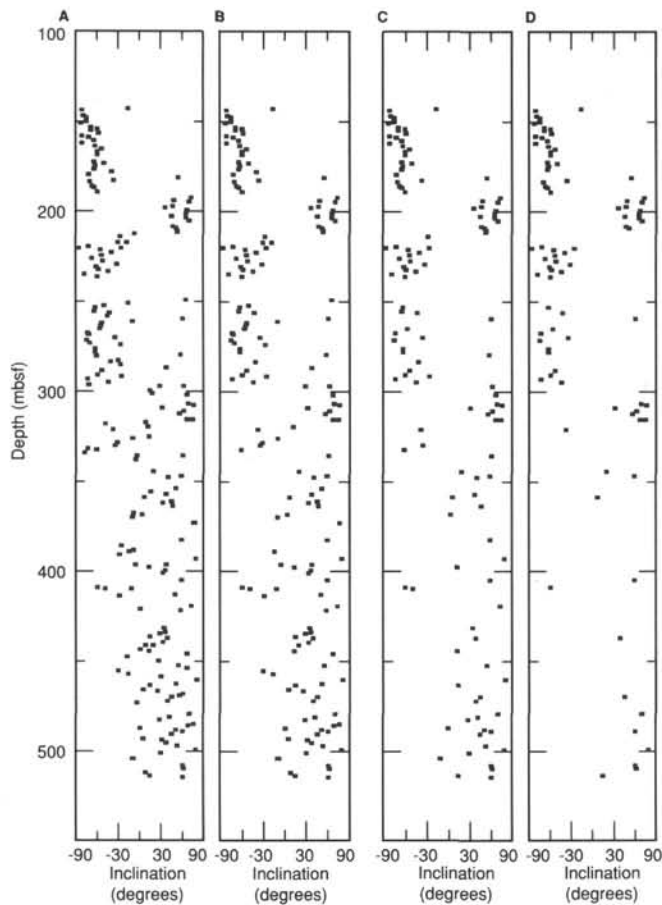


Figure 55. Depth plot of inclination for the XCB cores from Hole 798B. A. All samples. B. Samples having intensity greater than 0.5 mA/m. C. Intensity greater than 0.7 mA/m. D. Intensity greater than 1.0 mA/m.

sediments. The mechanisms responsible for this magnesium desorption are primarily ammonium exchange and ligand competition reactions resulting from the high levels of ammonium and carbonate ions in the pore fluids (von Breyman et al., in press).

Below 50 mbsf, magnesium decreases with depth because of the combined effects of carbonate diagenesis and basalt alteration reactions. Authigenic dolomite was observed at this site between 143 and 335 mbsf, both in the form of euhedral rhombic crystals and in cemented concretions (see "Lithostratigraphy" section, this chapter). Dolomitization reactions thus are partly responsible for the distributions of calcium and magnesium in this interval. The carbonate content of the sediments at this site decreases to less than 5% below 225 mbsf (see "Organic Geochemistry" section, this chapter). The distributions of calcium and magnesium below this depth probably result from basalt alteration processes (McDuff and Gieskes, 1981). Basement at this site is estimated as between 100 to 200 m below our deepest sample (see "Seismic Stratigraphy" section, this chapter). Tamaki (1988) considered that the Oki Ridge was underlain by granitic continental crust. However, the Oki Islands are well known for their alkalic basalts, and Tamaki et al. (1981) mapped much of the Oki Ridge as Tertiary volcanics. The distributions of calcium, magnesium, and strontium observed at Site 798 suggest that even though the crust itself might be continental in origin, a layer of altered volcanic material must be present at depth.

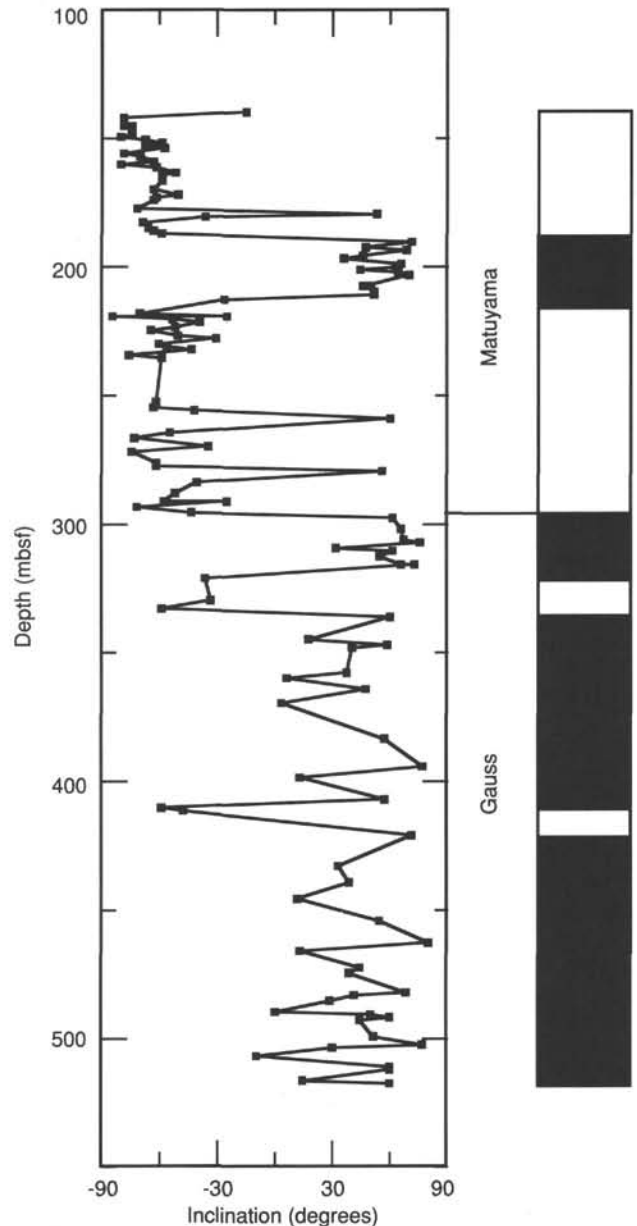


Figure 56. Polarity sequence obtained from the XCB section of Hole 798B, utilizing samples having intensity greater than 0.7 mA/m.

Silica, Lithium, and Potassium

The distribution of silica (Fig. 67) is governed primarily by dissolution of biogenic siliceous components above 425 mbsf and by silicification reactions at depth. The marked decrease in concentrations of dissolved silica below 425 mbsf coincides with a significant increase in wet-bulk density and a reduction in porosity of the sediments (see "Physical Properties" section, this chapter). The first recorded appearance of opal-CT phases in the sediments occurs at 455 mbsf (see "Lithostratigraphy" section, this chapter), which establishes this phase as a dissolved silica sink in the deepest sections of this hole.

Opal-A constitutes a good carrier phase for lithium (Gieskes, 1981). At this site, the concentration of lithium exhibits a steady increase with depth (Fig. 67), which parallels the silica profile. This relationship (Fig. 68) supports the mechanism whereby the dissolution of biogenic siliceous

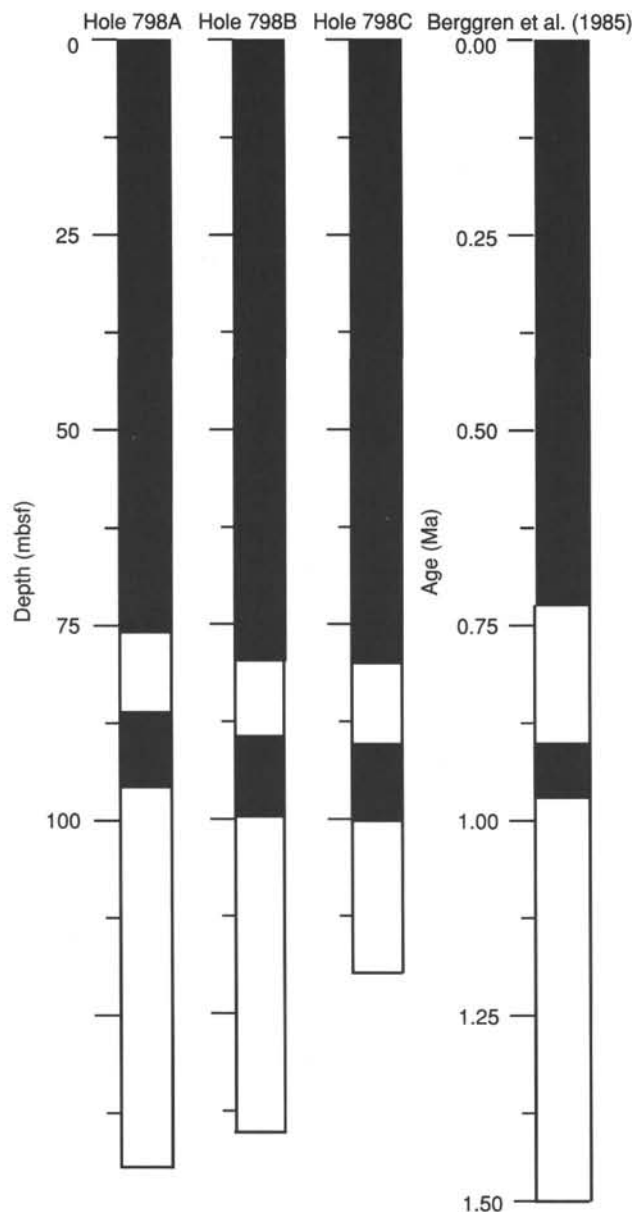


Figure 57. Polarity sequence obtained from APC cored sediments from Holes 798A, 798B, and 798C. Polarity time scale by Berggren et al. (1985) also is shown for comparison.

phases with depth results in the release of lithium into the pore fluids. Such a relationship was also noted during Leg 127 (Tamaki, Pisciotto, et al., in press). The decrease of dissolved lithium below 400 mbsf may be the result of incorporation of this element into clay-mineral lattices (Steiness et al., 1972).

The concentration of dissolved potassium remains constant at values near seawater to approximately 350 mbsf (Fig. 68). Removal of potassium in the deepest sections of the hole may be related to the incorporation of this cation into clay minerals, or it might reflect basalt alteration reactions.

ORGANIC GEOCHEMISTRY

The shipboard analyses of organic geochemicals in sediments from Site 798 included inorganic carbon; total carbon, nitrogen, and sulfur; and Rock-Eval pyrolysis; these were performed mainly on samples taken for measuring physical properties. In addition, gas (vacutainer) and sediment samples were collected for determining volatile hydrocarbons. For the latter, inorganic

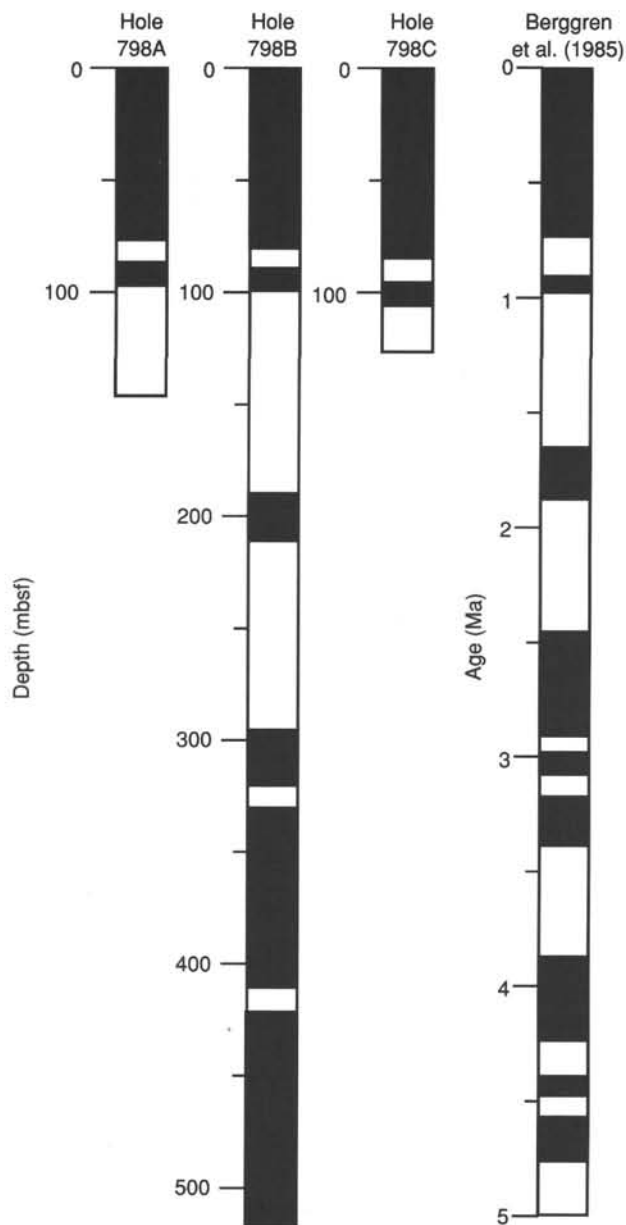


Figure 58. Polarity sequence obtained for the entire core sections from Holes 798A, 798B, and 798C, compared to the polarity time scale of Berggren et al. (1985).

and total carbon, nitrogen, and sulfur also were determined. The methods used for these determinations are outlined in the "Explanatory Notes" (this volume), while background and detailed descriptions are given in Emeis and Kvenvolden (1986).

Volatile Hydrocarbons

For safety considerations, hydrocarbon gases were routinely measured in sediment samples using the headspace technique. If gas pockets occurred in the uncut core liner, more gas samples were taken by vacutainers. The results of both vacutainer and headspace analyses are summarized in Tables 13 and 14.

In most of the cores, very high amounts of hydrocarbon gases were present. This resulted in distinct sediment disturbances and in the formation of many voids from gas expansion. In the vacutainer samples, methane concentrations vary between 160,000 and 720,000 ppm, while concentrations of ethane and

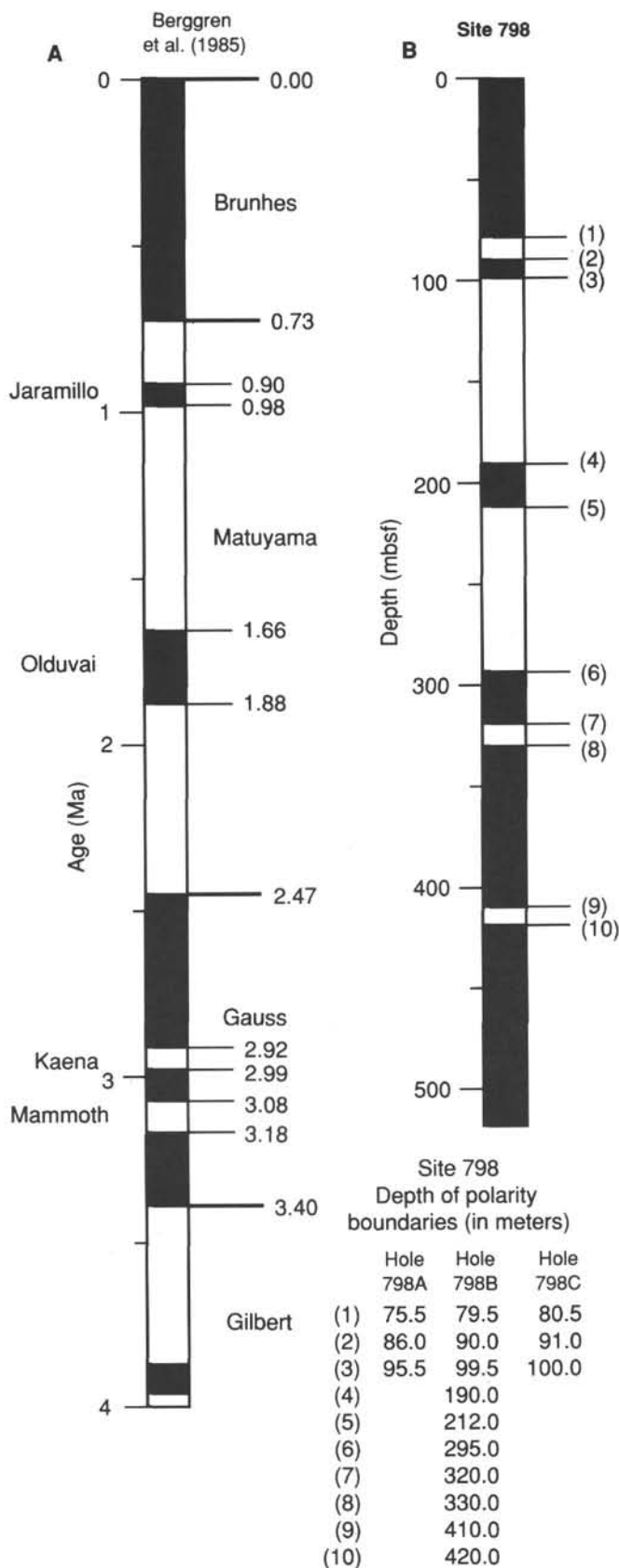


Figure 59. A. Polarity time scale by Berggren et al. (1985). B. Depth of the identified boundaries for Site 798.

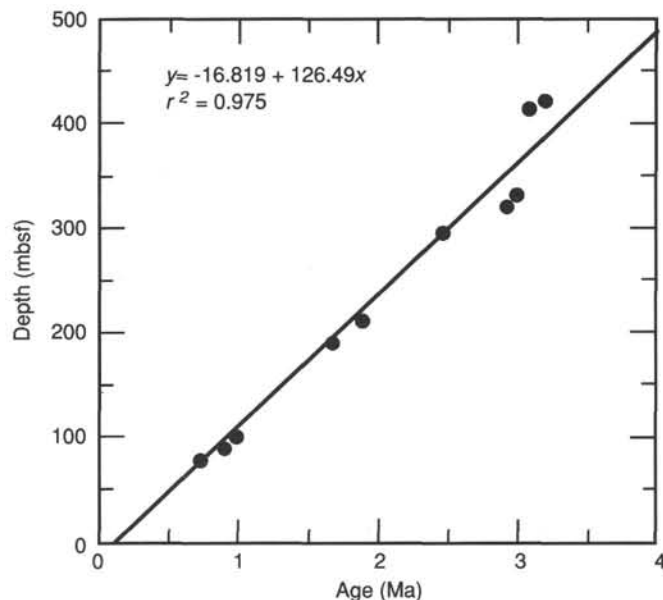


Figure 60. Age vs. depth relationship for cores from Hole 798B.

Table 11. Sedimentation and bulk accumulation rates for Site 798.

Datum levels	Age (Ma)	Depth (mbsf)	Sedimentation rate (m/m.y.)	MDBD ^a (g/cm ³)	Accumulation rate (g/cm ² /k.y.)
LAD <i>R. curvirostris</i>	0.34	39.00	120.00	0.71	8.52
LAD <i>P. lacunosa</i>	0.46	54.54	125.00	0.78	9.75
B/M boundary	0.73	75.34	91.00	0.81	7.37
Top Jaramillo	0.91	90.55	84.50	0.75	6.33
Bottom Jaramillo	0.98	94.65	45.00	0.82	3.69
LAD <i>H. sellii</i>	1.20	119.91	122.00	0.75	9.15
Top Olduvai	1.66	200.08	160.00	0.73	11.68
Bottom Olduvai	1.88	220.87	91.00	0.68	6.34
LAD <i>A. rectangularare</i>	2.04	229.20	93.00	0.65	6.11
Top Gauss	2.47	297.90	217.00	0.70	15.20
LAD <i>N. kamschatica</i>	2.60	325.15	138.00	0.68	9.39

^aMDBD = mean dry-bulk density.

propane range from 50 to 2,500 ppm and 10 to 270 ppm, respectively (Table 13). Methane was also the dominant hydrocarbon component in headspace gas samples, with concentrations ranging from 56 to 75,000 ppm, while concentrations of ethane and propane range from 2 to 440 ppm and 1 to 390 ppm, respectively (Table 14; Fig. 69). Near 450 mbsf, concentrations of both ethane and propane distinctly increased, resulting in a sharp decrease in the C₁/C₂ and C₁/C₃ ratios (Fig. 69). At the same depth, significant amounts of iso-butane and n-butane also occur, increasing to unusually high values of 117 and 44 ppm, respectively, at about 518 mbsf (Fig. 69; Table 14). Because the organic matter of sediments from the lowermost Cores 128-798B-52X to 128-798B-54X is still immature and has not reached the stage of *in-situ* gas generation (see "Rock-Eval Pyrolysis" section, this chapter), it is very likely that these hydrocarbons have migrated from other source rocks.

Because of the low C₁/C₂ ratios (Fig. 70) and the high concentrations of C₃ and C₅ hydrocarbons, drilling was terminated at about 517.9 mbsf for safety reasons.

Carbon, Nitrogen, and Sulfur

Results of determinations of inorganic carbon, total carbon, total nitrogen, and total sulfur are summarized in Tables 15 through 17. The carbonate and organic carbon records of

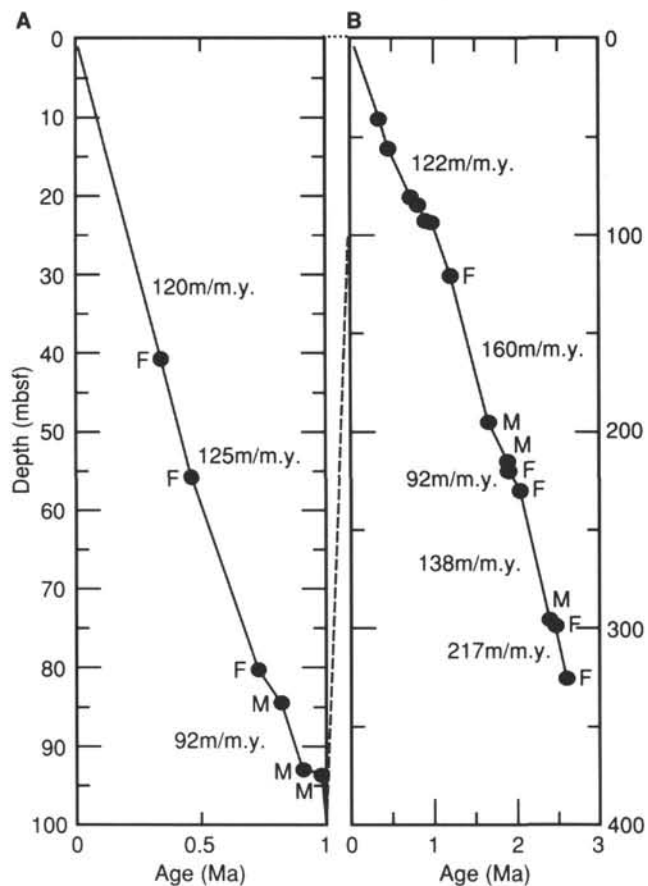


Figure 61. Sedimentation rates for Site 798. A. Sedimentation rates for selected intervals of the entire section. B. Sedimentation rates for the late Quaternary interval at Site 798.

Holes 798A and 798B are presented separately in Figures 71 and 72. Combined carbonate and organic carbon records of Holes 798A and 798B are presented in Figure 73. The depth values used in Figure 73 have not been corrected to a stratigraphic datum. This must be considered when looking at short-term carbonate and organic carbon fluctuations in the upper 150 m.

According to the carbonate content, the sediment sequence of Site 798 can be divided into two intervals. Interval I (0–220 mbsf), which corresponds to lithologic Unit I (see “Lithostratigraphy” section, this chapter), is characterized by carbonate values ranging between 1% and 35% (Fig. 73). In this interval, short-term, high-amplitude (glacial/interglacial-type?) variations are concentrated in the upper 140 m (i.e., the last 1.2 Ma), whereas the lower part (140–220 mbsf) displays carbonate contents of between 1% and 15% (Fig. 73). Maximum carbonate values were recorded in the interval between 38 and 78 mbsf (i.e., between 0.35 and 0.75 Ma) (Figs. 71 and 73).

Interval II (220–518 mbsf), which corresponds to lithologic Units II and III, is characterized by low carbonate values of less than 5% (Fig. 73).

The downhole distribution of total organic carbon in the sediments at Site 798 is characterized by predominantly high values that range between 1% and almost 6% (Figs. 71 and 73; Tables 15 through 17). The higher values of 3% to 5% are concentrated in the intervals from 0 to 140 mbsf (Holocene to 1.2 Ma) and 495 to 519 mbsf (early late Pliocene). The distinct light/dark sediment cycles recorded in the upper 100 m of the sequence (cf. “Lithostratigraphy” section, this chapter), are also reflected in the organic carbon content. The dark basal portion of a cycle is characterized by organic carbon contents

of up to 5%, whereas in the upper light portion of a cycle, organic carbon contents of 2% are more typical.

The total nitrogen and sulfur values vary between 0.10% and 0.67% and between 0.15% and 2.11%, respectively. The ratios of organic carbon to total nitrogen (C/N) and total carbon to total sulfur (C/S) range from 2 to 16 and from 0.6 to 11.2, respectively.

Rock-Eval Pyrolysis

Rock-Eval pyrolysis (Espitalié et al., 1977) was used to characterize the type and maturity of the organic matter. Results are summarized in Tables 18 and 19. Unfortunately, the Rock-Eval instrument broke down after the first 50 runs. Thus, Rock-Eval data are available only for samples from Hole 798A and from the lowermost part of Hole 798B.

The Rock-Eval instrument on board the *JOIDES Resolution* also allows one to determine total organic carbon (TOC). TOC values measured by means of the Rock-Eval and TOC values determined by difference between total (from C/N/S measurements) and inorganic carbon (from coulometer data) are compared in Figure 74. In general, Rock-Eval TOC values are too low. Because these TOC values were used to calculate the hydrogen and oxygen indexes in Table 18, the resulting indexes are too high. This explains the extremely high values of the hydrogen index (more than 1100) in sediment samples from the lowermost part of Hole 798B (Table 18). The Rock-Eval data were recalculated using TOC values obtained by difference from total and inorganic carbon data (Table 19). Hydrogen indexes in the recalculated data decrease to more reasonable values (380 to 580). The discussion that follows uses the recalculated values for hydrogen and oxygen indexes from Table 19.

The values for hydrogen and oxygen indexes are shown in Figure 75 in the form of a modified “van Krevelen” diagram (Tissot and Welte, 1984). The data suggest that most of the organic matter in sediments from Site 798 is a mixture of kerogen types II and III, i.e., a mixture of marine and terrigenous material. The data points of sediment samples from the lowermost organic-carbon-rich 50 m of Hole 798B fall into field I (Fig. 75), which suggests the predominance of marine (algal) organic matter. The occurrence of major quantities of marine organic carbon throughout the entire sediment sequence is also supported by C/N ratios of about 10 (Figs. 71 through 73). The unusually high oxygen indexes in samples from Hole 798A (Fig. 75) may result from significant amounts of labile organic matter (e.g., sugars, proteins) still present in very young and immature sediments, rather than from large amounts of terrigenous/oxidized organic matter.

In the upper 140 m, as well as in the lowermost part of the sediment sequence, the temperatures of maximum pyrolysis yield (T_{max}) are less than 420°C, indicating the immaturity of organic matter at Site 798.

Discussion

The sediments of Site 798 are characterized by organic carbon values of 1% to almost 6%, i.e., by values distinctly higher than those recorded in the “normal” open-ocean environment. Consequently, the deposition of these organic-carbon-rich sediments requires special environmental conditions, such as (1) increased preservation of organic matter in oxygen-deficient environments, (2) increased productivity of organic matter, (3) increased supply of terrigenous organic matter, or (4) rapid burial of organic matter (e.g., in turbidites; cf., Arthur et al., 1984; Meyers, 1984; Stein and Littke, 1989).

According to the Rock-Eval data and the C/N ratios (see above), the dominant portion of the organic matter is of marine origin. Thus, changes in the supply of terrigenous organic matter may have been of secondary importance for the organic carbon budget at Site 798. Because high organic-carbon values were recorded throughout the entire section,

Table 12. Results of interstitial water analysis, Site 798.

Core, section, interval (cm)	Depth (mbsf)	Vol (mL)	pH	Alk (mM)	Sal (g/kg)	Cl ⁻ (mM)	SO ₄ ⁻² (mM)	PO ₄ ⁻³ (μM)	NH ₄ ⁺ (μM)	SiO ₂ (μM)	Mg ⁺² (mM)	Ca ⁺² (mM)	K ⁺ (mM)	Mn ⁺² (μM)	Sr ⁺² (μM)	Mg/Ca ratio
128-798B-1H-1, 125-131	1.25	45	7.65	7.29	34.5	546	25.1	40.3	380	620	51.8	10.18	14	28	66	5.1
798A-1H-1, 145-150	1.45	56	7.57	21.34	34.6	544		95.8	580	663	50.4	8.22	12	11	56	6.1
798B-1H-2, 35-41	1.85	46	7.51	9.38	34.6	543	24.4	54.8	492	648	50.9	9.83	13	23	58	5.2
798B-1H-2, 127-133	2.77	48	7.53	13.56	34.5	546	21.5	64.3	667	49.5	9.20	13	11		53	5.4
798B-1H-3, 100-106	4.00	43	7.68	18.04	34.5	546	17.7	85.8	933	676	49.8	7.56	13	7	54	6.6
798C-1H-3, 145-150	4.45	65	7.69	20.88	34.5	546		67.9	590	718	50.0	8.36	12	10	60	6.0
798B-1H-4, 125-131	5.75	50	7.50	25.84	34.6	543	12.0	86.5	2,077	741	49.8	8.48	14	6	60	5.9
798B-2H-1, 45-51	9.85	50	7.62	40.85	33.8	550	0.6	56.1	2,560	769	49.6	5.88	16		58	8.4
798B-2H-1,45-51	12.85	60	7.64	43.26	33.7	547	0.3	68.1	3,340	778	50.1	5.67	16	4	56	8.8
798C-3H-4, 145-150	21.25	40	7.64	53.90	34.0	532		208.9	5,020	919	52.4	5.08	14	4	65	10.3
798A-3H-3, 145-150	22.75	42	7.50	55.81	34.6	531		289.5	5,260	741	53.8	5.32	12	4	60	10.1
798B-3H-4, 85-91	23.75	45	7.45	52.98	34.0	540	0.1	278.6	5,230	808	52.8	5.24	13	4	60	10.1
798B-4H-7, 56-61	36.96	45	7.43	61.66	34.7	535	0.0	280.2	6,630	825	54.9	4.61	15	4	56	11.9
798B-5H-4, 140-150	43.70	43	7.43	63.67	35.0	535	0.0	233.7	7,510	791	55.4	4.12	17	2	64	13.4
798A-6H-1, 145-150	47.65	46	7.36	68.52	35.2	537		256.9	7,940	818	57.6	4.44	13	2	66	13.0
798B-6H-4, 45-55	50.37	45	7.35	67.54	35.4	538	0.3	267.8	7,340	860	56.4	4.25	14		68	13.3
798B-7H-3, 140-150	59.98	45	7.29	69.19	35.3	543	0.1	286.4	7,840	858	56.4	4.52	16	4	68	12.5
798B-8H-4, 140-150	70.67	43	7.44	69.17	35.5	541			7,570	813	55.3	3.36	15	5	60	16.5
798B-9H-3, 123-133	78.57	45	7.37	72.34	35.6	538	0.4	249.2	7,850	897	54.3	4.26	15		70	12.7
798A-9H-3, 145-150	79.01	40	7.33	74.01	35.6	536		233.7	8,860	898	55.9	4.48	14	6	68	12.5
798B-12H-4, 145-150	108.81	35	7.37	76.34	35.6	542	0.1		7,890	823	53.4	5.48	15	7	81	9.7
798A-12H-4, 145-150	109.02	60	7.51	74.57	35.5	539		232.1	8,800	974	53.0	5.35	12	7	80	9.9
798B-14H-7, 123-133	133.13	45	7.24	71.62	35.5	540	0.0	188.7	7,340	974	49.4	5.05	13		87	9.8
798A-15H-3, 145-150	137.15	72	7.43	67.05	35.0	539		174.8	8,580	1,039	47.2	4.65	14		85	10.2
798B-15H-5, 140-150	139.96	45	7.21	71.62	35.5	538	0.0	153.1	7,660	914	47.6	4.91	16	5	81	9.7
798B-18X-6, 25-35	169.47	80	7.14	60.57	35.0	540	0.3	117.8	9,900	1,009	45.2	5.92	15	4	62	7.6
798B-21X-6, 140-150	198.76	70	7.42	67.20	35.0	544	0.1	117.8	10,850	1,061	42.0	6.77	17	6	96	6.2
798B-24X-2, 140-150	222.90	85	7.34	61.92	34.8	543	0.5	85.4	11,580	1,143	38.8	7.08	16	6	95	5.5
798B-27X-3, 105-115	252.59	65	7.51	52.12	33.5	546	2.1	46.7	12,170	1,050	36.6	7.22	16	81	77	5.1
798B-30X-2, 140-150	279.94	45	7.10	52.93	33.5	544	0.3	73.0	12,130	1,152	32.3	7.92	17	6	104	4.1
798B-33X-3, 140-150	309.65	50	7.08	46.31	33.0	541	0.4	46.7	11,670	1,206	28.0	7.96	16	3	100	3.5
798B-36X-2, 65-75	336.75	35	7.04	38.70	32.5	535	0.3	23.5	10,190	1,223	23.2	9.32	15	4	106	2.5
798B-39X-4, 140-150	369.50	15	7.28	38.80	32.0	533	0.0	42.1	9,780	1,335	18.6	9.98	17	4	106	1.9
798B-42X-5, 140-150	398.85	20	7.10	31.18	31.5	533	0.1	29.7	9,510	1,007	16.7	12.22	14	6	117	1.4
798B-45X-3, 60-70	424.75	21	6.98	22.31	31.5	527	2.0	5.0	8,430	1,262	15.5	11.02	13	8	79	1.4
798B-48X-5, 140-150	457.80	8	7.25	17.47	30.7	517	0.2	8.0	7,080	812	12.3	12.87	13	4	104	1.8
798B-51X-3, 140-150	483.80	12	7.01	18.68	30.9	520	0.1	5.0	5,830	823	13.7	13.02	11	5	110	1.1
798B-54X-6, 140-150	516.90	20	7.18	14.85	30.5	516	0.0	8.0	5,160	761	14.9	13.47	8	5	106	1.1

rapid burial by turbidites (which might have occurred occasionally, cf. "Lithostratigraphy" section, this volume) may also be excluded as a major factor controlling the accumulation of organic carbon at Site 798. Increased organic-carbon preservation in turbidites may explain only single events of organic-carbon enrichment. Consequently, a high surface-water productivity and/or a high preservation rate of organic carbon should have controlled mainly the deposition of organic matter on Oki Ridge during the last 3.5 Ma.

Very high sedimentation rates, high amounts of marine organic matter, and the dominance of biosiliceous (diatomaceous) sediments all may indicate an environment of high surface-water productivity (e.g., Mueller and Suess, 1979; Berger et al., 1989; Stein, in press). However, the dark organic-carbon-rich intervals are often finely laminated and rich in (pyritic) sulfur (Tables 16 and 17), which may support anoxic deep-water conditions (e.g., Leventhal, 1983). Short-term changes in productivity/preservation of organic carbon may have caused the cyclic changes between dark, finely laminated, and organic-carbon-rich sediments and light, bioturbated sediments, recorded in the upper 100 mbsf (see "Lithostratigraphy" section, this chapter). Thus, it is probable that phases of high oceanic productivity alternated with phases of increased preservation rate of organic matter at the Oki Ridge area during the last 3.5 Ma. For the reconstruction of this complex history of the accumulation of organic carbon and its relationship to paleoclimatic and paleoceanographic changes, more detailed organic and inorganic geochemical, sedimentological, and paleontological data will be required, and these have to be produced from future multidisciplinary shore-based studies.

MICROBIOLOGY

Introduction

Whelan et al. (1986) conducted the first search for subsurface bacterial activity during the DSDP-IPOD-ODP programs in samples taken from depths of 4 to 167 mbsf in the Gulf of Mexico. Results from analyzing pore waters and from culturing sediment samples suggested that bacterial activity probably was present at depth, but that further studies were needed. A more extensive program of microbiological sampling was undertaken during Leg 112 in the Peru margin area (Cragg et al., in press). These latter studies produced unequivocal evidence that bacteria were present to the maximum depth sampled (80 mbsf), including a variety of viable forms, some of which were observed as undergoing cell division. Based on these encouraging results, a program of microbiological sampling was planned for Site 798 in the Sea of Japan to take advantage of what we anticipated to be organic-rich, pelagic sediments deposited in a suboxic marginal basin setting.

Bacteria are intimately involved with diagenetic processes in marine sediments, although their role has yet to be detailed completely, especially in sediments far below the sediment/water interface. Bacteria are known to catalyze many chemical reactions in marine sediments, degrading and modifying deposited organic matter and contributing their own biomass to the pool of organic matter preserved in the geological record. Bacterial activity is most intense in surface sediments and declines with increasing depth below the surface layer. However, bacterial activity in deep subsurface horizons may

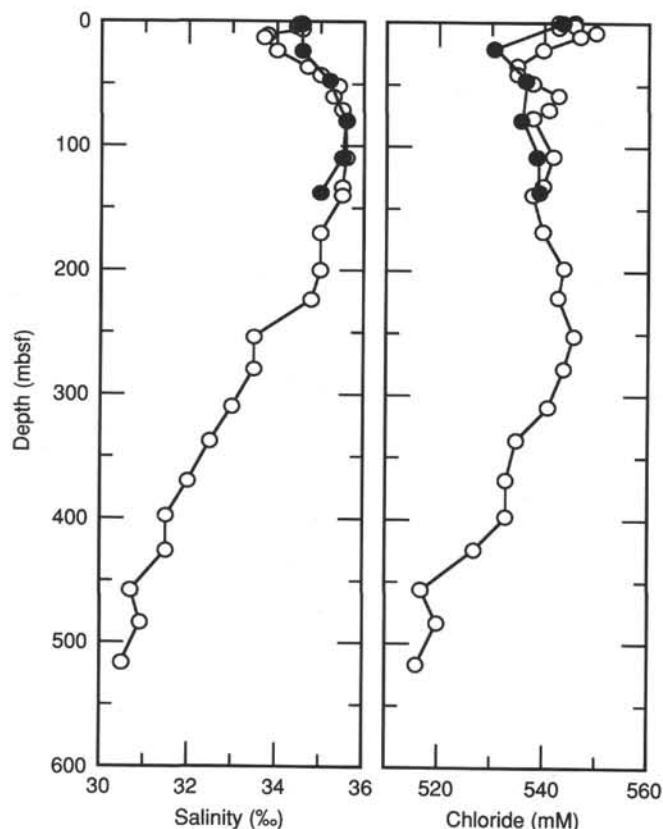


Figure 62. Downcore profile of salinity and dissolved chloride concentration. Data for Holes 798A and 798B are shown by closed and open circles, respectively.

still have a major effect on diagenesis because of the long time scales involved in the geological evolution of marine sediments. The aim of bacterial sampling and analysis at Site 798 was to quantify the role of bacteria in diagenesis by measuring their activity and biomass distribution within deep sediment layers.

Shipboard Sampling Procedures

Sediment samples were collected from cores in Hole 798B, whose upper part was dedicated to this task. Whole-round samples of 25 and 3 cm thick were collected in close order from upper cores and at increasing intervals downhole to a depth of about 510 mbsf (see Section 3, this volume). In addition, IW samples also were obtained within this sequence and were analyzed for dissolved nutrients and alkalinity (see "Inorganic Geochemistry" section, this chapter).

Effective handling of sediment samples for bacterial analysis is crucial to prevent contamination of the samples from alien bacteria in the atmosphere or in other sediment samples, etc. In addition, the sediment obtained from a few millimeters to centimeters below the sediment/water interface is anoxic, while exposure of samples to air must be prevented. To meet these requirements, whole-round samples were cut from intact cores using a special core-cutting rig that was routinely sterilized by flaming and that continually flushed the core with sterile oxygen-free nitrogen (OFN).

Specific procedures applied during sample collection were as follows:

1. The gas lines and filters were autoclaved and aseptically connected to the special core cutter.

2. The core cutter was wiped with alcohol and flamed using a portable Bunsen burner just prior to each use.

3. Each 9.5-m core was cut into 1.5-m sections, just as is done during normal ODP core processing, and then microbiological samples were cut from these sections well away from the ends of the core. The core section was wiped clean and then wiped with alcohol where cuts were to be made. Each core section was then placed in the special cutting rig, the top and ends of the rig were closed, and the core was flushed with OFN. The OFN gas enters the cutting rig from near the cutting slits and exits from these slits, preventing contamination during cutting.

4. Each core was cut using a hacksaw having a sterile blade that was flamed just prior to each use, and the cut ends were sealed with sterile slices. The cut, whole-round core sample was removed from the cutting rig with these sterile slices still covering the cut ends and was placed on one end. A sterile end-cap was then fitted onto the ends of the core after flaming exposed sediment surfaces at each end of the core, while simultaneously being gassed with OFN from a sterile gassing jet. The gassing jet was left under each cap for a short while to flush out any oxygen and then was removed while the cap was pushed firmly down; the other end of the core was similarly sealed.

5. The core caps were sealed with tape and then the entire core placed in an aluminum and plastic lined bag, to which an anaerobic gas generator and oxygen scrubber had been added. The bag was then heat-sealed, and the cores stored at 4°C.

6. Whole-round cores (3 cm) for bacterial lipid analysis were cut near or adjacent to the 25-cm whole-round core samples. These 3-cm samples were placed into clean glass jars, leaving a small amount of sample directly next to the core liner, which might have been contaminated from previous layers. These samples were then frozen.

7. Samples to be used for direct microscopic counts of bacteria were obtained from the samples saved for bacterial lipid analysis, as described in Step 6. Using a sterile plastic syringe, with the luer-tip removed, 1 mL of sediment was removed from the cut, whole-round core sample and placed in 9 mL of sterile, filtered, 4% formaldehyde in artificial seawater.

8. In addition, 5-mL samples for gas headspace analysis were removed from each 3-cm whole-round sample and analyzed for hydrocarbons (see "Organic Geochemistry" section, this chapter).

9. In the dedicated upper portion of Hole 798B, whole-round cores adjacent to those taken for bacterial analysis were removed for IW analysis.

Results of Shipboard Sampling and Plan for Laboratory Analysis

The sampling system described above worked well, with no real problems. A possible future improvement would be to conduct sampling inside a laminar-flow cabinet. It also would have been desirable to have several fully autoclavable core-cutting rigs. Unfortunately, we had no control over possible contamination during coring itself. However, samples will be removed from the center of each whole-round core in the laboratory, leaving the sediment next to the core liner, which is the most likely sediment to be contaminated during coring.

Bacterial samples collected from Hole 789B cores were offloaded from the *JOIDES Resolution* onto a specially chartered ship 3 days after their collection and were sent by air to the onshore laboratory. Laboratory analyses to be performed on these samples include (1) direct bacterial counts (epifluorescence microscopy); (2) bacterial composition (MPV viable counts); (3) bacterial activity, including heterotrophic poten-

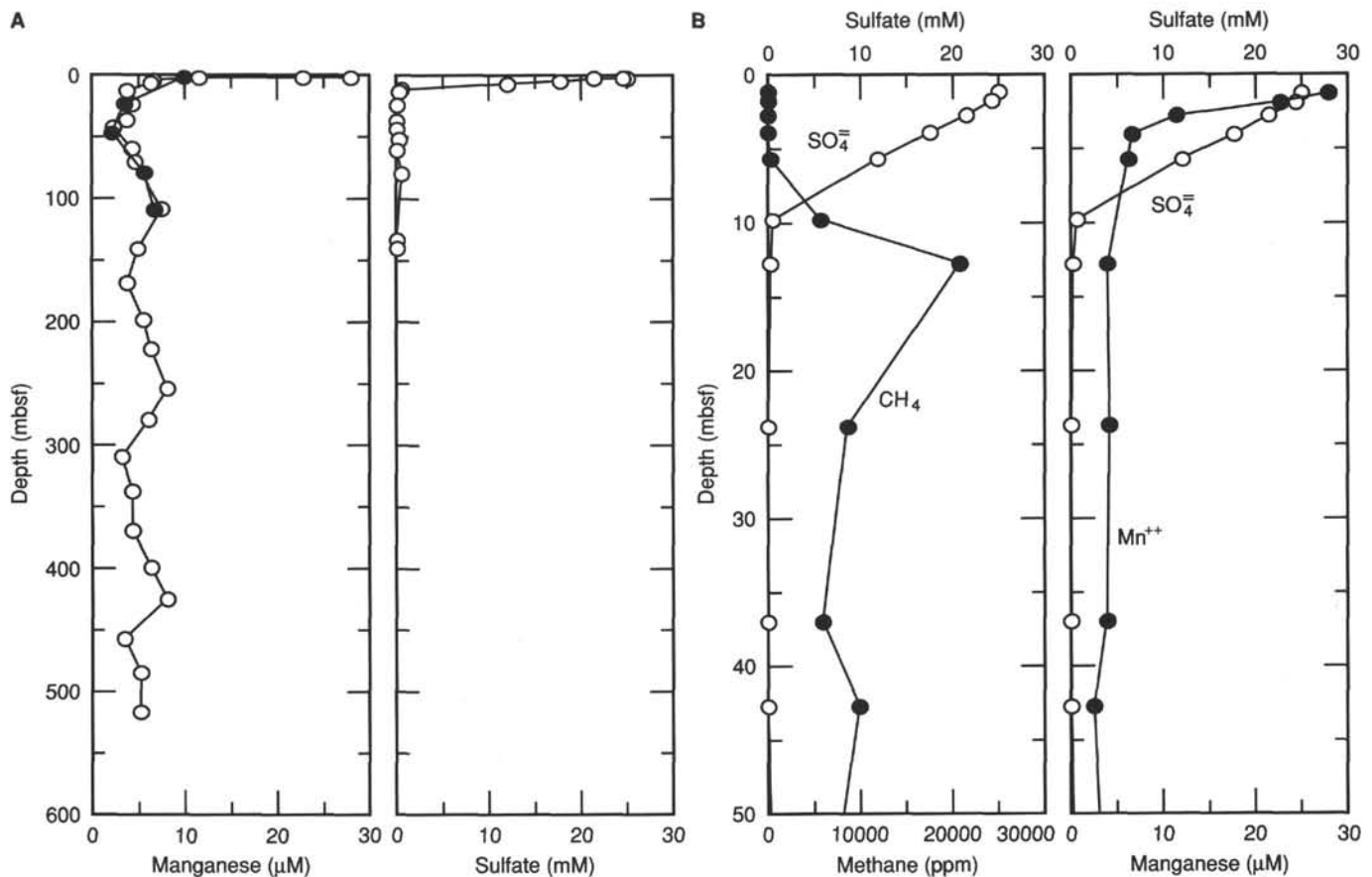


Figure 63. A. Downcore profiles of dissolved sulfate and manganese; data for Holes 798A and 798B are shown by closed and open circles, respectively. B. High-resolution distributions in the upper 50 mbsf of Hole 798B, also showing the onset of methanogenesis by the increase in methane concentration after sulfate depletion.

tial/nitrate reduction, bacterial production, sulfate reduction, methanogenesis, and acetogenesis (radiotracer technique); (4) bacterial lipids; and (5) interstitial water.

PHYSICAL PROPERTIES

Introduction

Coring during Leg 128 on the Oki Ridge sampled a 514-m-thick sedimentary sequence that ranged from Holocene to Pliocene in age. Cores were retrieved by the APC to a depth of 143 mbsf; the XCB was used below that depth. All cores of Hole 798A, Cores 128-798B-14H to 128-798B-54X, and Cores 128-798C-1H to 128-798C-3H were used for analyzing physical properties on board the ship.

Physical properties measured routinely on cores recovered at Site 798 include GRAPE density, compressional-wave velocity, and thermal conductivity from whole-round core sections. For split cores, index properties, such as wet-bulk density, dry-bulk density, water content (expressed as weight of water relative to total dry weight), grain density, porosity, and vane-shear strength, were determined. The methods used are described in detail in the "Explanatory Notes" (this volume). Results of physical properties determinations at Site 798 are summarized in Tables 20 through 25.

Index Properties

The distribution of index properties such as wet-bulk density, water content, porosity, and grain density are plotted relative to sub-bottom depth in Figures 76 through 79.

In this section, we refer to downhole variations of physical property units. Physical property units are defined as depth intervals where similar trends of physical properties were recorded.

Wet-bulk density (Fig. 76) generally ranges from 1.33 g/cm^3 to values higher than 1.90 g/cm^3 . A minimum value was determined at a depth of 9.75 mbsf, and a maximum value was measured at a depth of about 460 mbsf. With increasing depth below the seafloor, the wet-bulk density profile can be divided into four different units. Unit 1 corresponds to the upper 20 m of sediment, where wet-bulk density varies between 1.33 and 1.53 g/cm^3 . The upper boundary of Unit 2 is marked by an increase of wet-bulk density to values in ranging roughly between 1.50 and 1.62 g/cm^3 . Below this boundary, wet-bulk density exhibits cyclic variation and a generally decreasing trend. The low densities recorded at a depth of 140 mbsf may be result from drilling disturbance, caused by the change from APC to XCB coring. The lower boundary of Unit 2 is marked by an abrupt increase of wet-bulk density at a depth of about 320 mbsf. The wet-bulk densities of Unit 3 show a rapid increase from values of about 1.60 g/cm^3 near the upper boundary to values ranging between 1.80 and 1.90 g/cm^3 at a depth of 460 mbsf. Unit 4 is characterized by decreasing values of wet-bulk density from a depth of 460 mbsf to the base of the hole.

Water content, which is related to dry weight (Fig. 77), shows variations between 190% and about 40%. Like the profile for wet-bulk density, the profile for water content can be divided into four different units that correspond to the

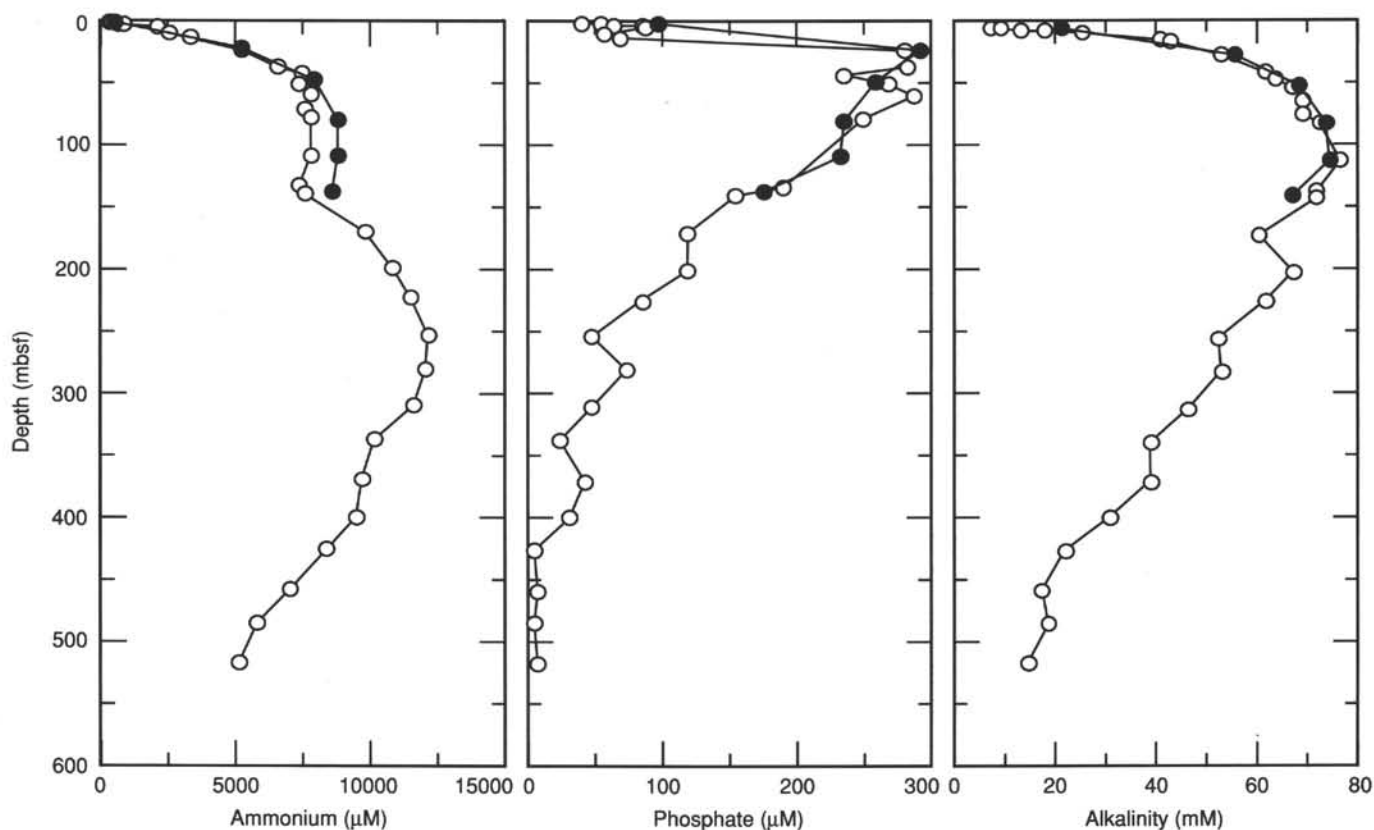


Figure 64. Distributions of alkalinity, phosphate, and ammonium with depth; data for Holes 798A and 798B are represented by closed and open circles, respectively.

depth intervals defined above. Unit 1 is characterized by high water content; Unit 2 shows a cyclic variation and an increase of water content with increasing depth below the seafloor; whereas Unit 3 is marked by an abrupt decrease in water content. Below the depth of 460 mbsf, water content shows a slight increase (Unit 4). The high water content values at the depth interval around 140 mbsf may result from drilling disturbance that was caused by the shift from the APC to the XCB.

Porosity (Fig. 78) ranges roughly between 50% and 80%. The porosity profile can also be divided into four different units with increasing depth below seafloor. In Unit 1, porosity values vary between 67% and 82%. Unit 2 is characterized by cyclic variation of porosity and a slight increase downhole, whereas Unit 3 is marked by an abrupt decrease in porosity. For Unit 4, a slight increase in porosity was recorded.

Grain density (Fig. 79) varied within the range of 2.15 and 2.85 g/cm³, values above and below these limits are subject to errors of determination.

GRAPE-Measured Density

Figure 80 shows the GRAPE-measured bulk density of Hole 798B. This figure illustrates the original data points, as recorded by the GRAPE, and a smoothed curve, showing the running average of five data points. GRAPE-measurements were restricted to a total depth of about 400 mbsf because of drilling disturbance and biscuiting in the deeper part of Hole 798B. In the upper section of Hole 798B (0–25 mbsf), densities ranged from 1.32 to 1.55 g/cm³. At a depth interval between 25 and roughly 50 mbsf, an increase of GRAPE-measured density can be observed. Below 50 mbsf, density generally decreases to values between 1.20 and 1.55 g/cm³ and show a cyclic variation. At a depth of

about 320 mbsf, density increases abruptly to values between 1.40 and 1.60 g/cm³. In the upper part of the profile, the GRAPE densities exhibit a good correlation to the wet-bulk densities determined by the pycnometer method. Below a depth of about 40 mbsf, the absolute values of the GRAPE-measured densities are generally lower than the wet-bulk densities determined by the pycnometer, but the general variation of the density profile shows a good correlation. An apparent reason for the generally lower density values determined by the GRAPE-method is the degassing of the sediment, which caused voids within the liner. These voids influence the gamma-ray attenuation of the sediment and yield lower values for GRAPE density, whereas the pycnometer method is not influenced by degassing.

Compressional-Wave Velocity

Sonic velocity measurements were performed by the continuous *P*-wave logger (Table 23). Because of the high amount of gas in the sediments, determination of sonic velocity was restricted to Core 128-798A-1H. In the upper 8 mbsf, the sonic velocity scattered around a mean value of about 1525 m/s.

Thermal Conductivity

Thermal conductivity was routinely determined for four sections from each core from the mud line to a total depth of 513 mbsf. Results are shown in Table 24 and Figure 81. Thermal conductivities varied between about 0.6 and 1.41 W/m · K. With increasing depth below seafloor, the profile for thermal conductivity can be divided into four different units that correspond to the same depth intervals as for water content and wet-bulk density. Unit 1 starts with low values near the mud line and shows an increasing trend to a depth of about 20 mbsf. Unit 2 ranges between 20 and about 320 mbsf.

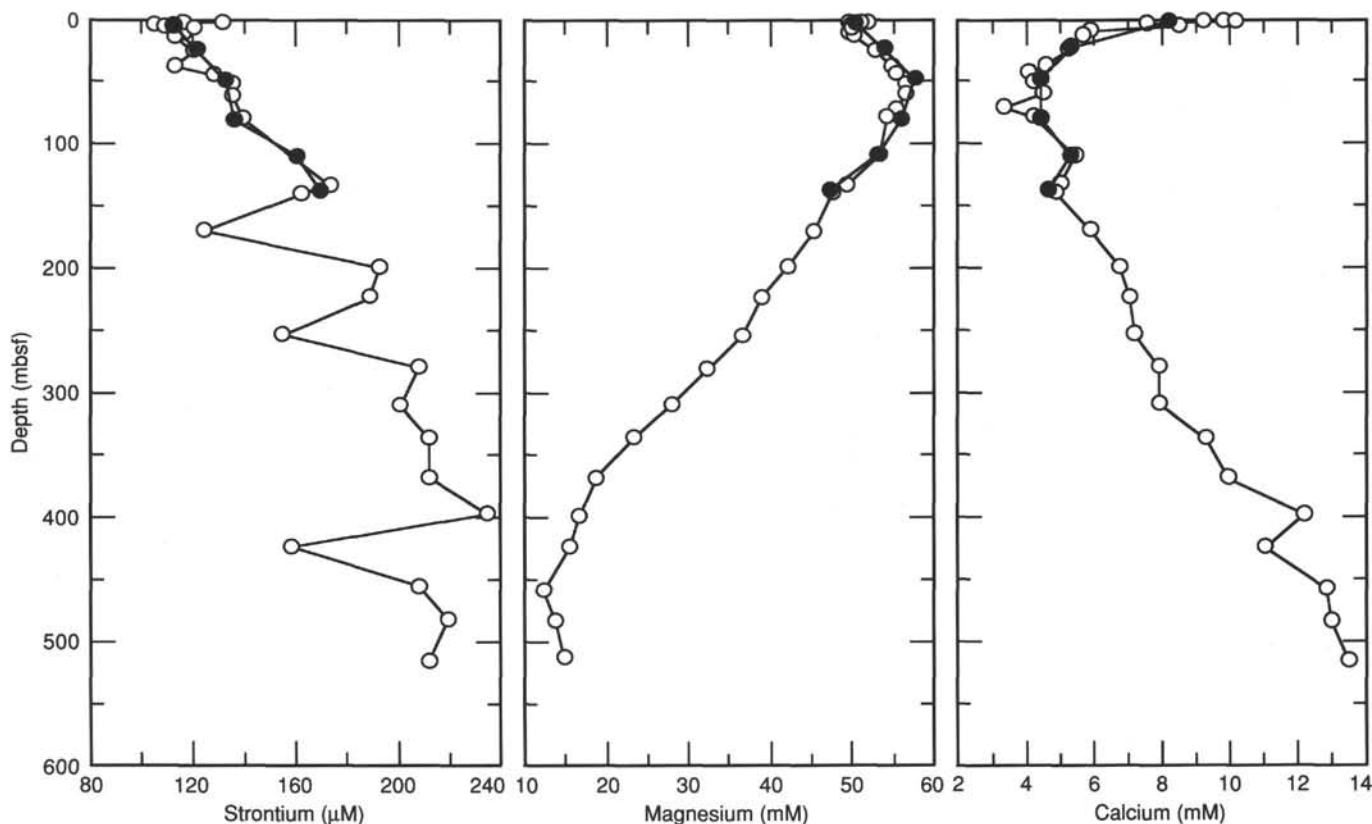


Figure 65. Distributions of dissolved calcium, magnesium, and strontium with depth; data for Holes 798A and 798B are indicated by closed and open circles, respectively.

The thermal conductivity of this unit shows a decreasing trend with increasing burial depth. The upper boundary of Unit 3 is marked by the depth of about 320 mbsf. An increase of thermal conductivity can be observed in this unit. The maximum value of $1.41 \text{ W/m} \cdot \text{K}$ was determined at a depth of about 460 mbsf. This depth marks the upper boundary of Unit 4. Below that boundary, thermal conductivity decreases.

Undrained Shear Strength

The values of Torvane-measured shear strengths are listed in Table 25 and plotted vs. depth in Figure 82. No data were collected in the strongly degassed upper 50 m of sediment, or in the more lithified sediments below 325 mbsf.

Shear strength values vary between about 15 and 93 kPa. A zone of high shear-strength values (40–80 kPa) is located at a depth interval of between 125 and about 175 mbsf.

Relationship of Physical Properties to Lithology

Based on visual core description and the evaluation of smear slides, the sedimentary record of Site 798 can be divided into three major lithologic units (see "Lithostratigraphy" section, this chapter). Unit I comprises the sediments from 0 to 220 mbsf; the upper 20 mbsf of this unit shows a greater influence of terrigenous material. The Unit I/Unit II boundary is located at a depth of 220 mbsf, where the carbonate content decreases abruptly. The beginning of Unit III is located at a depth of about 455 mbsf and is marked by the transition of opal-A to opal-CT.

A comparison of physical properties with lithology reveals that the upper 20 m of the section is characterized by a generally low wet-bulk density, whereas high values for water content and porosity were recorded in the same interval. The

decrease of carbonate content at a depth of about 220 mbsf has no dramatic influence on the physical properties, whereas the boundary between opal-A and opal-CT at a depth of about 455 mbsf is marked by high values for wet-bulk density, the maximum value for thermal conductivity, and low water content and porosity. The major change in physical properties at a depth of about 320 mbsf corresponds to a dramatic change in logging data (see "Downhole Measurements" section, this chapter) and is related to more lithified sediment below that depth and the beginning of silica diagenesis (see "Inorganic Geochemistry" section, this chapter).

DOWNHOLE MEASUREMENTS

Downhole measurements were completed at all three holes drilled at Site 798. The Barnes/Uyeda temperature probe was deployed during APC coring at Holes 798A and 798C, and a complete suite of four Schlumberger logs was run at Hole 798B. These logs consisted of the seismic stratigraphy, formation microscanner (FMS), lithoporosity, and geochemical tool combinations. In addition, the Lamont-Doherty Geological Observatory temperature logging tool (TLT) was attached to the base of each of the Schlumberger tool strings. These tool strings and their applications are described in the "Explanatory Notes" (this volume).

Drilling stopped at 517.9 mbsf with hole conditioning that consisted of a wiper trip and the pumping of a minimal amount of polymer mud of 2% KCl to help stabilize the clays (see "Operations" section, this chapter). Hole conditions were excellent and no bridges were encountered, nor was there any indication of clay swelling. This was in agreement with results of our capillary suction tests, which were performed on samples from the core and which suggested only minor clay

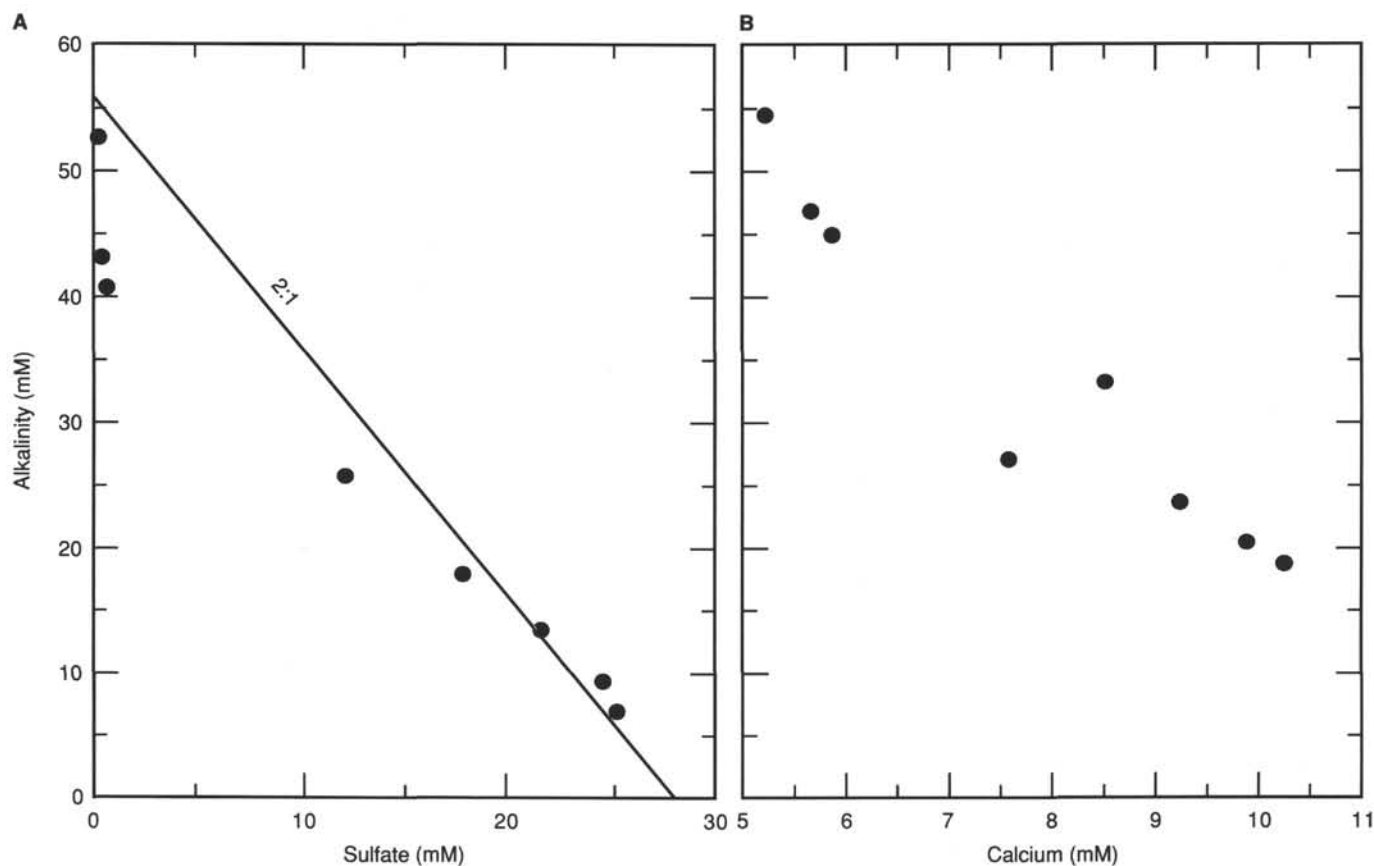


Figure 66. Alkalinity-sulfate (A) and alkalinity-calcium (B) relationships in the upper 25 mbsf of Hole 798B. The line in the alkalinity-sulfate diagram shows the stoichiometric production of alkalinity when organic matter has been decomposed by sulfate reduction.

swelling. Pipe was set at 85 mbsf, leaving 433 m of open hole. A summary of the actual logging sequence with times is shown in Table 26.

Quality of Logs

The quality of the logs obtained was generally excellent (Fig. 83). Tool sticking and borehole washouts are common problems that typically compromise log quality, but these did not occur at Hole 798B. The orthogonal FMS calipers indicated that the hole maintained a constant diameter of about 30 cm, except for the APC-cored interval from 180 to 100 mbsf, which was slightly elliptical. Tool calibration was performed both before and after each logging run to ensure quality control. The wireline heave compensator was used for all four logging runs to neutralize the effect of the ship's heave on the tool position. Depth correlation was good among all the logging runs, except for the lithoporosity tool combination, which needed to be shifted up nearly 4 m because of a problem with depth calibration when the wireline heave compensator was turned on. The log depths originally were measured in feet below the rig floor, but were corrected to meters below seafloor for ease of comparison with other data. Only the geochemical and natural gamma-ray tool measurements above 85 mbsf can be corrected for attenuation effects caused by the casing and drill pipe.

Considering the limited range of lithological variations observed in this hole, the logging data provide a great deal of information about the more subtle chemical and physical characteristics and cyclicity present in the formation. The high sampling resolution of logging measurements (every 15 cm)

allows for the delineation of more subtle changes in lithology, which would be more difficult to detect using discrete sampling techniques. Although core recovery at this site was generally excellent, gas expansion adversely affected true sediment recovery and some of the physical properties measured for discrete samples (see "Physical Properties" section, this chapter).

Temperature Gradients

The Barnes/Uyeda temperature probe was run every other core in Hole 798A from Cores 128-798A-5H to 128-798A-15H and in Hole 798C from Core 128-798C-5H to 128-798C-13H. Six readings were obtained from Hole 798A, with the deepest recording at a depth of 132.8 mbsf. Five readings were taken in Hole 798C between the depths of 33.7 and 110.4 mbsf. The combined Barnes/Uyeda temperature readings from Holes 798A and 798C indicate an average temperature gradient of approximately 111°C/km for the uppermost 130 m measured at Site 798 (Fig. 84).

The Lamont-Doherty TLT was deployed on three of the four logging runs. Pressure and temperature vs. time data from these three runs indicated that the bottom borehole temperature was gradually increasing during each of the three logging runs, which indicated that the borehole temperatures had not yet stabilized from drilling disturbance and circulation of drilling fluid. The highest temperature measured at the bottom of Hole 798B was 43°C at a depth of 517 mbsf, yielding a thermal gradient of 83°C/km. This reading was taken during the geochemical run, which was the last and slowest logging run (Fig. 85). The actual temperature gradient is almost surely higher than this because the bottom temperature had not

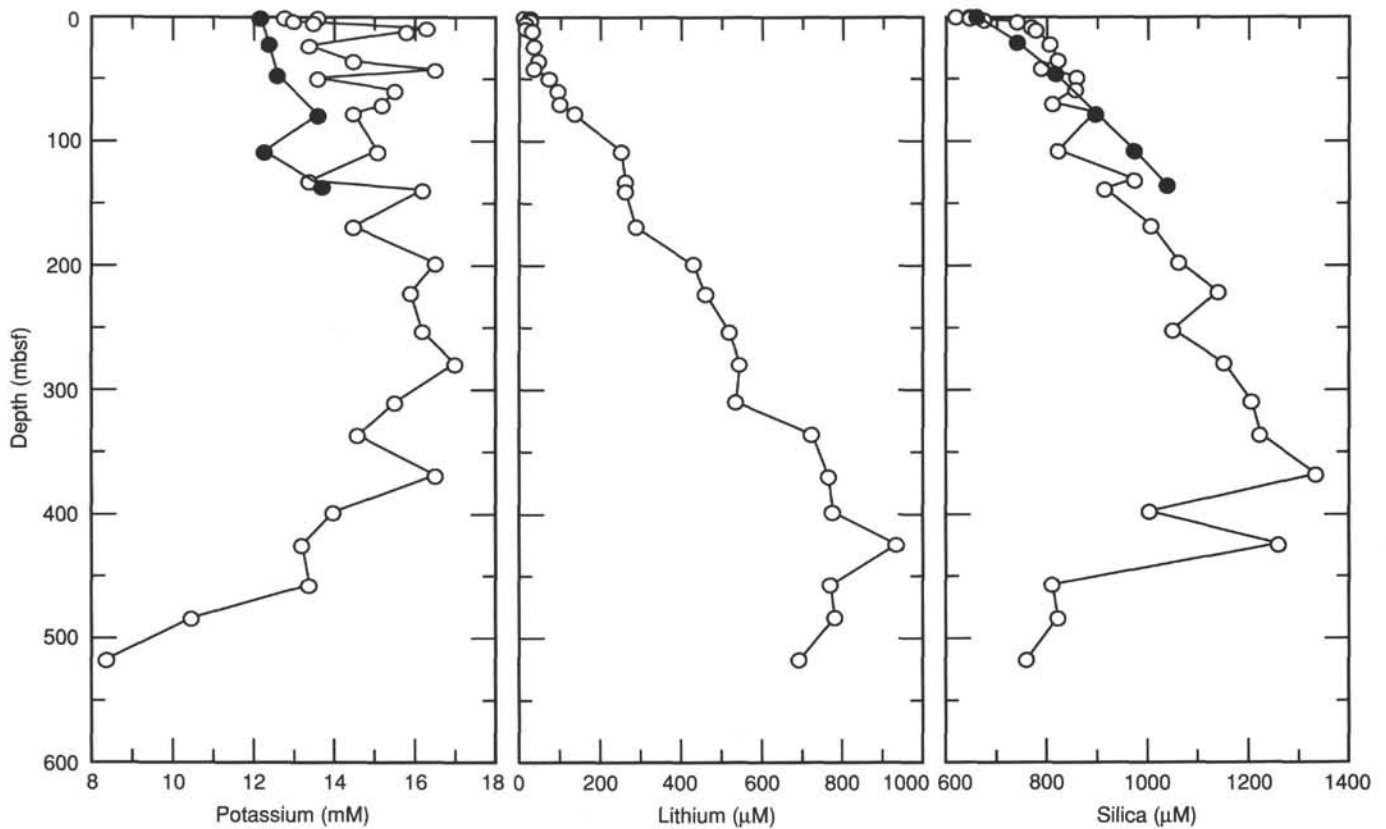


Figure 67. Distributions of dissolved potassium, lithium, and silica with depth; data for Holes 798A and 798B are shown by closed and open circles, respectively.

completely reached thermal equilibrium during the 22 hr of logging.

Although the lower temperature gradient obtained from the TLT most probably results from thermal disequilibrium, the higher temperature gradients obtained with the Barnes/Uyeda tool may reflect a change in the thermal conductivity of the drilled sediments (Fig. 86). Thermal conductivities measured in the Physical Properties laboratory show a monotonous increase that begins at 200 mbsf (see "Physical Properties" section, this chapter). Thus, the region of higher thermal conductivity may be partially responsible for the lower observed temperature gradient at depth.

Synthetic Seismogram

The velocity log at Hole 798B is of very good quality and provides a continuous and representative curve of velocity variations that can be used to link core depths and seismic traveltime. With virtually no noise or cycle skipping, the raw log needed little initial processing. It was used in combination with the bulk-density log to produce a synthetic seismogram that was calculated using a convolution model having internal multiples. The seismogram produced is shown in Figure 87, where it is compared with the seismic line shot over the site. The major reflectors apparent in the log-derived synthetic seismogram are clearly correlative with the reflectors shown in the seismic profile (Fig. 87). The sharp velocity/porosity contrasts of the dolomite and ash layers are clearly apparent in both profiles. The example shown is just a preliminary synthetic seismogram to give an indication of the quality of correlation we can expect from

these logs; a more accurate seismogram will be constructed after post-cruise processing of the logging data that will permit detailed comparisons of logs with seismic profiles, as well as interval velocity interpretations.

Formation Microscanner

The FMS tool measures the microresistivity character of the borehole wall using 16 electrode "buttons" on each of four pads, which are pressed against the borehole wall. Measurements were obtained at 2.5-mm intervals, and approximately 20% of the borehole surface was typically measured by the four pads. Two passes of the FMS tool were conducted at Hole 798B (see Table 26); thus, borehole coverage may approach nearly 40%. Unlike the other logging tools, the FMS data must go through several processing steps before the data can be interpreted. We had originally intended to do most of this processing on board the ship, but problems with hardware and software prevented any processing thus far. However, the raw images do provide a tantalizing glimpse of the detail expected after processing. In particular, the dolomite nodule described in the "Lithostratigraphy" section (this chapter) at 334 mbsf has a total recovered thickness of ~20 cm; in conjunction with the sonic velocity logs, the FMS images indicate that this unit is a discrete layer ~80 cm thick. The FMS images also record the numerous ash layers present at Hole 798B. In addition, the images resolve numerous finely laminated intervals that generally occur within the low gamma-ray troughs of the cyclic gamma-ray interval from 80 to 300 mbsf. The broadly laminated sediments, such as those observed below 500

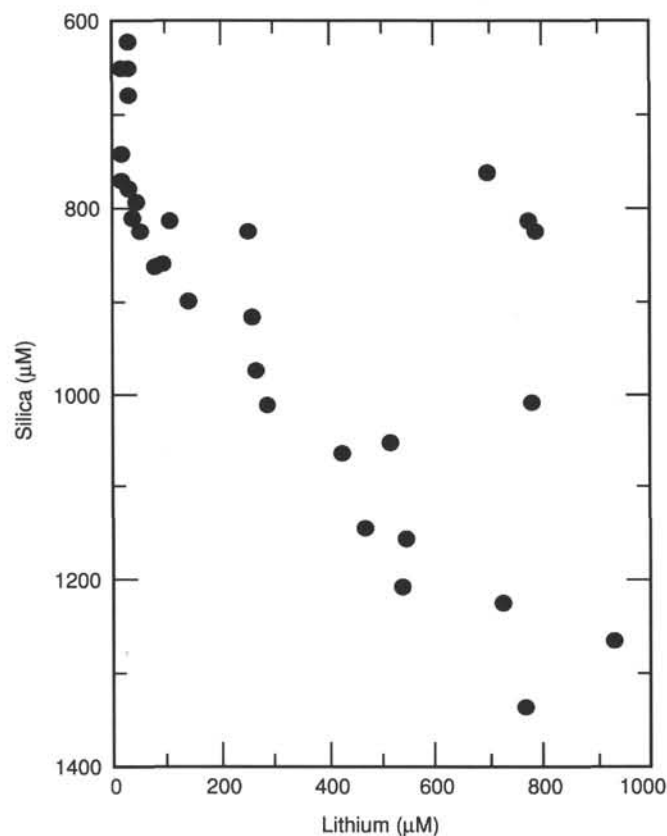


Figure 68. The silica-lithium relationship for Hole 798B. The linear trend suggests the incorporation of dissolved lithium into the pore fluids by dissolution of biogenic silica phases, the most likely sedimentary carriers for lithium.

mbsf (see "Lithostratigraphy" section, this chapter), are clearly apparent from the raw images. Because of the excellent condition of the borehole, we expect that processing will resolve features such as laminations, fractures, bioturbation and thin ash bands further throughout the length of the hole.

Variation of the Logs with Depth

Depth (80–286 mbsf)

Logs within this depth interval are characterized by a distinct cyclicity that is shown most clearly by the gamma-ray log (Fig. 83). Throughout this depth interval, the higher gamma-ray values correspond to higher bulk densities, higher resistivities (lower porosity), and higher contents of aluminum. These cycles are apparent in the recovered sediment record as well: the high density, high gamma ray, and low porosity levels correspond to the massive clay-rich intervals, whereas the lower density, low gamma ray, and higher porosity units correspond to the darker, organic-carbon-rich intervals that are also rich in diatoms (see "Lithostratigraphy" and "Inorganic Geochemistry" sections, this chapter). There is a significant increase in gamma ray, bulk density, and resistivity values between 278.6 and 286 mbsf, which suggests increasing clay content.

The hard dolomitic layer or concretion that was recovered at 142 mbsf in Hole 798A, but not in Holes 798B and 798C, is not recognizable in the log. At the depth where the dolomitic layer would be expected in Hole 798B, there is an increase in the gamma-ray reading and a small increase in resistivity.

Depth (286–319.3 mbsf)

Throughout this portion of Hole 798B, the logs are characterized by a resistivity of 0.4 ohm · m, gamma-ray readings of 40 to 60 API units, and densities of 1.3 to 1.4 g/cm³. The wireline logs reflect a decrease in clay content relative to the overlying sediments between 278 to 286 mbsf.

Depth (319.3–347 mbsf)

There is a well-defined increase in the average baseline resistivity of from 0.4 to 0.5 ohm · m at 319.3 mbsf. Also, the average density increases from 1.4 to 1.5 g/cm³.

At a depth of 332.1 to 333.3 mbsf, a 1.2-m-thick layer having low gamma-ray readings and high sonic velocities occurs. The density log has a peak reading of 2.42 g/cm³. Porosity of the layer was low relative to the rest of the hole. The geochemical log indicates an increase in calcium and a decrease in aluminium in this interval. This zone most likely is

Table 13. Light-hydrocarbon data from vacutainer analysis, Site 798.

Sample	Depth (mbsf)	C ₁ × 10 ⁴ (ppm)	C ₂ (ppm)	C ₃ (ppm)	C ₄ (ppm)	C ₅ (ppm)	C ₁ /C ₂	C ₁ /C ₃
1	157	15.96	52	11			3,071	14,517
2	167	57.58	371	103			1,552	5,591
3	174	47.85	438	156			1,093	3,067
4	185	62.21	432	128			1,440	4,861
5	197	57.50	400	131			1,438	4,390
6	206	48.78	364	120			1,340	4,066
7	224	67.02	615	214			1,090	3,132
8	231	53.19	485	167			1,097	3,186
9	255	21.71	138	46			1,574	4,721
10	264	62.83	472	145			1,331	4,333
11	283	61.68	627	204			984	3,024
12	292	64.10	546	169			1,174	3,793
13	302	71.86	559	154			1,286	4,666
14	312	39.85	317	96			1,257	4,152
15	359	48.84	663	181			737	2,699
16	369	57.80	640	144			903	4,014
17	377	68.73	736	143			934	4,807
18	388	55.06	655	122			841	4,514
19	396	60.94	670	98			910	6,218
20	405	44.94	788	90			570	4,994
21	415	33.95	361	15			940	22,634
22	424	51.41	609	30			844	17,138
23	436	27.34	462	25			592	10,938
24	450	34.62	500	55			693	6,296
25	513	71.94	2,494	272	34	10	288	2,645

Table 14. Light-hydrocarbon data from headspace technique, Site 798.

Sample	Depth (mbsf)	C ₁ × 10 ⁴ (ppm)	C ₂ (ppm)	C ₃ (ppm)	C ₄ (ppm)	C ₅ (ppm)	C ₁ /C ₂	C ₁ /C ₃	C ₁ /C ₄
1	1.5	0.06	2				31		
2	12.3	75.19	15				5,080		
3	22.8	65.45	14	1			4,675	65,450	
4	34.8	29.48	8				3,060		
5	38.2	9.67	12	1			806	9,678	
6	47.7	9.52	11	1			866	9,528	
7	57.7	9.12	8	1			1,141	9,129	
8	66.8	7.01	8	1			877	7,013	
9	79.3	7.74	7	1			1,107	7,746	
10	85.9	7.85	14	2			561	3,926	
11	95.6	7.68	17	5			452	1,536	
12	109.8	7.60	14	5			543	1,521	
13	116.4	8.31	10	3			832	2,772	
14	132.1	7.53	11	4			685	1,885	
15	138.8	7.78	9	4			865	1,947	
16	145.6	9.05	10	4			905	2,263	
17	169.4	7.00	10	6			700	1,168	
18	226.0	7.62	14	16			545	477	
19	253.5	5.15	6	12			859	429	
20	260.2	5.02	8	10			628	503	
21	280.2	5.95	14	117			426	51	
22	287.8	5.87	9	9			653	653	
23	309.8	8.64	15	23			576	376	
24	334.2	6.67	17	16			392	417	
25	336.5	11.89	36	26			331	458	
26	359.8	8.95	16	10			560	896	
27	369.9	14.24	28	15			509	950	
28	379.1	7.64	23	19			332	402	
29	399.9	9.54	52	29			183	329	
30	425.2	8.78	18	2			544	4,892	
31	430.2	29.82	62	9			481	3,314	
32	441.0	4.92	29	9			170	548	
33	451.4	6.71	19	9	3	3	353	746	2,237
34	451.9	7.72	59	43	12	10	131	180	644
35	457.9	0.79	9	13		7	88	61	
36	469.6	7.58	53	51	18	12	143	149	421
37	475.6	3.53	34	36	12	6	104	98	295
38	483.9	8.52	89	110	32	15	96	77	266
39	489.0	4.68	36	44	16	8	130	106	293
40	498.7	14.61	263	237	63	26	56	62	232
41	501.7	7.74	213	224	67	29	36	35	116
42	517.3	6.75	147	174	56	26	46	39	121
43	517.8	31.48	442	390	117	44	71	81	269

a dolomitized layer that was partially recovered in Section 128-798B-35X-CC, at 25 to 30 cm. The FMS microresistivity images indicate that a layer occurs at 334.2 mbsf (logging depths) and that it is approximately 80 cm thick.

Depth (347–402 mbsf)

Starting at a depth of 347 mbsf, both the density and gamma-ray readings decrease and then slowly increase, producing a "carrot" shape. In addition, a decrease in the baseline resistivity readings occurs at 347 mbsf. Through this portion of the hole, gamma-ray readings decrease from 70 to 50 API units and then slowly increase to 90 API units with depth. Density decreases to 1.4 g/cm³ and then increases to 1.75 g/cm³. The wire-line logs indicate that this is a large-scale sedimentary cycle that begins with a decrease in clay content, followed by a slow increase in clay content with depth.

Depth (402–447 mbsf)

Average gamma-ray readings are 60 to 70 API units throughout this portion of the log. Density decreases from 1.7 to 1.5 g/cm³ within this division. At 426.6 mbsf, a gamma-ray peak of 104 API units was found. Associated with this gamma-ray peak are peaks in the resistivity and sonic log. Density increases to 1.8 g/cm³ and then decreases to 1.5 g/cm³ at 447 mbsf.

Depth (447–total depth of 517.9 mbsf)

Density readings increase slowly from a low of 1.5 to a maximum of 1.85 g/cm³ at a depth of 490.5 mbsf. Below 495 mbsf, density decreases to 1.5 g/cm³. At a depth of 464 mbsf, density readings increase. Associated with this is an increase in gamma rays, sonic velocity, and resistivity and a decrease in neutron porosity.

Sonic velocity increases slowly throughout the hole; however, there is a noticeable or rapid increase in velocity at 464 mbsf. Also in this region, the geochemical log shows an increase in silica and a decrease in potassium. The increase in density at 447 mbsf and the decrease in porosity at 464 mbsf may be indications of the conversion of opal-A to opal-CT.

The gamma-ray logs for bulk density correlate well from below the drill pipe (80 mbsf) to 452 mbsf. However, from 452 mbsf to the base of the logged section at 517.9 mbsf, this correlation deteriorates. The increase in bulk density, the increase in sonic velocity, and the decrease in porosity observed in the logs from 447 to 465 mbsf may result from lithification, diagenesis, or transformation of opal-A to opal-CT, or a combination of all three processes through this depth interval. The increase in silica content that occurs between 457 and 465 mbsf (inferred from the raw geochemical log) may

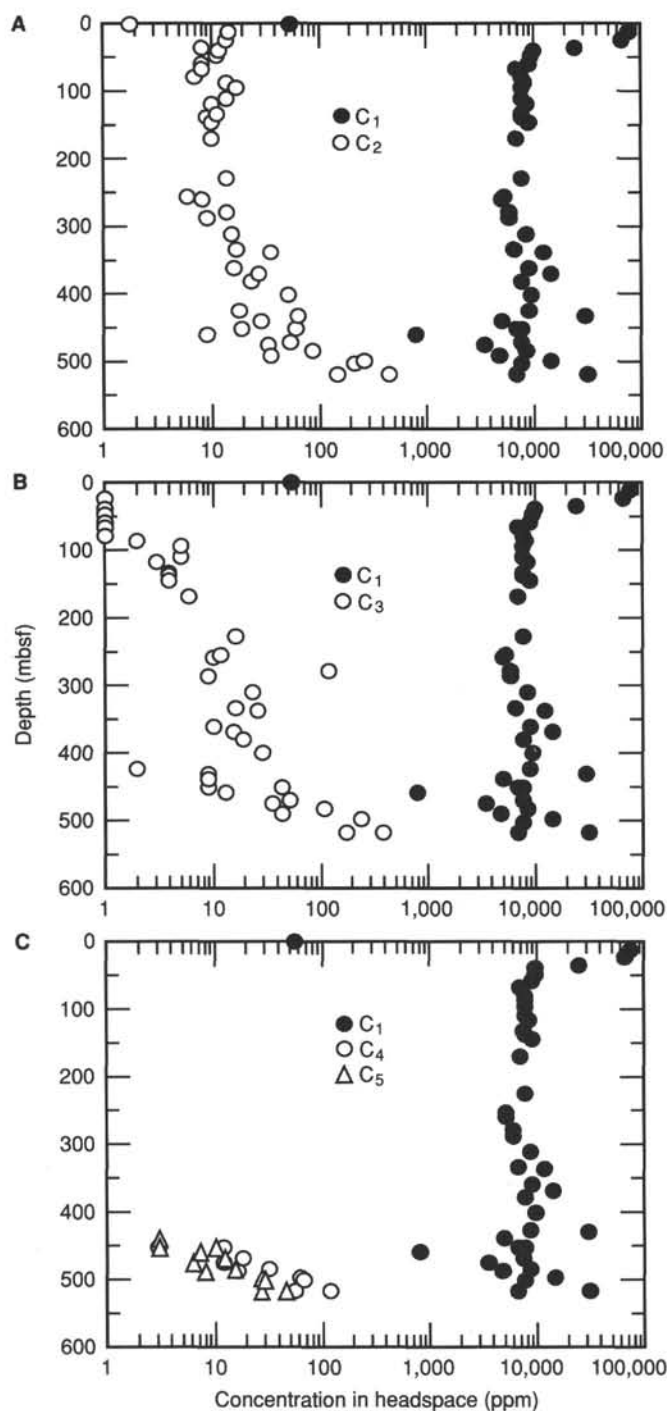


Figure 69. A. Concentrations of methane (C_1) and ethane (C_2). B. Concentrations of methane (C_1) and propane (C_3). C. Concentrations of methane (C_1), iso-butane ($i-C_4$), and n -butane (C_5) in sediments from Site 798. Data derived from headspace technique.

represent the region of the opal-A/opal-CT boundary within Hole 798B.

The bulk density measured with the LDT between 85 mbsf (bottom of drill pipe) to 400 mbsf (depth at which unreliable density results were obtained using the GRAPE) agrees well in magnitude and amplitude with GRAPE bulk density. The increase in GRAPE density at 275 mbsf agrees with the increase in LDT density at a depth of 279 to 286 mbsf. Also, the decrease at 286 mbsf and the subsequent increase at 319

mbsf of the LDT-measured bulk density is broadly similar to that from GRAPE data.

Geochemistry

Data recorded from the geochemical spectroscopy tool (GST) will require considerable post-cruise processing at Lamont-Doherty Geological Observatory. At this stage, the references made to silicon, iron, calcium, sulfur, chlorine, and hydrogen thus are only broadly qualitative, and logs are not shown. However, the natural gamma-ray spectroscopy tool (NGT) produced reliable values for the concentration of potassium, thorium, and uranium, and the aluminium log produced by the aluminium clay tool (ACT) is generally little affected by post-cruise processing. A crossplot of potassium vs. aluminium is shown in Figure 88A; the good correlation reflects varying clay content as potassium and aluminum are major constituents of these clays. The second crossplot in Figure 88B again shows a positive correlation between the compensated gamma ray (potassium plus thorium) and bulk density. This indicates that the bulk density of the formation is primarily a function of the clay mineral content. This correlation is present throughout the hole, but is best exhibited in the highly cyclic section of the log between the end of the drill pipe at ~85 and 300 mbsf. The positive correlation between bulk density and gamma rays suggests that there is a more unusual inverse relationship between the percentage of clay and porosity, while higher porosity is found in the less clay-rich, more diatom-rich layers. This cyclicity is not apparent in the sonic velocity and resistivity logs, rather these logs reflect velocity increases and porosity decreases associated with the increasing compaction of the formation. These logs define the thin dolomitic layer observed at 332 mbsf (see "Lithostratigraphy" section, this chapter) by a sharp increase in sonic velocity and decreased resistivity. This layer also is resolved by the geochemical data (GST data not shown) as a sharp increase in the calcium log, with a decrease in the silicon, aluminium, chlorine, and hydrogen logs, as well as a decrease in gamma rays, neutron porosity, and the photoelectric factor.

High uranium and thorium values often are associated with increases in organic material (Fertl, 1979) and when the uranium/thorium ratio is compared to the percentage of organic matter derived from discrete core samples, there is a broad positive correlation. The highest core-derived carbon content at around 100 mbsf has the highest uranium/thorium ratio.

Paleoclimatic Significance of Hole 798B Logs

One of the primary objectives of Leg 128 logging was to evaluate the paleoclimatic significance of the various downhole logging records. Unlike the recovered core material, downhole logs are continuous high-resolution records of the physical and chemical variability of the drilled sequence. Extracting paleoclimatic information from downhole logs previously has been compromised by relatively low accumulation rates in sediments that limit the temporal resolution of the logging measurements as well as the unsuitability of certain sites because of significant downslope sediment contributions. We anticipated that Site 798 on the Oki Ridge would present an ideal record of late Neogene (~4 Ma) paleoclimatic variability in the Sea of Japan region because this site is positioned on a bathymetric high above the modern lysocline and because sedimentation rates here are unusually high (~120 m/m.y.).

Specifically, the Oki Ridge sediments should present an excellent record of variations in the supply of eolian dust transported eastward from Asian source areas, as well as

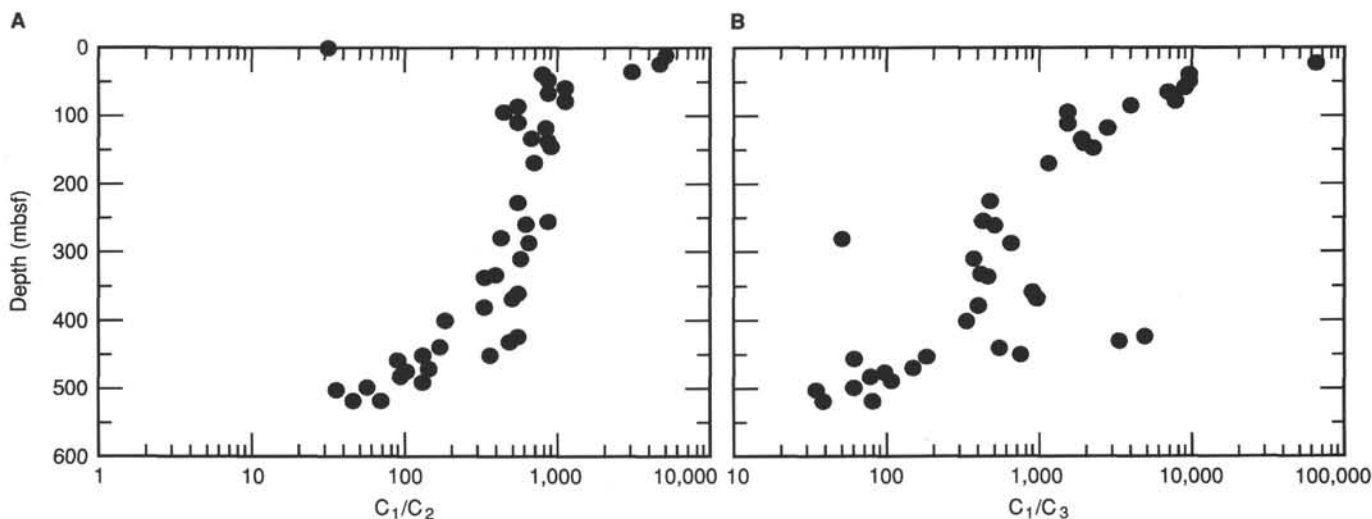


Figure 70. A. Methane/ethane (C_1/C_2) ratios. B. Methane/propane (C_1/C_3) ratios. Data derived from headspace technique.

other climatically or oceanographically induced cyclic signals in this sequence. In their studies of loess deposits in central China, Kukla et al. (1988) demonstrated that vast areas of central Asia experienced widespread aridity and soil deflation during Pleistocene (0–1.6 Ma) glacial intervals. More importantly, they also showed that the accumulation of loess deposits is directly correlated with the marine oxygen-isotopic record, indicating that Asian aridity is closely linked to variations in Northern Hemisphere ice volume. Imbrie et al. (1984) demonstrated that the succession of Pleistocene ice ages is largely attributable to the seasonal insolation variations caused by changes in Earth's orbital parameters, which result from gravitational interactions with the Sun, Moon, and larger planets. As discussed by Kukla et al. (1988), the similarity between the loess-accumulation and ice-volume records suggests a causal link between aridity and ice volume. Because the Sea of Japan is seasonally downwind of the Asian dust source areas (Mongolian and north China high-plateau deserts), the dust-transporting westerlies may be expected to transmit the aridity signal to sediments in the Sea of Japan.

The following analysis focuses on the spectral gamma-ray (SGR) log from 90 to 300 mbsf in Hole 798B. This log was selected because it is often used to indicate downhole variations in contents of clay minerals; thus, it may serve as a tracer for variations in the terrigenous (and perhaps, eolian) component. The log reflects total gamma-ray radioactivity from the decay of potassium, thorium, and uranium, the former two of which are common elements in clay-mineral structures, whereas uranium abundance can be strongly correlated with contents of organic carbon (Hassan et al., 1976). Comparisons of the SGR log with the CGR log (i.e., SGR corrected for uranium contents) at Hole 798B demonstrate that most of the gamma-ray variability in fact reflects variations in the contents of clay minerals. The lower depth limit is roughly equivalent to 2.5 Ma, and this marks the beginning of periodic SGR variations. The upper depth limit at 90 mbsf is roughly equivalent to 0.9 Ma and is a consequence of casing that was set at 85 mbsf; the SGR log above this depth may be used once data have been corrected for casing and the effects of drill-pipe attenuation.

The SGR and aluminium logs are shown as a function of depth (mbsf) in Figure 89. As discussed earlier in this section and shown in Figure 88A, the gamma-ray log correlates well with the aluminium log, which supports the interpretation of this log as a terrigenous indicator. Core recovery is shown on

the left in Figure 89; although reported core recovery was high, true recovery was considerably less owing to the effects of gas expansion. A preliminary age model was determined based on the stratigraphic positions of the Jaramillo (0.91–0.98 Ma) and Olduvai (1.66–1.88 Ma) subchronozones boundaries and the Matuyama/Gauss Chron boundary (2.47 Ma; see "Paleomagnetism" section, this chapter). The resulting time-series with the relative positions of the reversal boundaries is shown in the right-hand column of Figure 90. The cyclicity apparent in the depth log also is apparent in the time-series and is equivalent to a ~40-k.y. periodicity. The periodicity was quantitatively estimated using standard-power spectral analysis methods (e.g., Imbrie et al., 1984). The power spectra shown in Figure 91 demonstrate that the SGR log from 90 to 300 mbsf varies predominantly at periodicities between 33 to 50 k.y. and 100 k.y., based on the low-resolution model of paleomagnetic age.

Working with the assumption that the 40-k.y. peak is probably a climatic expression of the 41-k.y. periodicity of orbital obliquity, the orbital obliquity time-series (tilt variations) calculated by Berger (1978) is shown as the left-hand column of Figure 90; the tilt of the Earth's rotational axis varies from 22.5° to 25.5° relative to the pole of the orbital plane. One can see that the raw SGR log is similar in character to the record of orbital tilt variations, and if more detailed age control were available, the two signals might be even more similar. Assuming that variations in tilt are in some direct or indirect way influencing the supply of terrigenous sediment to the Sea of Japan (as will be discussed later), it is possible to correlate ("tune") the SGR signal to the tilt record. Methodological aspects of this "tuning" procedure were discussed by Imbrie et al. (1984). Briefly, the tuning procedure can be employed only when the power spectra of a given time-series demonstrates concentrations of variance at orbital periodicities.

We employed CORPAC software developed by Martinson et al. (1982), which uses a nonlinear inverse correlation approach to tune the SGR signal to the tilt record. The tuning procedure makes minor adjustments to sediment accumulation rates so that the zero-phase correlation between the tilt and SGR records is maximized the "tuned" SGR record is shown as the center column in Figure 90. The power spectra of this tuned time-series are shown in Figure 92; the age-depth datums that result from tuning are shown superimposed upon the paleomagnetic datums in Figure 93. One can see from this

Table 15. Concentrations of inorganic and organic carbon and total nitrogen and sulphur in sediments from Hole 798A.

Core, section, interval (cm)	Depth (mbsf)	Total carbon (%)	Inorganic carbon (%)	Organic carbon (%)	CaCO ₃ (%)	Nitrogen (%)	Sulfur (%)	OrgC/N	OrgC/S
128-798A-1H-2, 0-5	1.50	1.83	0.69	1.14	5.7	0.12	0.67	9.50	1.70
1H-2, 46-51	1.96	3.21	1.24	1.97	10.3	0.21	1.31	9.38	1.50
1H-4, 38-45	4.88	3.64	1.33	2.31	11.1	0.21	0.85	11.00	2.72
1H-6, 38-44	7.88	4.33	0.50	3.83	4.2	0.36	0.79	10.60	4.85
2H-2, 46-51	11.26	1.67	0.40	1.27	3.3	0.14	0.67	9.07	1.89
2H-3, 0-5	12.30	2.88	0.43	2.45	3.6	0.19	0.92	12.90	2.66
2H-4, 4-9	13.84	2.45	1.13	1.32	9.4	0.11	0.96	12.00	1.37
3H-2, 49-51	20.29	2.26	0.79	1.47	6.6	0.17	0.78	8.65	1.88
3H-4, 49-51	23.29	1.46	0.38	1.08	3.2	0.13	1.02	8.31	1.06
3H-6, 49-51	26.29	2.31	0.28	2.03	2.3	0.20	1.59	10.10	1.27
4H-2, 29-31	29.09	0.98	0.19	0.79	1.6	0.11	0.97	7.20	0.81
4H-4, 59-63	32.39	3.19	1.22	1.97	10.2	0.20	1.35	9.85	1.46
4H-5, 0-5	33.30	2.64	1.16	1.48	9.7	0.15	1.24	9.86	1.19
5H-2, 80-82	39.00	4.97	3.22	1.75	26.8	0.16	0.29	10.90	6.03
5H-4, 86-88	42.06	3.36	0.80	2.56	6.7	0.24	1.00	10.60	2.56
5H-7, 7-11	45.77	5.34	2.97	2.37	24.7	0.21	0.69	11.30	3.43
6H-2, 49-54	48.19	4.41	2.85	1.56	23.7	0.15	0.45	10.40	3.46
6H-4, 4-9	50.74	4.99	2.55	2.44	21.2	0.21	0.78	11.60	3.13
6H-6, 84-89	54.54	1.54	0.14	1.40	1.2	0.15	1.47	9.33	0.95
7H-2, 0-5	56.84	2.59	0.07	2.52	0.6	0.23	1.80	10.90	1.40
7H-2, 130-135	58.14	2.11	0.10	2.01	0.8	0.22	1.27	9.13	1.58
7H-4, 50-55	60.34	2.28	1.26	1.02	10.5	0.11	1.57	9.27	0.65
7H-6, 65-70	63.49	4.59	2.51	2.08	20.9	0.19	1.20	10.90	1.73
8H-2, 0-5	65.60	6.98	4.63	2.35	38.6	0.19	0.44	12.30	5.34
7H-8, 55-60	66.39	3.57	1.27	2.30	10.6	0.22	1.56	10.40	1.47
8H-3, 32-34	67.42	6.36	3.92	2.44	32.7	0.21	0.75	11.60	3.25
8H-5, 61-63	70.71	3.01	1.81	1.20	15.1	0.15	1.23	8.00	0.98
8H-7, 64-66	73.74	4.24	3.01	1.23	25.1	0.15	0.76	8.20	1.62
9H-2, 29-31	76.49	3.38	2.10	1.28	17.5	0.15	1.60	8.53	0.80
9H-4, 0-5	79.06	3.46	1.93	1.53	16.1	0.15	1.21	10.20	1.26
9H-4, 54-56	79.60	3.40	1.54	1.86	12.8	0.20	1.24	9.30	1.50
9H-6, 53-58	82.59	1.69	0.78	0.91	6.5	0.17	1.25	5.30	0.73
10H-2, 0-5	85.02	4.50	0.28	4.22	2.3	0.36	1.53	11.70	2.76
10H-3, 40-45	86.92	4.16	0.35	3.81	2.9	0.34	1.64	11.20	2.32
10H-5, 103-108	90.55	3.17	0.11	3.06	0.9	0.27	1.83	11.30	1.67
10H-7, 20-25	92.72	2.08	0.26	1.82	2.2	0.22	1.51	8.27	1.20
10H-7, 128-133	93.80	4.71	2.36	2.35	19.7	0.23	1.43	10.20	1.64
11H-2, 0-5	95.60	5.52	0.08	5.44	0.7	0.39	1.64	13.90	3.32
11H-2, 80-84	96.40	4.83	0.08	4.75	0.7	0.67	1.55	7.09	3.06
11H-4, 86-90	99.46	4.29	0.84	3.45	7.0	0.56	1.64	6.16	2.10
11H-6, 102-107	102.62	3.00	1.87	1.13	15.6	0.14	1.27	8.07	0.89
12H-2, 30-35	104.87	4.13	0.94	3.19	7.8	0.30	1.37	10.60	2.33
12H-5, 0-5	109.07	3.24	0.13	3.11	1.1	0.27	1.48	11.50	2.10
12H-6, 25-29	110.82	4.11	0.15	3.96	1.2	0.33	1.61	12.00	2.46
12H-8, 30-34	113.82	1.30	0.41	0.89	3.4	0.31	1.13	2.90	0.79
13H-2, 98-103	115.88	1.41	0.45	0.96	3.8	0.11	1.50	8.70	0.64
13H-3, 0-5	116.40	3.41	1.52	1.89	12.7	0.16	1.08	11.80	1.75
13H-4, 74-79	118.64	3.95	1.39	2.56	11.6	0.24	1.39	10.60	1.84
13H-5, 20-25	121.10	2.89	0.58	2.31	4.8	0.23	1.46	10.00	1.58
14H-2, 30-34	123.81	3.60	1.35	2.25	11.2	0.49	1.44	4.59	1.56
14H-4, 62-66	127.13	3.07	0.96	2.11	8.0	0.42	1.23	5.02	1.71
14H-6, 49-53	130.00	3.07	1.79	1.28	14.9	0.38	1.20	3.37	1.06
14H-8, 22-26	132.73	2.05	0.51	1.54	4.2	0.42	1.45	3.66	1.06
15H-2, 35-39	134.55	3.11	0.71	2.40	5.9	0.45	1.22	5.33	1.97
15H-4, 30-34	137.50	5.60	2.99	2.61	24.9	0.25	1.35	10.40	1.93
15H-5, 0-5	138.70	2.32	0.53	1.79	4.4	0.17	1.26	10.50	1.42
15H-6, 15-19	140.35	5.53	0.58	4.95	4.8	0.49	1.29	10.10	3.84
15H-8, 29-33	143.49	2.38	0.69	1.69	5.7	0.42	1.50	4.02	1.12

figure that the tuned time-scale datums are within the errors of the original paleomagnetic datums; maximum depth offsets between the original and tuned logs are ~1-2 m. These depth offsets are equivalent to 8 to 16 k.y. in time, which is roughly equivalent to the transition time required for reversals of magnetic polarity. However, the tuned time-scale does add considerable age control to those intervals between the reversal datums.

Once the SGR time-series has been tuned, it is possible to reexamine the power spectra for concentrations of variance that are not at the orbital periodicities. Figure 92 shows the power spectra calculated for the tuned time-series. Compari-

son with the untuned power spectra (Fig. 91) illustrates that while variance was broadly distributed over a range of periodicities from ~50 to 33 k.y. in the untuned (raw) time-series, tuning acts to focus this variance into one central peak at 41 k.y., while power at the 100-k.y. eccentricity periodicity remains unaffected. The absence of other nonorbital periodicities in the tuned record illustrates an important point: The SGR record, and hence the record of terrigenous clay content, is almost entirely driven at the orbital obliquity periodicity. While the concentration of variance at the obliquity periodicity is a consequence of tuning, the absence of other nonorbital periodicities is a real feature of the data.

Table 16. Concentrations of inorganic and organic carbon and total nitrogen and sulphur in sediments from Hole 798A.

Core, section, interval (cm)	Depth (mbsf)	Total carbon (%)	Inorganic carbon (%)	Organic carbon (%)	CaCO ₃ (%)	Nitrogen (%)	Sulfur (%)	OrgC/N	OrgC/S
128-798B-1H-2, 8-10	1.58	3.18	0.10	3.08	0.8	0.31	1.04	9.93	2.96
1H-2, 41-44	1.91	3.54	0.12	3.42	1.0	0.32	0.94	10.70	3.64
1H-2, 133-136	2.83	2.86	0.83	2.03	6.9	0.13	0.94	15.60	2.16
1H-3, 106-109	4.06	2.58	0.69	1.89	5.7	0.17	1.04	11.10	1.82
1H-4, 131-134	5.81	5.88	2.39	3.49	19.9	0.28	0.58	12.40	6.02
2H-1, 51-54	9.91	4.33	2.47	1.86	20.6	0.20	0.19	9.30	9.79
2H-3, 51-54	12.91	3.65	1.64	2.01	13.7	0.20	0.26	10.00	7.73
3H-4, 91-94	23.81	2.63	0.07	2.56	0.6	0.23	0.82	11.10	3.12
4H-7, 61-64	37.01	3.31	1.47	1.84	12.2	0.18	0.33	10.20	5.57
5H-4, 135-140	42.65	6.08	4.31	1.77	35.9	0.15	0.02	11.80	88.50
6H-4, 55-58	50.47	4.36	2.55	1.81	21.2	0.17	0.19	10.60	9.52
7H-3, 135-140	59.93	5.24	2.00	3.24	16.7	0.27	0.29	12.00	11.20
8H-4, 135-140	70.62	4.15	2.88	1.27	24.0	0.13	0.15	9.77	8.46
9H-3, 115-118	78.49	1.42	0.35	1.07	2.9	0.12	0.88	8.91	1.21
10H-4, 25-26	87.96	2.83	0.51	2.32	4.2	0.24	1.21	9.66	1.92
10H-4, 54-55	88.25	4.76	0.09	4.67	0.7	0.36	1.55	13.00	3.01
10H-4, 74-75	88.45	5.58	0.97	4.61	8.1	0.36	1.76	12.80	2.62
10H-4, 75-76	88.46	5.60	1.52	4.08	12.7	0.32	1.29	12.70	3.16
10H-4, 85-86	88.56	5.14	0.32	4.82	2.7	0.40	1.71	12.00	2.82
10H-4, 91-92	88.62	3.26	0.32	2.94	2.7	0.28	1.62	10.50	1.81
14H-2, 116-120	125.56	3.37	2.14	1.23	17.8	0.37	1.28	3.32	0.96
14H-4, 39-41	127.79	2.56	1.34	1.22	11.2	0.28	1.60	4.36	0.76
14H-6, 65-67	131.05	3.13	0.43	2.70	3.6	0.48	1.33	5.62	2.03
14H-7, 133-136	133.23	1.89	0.83	1.06	6.9	0.15	0.14	7.06	7.57
14H-8, 65-67	134.05	1.57	0.68	0.89	5.7	0.30	1.55	2.90	0.57
15H-2, 109-111	135.15	3.13	0.19	2.94	1.6	0.46	1.73	6.39	1.70
15H-4, 74-76	137.80	2.53	0.86	1.67	7.2	0.34	12.41	4.91	0.13
15H-6, 74-76	140.80	2.86	1.03	1.83	8.6	0.44	1.30	4.16	1.41
15H-8, 75-80	143.81	2.85	0.85	2.00	7.1	0.23	1.45	8.69	1.38
16X-2, 45-50	144.55	3.29	1.54	1.75	12.8	0.22	1.13	7.95	1.55
16X-3, 0-5	144.78	3.32	1.47	1.85	12.3	0.21	0.55	8.81	3.36
16X-4, 48-53	146.43	3.46	1.66	1.80	13.8	0.21	0.78	8.57	2.31
16X-6, 34-39	149.29	2.78	1.18	1.60	9.8	0.19	1.04	8.42	1.54
17X-2, 0-5	152.92	2.86	1.12	1.74	9.3	0.19	0.44	9.16	3.95
17X-2, 48-54	153.40	3.12	1.36	1.76	11.3	0.21	0.96	8.38	1.83
17X-4, 28-35	156.20	2.81	1.13	1.68	9.4	0.22	1.05	7.63	1.60
17X-6, 39-44	159.31	2.75	1.18	1.57	9.8	0.20	1.20	7.85	1.31
18X-5, 149-150	169.21	3.16	1.39	1.77	11.6	0.19	0.98	9.31	1.80
18X-6, 25-30	169.47	1.12	0.16	0.96	1.3	0.14	1.04	6.80	0.92
19X-2, 60-65	173.70	2.91	1.24	1.67	10.3	0.19	0.76	8.79	2.20
19X-4, 50-55	176.60	2.41	0.20	2.21	1.7	0.22	1.26	10.00	1.75
19X-6, 60-65	179.70	1.94	0.69	1.25	5.7	0.18	1.05	6.94	1.19
20X-2, 40-45	182.52	1.71	0.59	1.12	4.9	0.15	0.92	7.46	1.22
20X-4, 103-108	185.67	2.28	0.73	1.55	6.1	0.20	1.24	7.75	1.25
20X-5, 60-65	186.74	1.96	0.85	1.11	7.1	0.15	0.83	7.40	1.34
21X-2, 45-48	192.26	1.65	0.28	1.37	2.3	0.16	0.23	8.56	5.95
21S-3, 59-61	193.90	1.80	0.37	1.43	3.1	0.18	1.29	7.94	1.11
21X-4, 39-44	194.75	1.45	0.23	1.22	1.9	0.17	1.28	7.17	0.95
21X-6, 19-24	197.55	2.11	0.47	1.64	3.9	0.18	0.95	9.11	1.72
21X-6, 59-64	197.95	1.39	0.40	0.99	3.3	0.35	1.08	2.80	0.92
21X-7, 0-5	198.86	2.49	0.98	1.51	8.2	0.16	0.62	9.44	2.43
22X-2, 30-35	202.40	2.74	0.07	2.67	0.6	0.54	1.24	4.94	2.15
22X-4, 17-22	205.09	3.17	0.07	3.10	0.6	0.30	1.53	10.30	2.02
22X-7, 42-47	208.69	2.56	0.16	2.40	1.3	0.26	1.30	9.23	1.84
23X-2, 25-29	211.88	2.06	0.85	1.21	7.1	0.55	1.04	2.20	1.16
23X-5, 120-125	216.88	1.86	0.26	1.60	2.2	0.20	1.29	8.00	1.24
23X-7, 60-65	219.13	2.83	0.12	2.71	1.0	0.28	1.16	9.68	2.33
24X-2, 49-54	221.99	3.01	0.07	2.94	0.6	0.27	1.53	10.90	1.92
24X-3, 0-5	223.00	3.11	0.08	3.03	0.7	0.30	1.26	10.10	2.40
24X-4, 49-54	224.99	2.33	0.06	2.27	0.5	0.25	1.52	9.08	1.49
24X-6, 43-48	227.93	2.89	0.08	2.81	0.7	0.28	1.88	10.00	1.49
25X-2, 68-73	231.88	1.65	0.19	1.46	1.6	0.21	1.24	6.95	1.18
25X-4, 63-67	234.83	1.91	0.14	1.77	1.2	0.20	1.27	8.85	1.39
27X-2, 38-43	250.75	1.88	0.18	1.70	1.5	0.20	1.50	8.50	1.13
27X-3, 115-118	252.69	2.44	0.07	2.37	0.6	0.22	0.39	10.80	6.07
27X-4, 0-5	253.04	1.89	0.08	1.81	0.7	0.18	1.38	10.00	1.31
27X-4, 15-20	253.19	1.87	0.11	1.76	0.9	0.20	1.54	8.80	1.14
27X-6, 95-100	256.89	1.64	0.18	1.46	1.5	0.18	1.41	8.11	1.03
28X-2, 0-5	260.20	2.70	0.09	2.61	0.8	0.23	0.90	11.30	2.90
28X-4, 31-35	263.21	2.18	0.09	2.09	0.7	0.20	1.38	10.40	1.51
28X-6, 27-33	265.40	1.88	0.09	1.79	0.7	0.20	1.16	8.95	1.54
29X-4, 30-35	272.64	2.91	0.10	2.81	0.8	0.28	1.12	10.00	2.51
29X-6, 35-40	275.43	2.74	0.14	2.60	1.2	0.27	1.07	9.63	2.43
30X-3, 0-5	280.04	1.55	0.16	1.39	1.3	0.19	1.92	7.31	0.72
31X-2, 0-5	287.10	2.10	0.05	2.05	0.4	0.20	0.93	10.20	2.20

Table 16 (continued).

Core, section, interval (cm)	Depth (mbsf)	Total carbon (%)	Inorganic carbon (%)	Organic carbon (%)	CaCO ₃ (%)	Nitrogen (%)	Sulfur (%)	OrgC/N	OrgC/S
31X-2, 30-35	287.40	1.89	0.10	1.79	0.8	0.17	0.54	10.50	3.31
31X-4, 55-60	290.65	1.03	0.05	0.98	0.4	0.17	1.02	5.70	0.96
31X-6, 30-35	293.40	2.12	0.08	2.04	0.7	0.19	1.35	10.70	1.51
31X-8, 30-35	296.21	2.52	0.10	2.42	0.8	0.23	1.32	10.50	1.83
32X-2, 40-45	297.90	1.62	0.06	1.56	0.5	0.17	0.90	9.17	1.73
32X-4, 70-75	300.93	1.38	0.11	1.27	0.9	0.15	1.02	8.46	1.24
32X-8, 60-64	304.84	1.65	0.32	1.33	2.7	0.29	1.44	4.58	0.92
33X-3, 110-115	309.35	1.98	0.06	1.92	0.5	0.21	1.28	9.14	1.50
33X-4, 60-65	310.35	1.84	0.03	1.81	0.3	0.20	0.75	9.05	2.41
33X-6, 30-35	313.05	2.04	0.09	1.95	0.8	0.22	1.18	8.86	1.65
34X-2, 84-89	317.64	1.74	0.09	1.65	0.7	0.22	1.13	7.50	1.46
34X-4, 5-10	319.39	1.79	0.09	1.70	0.7	0.21	1.12	8.09	1.52
34X-C, 24-29	321.39	1.69	0.13	1.56	1.1	2.21	1.34	0.71	1.16
35X-2, 15-19	326.65	1.35	0.16	1.19	1.3	0.20	1.52	5.95	0.78
35X-4, 40-45	329.90	2.51	0.60	1.91	5.0	0.21	1.38	9.09	1.38
35X-6, 60-65	333.10	1.63	0.09	1.54	0.7	0.18	1.43	8.55	1.07
35X-7, 13-18	334.13	2.47	0.53	1.94	4.4	0.39	1.79	4.97	1.08
36X-1, 80-82	335.40	1.81	0.25	1.56	2.1	0.19	1.76	8.21	0.89
36X-2, 20-22	336.30	1.74	0.25	1.49	2.1	0.16	0.96	9.31	1.55
36X-2, 75-78	336.85	1.51	0.26	1.25	2.2	0.14	0.58	8.93	2.15
36X-3, 14-16	337.74	1.66	0.28	1.38	2.3	0.17	1.40	8.12	0.99
37X-2, 46-48	346.26	1.62	0.32	1.30	2.7	0.16	1.82	8.12	0.71
38X-2, 40-42	355.80	1.57	0.15	1.42	1.3	0.18	1.23	7.89	1.15
38X-4, 31-33	358.71	2.02	0.10	1.92	0.8	0.20	1.24	9.60	1.55
38X-4, 140-150	359.80	1.53	0.07	1.46	0.6	0.15	1.16	9.73	1.26
38X-6, 58-60	361.98	1.89	0.24	1.65	2.0	0.20	1.42	8.25	1.16
38X-4, 85-87	368.95	1.72	0.19	1.53	1.6	0.18	1.29	8.50	1.18
39X-5, 0-5	369.60	1.46	0.18	1.28	1.5	0.34	1.18	3.76	1.08
39X-6, 127-129	372.09	1.36	0.22	1.14	1.8	0.14	0.91	8.14	1.25
40X-2, 23-25	374.93	1.89	0.09	1.80	0.8	0.19	1.48	9.47	1.21
40X-2, 70-73	375.40	1.99	0.08	1.91	0.7	0.18	0.49	10.60	3.90
40X-4, 140-144	377.84	2.09	0.04	2.05	0.3	0.39	1.79	5.25	1.14
40X-5, 31-33	378.25	2.34	0.09	2.25	0.8	0.20	1.38	11.20	1.63
41X-3, 60-65	386.40	1.95	0.08	1.87	0.7	0.19	1.48	9.84	1.26
41X-5, 61-66	389.11	1.78	0.18	1.60	1.5	0.19	1.66	8.42	0.96
41X-5, 75-77	389.25	0.79	0.10	0.69	0.8	0.09	0.52	7.60	1.30
41X-6, 31-33	390.31	2.54	0.12	2.42	1.0	0.19	1.24	12.70	1.95
42X-3, 20-25	394.65	1.50	0.18	1.32	1.5	0.14	0.66	9.43	2.00
42X-5, 135-140	398.80	1.62	0.41	1.21	3.4	0.15	1.16	8.06	1.04
42X-6, 75-77	399.70	1.29	0.23	1.06	1.9	0.11	0.4	9.63	2.41
42X-7, 19-24	400.64	1.21	0.17	1.04	1.4	0.14	1.06	7.43	0.98
42X-7, 88-90	401.33	1.42	0.26	1.16	2.2	0.11	0.23	10.50	5.04
43X-2, 80-85	404.50	1.46	0.41	1.05	3.4	0.14	0.78	7.50	1.34
43X-4, 50-55	407.20	0.85	0.09	0.76	0.8	0.11	1.21	6.90	0.63
43X-6, 20-25	409.90	1.61	0.24	1.37	2.0	0.13	1.01	10.50	1.35
44X-2, 40-45	413.70	0.64	0.13	0.51	1.1	0.13	0.51	3.90	1.00
44X-2, 70-71	414.00	0.27	0.05	0.22	0.4	0.19	0.03	1.10	7.30
44X-7, 50-55	419.64	1.04	0.14	0.90	1.2	0.12	0.61	7.50	1.50
45X-3, 70-73	424.85	1.00	0.08	0.92	0.7	0.10	0.35	9.20	2.60
45X-6, 120-125	429.45	1.80	0.20	1.60	1.7	0.17	0.90	9.41	1.78
45X-7, 31-33	430.06	1.53	0.21	1.32	1.7	0.17	0.90	7.76	1.46
46X-1, 50-52	431.60	1.63	0.08	1.55	0.7	0.16	1.61	9.69	0.96
46X-3, 110-112	434.48	1.11	0.10	1.01	0.8	0.14	0.90	7.21	1.12
46X-5, 43-45	436.81	1.42	0.06	1.36	0.5	0.14	1.19	9.71	1.14
47X-1, 0-5	440.80	1.48	0.06	1.42	0.5	0.39	1.69	3.64	0.84
47X-1, 26-28	441.06	2.02	0.12	1.90	1.0	0.16	0.70	11.90	2.71
47X-2, 7-9	441.20	1.54	0.07	1.47	0.6	0.16	1.15	9.19	1.28
47X-4, 44-46	444.57	1.44	0.16	1.28	1.3	0.16	1.55	8.00	0.83
47X-6, 80-82	447.93	1.74	0.15	1.59	1.3	0.16	1.88	9.94	0.85
47X-8, 0-5	450.13	1.02	0.38	0.64	3.2	0.30	1.26	2.10	0.51
47X-8, 5-10	450.18	1.10	0.11	0.99	0.9	0.16	0.86	6.20	1.10
48X-2, 0-5	451.90	1.28	0.09	1.19	0.8	0.11	0.82	10.80	1.45
48X-2, 21-23	452.11	1.52	0.10	1.42	0.8	0.15	1.46	9.46	0.97
48X-4, 62-64	455.52	1.70	0.14	1.56	1.2	0.15	1.66	10.40	0.94
48X-5, 97-99	457.37	1.56	0.25	1.31	2.1	0.14	1.09	9.36	1.20
48X-6, 0-5	457.90	1.45	0.16	1.29	1.3	0.14	1.38	9.21	0.94
49X-2, 110-112	462.70	1.09	0.15	0.94	1.3	0.15	1.16	6.20	0.81
49X-4, 112-114	465.72	0.77	0.18	0.59	1.5	0.10	0.81	5.90	0.73
49X-6, 110-112	468.70	1.18	0.20	0.98	1.7	0.14	1.35	7.00	0.73
49X-7, 50-55	469.60	1.04	0.16	0.88	1.3	0.12	1.28	7.30	0.69
50X-2, 110-112	472.30	1.09	0.08	1.01	0.7	0.12	1.66	8.41	0.61
50X-3, 145-150	474.15	1.43	0.13	1.30	1.1	0.14	1.43	9.28	0.91
51X-4, 0-5	483.90	1.83	0.16	1.67	1.3	0.29	1.57	5.76	1.06
51X-4, 108-110	484.98	1.75	0.20	1.55	1.7	0.15	1.16	10.30	1.33
51X-5, 21-23	485.61	1.67	0.21	1.46	1.8	0.14	1.90	10.40	0.77
51X-6, 86-88	487.76	1.71	0.28	1.43	2.3	0.16	1.33	8.94	1.07

Table 16 (continued).

Core, section, interval (cm)	Depth (mbsf)	Total carbon (%)	Inorganic carbon (%)	Organic carbon (%)	CaCO ₃ (%)	Nitrogen (%)	Sulfur (%)	OrgC/N	OrgC/S
52X-1, 0-5	489.00	1.10	0.20	0.90	1.7	0.26	1.38	3.40	0.65
52X-4, 94-96	494.44	2.89	0.24	2.65	2.0	0.23	1.43	11.50	1.85
52X-6, 40-42	496.90	3.45	0.12	3.33	1.0	0.26	1.48	12.80	2.25
53X-1, 0-5	498.70	2.68	0.39	2.29	3.3	0.20	1.24	11.40	1.84
53X-3, 0-5	501.70	3.58	0.05	3.53	0.4	0.39	2.11	9.05	1.67
53X-3, 11-12	501.81	0.33	0.02	0.31	0.2	5.62	1.70	0.06	0.18
53X-4, 50-53	503.70	4.18	0.05	4.13	0.4	0.29	2.87	14.20	1.44
53X-4, 56-58	503.76	3.94	0.02	3.92	0.2	0.27	3.01	14.50	1.30
54X-1, 54-56	508.84	4.21	0.11	4.10	0.9	0.29	2.16	14.10	1.90
54X-2, 56-58	510.06	2.80	0.10	2.70	0.8	0.19	1.11	14.20	2.43
54X-7, 131-133	513.81	4.97	0.07	4.90	0.6	0.32	2.28	15.30	2.15
54X-7, 0-5	517.00	2.83	0.21	2.62	1.7	0.33	1.90	7.94	1.38
54X-C, 0-5	518.75	3.67	0.32	3.35	2.7	0.35	1.58	9.57	2.12

Table 17. Concentrations of inorganic and organic carbon and total nitrogen and sulfur in sediments from Hole 798C.

Core, section, interval (cm)	Depth (mbsf)	Total carbon (%)	Inorganic carbon (%)	Organic carbon (%)	CaCO ₃ (%)	Nitrogen (%)	Sulfur (%)	OrgC/N	OrgC/S
128-798C-1H-2, 106-108	2.56	1.85	0.70	1.15	5.8	0.11	0.47	10.40	2.44
1H-4, 0-5	4.50	2.04	0.56	1.48	4.7	0.13	0.52	11.40	2.84
1H-4, 106-108	5.56	2.74	1.15	1.59	9.6	0.15	0.36	10.60	4.41
2H-2, 34-36	8.14	3.84	2.14	1.70	17.8	0.15	0.15	11.30	11.30
2H-4, 34-36	11.14	3.10	1.04	2.06	8.7	0.18	0.63	11.40	3.27
2H-6, 34-36	14.14	1.84	0.40	1.44	3.3	0.13	0.43	11.10	3.35
3H-2, 78-82	17.58	3.96	0.74	3.22	6.2	0.26	0.76	12.40	4.23
3H-4, 77-79	20.57	3.93	0.08	3.85	0.7	0.31	1.56	12.40	2.47
3H-6, 0-5	22.80	4.20	1.35	2.85	11.2	0.23	0.48	12.40	5.94
3H-6, 59-61	23.39	2.38	0.40	1.98	3.3	0.16	0.82	12.40	2.41
6H-1, 0-5	43.20	4.31	0.42	3.89	3.5	0.32	0.93	12.10	4.18
8H-2, 0-5	63.11	7.13	1.29	5.84	10.7	0.41	0.64	14.20	9.12
9H-1, 0-5	71.80	4.97	2.94	2.03	24.5	0.17	0.28	11.90	7.25
12H-1, 0-5	100.80	3.43	2.19	1.24	18.2	0.15	1.04	8.26	1.19

The climatic significance of variations in the SGR log is most probably tied to the ice volume and continental aridity connection described by Kukla et al. (1988). Based on a detailed marine oxygen-isotopic record, Ruddiman et al. (1989) and Raymo et al. (1989) demonstrated that Pliocene to late Pleistocene ice sheets varied predominantly during the 41-k.y. periodicity corresponding to orbital obliquity. Their data confirm previous studies indicating that late Neogene ice sheets expanded rapidly at 2.4 Ma and varied predominantly at 41 k.y. until approximately 0.7 Ma. After 0.7 Ma, the amplitude of ice-sheet variations increased and the dominant periodicity of variation shifted to 100 k.y. The SGR log of variations in terrigenous fractions suggests that the source of terrigenous supply varied in concert with the variations in ice volume throughout the 2.5- to 0.9-Ma interval. Based on the Pleistocene results of Kukla et al. (1988), the terrigenous source apparently is eolian dust from central Asia. Hence, the periodic increases in SGR most probably reflect variations in source area aridity and dust loading of the westerlies. Shore-based terrigenous extractions, granulometry and mineralogical analyses of the Hole 798B sediments, and comparison of these data with the physical and chemical logs will help to constrain the origin of this signal.

SEISMIC STRATIGRAPHY

Available Data

Proposed Site JS2 (Site 798) on Oki Ridge originally was located at Shot 2048 of a 12-channel seismic reflection profile

obtained by the Geological Survey of Japan (GSJ) during cruise GH-86-04 in 1986. Other seismic reflection records in the Oki Ridge area include the multichannel data collected by the Japan National Oil Company and single-channel records obtained by the GSJ (see "Background and Scientific Objectives" section, this chapter). In addition, a single-channel seismic reflection record in close proximity to Site 798 was among a series of profiles that were run at a spacing of 15 nmi in 1978 (Honza, 1979).

Single-channel, digital, seismic reflection profiling was conducted during the approach to Site 798 of *JOIDES Resolution*, both for locating the site and for obtaining a line across this site. Figure 94 presents the track of this survey together with the reflection profiles obtained. The final location of Site 798 corresponds to Shot 2036 of GSJ line GH-86-04.

Seismic Stratigraphy

Three seismic intervals above acoustic basement can be readily recognized in the line GH-86-04 profile (Figs. 95 and 96), including (1) a thin stratified unit at the top of the section, (2) a middle unit characterized by several strong individual reflectors, and (3) a lower, less reflective, less stratified unit. Figure 96 represents a scheme of the line GH-86-04 profile, highlighting the most distinctive seismic intervals at a more exaggerated vertical scale than the original record. Note that all reflectors are continuous across the sediment-filled basin on Oki Ridge. In addition, this record illustrates that the second or middle seismic unit can be subdivided into three additional intervals, so that altogether five distinctive seismic intervals can

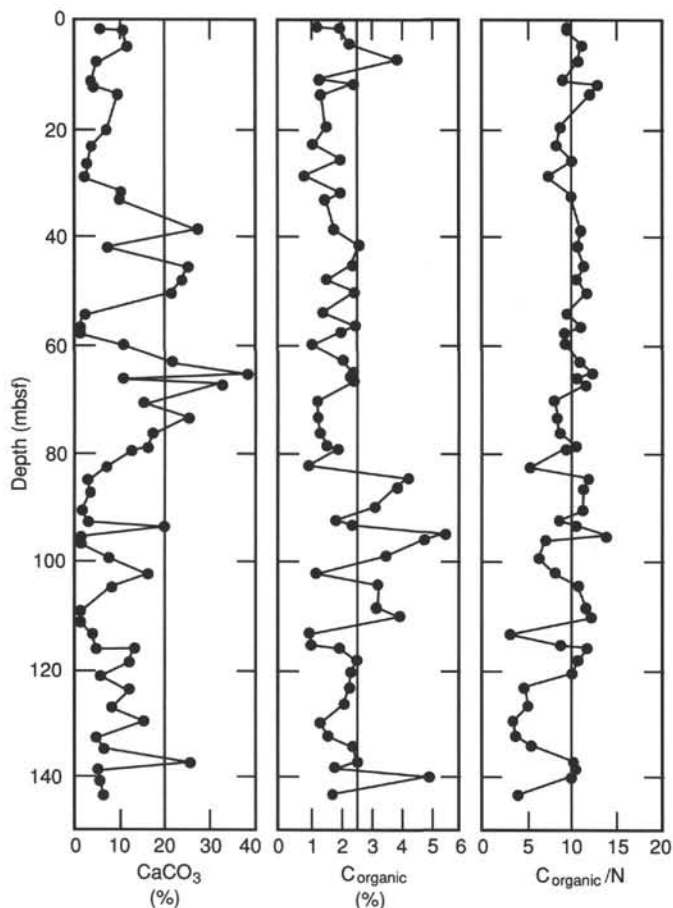


Figure 71. Carbonate, total organic carbon, and organic carbon/total nitrogen (C/N) ratios in sediments from Hole 798A.

be recognized in the sequence beneath Site 798 (Fig. 96). The single-channel seismic records obtained by the GSJ in 1978 (Honza, 1979) exhibit similar interval characteristics (Fig. 97).

Seismic Interval 1 is thin and represents about 0.1 s, expressed in two-way traveltimes (all subsequent references to time in this section also represent two-way traveltimes). This interval is best displayed in the 3.5-kHz record obtained during our *JOIDES Resolution* profiling survey conducted during the approach to the site (Fig. 98). Many of the reflectors displayed in this latter record can be firmly correlated with ash layers recovered at Site 798 (see "Lithostratigraphy" section, this chapter). Interval 1 varies little in thickness across the entire basin on Oki Ridge. Underlying Interval 2 is about 0.1 to 0.2 s thick, with the thickest portion of this interval on the southeast side of the basin, where acoustic basement also is deeper. Seismic Interval 3 is less reflective, but displays slight indications of deformation. The thickness of Interval 3 varies between 0.2 and 0.3 s and also increases in thickness toward the southeast and the basin margin. This latter interval includes some discontinuous reflectors. Interval 4 shows less deformation and is bounded by two very reflective horizons on the line GH-86-04 seismic record. This interval is about 0.2 s thick and shows only slight thickening toward the southeast. Interval 5 is transparent and exhibits great changes in apparent thickness; it is about 0.2 s thick directly beneath Site 798 (Fig. 96).

Single-channel, water-gun (80 in.³ × 2) records obtained during our approach to Site 798 are shown in Figures 99 and

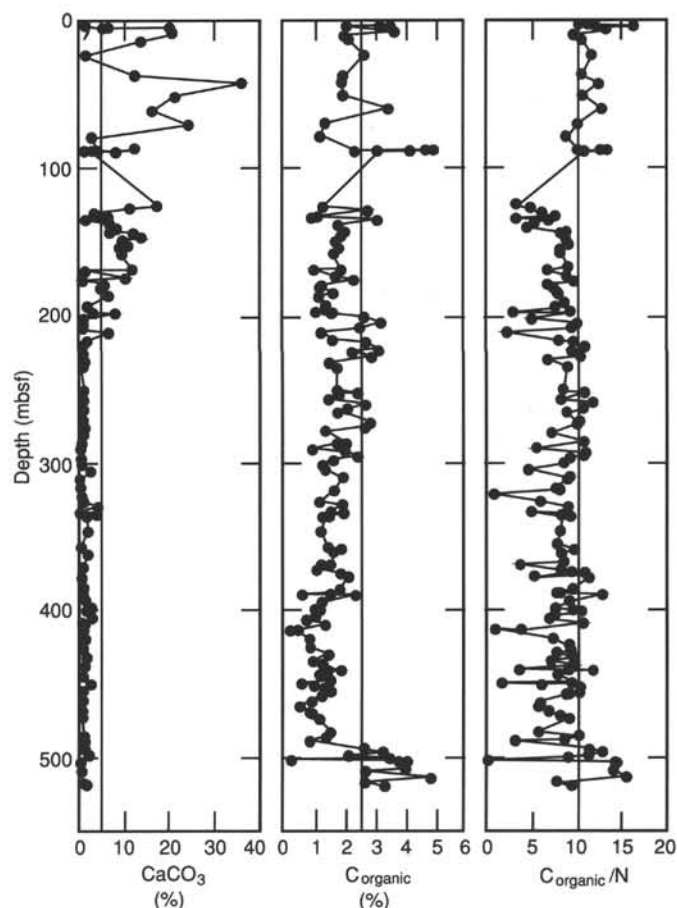


Figure 72. Carbonate, total organic carbon, and organic carbon/total nitrogen (C/N) ratios in sediments from Hole 798B.

100. Interestingly, the entire sediment section appears reflective in these records. However, it is possible to correlate these records with the five seismic intervals recognized in the older GSJ records using the deformational character of lower intervals and distinctive individual reflectors (Fig. 101).

Correlation of Seismic Stratigraphy With Lithology of Site 798

Figure 101 summarizes the seismic reflection record within the Oki Ridge Basin and correlates the seismic record with lithology, logging, and other characteristics measured at Site 798. The log of sonic traveltimes shows that seismic velocity increases linearly from about 1.6 km/s at 80 mbsf to 1.9 km/s at 330 mbsf, with a number of distinct spikes correlative with ash and dolomitic layers within this sequence. The largest spike of all occurs at 334 mbsf, which also corresponds to a 1-m-thick resistivity anomaly in the FMS record (see "Downhole Measurements" section, this chapter). The dolomite nodule recovered from Hole 798B may be correlated with this. Velocity increases with a larger gradient and additional spikes reaching 2.3 km/s at the bottom of the section. The opal-A/opal-CT boundary occurs at about 450 mbsf and is accompanied by other changes in lithology and physical properties.

Seismic Interval 1 represents sediments in which porosity and wet-bulk density increase. Logging data are absent for most of this interval. Interval 2 may not correlate with any major changes in other parameters, although sonic velocity and the percentage of diatom ooze increase within this interval. The highly reflective nature of Interval 3 can be correlated

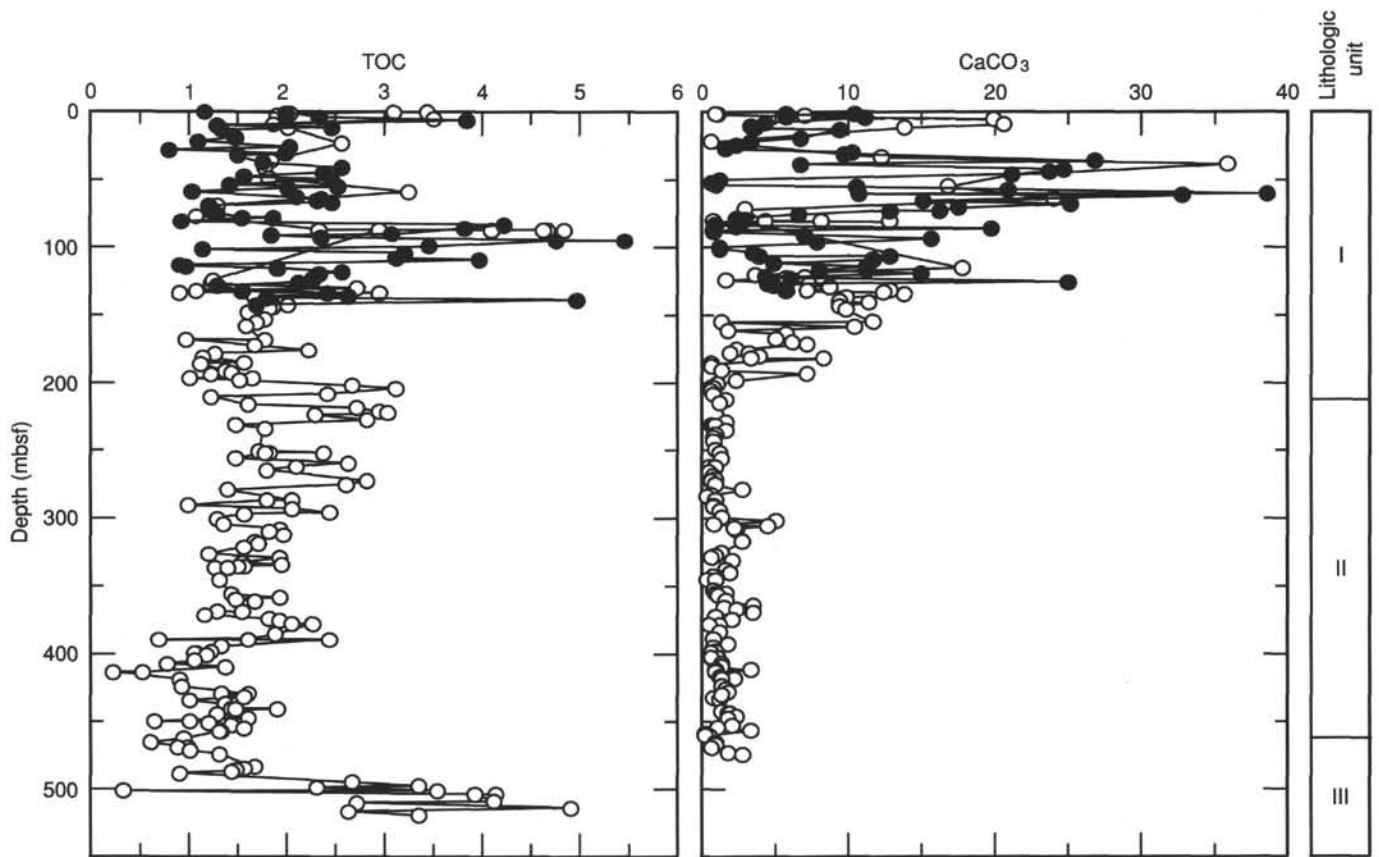


Figure 73. Total organic carbon and carbonate contents in sediments from Site 798 (combined record of Figs. 71 and 72). The position of lithologic units is shown for comparison.

with velocity spikes in the sonic log, although porosity and density remain more or less constant within this depth range. Interval 4 is bounded by the strongest individual reflectors recorded at Site 798, which in turn correspond to the largest spikes in the sonic log. The upper reflector of Interval 4 marks the dolomitic horizon (see "Downhole Measurements" section, this chapter). The lower reflector in this interval probably correlates with the spikes of the sonic log at about 420 mbsf. The opal-A/opal-CT boundary occurs below this latter horizon, with less dramatic changes in physical properties than those accompanying Interval 4. The upper part of Interval 5 corresponds to siliceous claystone.

CONCLUSIONS

Introduction

One of our primary goals for drilling in the Sea of Japan was to reconstruct the paleoceanographic history of the sea as it evolved from a proto-back-arc basin to its modern configuration marked by oceanic water depths (>3500 m) and shallow sills (<150 m). Previous studies of onshore sequences and cores from the Sea of Japan demonstrate that this sea has experienced a complex history, with local tectonic events and global evolution of Neogene climate forcing major changes in the structure of water mass, in circulation, and in productivity. Site 798 (proposed Site JS2) on Oki Ridge was aimed specifically at obtaining a Miocene to Holocene paleoceanographic reference section for the eastern Sea of Japan—the only site so targeted for drilling during Legs 127 and 128. We accomplished a major share of our paleoceanographic objectives at Site 798 in that we recovered an excellent late early

Pliocene through Holocene sequence in hemipelagic-pelagic sediments rich in siliceous and calcareous plankton. However, a rapid increase in hydrocarbon gases in Hole 798B caused us to halt drilling at Site 798 at a depth of 517.9 mbsf prior to penetration of Miocene strata. We estimate that the average rate of sedimentation for the Site 798 sequence was 120 m/m.y., emphasizing the expanded Pliocene-Pleistocene record contained in these sediments. A detailed summary of results at Site 798 is presented in the "Principal Results" section (this chapter). Here, we highlight three of our principal findings with regard to the tectonic, paleoceanographic, and volcanic history of this site.

Depositional History and Possible Quaternary Faulting of Oki Ridge

The 517.9 m of late early Pliocene through Holocene sediments cored at Site 798 can be conveniently divided into three lithologic units. Unit I consists of uppermost Pliocene to Holocene clays, silty clays, volcanic ashes, diatomaceous clays, and oozes, and displays high-frequency laminated/bioturbated depositional cycles. Unit II is formed of upper Pliocene bioturbated diatomaceous and silty clays; Unit III is composed of upper to upper lower Pliocene carbonate-poor siliceous claystone with volcanic ashes and glauconitic and quartz sands. Significantly, modern Oki Ridge is topographically isolated from the coarse terrigenous sediments rapidly filling the surrounding basins and troughs via gravity-flow processes. The terrigenous claystones and redeposited sands of Unit III thus suggest that these sediments may have accumulated prior to uplift of the present-day Oki Ridge. In addition, the absence of sands and decreasing terrigenous clays in Unit II and the abundance of

Table 18. Results of Rock-Eval pyrolysis of sediments from Site 798.

Core, section, interval (cm)	Depth (mbsf)	S ₁ (mg/g)	S ₂ (mg/g)	S ₃ (mg/g)	TOC (%)	PC	HI	OI	T _{max} (°C)	PI	S ₂ /S ₃
128-798A-1H-2, 46-51	1.96	0.89	4.12	6.43	1.67	0.41	246	385	394	0.18	0.64
1H-3, 37-39	3.37	0.59	3.05	6.88	1.16	0.30	262	593	411	0.16	0.44
1H-4, 38-45	4.88	0.98	4.78	8.60	1.90	0.48	251	452	403	0.17	0.55
1H-6, 38-44	7.88	1.28	11.68	10.30	3.64	1.08	320	282	398	0.10	1.13
2H-2, 46-51	11.26	0.35	2.65	3.62	1.12	0.25	236	323	392	0.12	0.73
2H-3, 46-48	12.76	0.22	1.56	4.23	1.04	0.14	150	406	416	0.12	0.36
2H-4, 4-9	13.84	0.21	1.24	3.59	0.91	0.12	136	394	395	0.15	0.34
3H-2, 50-54	20.30	0.49	2.73	4.48	1.40	0.26	195	320	408	0.15	0.60
3H-3, 49-51	21.79	0.59	4.54	4.44	1.89	0.42	240	234	400	0.12	1.02
3H-4, 50-54	23.30	0.30	1.87	1.91	0.94	0.18	198	203	413	0.14	0.97
3H-6, 50-54	26.30	0.67	5.65	4.20	1.82	0.52	310	230	403	0.11	1.34
4H-2, 29-31	29.09	0.15	1.67	0.86	0.77	0.15	216	111	473	0.08	1.94
4H-3, 29-31	30.59	0.38	2.04	2.63	1.01	0.20	201	260	405	0.16	0.77
4H-4, 59-61	32.39	0.78	6.42	6.72	1.84	0.60	348	365	407	0.11	0.95
5H-2, 80-82	39.00	0.37	3.14	7.32	1.16	0.29	270	631	417	0.11	0.42
5H-3, 49-51	40.19	1.07	7.87	10.78	2.69	0.74	292	400	412	0.12	0.73
5H-4, 86-88	42.06	0.82	6.12	6.97	2.34	0.57	261	297	413	0.12	0.87
5H-7, 7-9	45.77	0.78	6.25	10.15	2.00	0.58	312	507	416	0.11	0.61
6H-2, 49-54	48.19	0.40	2.33	7.35	1.18	0.22	197	622	410	0.15	0.31
6H-3, 46-48	49.66	0.74	3.61	8.63	1.77	0.36	203	487	409	0.17	0.41
6H-4, 4-9	50.74	0.83	6.46	9.11	2.13	0.60	303	427	411	0.11	0.70
6H-6, 84-89	54.54	0.41	4.05	1.19	1.35	0.37	300	88	394	0.09	3.40
7H-2, 130-135	58.14	0.88	7.19	3.59	1.95	0.67	368	184	397	0.11	2.00
7H-3, 51-53	58.85	1.12	11.90	5.96	3.10	1.08	383	192	408	0.09	1.99
7H-4, 50-55	60.34	0.25	1.18	3.01	0.82	0.11	143	367	391	0.18	0.39
7H-6, 65-70	63.49	0.00	0.00	7.42	1.40	0.00	0	530	381		0.00
7H-8, 55-60	66.39	0.71	6.28	6.69	2.19	0.58	286	305	411	0.10	0.93
8H-3, 32-34	67.42	0.96	6.21	10.03	2.12	0.59	292	473	405	0.13	0.61
8H-5, 61-63	70.71	0.45	1.95	5.99	0.74	0.20	263	809	402	0.19	0.32
8H-7, 64-66	73.74	0.35	2.35	6.22	0.22	0.22	1068	2827	408	0.13	0.37
9H-2, 29-31	76.59	0.35	1.75	5.27	0.17	0.17	1029	3100	401	0.17	0.33
9H-4, 54-56	79.84	0.49	4.30	7.34	1.53	0.39	281	479	413	0.10	0.58
9H-6, 53-58	82.83	0.48	2.44	4.80	1.00	0.24	244	480	402	0.16	0.50
10H-3, 40-45	86.92	1.74	15.06	8.19	4.07	1.40	370	201	408	0.10	1.83
10H-5, 103-108	90.55	1.48	14.03	5.81	2.36	1.29	594	246	404	0.10	2.41
10H-7, 20-25	92.72	0.57	4.85	3.94	1.46	0.45	332	269	405	0.11	1.23
10H-7, 128-133	93.80	0.71	6.19	7.90	1.59	0.57	389	496	413	0.10	0.78
12H-2, 30-35	104.87	1.05	10.47	8.01	2.35	0.96	445	340	410	0.09	1.30
12H-6, 25-30	110.82	1.38	16.68	6.71	3.36	1.50	496	199	406	0.08	2.48
13H-2, 98-103	115.88	0.11	1.06	1.50	0.62	0.09	170	241	416	0.09	0.70
13H-4, 74-79	118.64	0.64	7.08	7.40	1.46	0.64	484	506	411	0.08	0.95
13H-6, 20-25	121.10	0.73	6.83	5.61	2.05	0.63	333	273	412	0.10	1.21
128-798B-47X-8, 5-10	450.18	0.29	3.77	0.00	0.33	0.33	1142	0	404	0.07	
52X-1, 0-5	489.00	0.13	3.12	0.00	0.26	0.27	1200	0	409	0.04	
53X-1, 0-5	498.70	0.33	12.43	0.73	1.05	1.06	1183	69	417	0.03	17.02
53X-3, 0-5	501.70	0.54	14.33	0.69	1.23	1.23	1165	56	413	0.04	20.76
54X-7, 0-5	517.00	0.37	9.93	0.78	0.85	0.85	1168	91	409	0.04	12.73
54X-CC, 0-5	518.75	0.00	0.00	1.23	0.00	0.00	0	0	417	90.00	0.00

HI = hydrogen index; OI = oxygen index; PI = production index.

Note: Hydrogen and oxygen indexes were calculated using TOC data derived from Rock-Eval analysis. HI and OI values based on TOC data determined by difference (TC - IC) and listed in Table 19, are shown in Figure 75.

diatoms and common occurrence of biogenic carbonate in Unit I argue for increasing isolation and uplift of Oki Ridge above the CCD, sometime during latest Pliocene to early Pleistocene time. Alternatively, carbonate-poor sediments may simply represent a shallow excursion of the CCD.

Although no significant hiatus is apparent in the Site 798 section, widespread evidence does support a major late Pliocene-early Pleistocene episode of tectonic deformation in the eastern Sea of Japan. This event clearly is manifested by a ubiquitous unconformity separating deformed pre-late Pleistocene strata from younger, relatively undeformed sediments and can be readily identified in onshore sections and in offshore reflection profiles. Reflection profiles clearly depict this feature within the insular shelf areas of Honshu due east of Oki Ridge (Tamaki et al., 1981; Tamaki, 1988), with Pliocene strata folded and faulted on the Oki Islands to the southwest of Site 798. The widespread nature of this unconformity points to significant tectonic reorganization of the eastern and southern Sea of Japan

about 2 to 1 Ma, marked by faulting of many of the ridges and banks in this region including areas surrounding Oki Ridge and possibly involving the ridge proper.

Cyclic Deposits and Quaternary Paleocyanography

The most distinctive lithology in the stratigraphic column at Site 798 is the series of latest Pliocene through Pleistocene depositional cycles that involve high-frequency alternations of two fundamentally different lithofacies. Although these cycles initially appear in upper lower Pliocene sediments, they do not become common until 1.5 Ma and are best developed during the last 0.4 m.y. Each depositional couplet in this series consists of (1) a dark, laminated diatomaceous unit rich in organic matter (about 5%), abundant diatoms, and low amounts of terrigenous clay and (2) a light-colored, intensely bioturbated to homogeneous unit containing abundant terrigenous clay and relatively low amounts of organic matter. Although the thickness of the cycles varies, the vertical lithologic variation within individual

Table 19. Hydrogen and oxygen index values based on TOC data.

Core, section, interval (cm)	HI	OI
128-798A-1H-2, 46	209	326
1H-4, 38	206	372
1H-6, 38	304	268
2H-2, 46	208	285
2H-4, 04	94	272
3H-2, 50	186	305
3H-4, 50	172	177
4H-2, 29	211	108
4H-4, 59	325	341
5H-2, 80	179	418
5H-4, 86	239	271
5H-7, 07	76	124
6H-2, 49	149	470
6H-3, 46	265	373
6H-6, 84	289	85
7H-2, 130	809	405
7H-4, 50	120	307
8H-3, 32	253	411
8H-5, 61	162	499
8H-7, 64	191	380
9H-2, 29	137	412
9H-4, 54	231	394
9H-6, 53	268	437
10H-3, 40	1167	644
10H-5, 103	458	190
10H-7, 20	268	217
10H-7, 128	263	335
12H-2, 30	328	250
12H-6, 25	421	169
13H-2, 98	110	156
13H-4, 74	276	289
128-798B-47X-8, 5	589	0
52X-1, 0	347	0
53X-1, 0	542	31
53X-3, 0	406	20
54X-7, 0	378	30

Note: TOC data determined from difference (TC - IC).

couplets is remarkably constant. A sharp but non-erosional boundary is commonly present at the base of laminated units, signaling the abrupt initiation of each depositional cycle.

These cycles clearly reflect systematic paleoceanographic changes in the Sea of Japan during late Pliocene-Quaternary time and involve major variations in productivity of surface water, in bottom-water oxygen levels, and in deposition of terrigenous clays. Severe reductions in dissolved oxygen of bottom waters probably are responsible for deposition of the laminated organic-rich units, with the overlying bioturbated-to-massive units suggestive of increasing levels of oxygen under fully oxic conditions during the final phase of each cycle. Changes in the relative abundances among diatoms, calcareous nannofossils, and planktonic foraminifers in these sediments likely reflect changes in productivity and/or dilution by terrigenous clays. Rhythmic variations in the abundance of terrigenous clays probably represent changes in the availability of river-borne suspensates and/or eolian transport of these sediments. In fact, preliminary analysis of cyclic patterns in the natural gamma-ray log through a portion of these sediments (2.5–0.9 Ma) suggests that pulses in the flux of terrigenous clays to this site have a periodicity of ca. 40 k.y.—near the 41 k.y. of Earth's orbital tilt, which is thought to be a major factor controlling Pliocene-Pleistocene climate. Whatever the origins of these depositional cycles, they call for repeated and profound changes in the oceanographic, geochemical, and sedimentologic character of the Sea of Japan on relatively short time scales. In particular, evidence

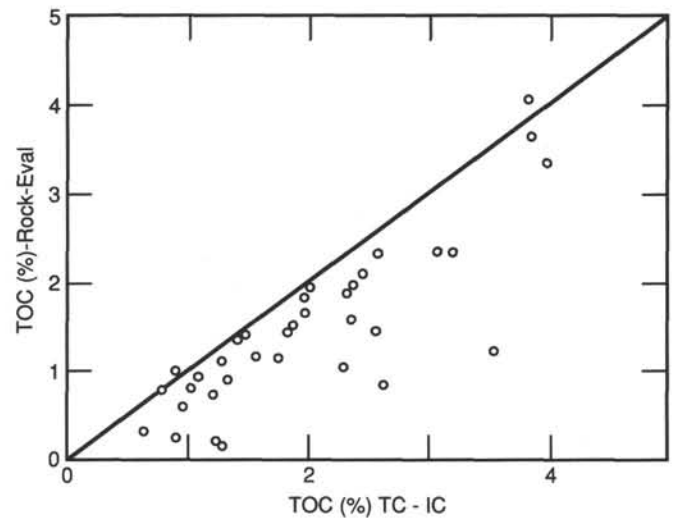


Figure 74. Correlation between total organic carbon content obtained by Rock-Eval pyrolysis and total organic carbon contents obtained by difference (TC—IC). See text for explanation.

for repetitive suboxic to near-anoxic bottom conditions stands in stark contrast to the modern hyperventilated and fully oxic character of the modern Sea of Japan.

The rhythmic lithofacies so evident in Site 798 cores have also been reported in late Pleistocene piston cores and Leg 127 sites elsewhere in the Sea of Japan, indicating basinwide control of the processes governing these patterns. Some scientists have suggested repeated Quaternary eustatic isolation and reconnection of the Sea of Japan with the open Pacific as a possible mechanism producing these cycles. We reserve judgment on this suggested origin until completion of our detailed studies. However, we point to the fact that similar depositional cycles are present in lower Pliocene sediments at Site 798, representing a time when global climate and paleogeography of the Sea of Japan surely were different than during the late Quaternary.

Tephrochronology and Pliocene-Pleistocene Volcanic History

The sediment sequence at Site 798 contains 113 discrete volcanic ash beds that, together with the well-constrained sedimentation curve at this site, offer a detailed record of explosive volcanic events in this region over the past 3.5 to 4 Ma. Indeed, the age of each ash layer was extrapolated using

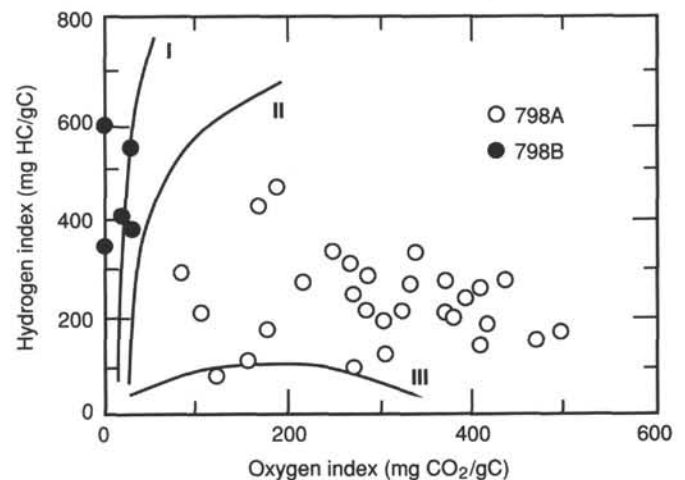


Figure 75. Hydrogen index vs. oxygen index ("van Krevelen diagram") of organic matter at Site 798 (data from Table 18).

Table 20. Index properties for Hole 798A.

Core, section, interval (cm)	Depth (mbsf)	Wet-bulk density (g/cm ³)	Dry-bulk density (g/cm ³)	Grain density (g/cm ³)	Porosity (%)	Wet water content (%)	Dry water content (%)	Void ratio
128-798A-1H-1, 39-41	0.39	1.42	0.69	2.37	71.1	51.2	104.9	2.42
1H-2, 36-39	1.86	1.46	0.65	2.64	76.6	55.5	124.6	3.21
1H-2, 46-51	1.96	1.46	0.65	2.64	76.6	55.5	124.6	3.21
1H-3, 37-39	3.37	1.44	0.64	2.64	76.5	55.3	123.9	3.20
1H-4, 38-45	4.88	1.46	0.68	2.64	75.0	53.4	114.6	2.95
1H-5, 38-40	6.38	1.43	0.66	2.54	74.8	54.0	117.5	2.91
1H-6, 38-44	7.88	1.35	0.64	2.09	69.7	52.5	110.6	2.26
2H-1, 45-47	9.75	1.33	0.65	1.97	67.2	51.1	104.5	2.01
2H-2, 46-51	11.26	1.42	0.74	2.17	66.3	47.7	91.3	1.94
2H-3, 46-47	12.76	1.51	0.83	2.45	66.7	45.2	82.5	1.97
2H-4, 4-9	13.84	1.53	0.81	2.62	70.1	47.5	90.5	2.32
3H-1, 70-72	19.00	1.35	0.51	2.55	80.6	62.1	163.8	4.08
3H-2, 49-51	20.29	1.53	0.78	2.68	72.0	49.2	96.9	2.54
3H-3, 49-51	21.79	1.46	0.70	2.57	73.5	52.1	108.8	2.73
3H-4, 49-51	23.29	1.54	0.80	2.67	71.0	48.2	92.9	2.42
3H-5, 49-51	24.79	1.41	0.62	2.46	75.7	56.0	127.5	3.06
3H-6, 49-51	26.29	1.52	0.76	2.61	71.8	49.7	98.7	2.51
4H-1, 29-31	27.59	1.48	0.70	2.63	74.3	52.5	110.6	2.84
4H-2, 29-31	29.09	1.58	0.88	2.69	68.0	44.4	79.9	2.10
4H-3, 29-31	30.59	1.57	0.84	2.69	70.0	46.7	87.6	2.30
4H-4, 59-61	32.39	1.59	0.83	2.98	72.9	47.7	91.1	2.65
4H-5, 59-61	33.89	1.57	0.84	2.63	69.1	46.3	86.2	2.21
5H-1, 94-96	37.64	1.50	0.74	2.61	72.6	50.6	102.3	2.61
5H-2, 80-82	39.00	1.58	0.86	2.63	68.5	45.5	83.6	2.15
5H-3, 49-51	40.19	1.49	0.73	2.56	72.8	51.3	105.3	2.63
5H-4, 86-88	42.06	1.47	0.71	2.32	71.3	51.9	107.9	2.45
5H-6, 34-36	44.54	1.57	0.82	2.73	71.1	47.6	91.0	2.43
5H-7, 7-9	45.77	1.51	0.78	2.55	70.4	48.4	94.0	2.34
6H-1, 58-60	46.78	1.54	0.81	2.59	69.9	47.6	90.7	2.29
6H-2, 49-54	48.19	1.56	0.83	2.66	69.9	46.9	88.3	2.29
6H-3, 46-48	49.66	1.56	0.83	2.73	70.4	46.8	88.1	2.34
6H-4, 4-9	50.74	1.53	0.79	2.91	73.2	48.7	94.9	2.69
6H-5, 69-71	52.89	1.56	0.83	2.72	70.6	47.2	89.3	2.37
6H-6, 84-89	54.54	1.55	0.83	2.60	69.2	46.7	87.5	2.22
6H-7, 4-6	55.24	1.53	0.79	2.65	71.1	48.4	93.8	2.42
7H-1, 49-51	56.19	1.49	0.75	2.70	72.7	49.8	99.3	2.62
7H-2, 130-135	58.14	1.49	0.73	2.66	73.4	51.1	104.6	2.72
7H-3, 51-53	58.85	1.46	0.69	2.54	73.4	52.3	109.5	2.71
7H-4, 50-55	60.34	1.62	0.92	2.83	68.0	43.2	76.0	2.10
7H-5, 50-52	61.84	1.49	0.74	2.44	71.2	50.5	102.1	2.43
7H-6, 65-70	63.49	1.53	0.81	2.61	69.6	47.0	88.6	2.26
7H-7, 49-51	64.83	1.49	0.75	2.70	72.7	49.8	99.3	2.62
7H-7, 66-68	65.00	1.51	0.78	2.55	70.3	48.4	93.7	2.33
7H-8, 55-60	66.39	1.52	0.79	2.60	70.2	47.7	91.4	2.32
8H-2, 61-63	66.21	1.63	0.93	2.84	68.0	43.2	76.0	2.10
8H-3, 32-34	67.42	1.53	0.78	2.63	71.5	49.0	96.2	2.47
8H-4, 78-80	69.38	1.49	0.74	2.61	72.4	50.4	101.6	2.59
8H-5, 61-63	70.71	1.57	0.86	2.65	68.5	45.3	82.8	2.14
8H-5, 61-93	70.71	1.57	0.86	2.65	68.5	45.3	82.8	2.14
8H-6, 37-39	71.97	1.55	0.83	2.81	70.6	46.3	86.3	2.37
8H-7, 64-66	73.74	1.60	0.88	2.71	68.6	44.8	81.3	2.15
8H-8, 44-46	75.04	1.53	0.79	2.70	71.4	48.3	93.4	2.46
9H-1, 54-56	75.34	1.65	0.97	2.69	64.8	41.0	69.4	1.82
9H-2, 29-31	76.59	1.61	0.90	2.73	67.8	43.8	78.0	2.08
9H-3, 54-56	78.34	1.34	0.86	2.71	59.5	35.5	55.0	1.46
9H-4, 54-56	79.84	1.47	0.71	2.57	73.1	51.6	106.7	2.67
9H-5, 53-55	81.33	1.53	0.79	2.62	71.1	48.7	94.8	2.42
9H-6, 53-58	82.83	1.50	0.75	2.58	71.9	50.0	100.2	2.52
9H-7, 53-55	84.33	1.47	0.70	2.51	73.0	52.1	108.6	2.66
10H-1, 20-25	84.60	1.49	0.73	2.57	72.6	51.0	104.1	2.61
10H-2, 34-36	85.36	1.46	0.71	3.02	76.1	51.6	106.8	3.14
10H-3, 40-45	86.92	1.44	0.68	2.46	73.4	53.1	113.2	2.71
10H-4, 44-46	88.46	1.55	0.83	2.61	69.1	46.4	86.5	2.21
10H-5, 103-108	90.55	1.45	0.67	2.55	74.8	54.0	117.6	2.92
10H-6, 45-47	91.47	1.47	0.71	2.52	72.7	51.6	106.7	2.62
10H-7, 128-133	93.80	1.56	0.85	2.61	68.3	45.6	83.7	2.13
10H-8, 63-65	94.65	1.60	0.90	3.08	70.4	43.9	78.2	2.35
11H-1, 132-134	95.42	1.37	0.56	2.43	77.6	59.0	143.8	3.40
11H-2, 80-85	96.40	1.47	0.71	2.49	72.9	52.1	109.0	2.65
11H-3, 45-47	97.55	1.58	0.86	2.72	69.2	45.5	83.5	2.22
11H-4, 86-91	99.46	1.47	0.69	2.55	74.0	53.0	112.7	2.80
11H-5, 40-42	100.50	1.51	0.77	2.51	70.6	49.1	96.6	2.37
11H-6, 102-107	102.62	1.65	0.95	2.75	66.6	42.3	73.3	1.97
11H-7, 16-18	103.26	1.61	0.89	2.74	68.6	44.6	80.6	2.16
12H-1, 30-32	104.10	1.50	0.73	2.64	73.3	51.3	105.2	2.71
12H-2, 30-35	104.87	1.49	0.74	2.57	72.2	50.5	102.0	2.56

Table 20 (continued).

Core, section, interval (cm)	Depth (mbsf)	Wet-bulk density (g/cm ³)	Dry-bulk density (g/cm ³)	Grain density (g/cm ³)	Porosity (%)	Wet water content (%)	Dry water content (%)	Void ratio
12H-3, 86-88	106.93	1.41	0.63	2.53	75.6	55.2	123.3	3.04
12H-4, 30-35	107.87	1.44	0.66	2.75	76.2	54.1	117.7	3.16
12H-5, 30-32	109.37	1.46	0.68	2.43	73.1	53.0	112.8	2.67
12H-6, 25-30	110.82	1.44	0.67	2.48	73.9	53.6	115.3	2.79
12H-7, 110-112	113.17	1.64	0.93	2.75	67.6	43.4	76.6	2.06
12H-8, 30-35	113.87	1.65	0.94	2.83	67.6	42.7	74.6	2.07
13H-1, 19-21	113.59	1.47	0.71	2.66	73.6	51.4	105.6	2.74
13H-2, 98-103	115.88	1.74	1.11	2.75	60.7	36.3	56.9	1.53
13H-3, 50-52	116.90	1.64	0.94	2.72	66.5	42.6	74.1	1.96
13H-4, 74-79	118.64	1.56	0.81	2.82	72.1	48.1	92.5	2.55
13H-5, 51-53	119.91	1.47	0.71	2.52	72.7	51.6	106.6	2.62
13H-6, 20-25	121.10	1.50	0.72	2.54	73.0	51.8	107.5	2.66
13H-7, 45-47	122.85	1.61	0.90	2.82	69.1	44.5	80.1	2.20
14H-1, 21-23	123.31	1.44	0.70	1.96	67.2	51.2	105.0	2.01
14H-2, 30-35	123.81	1.51	0.76	2.55	71.3	49.5	98.0	2.44
14H-3, 70-72	125.71	1.51	0.74	2.63	73.2	51.1	104.5	2.69
14H-4, 62-67	127.13	1.59	0.86	2.63	69.0	46.0	85.3	2.19
14H-5, 49-51	128.50	1.64	0.96	2.84	66.7	41.7	71.5	1.98
14H-6, 49-54	130.00	1.61	0.92	2.73	67.2	43.2	76.0	2.03
14H-7, 22-24	131.23	1.51	0.78	2.68	71.5	48.5	94.4	2.47
14H-8, 22-27	132.73	1.48	0.69	2.72	75.7	53.6	115.5	3.06
15H-1, 30-32	133.10	1.57	0.86	2.75	69.3	45.4	83.1	2.23
15H-2, 35-40	134.55	1.45	0.68	2.56	74.3	53.2	113.9	2.85
15H-3, 30-32	136.00	1.48	0.73	2.62	72.6	50.6	102.3	2.61
15H-4, 30-35	137.50	1.45	0.68	2.52	73.9	53.1	113.3	2.79
15H-5, 30-32	139.00	1.60	0.93	2.74	66.1	41.9	72.1	1.93
15H-6, 15-20	140.35	1.58	0.87	2.71	68.7	45.0	81.9	2.17
15H-7, 30-32	142.00	1.42	0.62	2.54	76.3	56.1	127.9	3.17
15H-8, 30-35	143.50	1.39	0.60	2.39	75.9	56.9	132.2	3.08

this curve and associated paleomagnetic datums. Variations in the frequency, thickness, and petrology of these ashes provide details of the volcanic activity and a guide to their origin. The first important activity recorded in this section is represented by Pliocene ashes deposited between 4.0 and 3.5 Ma, followed by a gap in the occurrence of ashes in late Pliocene sediments. Moderate activity is indicated by the reappearance of ashes beginning at 2.5 Ma and continuing through 1.3 Ma. The frequency of ashes increases dramatically in lower Pleistocene sediments, with numerous ashes deposited between 1.3 and 0.9 Ma, followed by a major pulse of explosive activity and ash deposition between 0.9 and 0.3 Ma. This paroxysmal explosive activity apparently occurred between 0.7 and 0.55 Ma. Based upon composition and thickness, the most likely sources for the various ashes present at Site 798 are the large acidic-to-intermediate and calc-alkaline volcanoes of the southwestern Japan Arc (Izu, Kyushu, etc.) and the north-eastern Japan Arc (Tohoku). Alkaline volcanic islands near Site 798, including Oki-Dogo and Ulleung-Do, may also have contributed to this record. The youngest ashes present in the Site 798 sequence may correlate with established Holocene tephra markers in the southern Sea of Japan, although actual correlations and age assignments must await post-cruise chemical analysis.

REFERENCES

- Arai, F., Oba, T., Kitazato, H., Horibe, Y., and Machida, H., 1981. Late Quaternary tephrochronology and paleoceanography of the sediments of the Japan Sea. *Quat. Res.*, 20:209-230.
- Arthur, M. A., Dean, W. E., and Stow, D.A.V., 1984. Models for the deposition of Mesozoic-Cenozoic fine-grained organic-carbon-rich sediments in the deep sea. In Stow, D.A.V., and Piper, D.J.W. (Eds.), *Fine-Grained Sediments: Deep-Water Processes and Facies*. Geol. Soc. London, Spec. Publ., 15:527-560.
- Balzer, W., 1984. Organic matter degradation and biogenic element cycling in a nearshore sediment (Kiel Bight). *Limnol. Oceanogr.*, 29:1231-1246.
- Barron, J. A., 1980. Lower Miocene to Quaternary diatom biostratigraphy of Leg 57, off northeastern Japan, Deep Sea Drilling Project. In Scientific Party, *Init. Repts. DSDP*, 56, 57 (Pt. 2): Washington (U.S. Govt. Printing Office), 641-685.
- Berger, A. L., 1978. Long-term variations of caloric solar insolation resulting from Earth's orbital variations. *Quat. Res.*, 9:139-167.
- Berger, W. H., Smetacek, V., and Wefer, G., 1989. *Productivity of the Ocean: Present and Past*: New York (Wiley & Sons).
- Berger, W. H., and Soutar, A., 1970. Preservation of plankton shells in an anaerobic basin off California. *Geol. Soc. Am. Bull.*, 81:275-282.
- Berggren, W. A., Kent, D. V., Flynn, J. J., and Van Couvering, J. A., 1985. Cenozoic Geochronology. *Geol. Soc. Am. Bull.*, 96:1407-1418.
- Bromley, R. G., and Ekdale, A. A., 1984. *Chondrites*: a trace fossil indicator of anoxia in sediments. *Nature*, 224:872-874.
- Burckle, L., and Akiba, F., 1977. Implication of late Neogene freshwater sediment in the Sea of Japan. *Geology*, 6:123-127.
- Byrne, D. A., Harris, D., Duennebie, F. K., and Cessaro, R., 1987. The ocean sub-bottom seismometer system installed in Deep Sea Drilling Project Hole 581C, Leg 88: a technical review. In Stephen, F. K., Gettrust, J. F., et al., *Init. Reports DSDP*, 88: Washington (U.S. Govt. Printing Office), 65-88.
- Carson, B., von Huene, R., and Arthur, M., 1982. Small-scale deformation structures and physical properties related to convergence in Japan Trench slope sediments. *Tectonics*, 1(3):277-302.
- Charvet, J., and Fabbri, O., 1987. Vue generale sur l'orogenese Shimanto et l'evolution tertiaire du Japon sud-ouest. *Bull. Soc. Geol. France*, 6:1171-1188.
- Cragg, B. A., Parkes, R. J., Fry, J. C., Herbert, R. A., Wimpenny, J.W.T., and Getliff, J. W., in press. Bacterial biomass and activity profiles within deep sediment layers. In Suess, E., von Huene, R., et al., *Proc. ODP, Sci. Results*, 112B: College Station, TX (Ocean Drilling Program).

- DeMaster, D. J., 1979. The marine budgets of silica and Si-32 [Ph.D. dissert.]. Yale University, New Haven.
- Emeis, K.-C., and Kvenvolden, K. A., 1986. *Shipboard Organic Geochemistry on JOIDES Resolution*. ODP Tech. Note 7: College Station, TX (Ocean Drilling Program).
- Espitalié, J., Laporte, J. L., Madec, M., Marquis, F., Leplat, P., Paulet, J., and Boutefeu, A., 1977. Méthode rapide de caractérisation des roches-mères, de leur potentiel pétrolier et de leur degré d'évolution. *Rev. Inst. Français Pétrol.*, 32:23-42.
- Fertl, H. H., 1979. Gamma-ray spectral data assists in complex formation evaluation. *The Log Analyst*, 20:3-37.
- Gartner, S., 1977. Calcareous nannofossil biostratigraphy and revised zonation of the Pleistocene. *Mar. Micropaleontol.*, 2:1-25.
- Geological Survey of Japan, 1982. *Geological Atlas of Japan*: Tokyo (Geological Surv. Japan).
- Gieskes, J. M., 1981. Deep-sea drilling interstitial water studies: implications for chemical alteration of oceanic crust, layers I and II. In Warne, J. E., Douglas, R. G., and Winterer, E. L. (Eds.), *The Ocean Drilling Project: A Decade of Progress*. Soc. Econ. Paleontol. Mineral. Spec. Publ., 32:149-167.
- Gieskes, J. M., and Peretsman, G., 1986. *Water Chemistry Procedures Aboard JOIDES Resolution—Some Comments*. ODP Tech. Note 5: College Station, TX (Ocean Drilling Program).
- Hanshaw, B., and Copen, T. B., 1973. Ultrafiltration by a compacted clay membrane. II. Sodium ion exclusion at various ionic strengths. *Clay and Clay Min.*, 12:397-421.
- Hassan, M., Hossin, A., and Combaz, A., 1976. Fundamentals of the differential gamma-ray log. *Trans. SPWLA, 17th Ann. Logging Symp.*, Pap. H, 1-18.
- Hays, J. D., Saito, T., Opydyke, N. D., and Burckle, L. H., 1969. Pliocene-Pleistocene sediment of the equatorial Pacific: their paleomagnetic, biostratigraphic and climatic record. *Geol. Soc. Am. Bull.*, 80:1481-1514.
- Hirata, N., Kinoshita, H., Suyehiro, K., Suyemasu, M., Matsuda, N., Ouchi, T., Katao, H., Koresawa, S., and Nagumo, S., 1987. Report on the DELP 1985 cruises in the Japan Sea. Part II: Seismic refraction experiment conducted in the Yamato Basin, southeast Japan Sea. *Bull. Earthq. Res. Inst.*, Univ. of Tokyo, 62:347-365.
- Honza, E., 1979. Geological investigation of the Japan Sea. April-June 1978 (GH78-2). *Geol. Surv. of Japan Cruise Rept.*, 13:1-99.
- Huchon, P., and Angelier, J., 1987. From subduction to collision: the Suruga-Fujigawa belt, Izu collision zone, central Japan. *Bull. Soc. Geol. France*, 3:511-521.
- Ichikura, M., and Ujiie, H., 1976. Lithology and planktonic foraminifera of the Sea of Japan piston cores. *Bull. Nat. Sci. Mus., Ser. C (Geol.)*, 2:151-177.
- Imbrie, J. J., Hays, J. D., Martinson, D. G., McIntyre, A., Mix, A. C., Morley, J., Pisias, N. J., Prell, W. L., Shackleton, N. J., 1984. The orbital theory of Pleistocene climate: support from a revised chronology of the marine oxygen-isotopic record. In Berger, A., Imbrie, J., Hays, J., Kukla, G., Saltzman, B. (Eds.), *Milankovitch and Climate, Part I: Dorrecht, Holland (D. Reidel Publ. Co.)*, 269-305.
- Ingle, J. C., Jr., 1975a. Summary of late Paleogene-Neogene stratigraphy, paleobathymetry, and correlations, Philippine Sea and Sea of Japan region. In Karig, D. E., Ingle, J. C., et al., *Init. Repts. DSDP*, 31: Washington (U.S. Govt. Printing Office), 837-855.
- , 1975b. Pleistocene and Pliocene foraminifera from the Sea of Japan. In Karig, D. E., Ingle, J. C., Jr., et al., *Init. Repts. DSDP*, 31: Washington (U.S. Govt. Printing Office), 693-701.
- , 1977. Summary of late Neogene planktic foraminiferal biofacies, biostratigraphy, and paleoceanography of the marginal North Pacific Ocean. In Saito, T., and Ujiie, H. (Eds.), *Proc. First Int. Congr. on Pacific Neogene Stratigr.*, Tokyo, 1976: Tokyo (Kaiyo Shuppan).
- , 1981. Origin of Neogene diatomites around the North Pacific Rim. In Garrison, R. E., and Douglas, R. G. (Eds.), *The Monterey Formation and Related Siliceous Rocks of California*: Los Angeles, Soc. Econ. Paleontol. Mineral., *Pacific Sect.*, 159-179.
- Isezaki, N., 1986. A magnetic anomaly map of the Japan Sea. *J. Geomag. Geoelec.*, 38:403-410.
- Ishiwada, Y., Honza, E., and Tamaki, K., 1984. Sedimentary basins of the Japan Sea. *Proc. 27th Int. Geol. Congr. (Moscow)*, 23:43-65.
- Jolivet, L., 1986. America-Eurasia plate boundary in eastern Asia and the opening of marginal basins. *Earth Planet. Sci. Lett.*, 81:293-304.
- Kagami, H., Karig, D. E., Coulbourn, W. T., et al., 1986. *Init. Repts. DSDP*, 87: Washington (U.S. Govt. Printing Office), 35-122.
- Kaneoka, I., 1986. Constraints on the time of the evolution of the Japan Sea based on radiometric ages. *J. Geomag. Geoelec.*, 38:475-485.
- Karig, D. E., Ingle, J. C., Jr., et al., 1975. *Init. Repts. DSDP*, 31: Washington (U.S. Govt. Printing Office).
- Keller, M. A., and Isaacs, C. M., 1985. An evaluation of temperature scales for silica diagenesis in diatomaceous sequences including a new approach based on the Miocene Monterey Formation, California. *Geo-Mar. Lett.*, 5:31-35.
- Knipe, R. J., 1986. Microstructural evolution of vein arrays preserved in Deep Sea Drilling Project cores from the Japan Trench, Leg 57. In Moore, J. C. (Ed.), *Structural Fabric in Deep Sea Drilling Cores From Forearcs*. Geol. Soc. Am. Mem., 166:75-87.
- Kobayashi, K., 1985. Sea of Japan and Okinawa Trough. In Nairn, A.E.M., Stehli, F. G., and Uyeda, S. (Eds.), *The Ocean Basins and Margins, Vol. 7A. The Pacific Ocean*: New York (Plenum Press), 419-458.
- Koizumi, I., and Tanimura, Y., 1985. Neogene diatom biostratigraphy of the middle latitude western North Pacific, Deep Sea Drilling Project, Leg 86. In Heath, G. R., Burckle, L. H., et al., *Init. Rept. DSDP*, 86: Washington (U.S. Govt. Printing Office), 269-300.
- Kukla, G., Heller, L., Ming, X., Chun, X. T., Sheng, L. T., Sheng, A. Z., 1988. Pleistocene climates in China dated by magnetic susceptibility. *Geology*, 16:811-814.
- Lago, M. B., and Thompson, P. R., 1988. Chronostratigraphic significance of late Cenozoic planktonic foraminifera from the Ventura Basin, California: potential for improving tectonic and depositional interpretation. *J. Foramin. Res.*, 18(3):250-266.
- Lallemand, S., Okada, H., Otsuka, K., and Labeyrie, L., 1985. Tectonique en compression sur la marge Est de la Mer du Japon: mise en évidence de chevauchements a vergence orientale. *C. R. Acad. Sci. Paris*, 301:201-206.
- Leventhal, J. S., 1983. An interpretation of carbon and sulphur relationships in Black Sea sediments as indicators of environments of deposition. *Geochim. Cosmochim. Acta*, 47:133-137.
- Ling, H. Y., 1970. Silicoflagellates from central North Pacific core sediments. *Bull. Am. Paleontol.*, 58:85-129.
- , 1975a. Radiolaria: Leg 31 of the Deep Sea Drilling Project. In Karig, D. E., Ingle, J. C., Jr., *Init. Repts. DSDP*, 31: Washington (U.S. Govt. Printing Office), 703-761.
- , 1975b. Silicoflagellates and ebridians from Leg 31. In Karig, D. E., Ingle, J. C., Jr., *Init. Repts. DSDP*, 31: Washington (U.S. Govt. Printing Office), 763-777.
- Ludwig, W. J., Murauchi, S., and Houtz, R. E., 1975. Sediments and structure of the Japan Sea. *Geol. Soc. Am. Bull.*, 86:651-664.
- Lundberg, N., and Karig, D. E., 1986. Structural features in cores from the Nankai Trough, Deep Sea Drilling Project Leg 87A. In Kagami, H., Karig, D. E., Coulbourn, W. T., et al., *Init. Repts. DSDP*, 87: Washington (U.S. Govt. Printing Office), 797-808.
- Lundberg, N., and Moore, J. C., 1986. Macroscopic structural features in Deep Sea Drilling Project cores from forearc regions. In Moore, J. C. (Ed.), *Structural Fabric in Deep Sea Drilling Project Cores From Forearcs*. Geol. Soc. Am. Mem., 166:13-44.
- Machida, H., 1981. Tephrocronology and Quaternary studies in Japan. In Self, S., and Sparks, R.S.J. (Eds.), *Tephra Studies*: Detrecch, Holland (D. Riedel Publ. Co.), 161-191.
- Machida, H., and Arai, F., 1981. Late Quaternary large eruption recorded in distal areas around Japan. *IAVCEI Symp. Arc Volcanism, Volcanol. Soc. Japan, and Int. Assoc. Volcanol., Chem. Earth's Interior*, 214-215 (Program and Abstract).
- Maiya, S., Saito, T. and Sato, T., 1976. Late Cenozoic planktonic foraminiferal biostratigraphy of northwest Pacific sedimentary

- sequences. In Takayanagi, Y., and Saito, T. (Eds.), *Progress in Micropaleontology*: New York (Micropaleontology Press), 395–422.
- Marine, I. W., and Fritz, S. J., 1981. Osmotic model to explain anomalous hydraulic heads. *Water Res.*, 17:73.
- Martinson, D. G., Menke, W., and Stoffa, P., 1982. An inverse approach to signal correlation. *J. Geophys. Res.*, 87:4807–4818.
- Masclé, A., Moore, J. C., et al., 1988. *Proc. ODP, Init Repts.*, 110: College Station, TX (Ocean Drilling Program).
- Matoba, Y., 1983. Paleoenvironment of the Sea of Japan. *Benthos '83*: Pau (Elf Aquitaine), 409–414.
- , 1984. Paleoenvironment of the Sea of Japan. In Oertl, H. J. (Ed.), *Benthos '83*, 2nd Int. Symp. Benthic foraminifera (Pau, April 1983), Pau and Bordeaux, 409–414.
- Matsuda, T., 1978. Collision of the Izu-Bonin arc with central Honshu: Cenozoic tectonics of the Fossa Magna, Japan. *J. Phys. Earth, Tokyo, Suppl.*, 26:409–421.
- McDuff, R. E., and Gieskes, J. M., 1981. Major cation gradients in DSDP interstitial waters: the role of diffusive exchange between seawater and upper oceanic crust. *Geochim. Cosmochim. Acta*, 45:1705–1713.
- Meyers, P. A., 1984. Organic geochemistry of sediments from the Angola Basin and the Walvis Ridge: a synthesis of studies from Deep Sea Drilling Project Leg 75. In Hay, W. W., Sibuet, J.-C., et al. (Eds.), *Init. Repts. DSDP*, 75: Washington (U.S. Govt. Printing Office), 459–467.
- Morozumi, Y., and Koizumi, I., 1981. Himi and Yatsuo areas. In Tsuchi, R. (Ed.), *Neogene of Japan—Its Biostratigraphy and Chronology*: Shizuoka (Kurofune Printing Co., Ltd.), 65–67.
- Morozumi, Y., and Koizumi, I., 1981. Stratigraphic outlines: Himi and Yatsuo areas. In Tsuchi, R., (Ed.), *Neogene of Japan*: Shizuoka (Geoscience Inst., Univ. of Shizuoka).
- Mueller, P., and Suess, E., 1979. Productivity, sedimentation rate and sedimentary organic matter in the oceans. I. Organic matter preservation. *Deep-Sea Res.*, 26:1347–1362.
- Murauchi, S., 1966. Explosion seismology. In 2nd Progress Rept. on the Upper Mantle Project of Japan (1965–1966), Natl. Comm. for UMP, Sci. Council of Japan, 11–13.
- Nakamura, K., 1983. Possible nascent trench along the eastern Japan Sea as the convergent boundary between Eurasian and North American plates. *Bull. Earthq. Res. Inst., Univ. of Tokyo*, 58:711–722.
- Niitsuma, N., and Matsuda, T., 1985. Collision in the South Fossa Magna area, central Japan. *Recent Progr. Natural Sci. Japan*, 10:41–50.
- Phleger, F. B., and Soutar, A., 1973. Production of benthic foraminifera in three east Pacific oxygen minima. *Micropaleontology*, 19:110–115.
- Poulet, A., Cadet, J. P., Fujioka, K., and Bourgeois, J., 1985a. Ash layers from Deep Sea Drilling Project Leg 84: Middle America Trench transect. In von Huene, R., Aubouin, J., et al., *Init. Repts. DSDP*, 84: Washington (U.S. Govt. Printing Office), 609–618.
- Poulet, A., Fujioka, K., Charvet, J., and Cadet, J. P., 1985b. Petrography and geochemistry of volcanic ash layers from Leg 87A, Nankai Trough (South Japan). In Kagami, H., Karig, D. E., Coulbourn, W. T., et al., *Init. Repts. DSDP*, 87: Washington (U.S. Govt. Printing Office), 695–701.
- Poulet, A., and Lee, J. S., 1988. Tectonic evolution of the Asian Margin since Cretaceous: implications from the geochronology of volcanism in the Korean peninsula. *Int. Symp. Geodyn. Evol. Eastern Eurasian Margin*, Paris, 13–20 Sept. 1988. (Abstract).
- Poulet, A., Cambay, H., Cadet, J. P., Bourgeois, J., and DeWever, P., in press. Volcanic ash from Ocean Drilling Program Leg 112 off Peru. In Suess, E., von Huene, R., et al., *Proc. ODP, Sci. Results*, 112: College Station, TX (Ocean Drilling Program).
- Prell, W., 1985. Pliocene stable isotope and carbonate stratigraphy (Holes 572C and 573A): paleoceanographic data bearing on the question of Pliocene glaciation. In *Init. Repts. DSDP* 85. Washington (U.S. Govt. Printing Office), 723–734.
- Prell, W. L., Niitsuma, N., et al., 1989. *Proc. ODP, Init. Repts.*, 117: College Station, TX (Ocean Drilling Program).
- Raiswell, R., 1987. Nonsteady-state microbiological diagenesis. In Marshal, J. D. (Ed.), *Diagenesis of Sedimentary Sequences*. Geol. Soc. (London) Spec. Publ., 36:41–54.
- , 1988. Chemical model for the origin of minor limestone-shale cycles by anaerobic methane oxidation. *Geology*, 16:641–644.
- Raymo, M. E., Ruddiman, W. F., Backman, J., Clement, B., and Martinson, D. G., 1989. Late Pliocene variation in Northern Hemisphere ice sheets and North Atlantic deep water circulation. *Paleoceanography*, 4:413–446.
- Ruddiman, W. F., Raymo, M. E., Martinson, D. G., Clement, B., and Backman, J., 1989. Pleistocene evolution: Northern Hemisphere ice sheets and the North Atlantic Ocean. *Paleoceanography*, 4:353–412.
- Rosenfeld, J. K., 1979. Ammonium adsorption in nearshore anoxic sediments. *Limnol. Oceanogr.*, 24:356–364.
- Savdra, C. E., and Bottjer, D. J., 1986. Trace-fossil model for reconstruction of paleo-oxygenation in bottom waters. *Geology*, 14:3–6.
- Scheidegger, K. F., and Kriesek, L. A., 1983. Zooplankton and nekton: natural barriers to the seaward transport of suspended terrigenous particles off Peru. In Suess, E., and Thiede J. (Eds.), *Coastal Upwelling: Its Sediment Record*: New York (Plenum Press), 303–333.
- Shackleton, N. J., and Opdyke, N. D., 1977. Oxygen isotope and paleomagnetic evidence for early Northern Hemisphere glaciation. *Nature*, 270:216–219.
- Shackleton, N. J., Backman, J., Zimmerman, H., Kent, D. V., Hall, M. A., Roberts, D. G., Schnitker, D., Baldut, J. G., Desprairies, A., Homrighausen, R., Huddleston, P., Keene, J. B., Kaltenback, A. J., Krumsiek, K.A.O., Morton, A. C., Murray, J. W., and Westburg-Smith, J., 1984. Oxygen isotope calibration of the onset of ice rafting in DSDP Site 552: a history of glaciation in the North Atlantic region. *Nature*, 307:620–623.
- Stein, R., in press. Organic carbon content/sedimentation rate relationship and its paleoenvironmental significance for marine sediments. *Geo. Mar. Lett.*
- Stein, R., and Littke, R., 1989. Organic-carbon-rich sediments and paleoenvironment: results from Baffin Bay (ODP-Leg 105) and the upwelling area off Northwest Africa (ODP-Leg 108). In Huc, A. (Ed.), *Deposition of Organic Facies*. Proc. Mediterranean Basin Conf. (Nice, September 1988).
- Steiness, E., Heir, K. S., and Billings, G. K., 1972. Lithium. In Wedepohl, K. H. (Ed.), *Handbook of Geochemistry*: Berlin-Heidelberg-New York (Springer-Verlag), Vol. II, Sect. 3K.
- Suess, E., von Huene, R. et al., 1988. *Proc. ODP, Init. Repts.*, 112: College Station, TX (Ocean Drilling Program).
- Taisuke, T., and Matoba, Y., 1976. Guidebook for Excursion 1, Oga Peninsula. *Proc. First Int. Congr. Pacific Neogene Stratigr.* (Tokyo).
- Tamaki, K., 1988. Geological structure of the Japan Sea and its implications. *Bull. Geol. Survey Japan*, 39:269–365.
- Tamaki, K., Honza, E., Yuasa, M., Nishimura, K., and Murakami, F., 1981. Geological map of the central Japan Sea. *Geol. Survey Japan, Mar. Geol. Map Ser. 15*. Scale 1:1,000,000.
- Tamaki, K., Pisciotto, K., Allan, J., et al., in press. *Proc. ODP, Init. Repts.*, 127: College Station, TX (Ocean Drilling Program).
- Tissot, B., and Welte, D. H., 1984. *Petroleum Formation and Occurrence*: Heidelberg-Berlin-New York (Springer-Verlag).
- Ujiié, H., and Ichikura, M., 1973. Holocene to uppermost Pleistocene planktonic foraminifers in a piston core from off the San'in District, Sea of Japan. *Trans. Palaeont. Soc. Japan, New Ser.*, 9:137–150.
- van Morkhoven, F.P.C.M., Berggren, W. A., and Edward, A. S., 1986. *Cenozoic Cosmopolitan Deep-Water Benthic Foraminifera*: Pau (Elf Aquitaine).
- von Breymann, M. T., Collier, R., and Suess, E., in press. Magnesium adsorption and ion exchange in marine sediments: A multi-component model. *Geochim. Cosmochim. Acta*.
- von Huene, R., and Lee, H., 1982. The possible significance of pore fluid pressures in subduction zones. Studies in continental margin geology. *AAPG Mem.*, 37:781–789.
- Whelan, J. K., Oremland, R., Tarafa, M., Smith, R., Howarth, R., and Lee, C., 1986. Evidence for sulfate-reducing and methane-producing microorganisms in sediments from Sites 618, 619, and 622. In Bouma, A. H., Coleman, J. M., et al., *Init. Repts. DSDP*, 96: Washington (U.S. Govt. Printing Office), 767–776.

Wlotzka, F., 1972. Nitrogen. In Wedepohl, K. H. (Ed.), *Handbook of Geochemistry*: Berlin-Heidelberg-New York (Springer-Verlag), Vol II, Sect. 7K.

Yuasa, M., Kanaya, H., and Terashima, S., 1979. Rocks and sediments. In Honza, E. (Ed.), *Geological Investigation of the Japan*

Sea. April-June 1978 (GH78-2 Cruise). Geol. Survey Japan Cruise Rept., 13:54-63.

Ms 128A-105

Table 21. Index properties for Hole 798B.

Core, section, interval (cm)	Depth (mbsf)	Wet-bulk density (g/cm ³)	Dry-bulk density (g/cm ³)	Grain density (g/cm ³)	Porosity (%)	Wet water content (%)	Dry water content (%)	Void ratio
128-798B-14H-1, 87-89	124.07	1.52	0.77	2.64	71.8	49.3	97.40	2.51
14H-2, 116-118	125.56	1.63	0.92	2.66	67.0	43.6	77.40	2.01
14H-3, 89-91	126.79	1.61	0.93	2.70	66.2	42.4	73.60	1.94
14H-4, 39-41	127.79	1.63	0.95	2.74	66.2	42.0	72.40	1.94
14H-5, 39-41	129.29	1.43	0.66	2.47	73.9	53.6	115.70	2.79
14H-6, 65-67	131.05	1.51	0.78	2.65	71.3	48.6	94.60	2.45
14H-7, 65-67	132.55	1.63	0.95	2.77	66.2	41.7	71.60	1.94
14H-8, 65-67	134.05	1.63	0.94	2.75	66.4	42.1	72.80	1.95
15H-1, 59-61	133.49	1.48	0.69	2.66	75.1	53.4	114.50	2.97
15H-2, 109-111	135.27	1.53	0.81	2.61	69.7	47.2	89.20	2.27
15H-3, 22-24	135.90	1.56	0.83	2.69	70.0	46.7	87.50	2.30
15H-5, 75-79	139.43	1.45	0.68	2.51	73.7	52.9	112.40	2.75
15H-6, 74-76	140.92	1.52	0.78	2.58	70.9	48.8	95.30	2.40
15H-7, 75-77	142.43	1.53	0.69	2.72	76.5	54.7	120.60	3.20
15H-8, 75-80	143.93	1.51	0.90	2.63	63.8	40.4	67.90	1.74
16X-1, 45-47	143.05	1.50	0.73	2.67	73.3	51.0	103.90	2.71
16X-2, 45-50	144.55	1.44	0.60	2.75	79.2	58.2	139.00	3.73
16X-3, 110-112	145.88	1.37	0.54	2.52	79.6	60.8	155.40	3.82
16X-4, 48-53	146.76	1.40	0.61	2.61	77.1	56.4	129.60	3.30
16X-5, 57-59	148.35	1.40	0.57	2.58	78.8	59.1	144.50	3.64
16X-6, 34-39	149.62	1.37	0.54	2.67	80.3	60.5	153.30	4.00
16X-7, 47-49	151.25	1.38	0.58	2.62	78.4	58.2	139.40	3.56
17X-1, 45-47	152.75	1.35	0.49	2.11	79.0	64.0	177.60	3.66
17X-2, 48-54	153.56	1.36	0.53	2.66	80.7	61.3	158.20	4.10
17X-3, 49-51	155.07	1.34	0.51	2.54	80.6	62.2	164.40	4.08
17X-4, 28-35	156.36	1.37	0.53	2.53	79.7	60.9	156.00	3.86
17X-5, 29-31	157.87	1.38	0.55	2.59	79.2	59.7	148.30	3.74
17X-6, 39-44	159.47	1.39	0.58	2.58	78.3	58.5	140.90	3.54
17X-7, 39-41	160.97	1.61	0.90	2.84	69.0	44.2	79.30	2.20
18X-1, 30-32	162.20	1.57	0.84	2.71	70.0	46.5	87.00	2.30
18X-2, 30-35	163.70	1.41	0.63	2.48	75.4	55.4	124.30	3.01
18X-3, 43-45	165.33	1.47	0.71	2.56	72.9	51.4	105.90	2.65
18X-4, 30-35	166.70	1.36	0.55	1.68	71.3	59.5	147.00	2.41
18X-5, 130-132	169.20	1.36	0.54	2.48	78.9	60.2	151.40	3.67
18X-6, 25-30	169.65	1.81	1.22	2.72	56.4	32.5	48.10	1.28
19X-1, 60-62	172.20	1.52	0.75	2.75	73.6	50.5	102.20	2.75
19X-2, 60-65	173.70	1.23	0.56	2.59	75.5	54.6	120.10	3.04
19X-3, 60-62	175.20	1.54	0.84	2.50	67.5	45.6	83.70	2.05
19X-4, 50-55	176.60	1.56	0.85	2.60	68.1	45.4	83.20	2.11
19X-5, 50-52	178.10	1.41	0.64	2.43	74.2	54.4	119.10	2.83
19X-6, 60-65	179.70	1.66	0.98	2.73	65.2	41.0	69.40	1.85
20X-1, 40-42	181.70	1.50	0.79	2.80	71.3	47.4	90.00	2.46
20X-2, 40-45	182.67	1.62	0.91	2.71	67.7	43.8	78.10	2.07
20X-3, 40-42	184.17	1.60	0.88	2.67	68.5	45.2	82.40	2.15
20X-4, 103-108	186.30	1.42	0.62	2.54	76.4	56.1	128.00	3.17
20X-5, 46-48	187.23	1.42	0.60	2.49	77.1	57.6	135.60	3.30
20X-5, 60-65	187.37	1.52	0.76	2.49	71.3	50.2	100.80	2.45
21X-1, 29-31	191.29	1.50	0.72	2.69	74.2	51.9	107.80	2.83
21X-2, 77-82	192.58	1.48	0.72	2.54	72.4	51.1	104.50	2.59
21X-3, 59-61	193.90	1.46	0.92	3.38	66.0	36.8	58.20	1.92
21X-4, 39-44	195.20	1.49	0.74	2.80	73.9	50.5	101.90	2.79
21X-5, 35-37	196.66	1.53	0.78	2.61	71.4	49.1	96.40	2.46
21X-6, 19-24	198.00	1.39	0.56	2.52	78.5	59.3	145.50	3.57
21X-6, 59-64	198.40	1.66	0.97	2.78	66.1	41.6	71.20	1.93
21X-7, 77-80	200.08	1.39	0.60	2.36	75.6	57.0	132.40	3.04
22X-1, 40-42	201.00	1.39	0.58	2.42	77.0	58.2	139.10	3.28
22X-2, 30-35	202.40	1.38	0.59	1.06	65.4	57.1	133.30	1.38
22X-3, 71-73	204.31	1.38	0.59	2.46	76.9	57.7	136.20	3.27
22X-4, 17-22	205.27	1.39	0.60	2.46	76.3	56.8	131.70	3.16
22X-6, 90-92	209.00	1.53	0.79	2.71	71.6	48.4	93.90	2.49
22X-7, 42-47	209.57	1.50	0.75	2.62	71.8	49.6	98.30	2.51
22X-8, 77-79	211.42	1.62	0.91	2.69	67.8	44.2	79.20	2.08
23X-1, 60-52	210.90	1.41	0.60	2.54	77.3	57.4	134.90	3.34
23X-2, 25-29	211.88	1.40	0.60	2.43	76.4	57.3	134.10	3.18
23X-3, 25-27	213.38	1.38	0.58	2.14	74.9	58.3	139.80	2.92
23X-5, 120-125	217.33	1.45	0.64	2.79	77.5	55.4	124.40	3.39
23X-6, 61-63	218.24	1.52	0.76	2.56	71.6	49.8	99.30	2.48
23X-7, 60-65	219.73	1.58	0.86	2.61	68.5	45.7	84.00	2.14
23X-8, 24-26	220.87	1.48	0.70	2.65	74.2	52.3	109.50	2.84
24X-1, 49-51	220.49	1.38	0.60	2.36	75.3	56.6	130.40	3.00
24X-2, 49-54	221.99	1.43	0.66	2.45	74.1	54.0	117.60	2.81
24X-3, 49-51	223.49	1.45	0.69	2.38	72.1	52.3	109.80	2.55
24X-4, 49-54	224.99	1.41	0.64	2.42	74.5	54.9	121.60	2.87
24X-5, 49-51	226.49	1.41	0.63	2.44	75.3	55.8	126.00	3.00
24X-6, 43-48	227.93	1.44	0.68	2.40	72.8	52.9	112.40	2.63
24X-7, 20-22	229.20	1.48	0.70	2.44	73.0	52.8	112.00	2.66

Table 21 (continued).

Core, section, interval (cm)	Depth (mbsf)	Wet-bulk density (g/cm ³)	Dry-bulk density (g/cm ³)	Grain density (g/cm ³)	Porosity (%)	Wet water content (%)	Dry water content (%)	Void ratio
24X-1, 99-101	230.69	1.54	0.78	1.76	63.0	49.2	96.80	1.67
25X-2, 68-73	231.88	1.43	0.63	2.54	75.9	55.5	124.90	3.09
25X-3, 68-70	233.38	1.43	0.69	2.54	72.9	51.6	106.50	2.65
25X-4, 63-67	234.83	1.54	0.75	2.54	72.4	51.0	103.90	2.58
25X-5, 60-62	236.30	1.41	0.65	2.49	74.4	54.0	117.40	2.86
27X-1, 66-68	249.66	1.66	0.99	2.80	64.8	39.9	66.40	1.82
27X-2, 38-43	250.88	1.63	0.95	2.64	65.2	41.8	71.90	1.85
27X-3, 38-40	252.38	1.49	0.74	2.55	71.9	50.3	101.30	2.52
27X-4, 15-20	253.65	1.41	0.62	2.54	76.4	56.2	128.10	3.18
27X-5, 95-97	255.95	1.52	0.79	2.55	69.7	47.7	91.30	2.27
27X-6, 95-100	257.45	1.64	0.91	2.69	68.1	44.6	80.40	2.11
27X-7, 31-33	258.31	1.37	0.55	2.39	78.0	59.8	148.90	3.47
28X-1, 31-33	259.01	1.38	0.56	2.43	77.9	59.4	146.10	3.46
28X-2, 27-32	260.47	1.50	0.78	2.50	69.6	48.0	92.20	2.25
28X-3, 30-32	262.00	1.49	0.77	2.51	69.8	48.2	93.00	2.28
28X-4, 31-35	263.51	1.41	0.66	2.58	74.6	53.4	114.80	2.89
28X-5, 29-31	264.99	1.45	0.64	2.71	77.4	56.1	127.50	3.37
28X-6, 27-33	266.47	1.34	0.51	2.36	79.4	62.2	164.30	3.78
28X-7, 27-29	267.97	1.35	0.54	2.32	77.9	60.3	151.90	3.44
29X-1, 30-32	268.60	1.52	0.79	2.58	70.6	48.4	93.90	2.36
29X-2, 30-35	269.80	1.34	0.50	2.43	80.1	62.4	166.00	3.94
29X-3, 30-32	271.30	1.36	0.53	2.55	79.8	61.0	156.30	3.88
29X-4, 30-32	272.80	1.37	0.57	2.29	76.5	58.8	142.50	3.19
29X-5, 30-32	274.30	1.42	0.64	2.48	74.9	54.9	121.50	2.94
29X-6, 35-40	275.85	1.51	0.75	2.57	72.1	50.4	101.60	2.55
29X-7, 35-37	277.35	1.40	0.62	2.35	74.9	56.1	127.60	2.92
30X-1, 100-102	278.20	1.45	0.66	2.60	75.4	54.3	118.60	3.01
30X-2, 100-105	279.70	1.65	0.95	2.75	66.9	42.7	74.40	2.00
30X-3, 100-102	281.20	1.63	0.96	2.74	65.4	41.1	69.80	1.87
30X-4, 100-105	282.70	1.52	0.79	2.60	70.2	47.8	91.50	2.32
30X-5, 100-102	284.20	1.79	1.16	2.70	59.0	35.1	54.00	1.43
30X-6, 100-105	285.70	1.48	0.50	2.48	82.9	66.2	195.50	4.74
31X-1, 30-32	286.70	1.36	0.56	2.41	77.5	59.0	144.20	3.39
31X-2, 30-35	287.40	1.37	0.60	2.34	74.7	55.9	126.90	2.89
31X-4, 55-60	290.65	1.44	0.71	2.40	70.8	50.5	101.90	2.39
31X-6, 30-35	293.40	1.42	0.64	2.55	75.4	54.8	121.00	3.01
31X-7, 91-93	295.51	1.43	0.66	2.53	74.8	54.1	118.00	2.91
31X-8, 30-35	296.40	1.41	0.66	2.45	73.4	53.2	113.60	2.72
32X-1, 130-132	297.30	1.40	0.61	2.42	75.7	56.5	129.60	3.07
32X-2, 40-45	297.90	1.43	0.66	2.53	74.8	54.2	118.10	2.92
32X-3, 20-22	299.20	1.38	0.61	2.44	75.3	55.8	126.30	3.00
32X-4, 70-75	301.20	1.38	0.57	2.44	77.4	58.5	141.10	3.36
32X-5, 20-22	302.20	1.39	0.59	2.43	76.6	57.5	135.50	3.21
33X-1, 20-22	305.90	1.37	0.60	2.42	75.6	56.3	128.70	3.04
33X-2, 20-25	307.40	1.40	0.61	2.48	76.0	56.3	128.70	3.12
33X-3, 79-81	309.49	1.42	0.64	2.52	75.2	54.8	121.30	2.98
33X-4, 60-65	310.80	1.42	0.64	2.52	75.3	54.9	121.70	2.99
33X-5, 19-21	311.89	1.42	0.63	2.48	75.5	55.5	124.80	3.03
33X-6, 30-35	313.50	1.42	0.65	2.41	73.9	54.2	118.40	2.78
34X-1, 90-92	316.20	1.45	0.69	2.47	72.9	52.4	109.90	2.65
34X-2, 83-88	317.63	1.43	0.67	2.46	73.7	53.5	115.10	2.76
34X-3, 87-89	319.17	1.41	0.62	2.51	75.9	55.8	126.30	3.09
34X-4, 8-12	319.88	1.44	0.66	2.51	74.7	54.3	118.70	2.91
34X-5, 40-42	321.26	1.53	0.79	2.56	70.1	48.0	92.40	2.31
34X-CC, 23-25	321.84	1.65	0.98	2.72	64.8	40.7	68.70	1.82
35X-1, 15-17	325.15	1.62	0.94	2.75	66.2	41.8	71.90	1.93
35X-2, 15-17	326.65	1.63	0.92	2.65	66.7	43.3	76.50	1.98
35X-3, 40-42	328.40	1.60	0.88	2.75	68.9	44.8	81.20	2.18
35X-4, 40-45	329.90	1.62	0.94	2.73	66.1	41.9	72.10	1.92
35X-5, 40-42	331.40	1.63	0.97	2.75	65.0	40.6	68.30	1.83
35X-7, 5-7	334.05	1.54	0.82	2.79	70.9	47.0	88.60	2.41
36X-1, 40-45	335.00	1.63	0.91	2.67	67.7	44.3	79.40	2.07
36X-2, 20-22	336.30	1.73	1.06	2.83	63.8	38.7	63.10	1.74
36X-3, 14-16	337.74	1.69	1.03	2.71	63.3	39.2	64.50	1.71
37X-1, 60-62	344.90	1.68	1.01	2.65	63.2	39.6	65.60	1.69
37X-2, 46-48	346.26	1.65	1.01	2.80	63.9	39.0	64.00	1.75
37X-3, 44-46	347.74	1.62	0.92	2.68	66.9	43.3	76.50	2.00
38X-1, 18-20	354.08	1.55	0.80	2.58	70.4	48.2	93.00	2.34
38X-2, 40-42	355.80	1.59	0.82	2.56	70.7	48.7	95.00	2.38
38X-3, 31-33	357.21	1.49	0.73	2.46	71.6	50.9	103.70	2.49
38X-4, 31-33	358.71	1.48	0.71	2.42	72.3	52.1	108.70	2.57
38X-5, 24-26	360.14	1.58	0.82	2.72	71.5	48.2	93.00	2.47
38X-6, 58-60	361.98	1.56	0.81	2.55	69.9	47.9	91.80	2.29
39X-1, 14-16	363.74	1.47	0.70	2.43	72.5	52.2	109.30	2.59
39X-2, 83-85	365.93	1.50	0.72	2.48	72.4	51.6	106.50	2.58
39X-4, 85-87	368.95	1.49	0.73	2.52	72.6	51.4	105.90	2.60

Table 21 (continued).

Core, section, interval (cm)	Depth (mbsf)	Wet-bulk density (g/cm ³)	Dry-bulk density (g/cm ³)	Grain density (g/cm ³)	Porosity (%)	Wet water content (%)	Dry water content (%)	Void ratio
39X-6, 127-129	372.37	1.52	0.80	2.61	70.3	47.7	91.30	2.33
40X-1, 24-26	373.44	1.51	0.78	2.44	69.3	48.2	93.20	2.22
40X-2, 23-25	374.93	1.51	0.76	2.50	70.7	49.3	97.40	2.37
40X-4, 131-133	379.01	1.47	0.74	2.48	70.7	49.5	98.10	2.37
40X-5, 31-33	379.51	1.52	0.76	2.52	71.3	49.8	99.30	2.44
41X-1, 60-62	383.50	1.63	0.93	2.69	66.8	43.1	75.60	1.98
41X-3, 60-65	386.50	1.50	0.76	2.59	71.3	49.2	96.70	2.45
41X-4, 60-62	388.00	1.55	0.83	2.61	69.1	46.4	86.60	2.21
41X-5, 60-65	389.50	1.63	0.94	2.91	67.8	42.3	73.30	2.08
41X-6, 20-22	390.60	1.56	0.86	2.70	68.7	45.0	81.90	2.16
42X-2, 20-22	393.15	1.67	1.02	2.77	64.0	39.3	64.90	1.75
42X-3, 20-25	394.65	1.74	1.12	2.66	59.6	36.0	56.30	1.46
42X-4, 20-22	396.15	1.76	1.13	2.92	61.8	35.9	56.00	1.60
42X-7, 19-24	400.64	1.79	1.21	2.83	57.0	32.2	47.50	1.31
43X-1, 13-15	402.33	1.54	0.83	2.70	69.7	46.3	86.10	2.27
43X-2, 80-85	404.50	1.77	1.14	2.93	61.4	35.6	55.20	1.58
43X-3, 20-22	405.40	1.75	1.09	2.82	62.7	37.6	60.30	1.66
43X-4, 50-55	407.20	1.79	1.15	2.80	60.6	35.7	55.60	1.52
43X-5, 41-43	408.61	1.84	1.21	2.84	59.2	34.1	51.80	1.44
43X-6, 20-25	409.90	1.77	1.01	2.67	66.8	43.2	76.10	1.99
44X-1, 40-42	412.20	1.34	1.07	2.83	41.3	20.2	25.30	0.70
44X-2, 40-45	413.70	1.71	1.07	2.72	61.4	37.1	59.10	1.57
44X-6, 50-52	419.80	1.69	1.01	2.75	64.5	40.0	66.80	1.79
44X-7, 50-55	420.84	1.78	1.19	2.82	57.9	33.1	49.50	1.36
45X-1, 33-35	421.83	1.73	1.08	2.71	61.6	37.4	59.80	1.58
45X-7, 31-33	430.46	1.64	0.97	2.73	65.3	41.1	69.80	1.86
46X-1, 50-52	431.60	1.66	0.95	2.61	65.9	42.9	75.00	1.91
46X-2, 131-133	433.91	1.71	1.05	2.66	62.2	38.5	62.70	1.63
46X-3, 110-112	435.20	1.77	1.09	2.82	63.6	38.6	62.90	1.73
46X-4, 70-72	436.30	1.78	1.05	2.54	63.3	40.7	68.80	1.71
46X-5, 43-45	437.53	1.76	1.05	2.69	64.4	40.5	67.90	1.79
46X-6, 113-115	439.73	1.86	1.17	2.75	61.5	37.1	58.90	1.58
47X-1, 26-28	441.06	1.68	0.99	2.60	64.1	41.0	69.40	1.76
47X-2, 7-9	441.20	1.70	1.05	2.67	62.1	38.3	62.10	1.62
47X-3, 74-77	443.37	1.65	0.97	2.62	64.3	41.0	69.40	1.77
47X-4, 44-46	444.57	1.65	0.94	2.62	66.4	43.2	76.10	1.95
47X-5, 43-45	446.06	1.67	0.97	2.70	65.7	41.8	71.70	1.89
47X-6, 80-82	447.93	1.63	0.91	2.53	66.8	44.6	80.40	1.99
47X-7, 23-25	448.86	1.59	0.90	2.64	66.8	43.5	77.0	1.98
48X-1, 44-45	450.84	1.80	1.20	2.73	57.4	33.4	50.10	1.34
48X-2, 21-23	452.11	1.77	1.11	2.73	61.6	37.3	59.60	1.59
48X-3, 104-106	454.44	1.78	1.14	2.68	60.0	36.2	56.60	1.48
48X-5, 97-99	457.37	1.85	1.26	2.73	55.7	31.8	46.70	1.24
49X-1, 66-67	460.76	1.93	1.29	2.72	57.2	33.2	49.70	1.32
49X-2, 110-112	462.70	1.76	1.05	2.85	65.7	40.5	68.10	1.89
49X-3, 75-76	463.85	1.79	1.15	2.79	60.2	35.5	55.00	1.49
49X-4, 112-114	465.72	1.78	1.10	2.83	63.0	37.9	61.00	1.68
49X-5, 63-64	466.73	1.97	1.41	2.77	51.9	28.3	39.50	1.07
49X-6, 110-112	468.70	1.92	1.36	2.69	52.4	29.3	41.50	1.09
49X-7, 23-24	469.33	1.97	1.39	2.80	53.3	29.3	41.30	1.13
50X-1, 75-77	470.45	1.89	1.33	2.79	53.5	29.6	42.00	1.14
50X-2, 110-112	472.30	1.84	1.21	2.92	59.9	34.1	51.80	1.48
50X-3, 29-31	472.99	1.88	1.35	2.66	50.8	28.2	39.30	1.02
51X-1, 41-43	479.81	1.90	1.34	2.59	51.2	29.1	41.00	1.04
51X-2, 23-25	481.13	1.87	1.34	2.61	50.3	28.2	39.40	1.00
51X-3, 84-86	483.24	1.85	1.29	2.79	54.0	30.0	42.80	1.16
51X-4, 108-110	484.98	1.89	1.30	2.69	54.2	30.9	44.70	1.17
51X-5, 31-33	485.71	1.84	1.26	2.64	54.3	31.3	45.50	1.17
51X-6, 86-88	487.76	1.90	1.36	2.75	52.0	28.5	40.00	1.07
52X-1, 19-21	489.19	1.89	1.37	2.59	49.3	27.6	38.10	0.96
52X-2, 17-19	490.67	1.84	1.29	2.43	50.9	30.1	43.10	1.02
52X-3, 93-95	492.93	1.88	1.32	2.67	52.8	29.8	42.50	1.11
52X-4, 94-96	494.44	1.86	1.29	2.60	53.1	30.6	44.10	1.12
52X-5, 91-93	495.91	1.82	1.23	2.65	55.8	32.6	48.40	1.25
52X-6, 40-42	496.90	1.81	1.25	2.62	53.6	30.8	44.60	1.14
53X-1, 121-123	499.91	1.85	1.30	2.54	51.7	29.9	42.70	1.06
53X-2, 131-133	501.51	1.80	1.26	2.36	50.1	30.1	43.10	0.99
53X-4, 95-97	504.15	1.84	1.29	2.54	51.6	29.9	42.60	1.06
53X-5, 8-10	504.78	1.83	1.31	2.60	50.2	28.2	39.30	1.00
54X-1, 43-46	508.73	1.79	1.27	2.43	50.0	29.4	41.60	0.99
54X-2, 56-58	510.06	1.84	1.07	2.61	65.0	41.8	71.90	1.83
54X-3, 122-124	512.22	1.77	1.25	2.52	51.0	29.5	41.80	1.03
54X-4, 131-133	513.81	1.84	1.33	2.62	49.3	27.3	37.60	0.96
54X-5, 92-94	514.92	1.83	1.32	2.51	49.0	27.9	38.70	0.95

Table 22. Index properties for Hole 798C.

Core, section, interval (cm)	Depth (mbsf)	Wet-bulk density (g/cm ³)	Dry-bulk density (g/cm ³)	Grain density (g/cm ³)	Porosity (%)	Wet water content (%)	Dry water content (%)	Void ratio
128-798C-1H-1, 106-108	1.06	1.26	0.37	2.45	85.4	70.4	238.4	5.70
1H-2, 106-108	2.56	1.43	0.59	2.61	79.0	59.1	144.6	3.68
1H-3, 106-108	4.06	1.42	0.61	2.71	78.3	57.3	134.2	3.55
1H-4, 106-108	5.56	1.42	0.62	2.60	76.9	56.3	128.9	3.27
2H-1, 34-36	6.64	1.50	0.72	2.78	75.0	52.1	108.8	2.96
2H-2, 34-36	8.14	1.51	0.72	2.70	74.6	52.4	110.0	2.90
2H-3, 34-36	9.64	1.48	0.67	2.70	76.4	54.8	121.2	3.19
2H-4, 34-36	11.14	1.51	0.70	2.73	75.6	53.4	114.6	3.05
2H-5, 34-36	12.64	1.45	0.65	2.64	76.1	54.8	121.4	3.12
2H-6, 34-36	14.14	1.42	0.60	2.69	78.3	57.4	134.8	3.54
2H-7, 34-36	15.64	1.47	0.79	2.67	69.4	46.2	85.7	2.24
3H-1, 78-80	16.08	1.57	0.82	2.86	72.5	48.2	92.9	2.60
3H-2, 78-80	17.58	1.44	0.66	2.51	74.8	54.4	119.2	2.92
3H-3, 77-79	19.07	1.53	0.86	2.49	66.0	44.1	78.8	1.91
3H-4, 77-79	20.57	1.46	0.66	2.57	75.3	54.4	119.2	2.99
3H-5, 79-81	22.09	1.60	0.67	2.69	78.6	57.9	137.7	3.61
3H-6, 59-61	23.39	1.54	0.78	2.64	71.5	49.0	96.0	2.47
3H-7, 59-61	24.89	1.52	0.76	2.73	72.9	49.9	99.6	2.65

Table 23. Sonic velocity of Core 128-798A-1H.

Depth (mbsf)	P-wave velocity (m/s)	Depth (mbsf)	P-wave velocity (m/s)
0.2	1515.5	4.5	1511.0
0.3	1514.0	4.7	1517.8
0.4	1512.9	4.8	1515.6
0.5	1511.3	4.9	1517.0
0.6	1527.5	5.0	1519.5
0.7	1537.7	5.1	1522.3
0.8	1548.9	5.2	1514.5
0.9	1510.8	5.3	1517.0
1.0	1511.6	5.4	1521.3
1.1	1510.4	5.5	1524.4
1.2	1515.8	5.6	1515.1
1.3	1512.5	5.7	1516.8
1.4	1520.8	5.8	1520.9
1.7	1516.3	5.9	1523.5
1.8	1543.2	6.0	1525.3
1.9	1518.6	6.2	1533.1
2.0	1523.0	6.3	1533.9
2.1	1516.9	6.4	1532.8
2.2	1520.1	6.5	1529.2
2.3	1523.1	6.6	1524.1
2.4	1522.9	6.7	1522.8
2.5	1512.9	6.8	1527.3
2.6	1515.4	6.9	1535.0
2.7	1519.0	7.0	1524.4
2.8	1523.3	7.1	1521.8
2.9	1526.8	7.2	1526.3
3.0	1526.7	7.3	1528.6
3.2	1527.5	7.4	1527.1
3.3	1523.1	7.5	1526.5
3.4	1522.6	7.8	1529.6
3.5	1522.4	7.9	1527.1
3.6	1522.6	8.0	1530.3
3.7	1517.9	8.1	1526.5
3.8	1513.5	8.2	1526.1
3.9	1511.1	8.3	1526.1
4.0	1511.3	8.4	1522.9
4.1	1508.6	8.5	1524.8
4.2	1512.1	8.6	1524.7
4.3	1508.8	8.7	1522.3
4.4	1509.3	8.8	1523.8

Table 24 (continued).

Core, section, interval (cm)	Depth (mbsf)	Thermal conductivity (W/m · K)
128-798B-1H-3, 40-41	3.40	0.929
1H-4, 60-61	5.10	0.913
1H-5, 60-61	6.60	0.999
1H-6, 60-61	8.10	1.030
2H-2, 60-61	11.50	0.995
2H-4, 60-61	14.50	0.926
2H-5, 60-61	16.00	1.015
2H-6, 60-61	17.50	1.020
3H-1, 70-71	19.10	0.912
3H-2, 70-71	20.60	0.867
3H-3, 60-61	22.00	0.907
3H-5, 60-61	25.00	0.675
4H-1, 70-71	28.10	0.999
4H-2, 70-71	29.60	0.901
4H-3, 70-71	31.10	0.977
4H-4, 70-71	32.60	1.042
5H-1, 65-66	37.45	0.922
5H-2, 65-66	38.95	0.958
5H-3, 65-66	40.45	1.020
5H-4, 60-61	41.90	1.012
6H-3, 142-143	50.06	1.010
6H-5, 77-78	52.41	0.856
6H-6, 77-78	53.91	0.985
6H-7, 57-58	55.21	0.791
7H-3, 75-76	59.33	0.813
7H-4, 70-71	60.78	0.972
7H-5, 74-75	62.32	0.871
7H-6, 75-76	63.83	0.855
8H-2, 75-76	67.02	0.892
8H-3, 75-76	68.52	0.959
8H-4, 75-76	70.02	1.111
8H-5, 75-76	71.52	1.049
10H-3, 75-76	86.96	1.013
10H-4, 65-66	88.36	0.720
10H-5, 82-83	90.03	0.625
11H-2, 40-41	96.10	0.778
11H-3, 40-41	97.60	0.709
11H-4, 40-41	99.10	0.917
11H-5, 50-51	100.70	0.602
12H-3, 46-47	106.56	0.765
12H-4, 38-39	107.98	0.878
12H-5, 53-54	109.63	0.852
12H-6, 47-48	111.07	0.780
13H-3, 63-64	116.82	0.903
13H-4, 64-65	118.33	0.843
13H-5, 78-79	119.97	0.901
13H-6, 64-65	121.33	0.875
14H-3, 80-81	126.70	1.176
14H-4, 80-81	128.20	0.818
14H-5, 80-81	129.70	1.058
14H-6, 80-81	131.20	0.774
15H-3, 80-81	136.48	1.150
15H-3, 82-83	136.50	0.989
15H-4, 72-73	137.90	0.971
15H-4, 80-81	137.98	1.122
15H-5, 74-75	139.42	0.808
15H-5, 80-81	139.48	0.971
15H-6, 65-66	140.83	0.920
15H-6, 80-81	140.98	1.001
16X-1, 50-51	143.10	0.865
16X-2, 50-51	144.60	0.776
16X-3, 55-56	145.33	0.801
16X-4, 55-56	146.83	0.784
17X-4, 75-76	156.83	0.749
17X-5, 125-126	158.83	0.760
17X-6, 31-32	159.39	0.816
17X-7, 75-76	161.33	0.719
18X-2, 100-101	164.40	0.782
18X-3, 35-36	165.25	0.804
18X-4, 25-26	166.65	0.870
18X-5, 25-26	168.15	1.076
19X-1, 80-81	172.40	0.875
19X-3, 80-81	175.40	0.685
19X-4, 80-81	176.90	0.851
19X-6, 40-41	179.50	1.021
20X-2, 40-41	182.67	1.024

Table 24 (continued).

Core, section, interval (cm)	Depth (mbsf)	Thermal conductivity (W/m · K)
20X-3, 33-34	184.10	0.793
20X-5, 33-34	187.10	0.706
20X-6, 33-34	188.60	0.810
21X-4, 25-26	195.06	0.885
21X-5, 25-26	196.56	0.931
21X-6, 40-41	198.21	1.045
21X-7, 65-66	199.96	0.852
22X-1, 60-61	201.20	0.655
22X-2, 30-31	202.40	0.752
22X-3, 60-61	204.20	0.539
22X-6, 60-61	208.70	0.857
23X-2, 80-81	212.43	0.813
23X-3, 80-81	213.93	0.681
23X-4, 80-81	215.43	0.034
23X-5, 80-81	216.93	0.957
24X-2, 50-51	222.00	0.809
24X-3, 50-51	223.50	0.909
24X-4, 50-51	225.00	0.864
24X-5, 50-51	226.50	0.768
25X-2, 75-76	231.95	0.910
25X-3, 75-76	233.45	0.677
25X-4, 75-76	234.95	0.917
25X-5, 51-52	236.21	0.833
27X-1, 50-51	249.50	1.076
27X-2, 50-51	251.00	0.973
27X-4, 78-79	254.28	0.904
27X-5, 78-79	255.78	0.902
28X-2, 44-45	260.64	0.522
28X-5, 44-45	265.14	0.904
28X-6, 44-45	266.64	0.389
28X-7, 27-28	267.97	0.794
29X-2, 78-79	270.28	0.760
29X-3, 64-65	271.64	0.788
29X-6, 60-61	276.10	0.935
29X-7, 63-64	277.63	0.791
30X-2, 80-81	279.50	1.107
30X-3, 50-51	280.70	0.984
30X-4, 30-31	282.00	0.956
30X-5, 30-31	283.50	0.822
31X-2, 100-101	288.10	0.767
31X-2, 100-101	288.10	0.704
31X-4, 107-108	291.17	0.799
31X-4, 107-108	291.17	0.836
31X-6, 100-101	294.10	0.781
31X-7, 100-101	295.60	0.640
32X-1, 40-41	296.40	0.755
32X-1, 122-123	297.22	0.820
32X-2, 35-36	297.85	0.916
32X-2, 40-41	297.90	0.809
32X-3, 35-36	299.35	0.770
32X-4, 35-36	300.85	0.831
32X-4, 40-41	300.90	0.850
32X-5, 40-41	302.40	0.770
34X-1, 119-120	316.49	0.772
34X-2, 30-31	317.10	0.783
34X-3, 30-31	318.60	0.844
34X-4, 9-10	319.89	0.848
35X-1, 47-48	325.47	1.058
35X-2, 47-48	326.97	0.880
35X-3, 47-48	328.47	0.950
35X-4, 47-48	329.97	1.004
36X-1, 52-53	335.12	0.884
37X-1, 70-71	345.00	1.040
37X-2, 70-71	346.50	1.048
37X-3, 35-36	347.65	1.039
38X-2, 51-52	355.91	0.868
38X-3, 58-59	357.48	0.878
38X-4, 40-41	358.80	0.803
38X-5, 65-66	360.55	0.933
39X-1, 100-101	364.60	0.844
39X-2, 80-81	365.90	0.895
39X-3, 63-64	367.23	0.920
39X-4, 31-32	368.41	0.778
41X-1, 50-51	383.40	1.039
41X-3, 71-72	386.61	0.892
41X-4, 87-88	388.27	0.895

Table 24 (continued).

Core, section, interval (cm)	Depth (mbsf)	Thermal conductivity (W/m · K)
41X-5, 88-89	389.78	0.991
42X-2, 36-37	393.31	0.971
42X-3, 36-37	394.81	0.957
42X-4, 45-46	396.40	1.108
42X-5, 67-68	398.12	1.091
43X-1, 50-51	402.70	1.090
43X-2, 50-51	404.20	1.118
43X-3, 50-51	405.70	1.103
43X-4, 50-51	407.20	1.108
44X-1, 40-41	412.20	0.944
44X-2, 40-41	413.70	1.047
44X-3, 40-41	415.20	0.982
44X-6, 40-41	419.70	1.009
45X-1, 40-41	421.90	0.997
45X-2, 40-41	423.40	0.815
45X-3, 106-107	425.21	0.907
45X-4, 33-34	425.98	0.767
46X-1, 40-41	431.50	0.903
46X-2, 40-41	433.00	0.855
46X-3, 40-41	434.50	0.894
46X-4, 40-41	436.00	0.793
47X-2, 40-41	441.53	0.744
47X-3, 40-41	443.03	0.932
47X-4, 40-41	444.53	1.030
47X-5, 40-41	446.03	1.145
48X-2, 40-41	452.30	1.056
48X-3, 40-41	453.80	1.026
48X-4, 40-41	455.30	1.115
48X-5, 40-41	456.80	1.141
49X-1, 40-41	460.50	1.137
49X-2, 40-41	462.00	1.006
49X-3, 40-41	463.50	1.141
49X-4, 40-41	465.00	1.450
50X-1, 50-51	470.20	1.390
50X-2, 50-51	471.70	1.405
50X-3, 50-51	473.20	1.285
51X-1, 50-51	479.90	1.138
51X-2, 50-51	481.40	1.083
51X-3, 50-51	482.90	1.117
51X-4, 50-51	484.50	1.056
52X-1, 50-51	489.50	1.187
52X-2, 50-51	491.00	1.283
52X-3, 50-51	492.50	1.219
52X-4, 50-51	494.00	1.166
53X-1, 50-51	499.20	0.065
53X-2, 50-51	500.70	0.866
53X-3, 50-51	502.20	0.826
54X-2, 40-41	509.90	1.138
54X-4, 40-41	512.90	0.551
54X-5, 40-41	514.40	0.952

Table 25. Torvane-measured shear strengths at Site 798.

Core, section, interval (cm)	Depth (mbsf)	Shear strength (kPa)
128-798A-6H-2, 60-62	48.30	34.30
6H-6, 135-137	55.05	27.50
7H-1, 5-7	55.75	34.30
7H-3, 5-7	58.39	32.40
8H-2, 4-6	65.64	34.30
8H-4, 4-6	68.64	27.50
8H-8, 19-21	74.79	44.10
9H-2, 120-121	77.50	50.00
9H-5, 21-23	81.01	36.30
9H-6, 140-141	83.70	55.90
9H-7, 60-61	84.40	56.90
11H-5, 137-139	101.47	39.20
11H-7, 12-14	103.22	51.00
12H-3, 125-126	107.32	41.20
12H-5, 50-52	109.57	68.60
12H-7, 97-99	113.04	53.90
13H-1, 25-27	113.65	27.50
13H-3, 129-131	117.69	29.40
13H-5, 112-114	120.52	34.30
13H-7, 42-44	122.82	35.30
14H-2, 10-12	123.61	70.60
14H-5, 20-22	128.21	68.60
14H-8, 40-42	132.91	80.40
15H-2, 135-137	135.55	53.90
15H-4, 130-132	138.50	45.10
15H-6, 25-27	140.45	66.70
15H-8, 20-22	143.40	46.10
128-798B-14H-2, 133-135	125.73	60.8
14H-4, 110-112	128.50	56.9
14H-6, 102-104	131.42	58.8
14H-8, 79-91	134.19	64.7
15H-2, 119-121	135.37	58.8
15H-4, 86-88	138.04	70.6
15H-6, 69-71	140.87	77.5
16X-2, 52-54	144.62	21.6
16X-4, 54-56	146.82	42.2
16X-6, 33-35	149.61	45.1
17X-2, 100-102	154.08	46.1
17X-4, 110-112	157.18	45.1
17X-7, 60-62	161.18	65.7
18X-2, 20-22	163.60	42.2
18X-4, 20-22	166.60	36.3
18X-6, 9-11	169.49	93.2
19X-2, 65-67	173.75	43.1
19X-4, 55-57	176.65	52
19X-6, 58-60	179.68	55.9
20X-2, 46-48	182.73	29.4
20X-4, 109-111	186.36	34.3
20X-6, 65-67	188.92	47.1
22X-2, 136-138	203.46	24.5
22X-3, 63-65	204.23	23.5
22X-6, 130-132	—	33.3
23X-2, 22-24	211.85	17.7
23X-3, 28-30	213.41	17.7
23X-6, 66-68	218.29	27.5
23X-7, 56-58	219.69	37.3
24X-2, 20-22	221.70	18.6
24X-4, 80-82	225.30	19.6
24X-6, 110-112	228.60	31.4
25X-2, 20-22	231.40	20.6
25X-4, 110-112	235.30	33.3
25X-5, 131-133	237.01	23.5
28X-2, 10-12	260.30	42.2
28X-4, 25-27	263.45	34.3
28X-6, 23-25	266.43	29.4
29X-2, 25-27	269.75	33.3
29X-4, 28-30	272.78	40.2
29X-6, 23-25	275.73	31.4
29X-7, 130-132	278.30	61.8
30X-2, 98-100	279.68	45.1
30X-4, 98-100	282.68	40.2
30X-6, 98-100	285.68	39.2
31X-6, 35-37	293.45	31.4
31X-8, 34-36	296.44	31.4
35X-1, 132-134	326.32	27.5
35X-4, 130-132	330.80	45.1
35X-6, 122-124	333.72	58.8

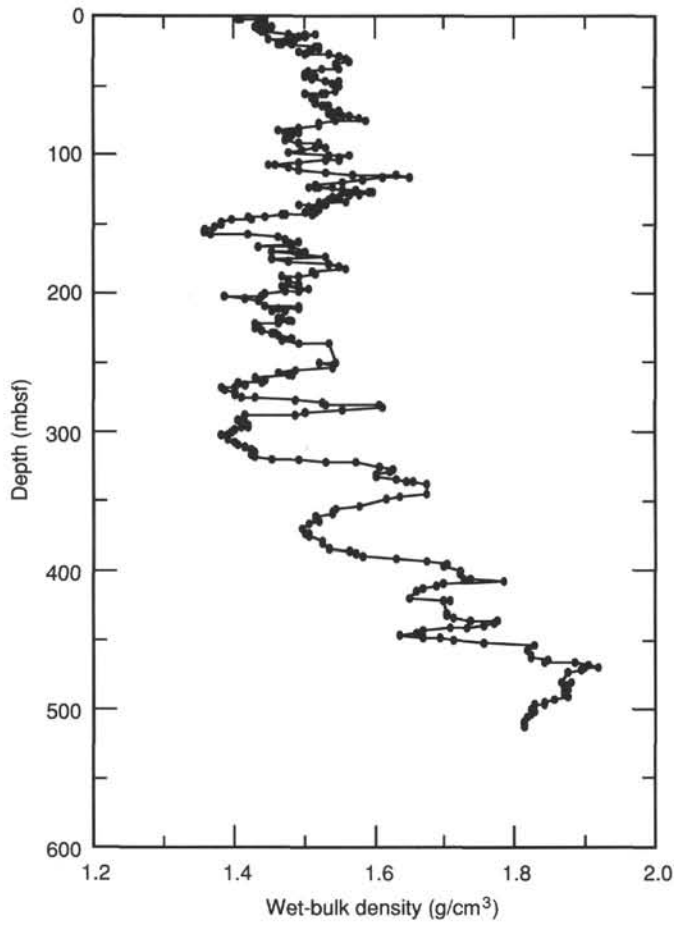


Figure 76. Wet-bulk density vs. depth for Site 798.

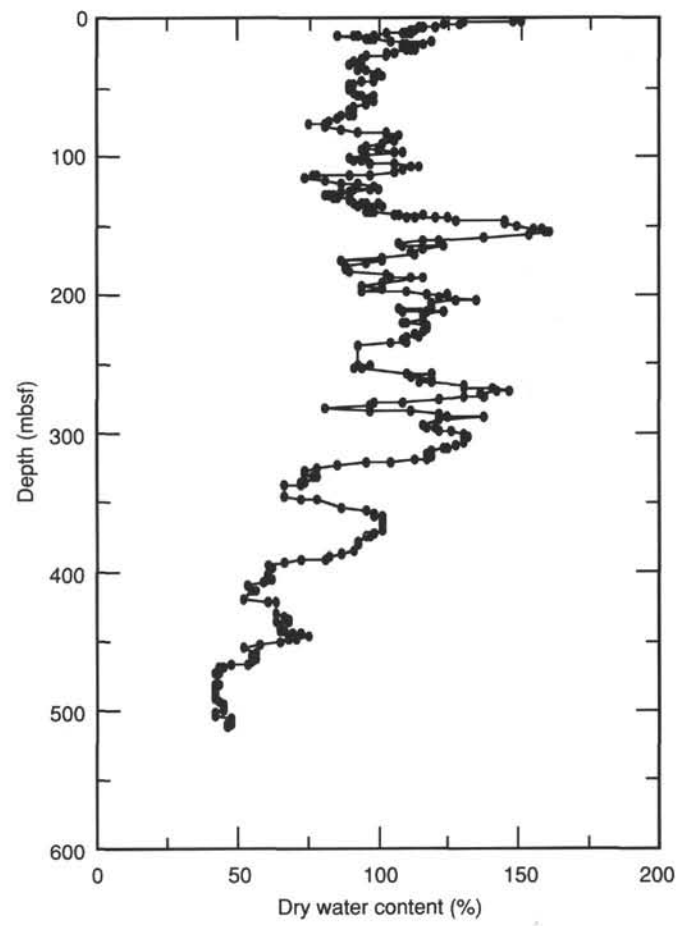


Figure 77. Water content (related to dry weight) vs. depth for Site 798.

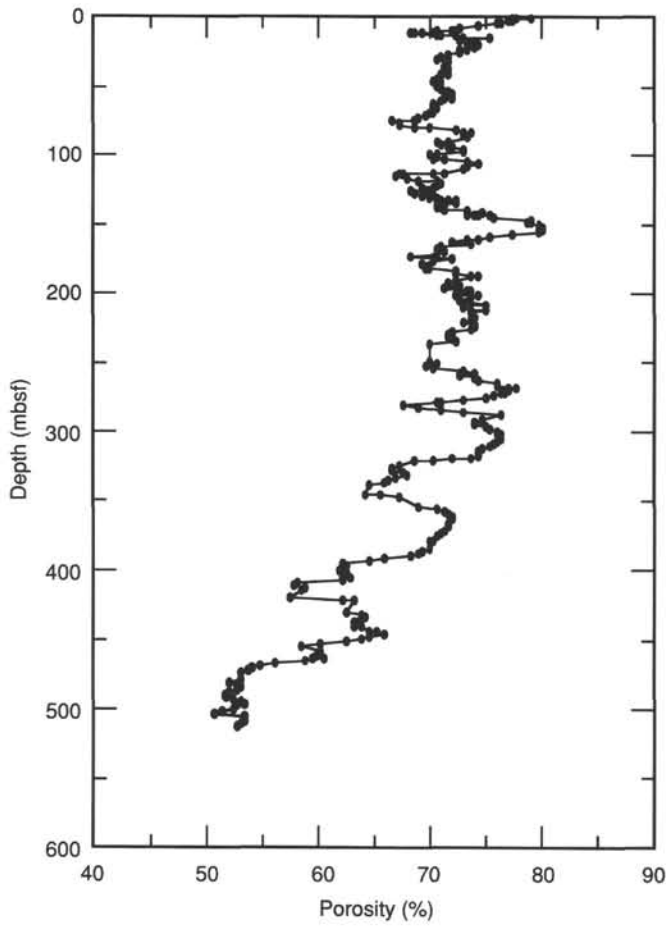


Figure 78. Porosity vs. depth for Site 798.

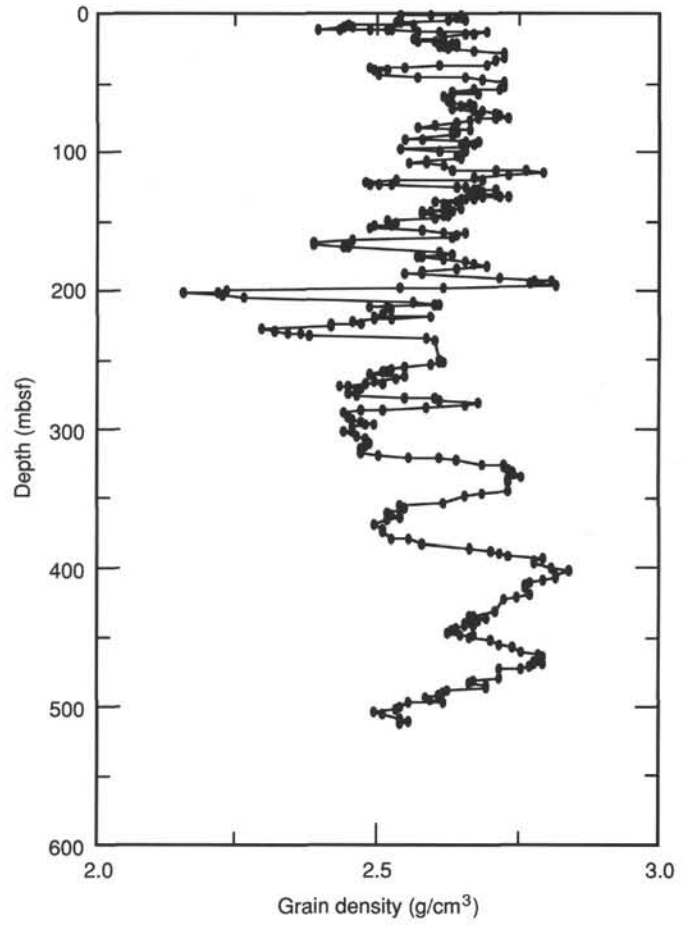


Figure 79. Grain density vs. depth for Site 798.

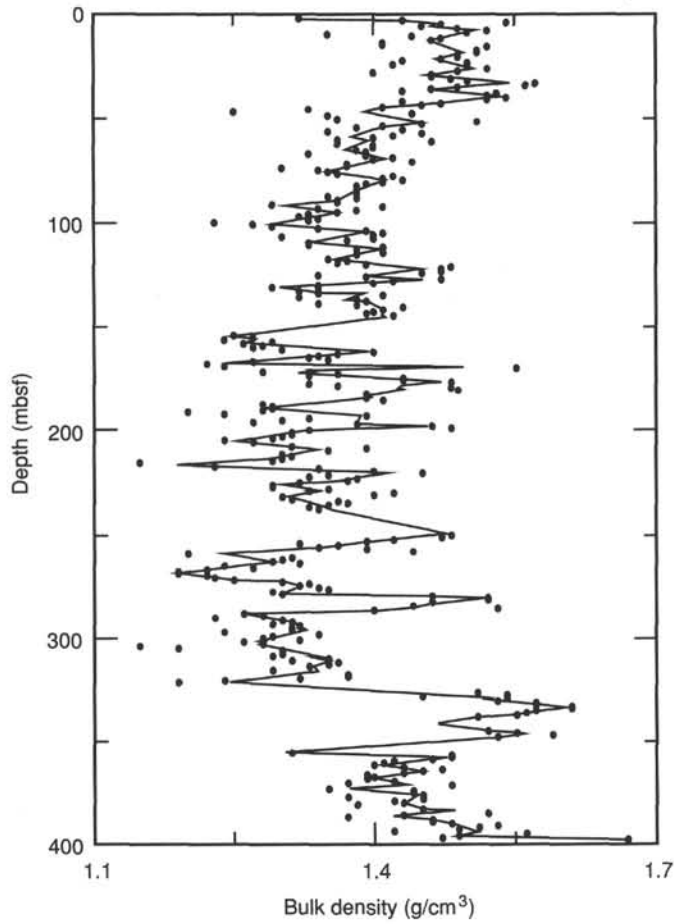


Figure 80. GRAPE-measured density vs. depth for Site 798.

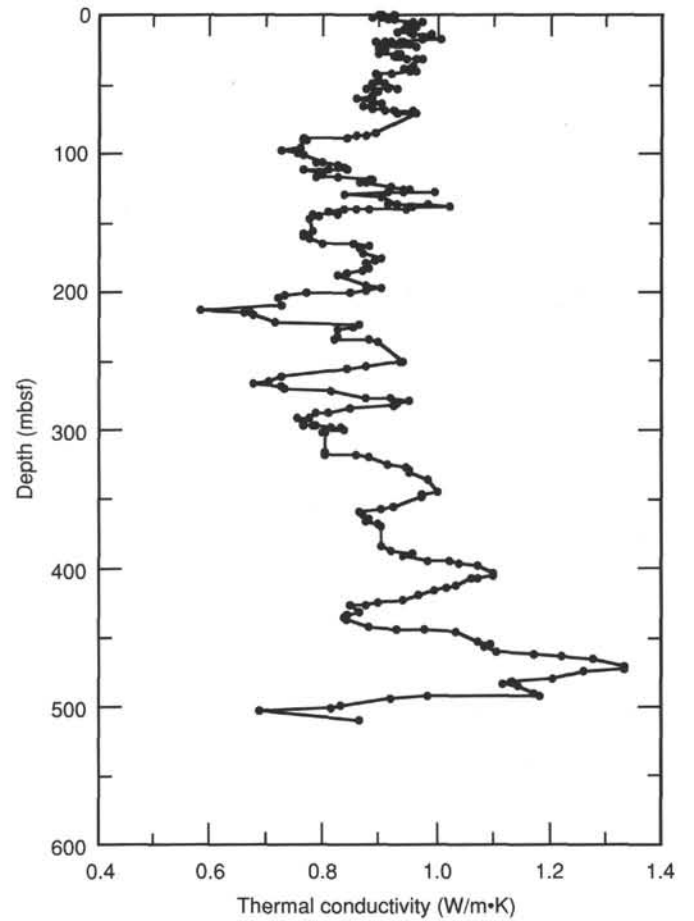


Figure 81. Thermal conductivity vs. depth for Site 798.

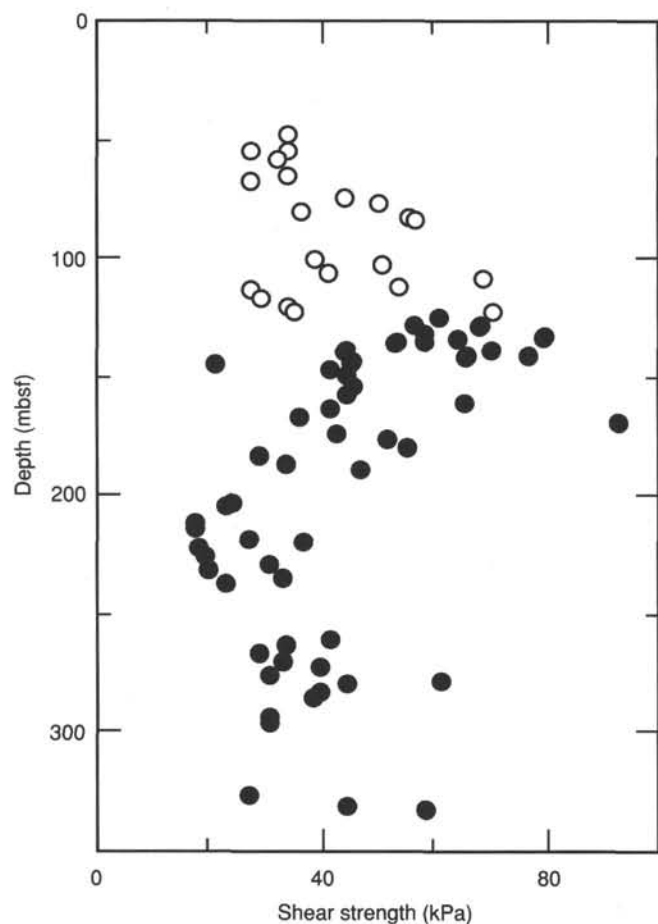


Figure 82. Undrained shear strength vs. depth for Site 798. Open circles represent data for Hole 798A and closed circles represent data from Hole 798B.

Table 26. Time schedule for logging operations at Hole 798B.

Tool string	Time (UTC)	Procedure
Seismic stratigraphy (DIT-SDT-NGT)	RIH 2345 (8/29/89) POOH 0200 (8/30/89)	Log down to TD. Log up to mud line.
Formation microscanner	RIH 0320 POOH 0614	Run down to TD, log up to end of pipe. Run down to 380 mbsf for repeat section 370-110 mbsf.
Lithoporosity combination (LDT-CNT-NGT)	RIH 0745 POOH 1053	Run down to TD. Log up to end of pipe.
Geochemical combination (ACT-GST-NGT)	RIH 1224 POOH 2155	Run down to TD, log up to mud line. Run down to TD for repeat run up to mud line. Pipe raised 30 m for second run.

DITE = phaser induction tool, SDT = digital sonic tool, NGT = natural spectrometry tool, LDT = lithodensity tool, CNT = compensated neutron tool, ACT = aluminum clay tool, GST = induced gamma-ray spectrometry tool, TD = total depth (518 mbsf), RIH = run in to hole, POOH = pull out of hole. End of pipe = 85 mbsf. Total logging time = 22.17 hr.

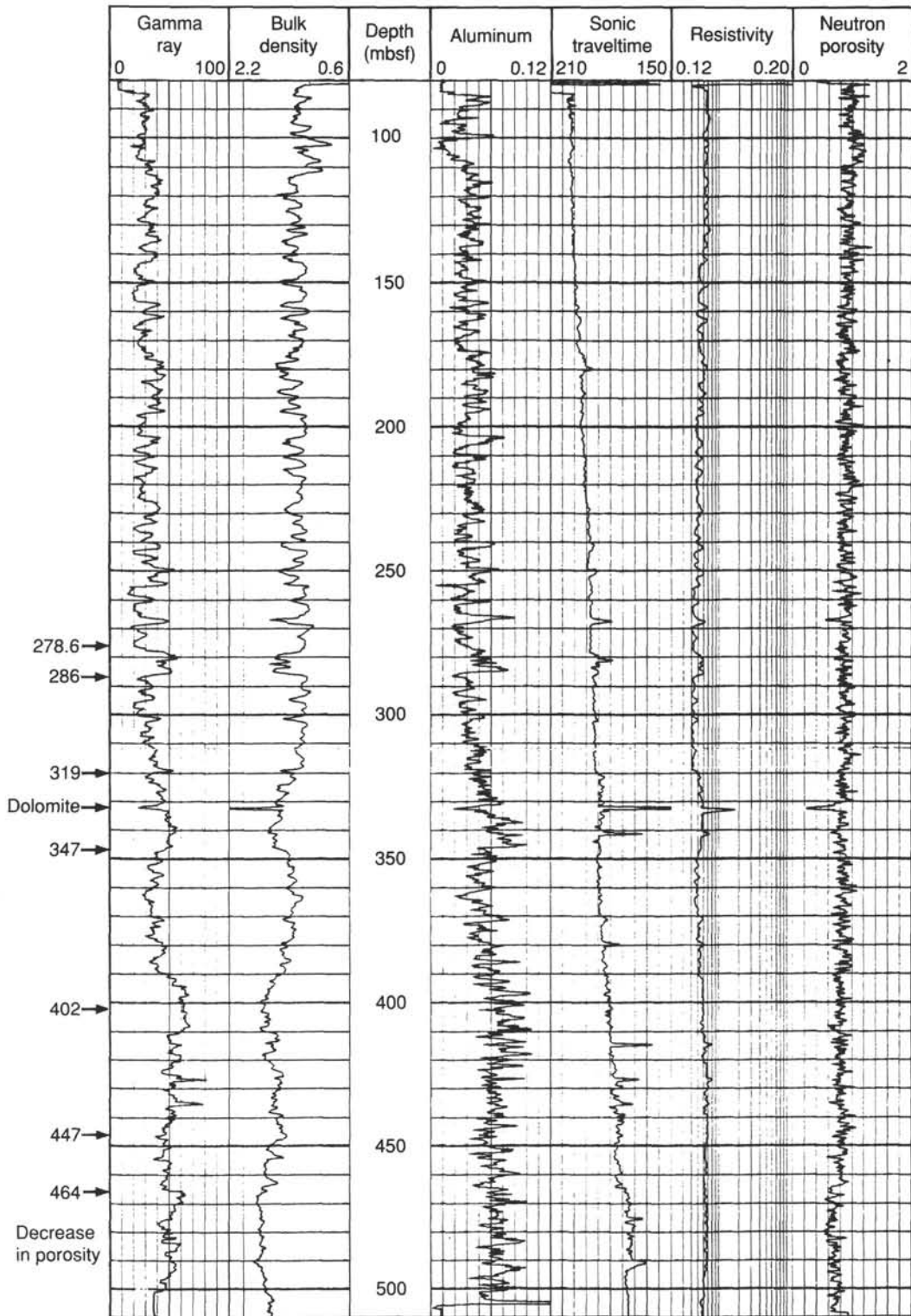


Figure 83. Logging curves for Hole 798B: Compensated gamma-ray log (API units); bulk density (g/cm³); depth (mbsf); aluminium (wt%); sonic traveltime (μs); resistivity (ohm · m) and porosity as determined from the CNT.

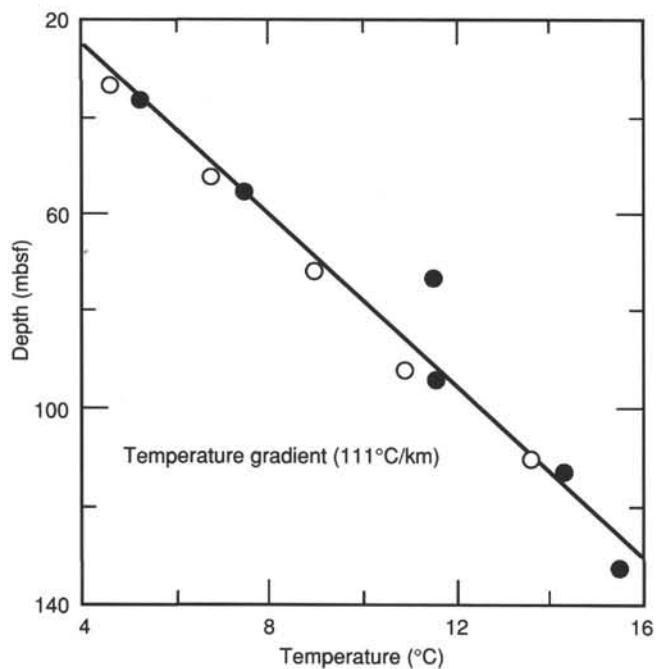


Figure 84. Barnes/Uyeda heat flow measurements for Holes 798A (closed circles) and 798C (open circles). Calculated temperature gradient from a best-fit line is 111°C/km.

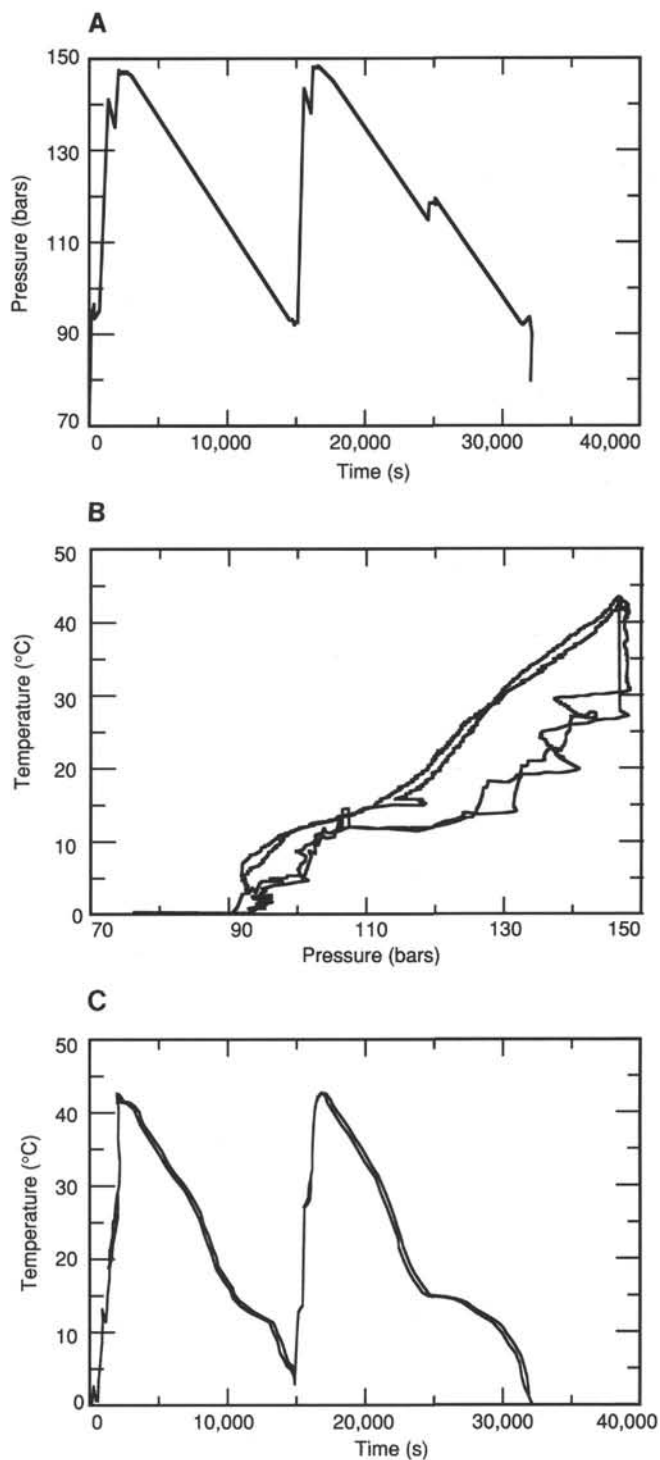


Figure 85. Lamont-Doherty TLT results for Hole 798B, fourth logging run with TLT with the geochemical logging combination. A. Pressure vs. time. B. Pressure vs. temperature. C. Temperature vs. time.

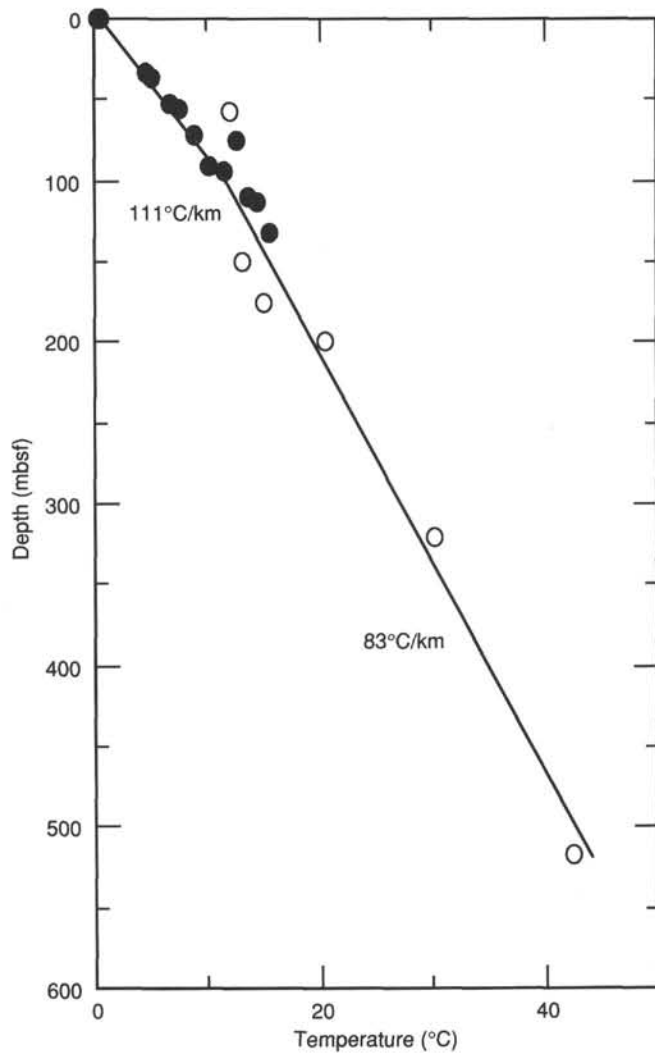


Figure 86. Heat flow measurements at Site 798. Solid circles represent temperature measurements using the Barnes/Uyeda temperature probe in Holes 798A and 798C. Open circles indicate temperature measurements made using the Lamont-Doherty TLT in Hole 798B.

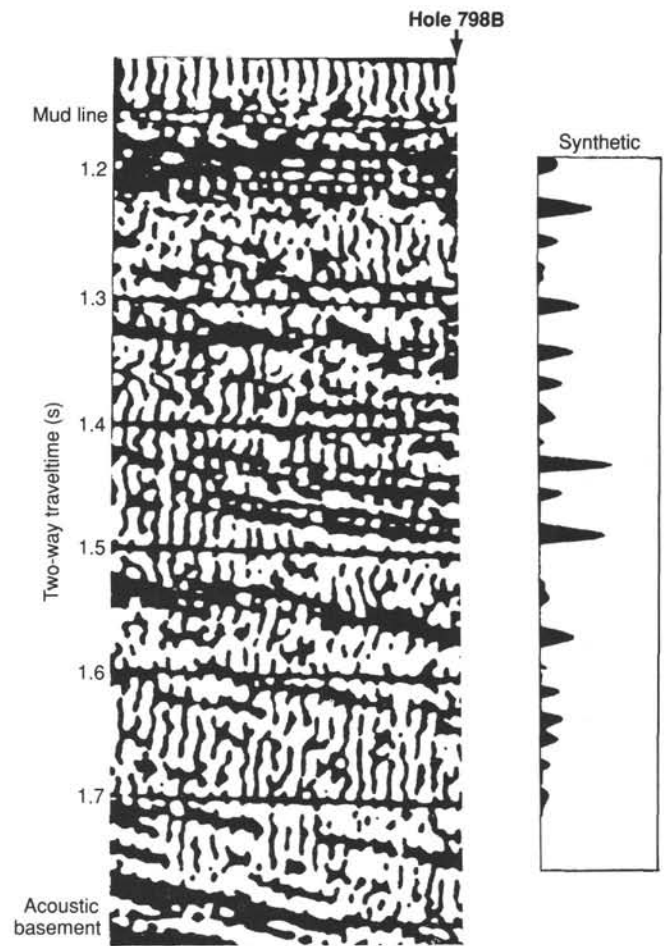


Figure 87. Comparison of synthetic seismogram with seismic profile. The two-way traveltimes is marked for the seismic profile and is valid for the synthetic seismogram shown on the right side.

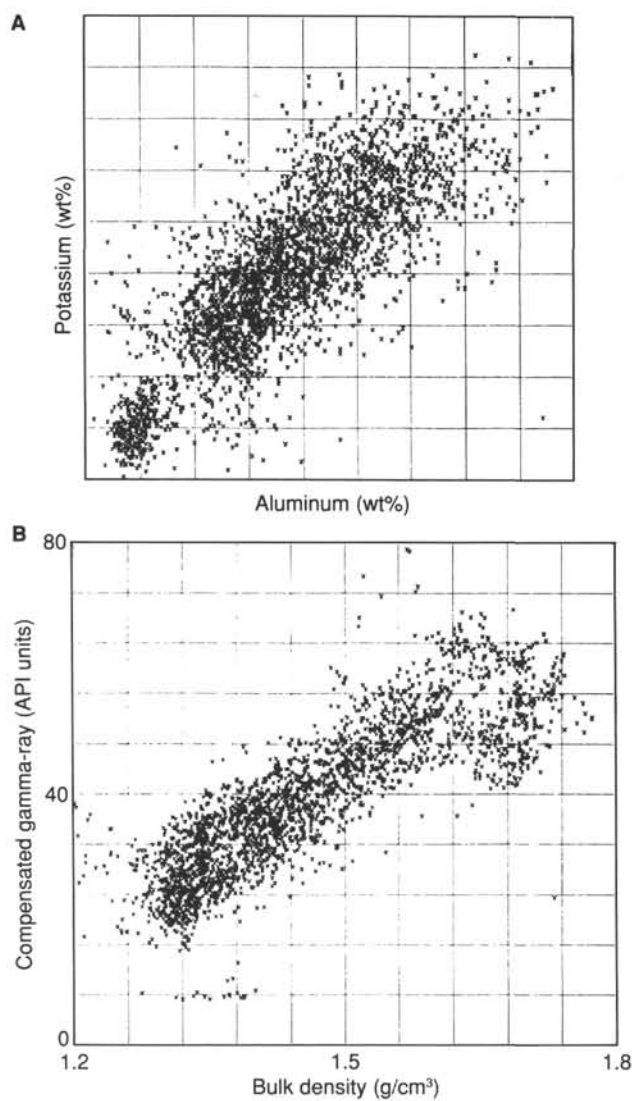


Figure 88. A. Crossplot of aluminium and potassium (in comparative wt% units) from the GST. The small cluster of points in the lower left corner represents measurements collected through casing and drill pipe. The linearity of the plot suggests that aluminium and potassium are in similar phases, most probably clays. B. Crossplot of bulk density and gamma rays (compensated for uranium content) from the LDT. The linearity suggests that sediment bulk density is primarily responding to changes in clay mineral content. The range in bulk density values obtained from the LDT agrees with the shipboard values determined by in the Physical Properties laboratory.

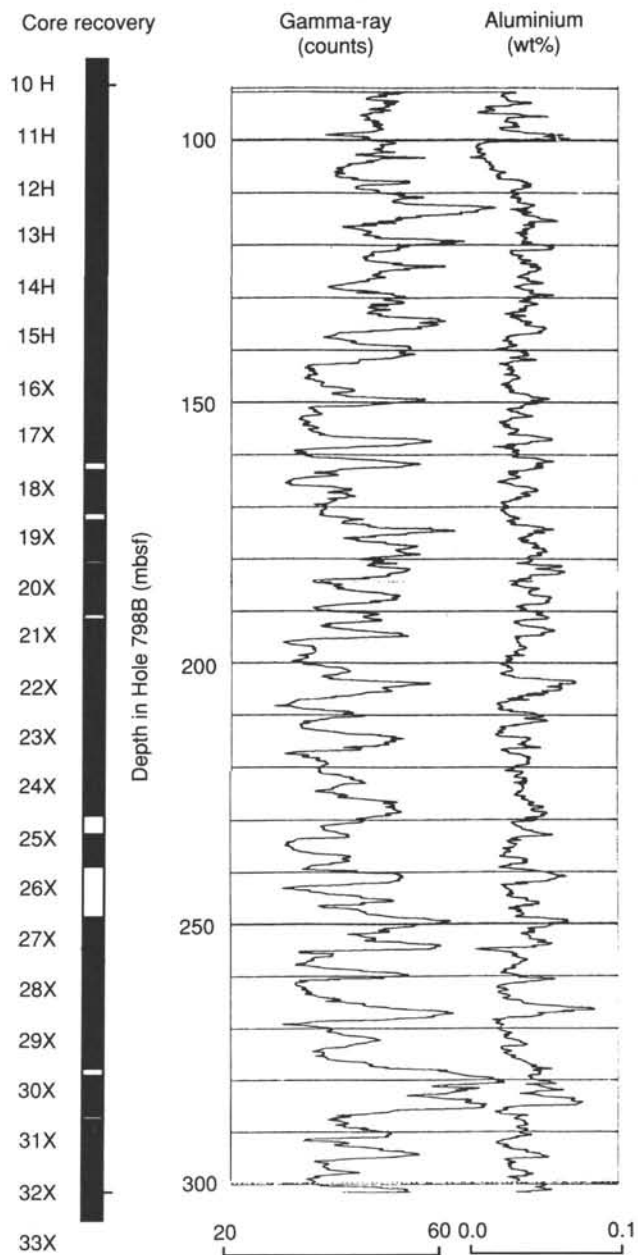


Figure 89. Depth plot of the SGR and aluminium logs, measured at Hole 798B using the GST. Sediment core recovery is shown on the left; true sediment recovery is considerably less than that shown because of gas expansion. Note the strong correlation between the SGR and aluminium logs, suggesting that both are responding to sediment clay content.

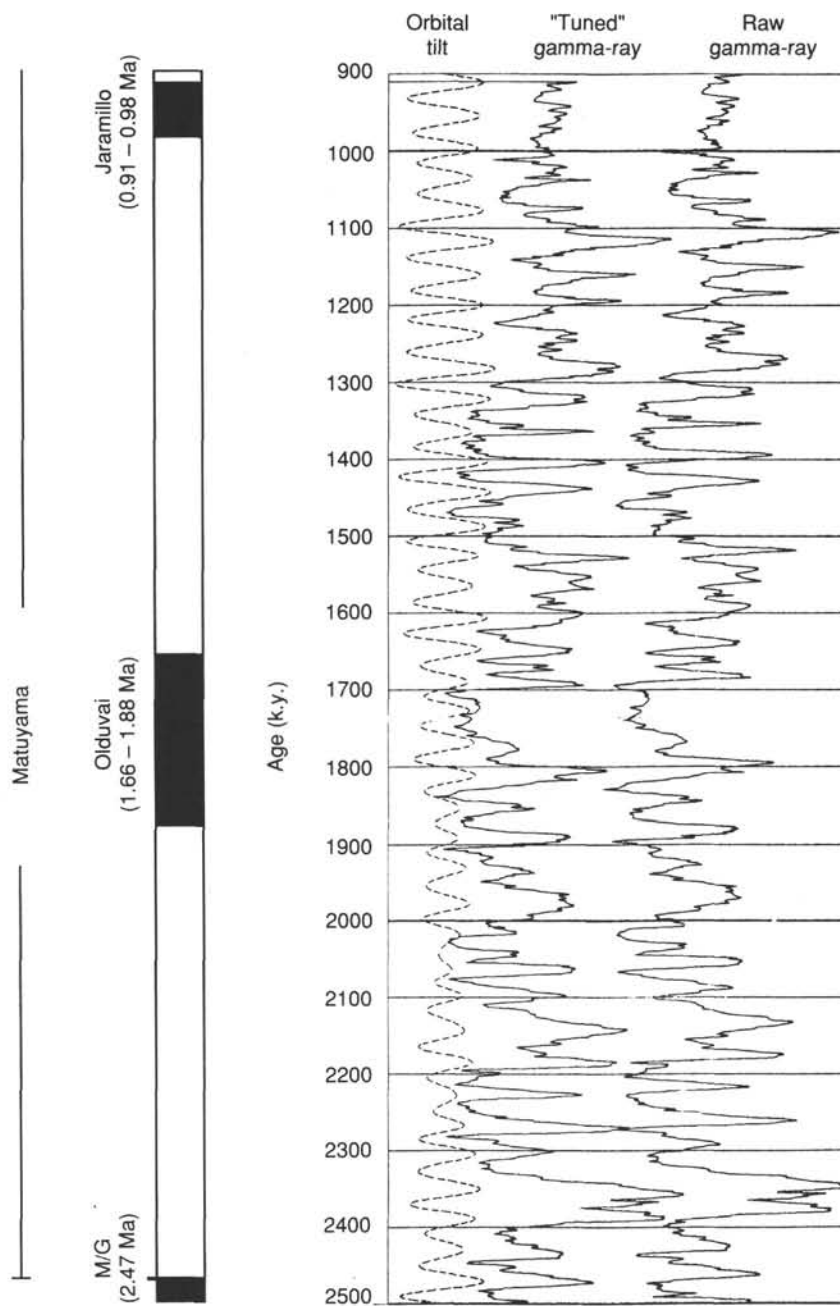


Figure 90. Plot of SGR log time-series. Age control for the "raw" SGR log (right curve) was based on the paleomagnetic reversal datums shown in the right side of the figure. Power spectra for this time-series are shown in Figure 91. Variations in Earth's orbital tilt axis (from 22.5° to 25.5°) are shown by the leftmost curve. Minor adjustments were made to the raw gamma-ray time-series in a way that gamma-ray maxima were coincident with tilt maxima, using a nonlinear inverse correlation method (Martinson et al., 1982). Power spectra for this "tuned" time-series are shown in Figure 92. The mean sampling interval of the 2.5- to 0.9-Ma record is roughly equivalent to 1 k.y.

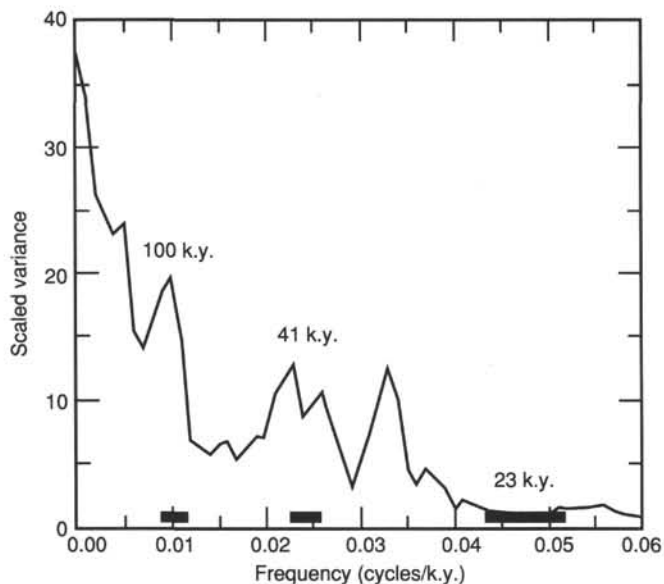


Figure 91. Power spectra of the gamma-ray time-series from 2.5 to 0.9 Ma, based on paleomagnetic datums. Spectra were calculated using standard procedures (Imbrie et al., 1984) and a mean sampling interval of 1 k.y. (1600 points). Note the variance peaks centered at ~100, 40, and 33 k.y.

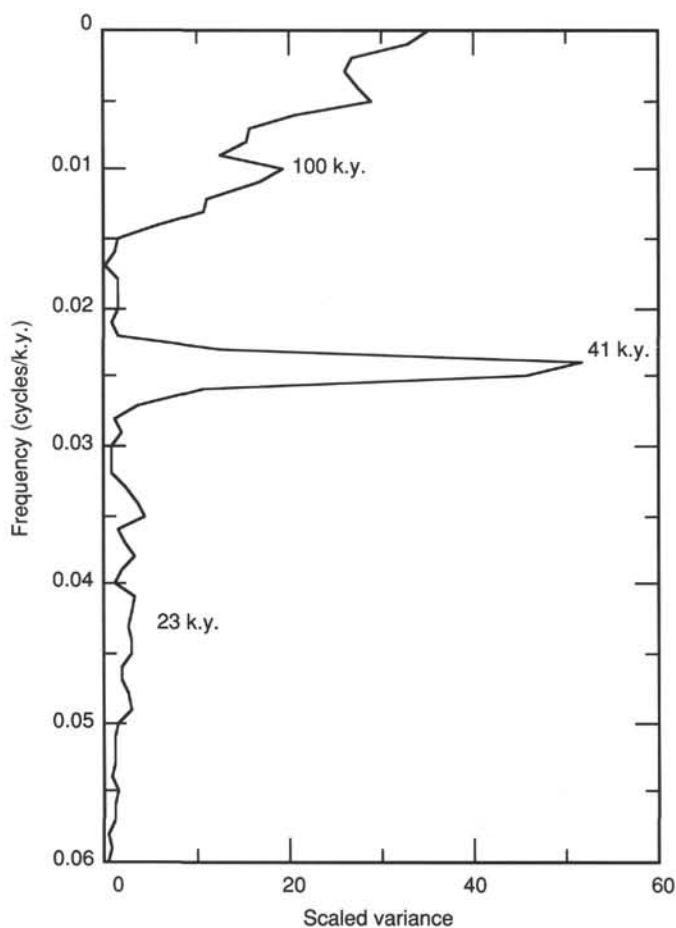


Figure 92. Power spectra of the gamma-ray time-series "tuned" to orbital obliquity (see Fig. 90). Note that virtually all variance is concentrated at the 41- and 100-k.y. orbital periodicities. Although the tuning procedure serves to focus variance at the obliquity periodicity, the persistence of the 100-k.y. peak and the virtual absence of power at other nonorbital periodicities suggests that the record is dominated by orbital-scale variability.

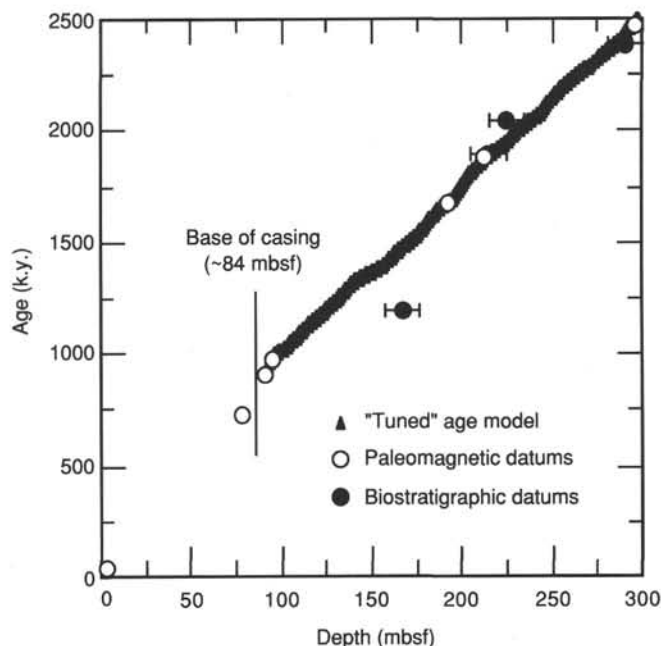


Figure 93. Age vs. depth plot showing the paleomagnetic datums (open circles) and the biostratigraphic datums (closed circles with error bars). The preliminary ("raw") gamma-ray time-series was based on paleomagnetic datums. The "tuned" time scale is shown by the curved line. This line is the result of correlating gamma-ray maxima to orbital tilt maxima. Note that the tuned age-vs.-depth curve does not deviate significantly from the paleomagnetic datums.

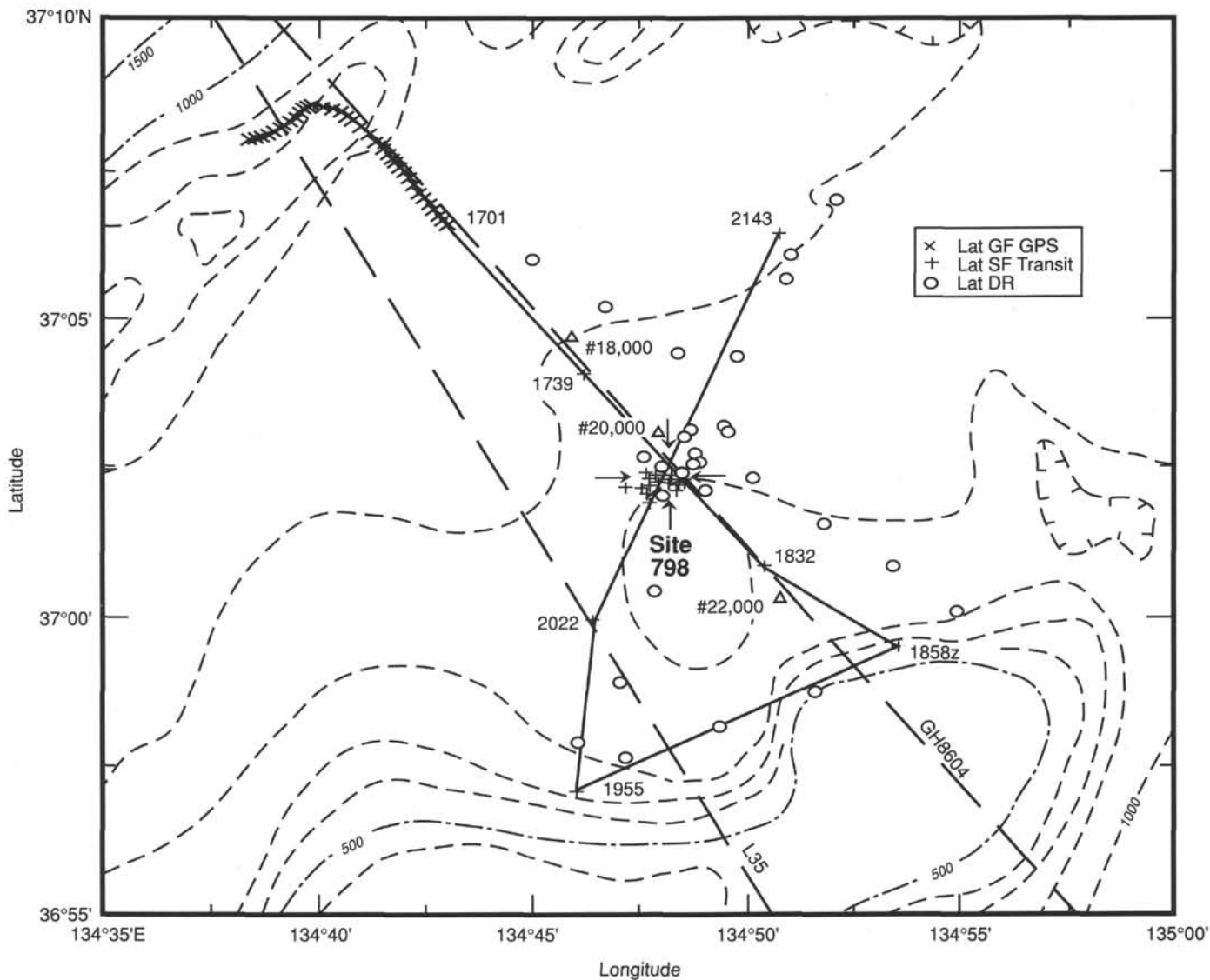


Figure 94. Location map of the immediate area surrounding Site 798. Seismic reflection lines shot by *JOIDES Resolution* are marked by solid lines; those run by the Geological Survey of Japan are marked by dashed lines. Position of *JOIDES Resolution* by GPS location, NNSS, and dead reckoning are indicated by crosses, pluses, and circles, respectively. Dead reckoning positions were not used. Bathymetry is shown by dotted lines having a contour interval of 100 m.

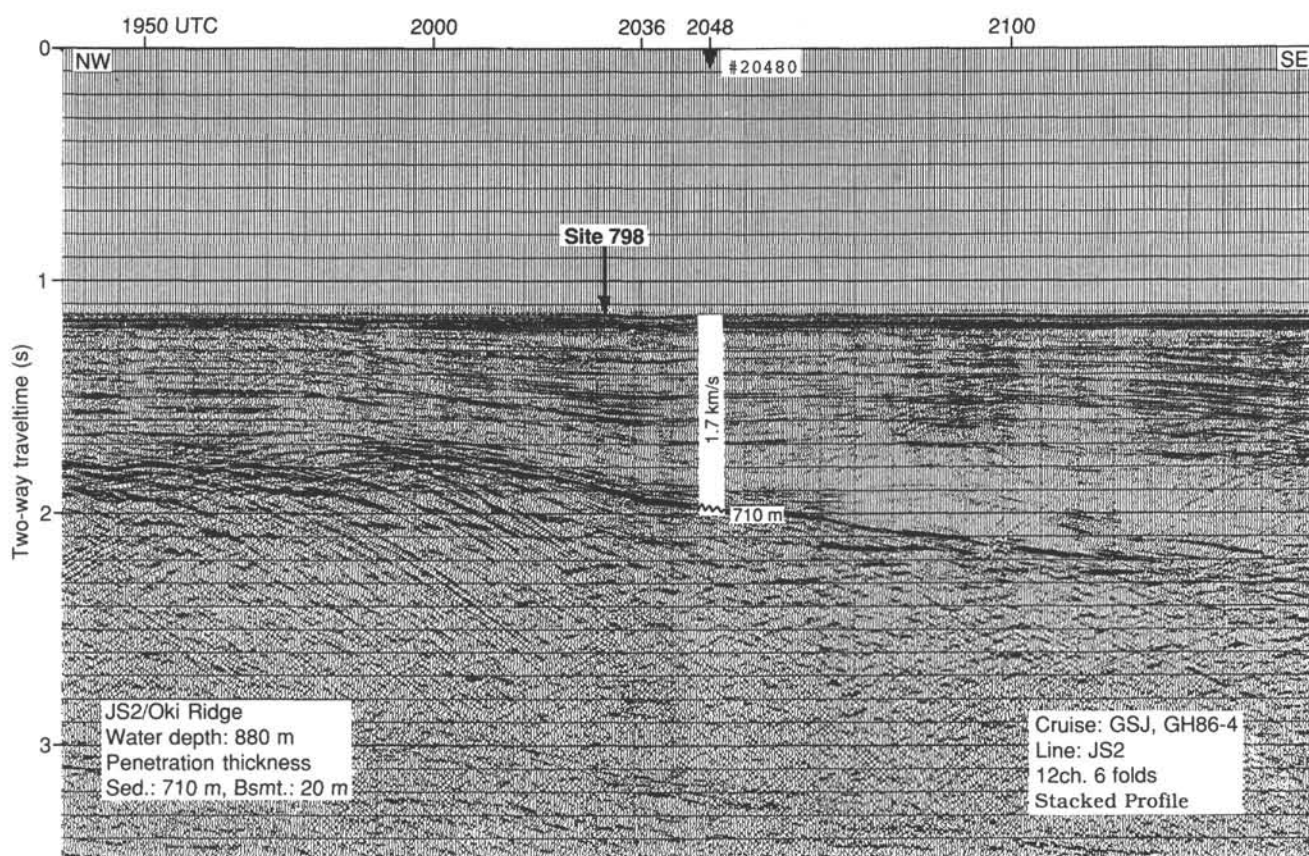


Figure 95. Seismic reflection record obtained by the Geological Survey of Japan during cruise GH86-4. The original location proposed for Site 798 (= proposed Site JS2) was located during shot 2048(0). The final location of this site is nearest shot point 2036(0).

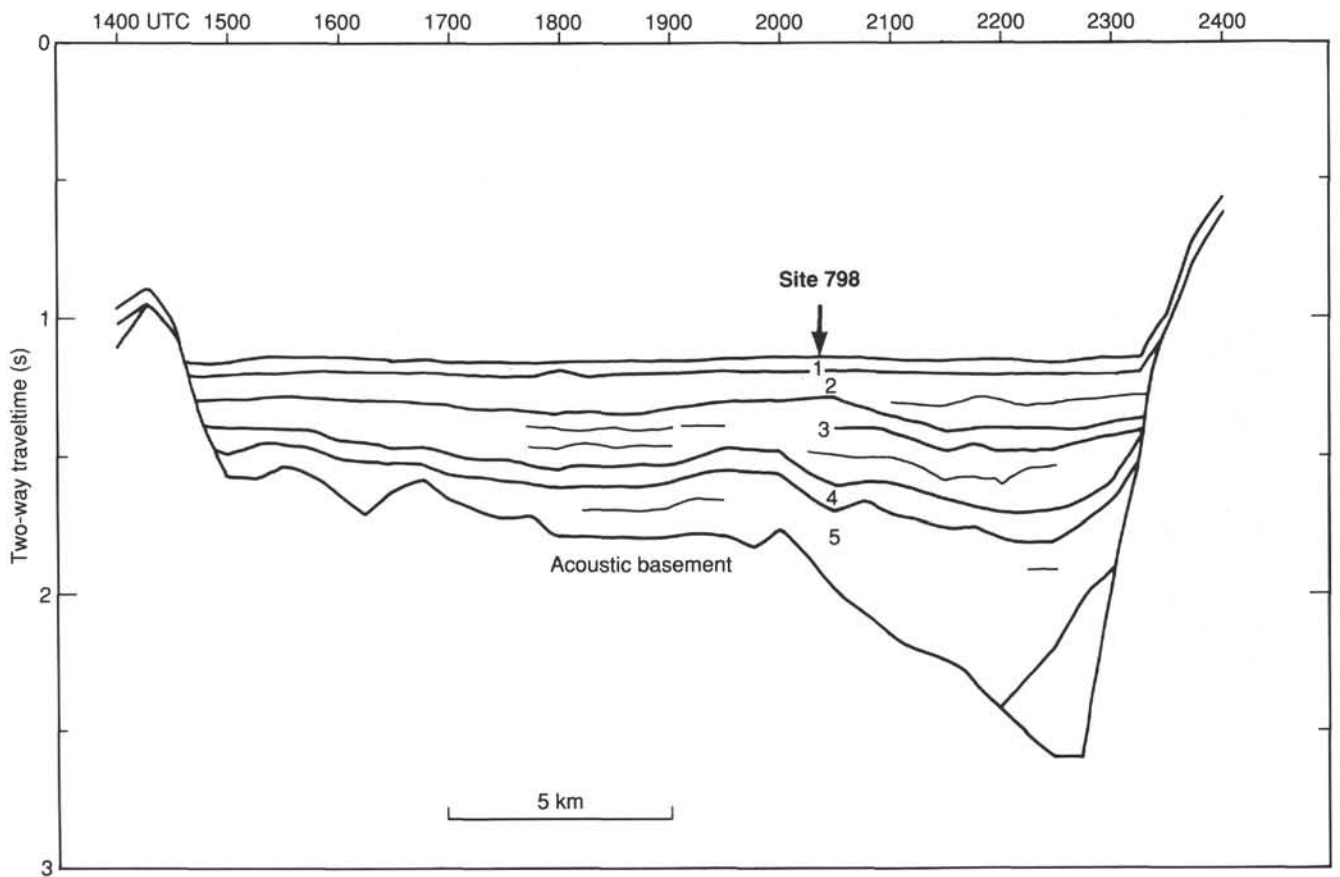


Figure 96. Schematically drawn seismic reflection section across the Oki Ridge Basin, based on the GH86-04 profile (Fig. 95), but having a greater vertical exaggeration than the original record (about $\times 8.3$). The five seismic intervals recognized in this sequence are labeled.

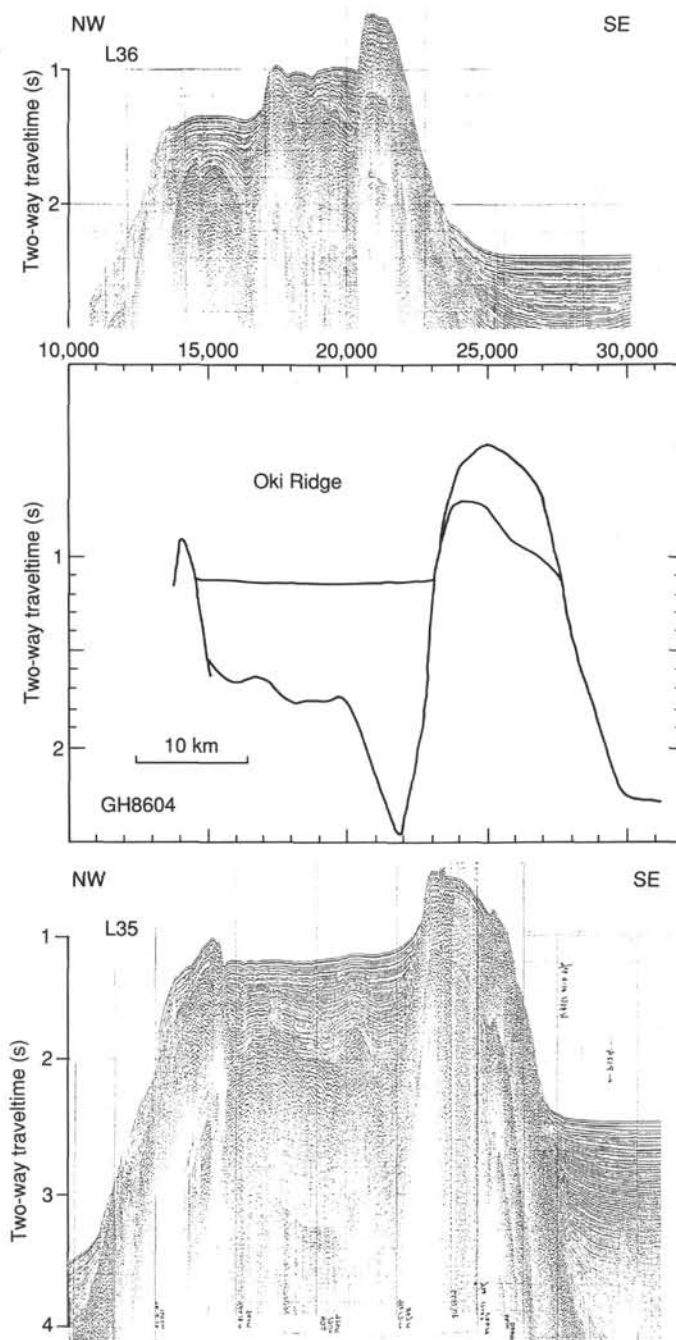


Figure 97. Single-channel seismic reflection profiles L36 and L34 obtained by the Geological Survey of Japan during cruise GH78-02. A schematic view of GSJ profile GH86-04 illustrating acoustic basement configuration is also shown.

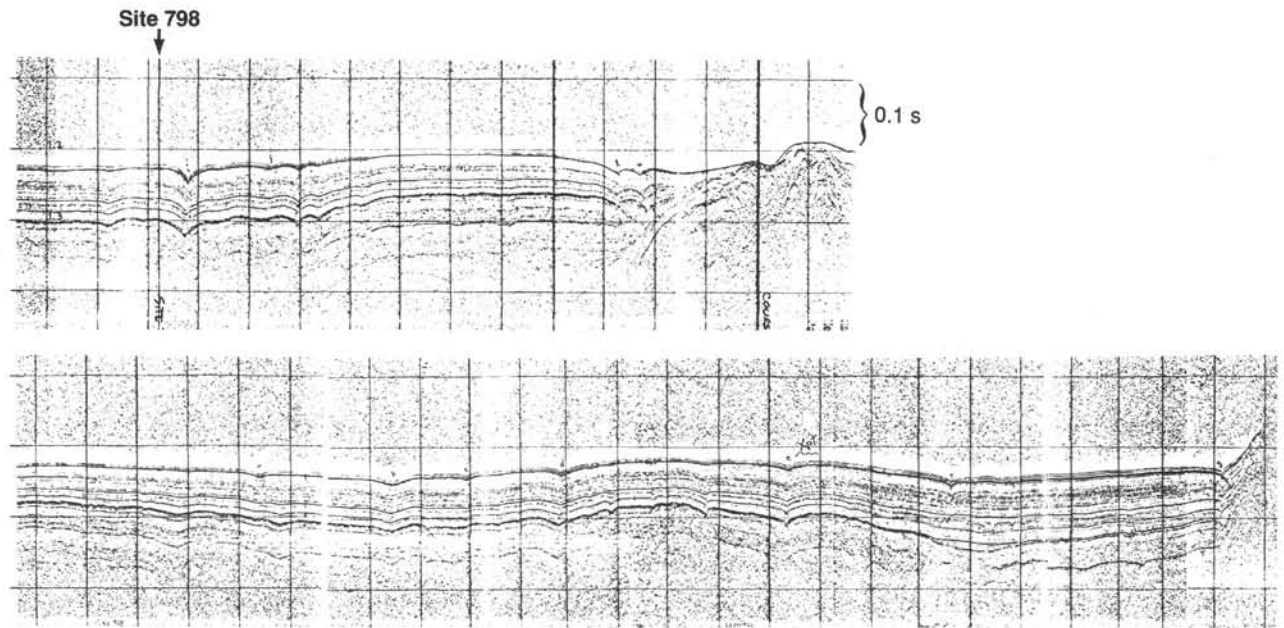


Figure 98. The 3.5-kHz seismic reflection record obtained during approach of *JOIDES Resolution* to Site 798 (1650 to 1850 UTC, bottom, and 2040 to 2200 UTC, top; see Fig. 94).

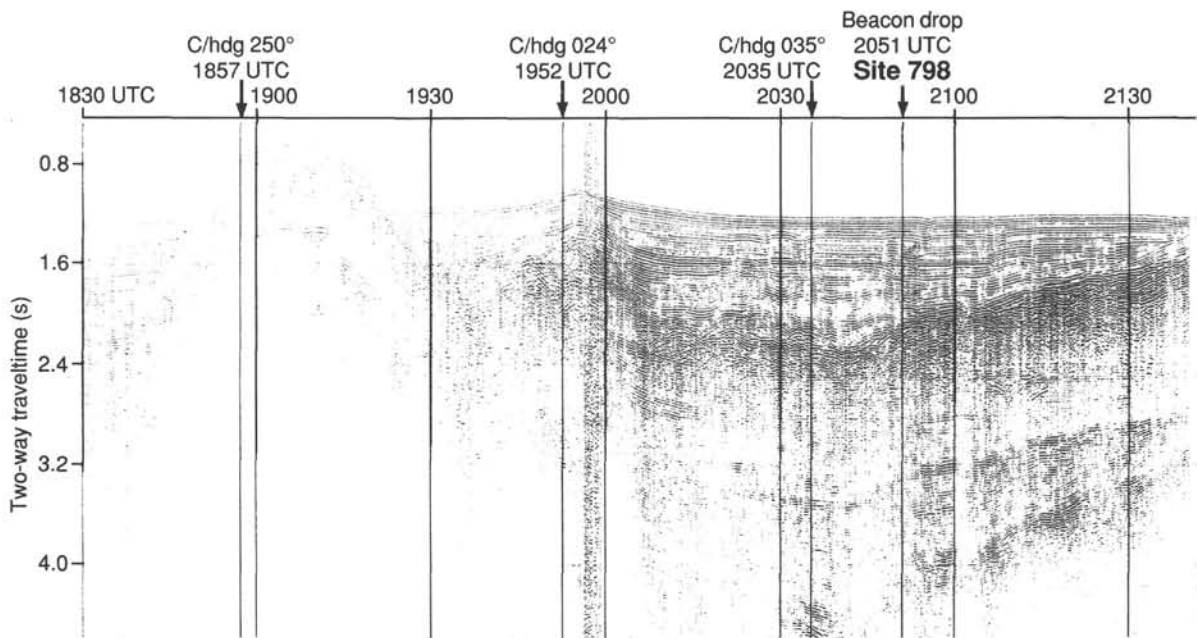


Figure 99. Single-channel seismic reflection record obtained by water gun aboard the *JOIDES resolution* during approach to Site 798. The analog monitor record, with 0.8-s divisions, is shown along the vertical axis.

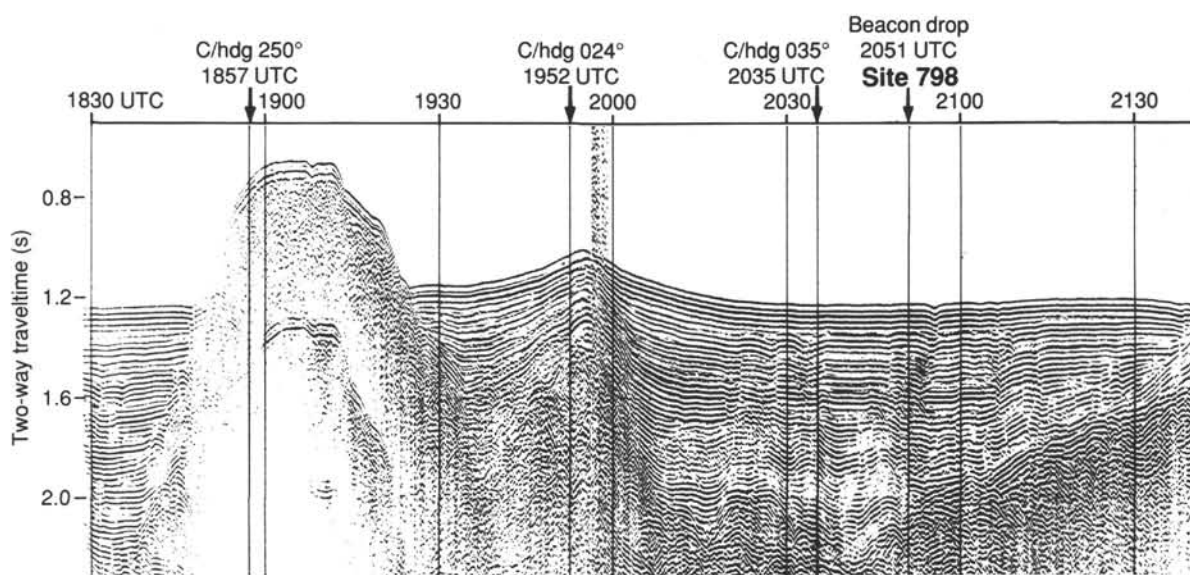


Figure 100. Single-channel seismic reflection record obtained by water gun aboard the *JOIDES Resolution* during approach to Site 798. The analog monitor record, with 0.4-s divisions, is shown on the vertical axis.

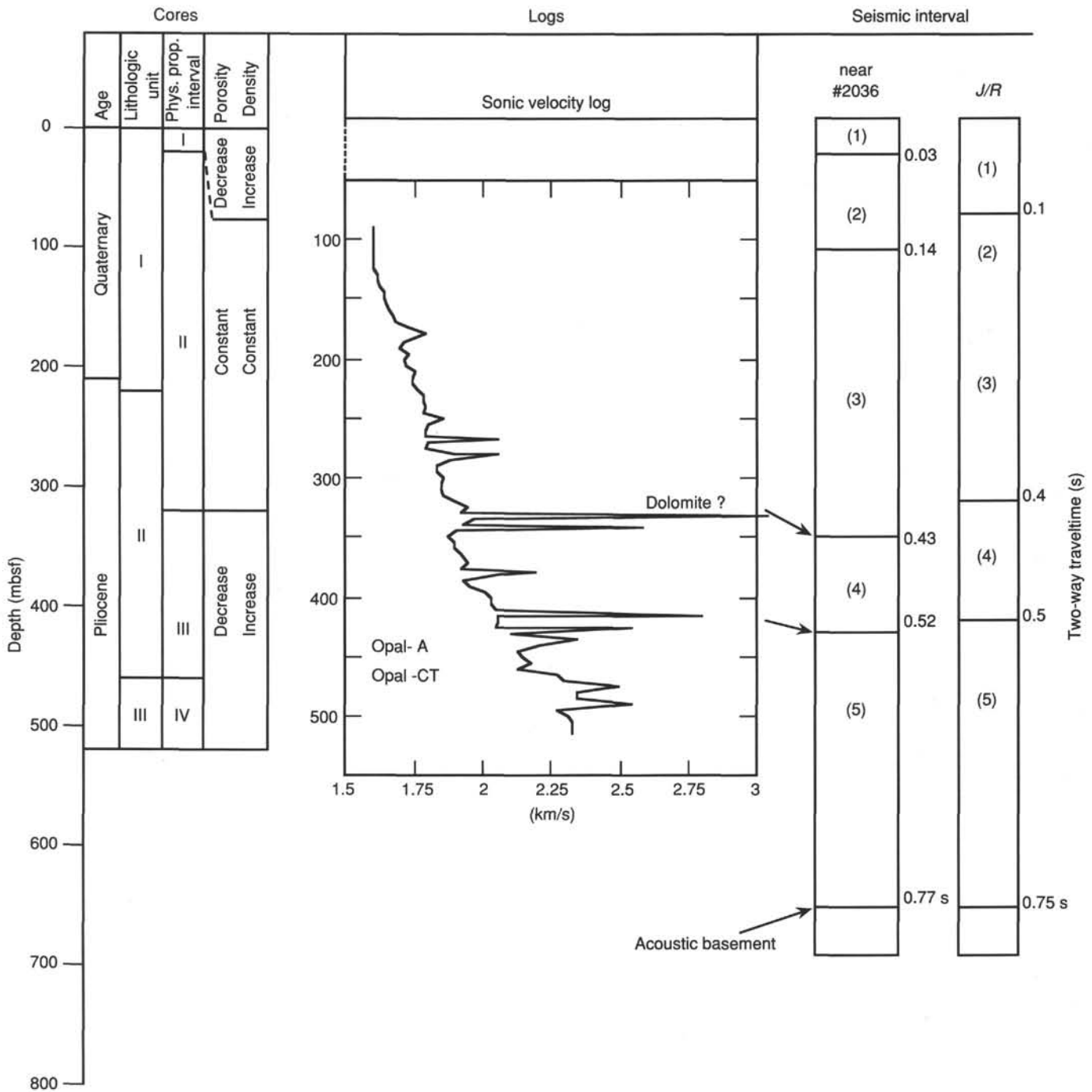
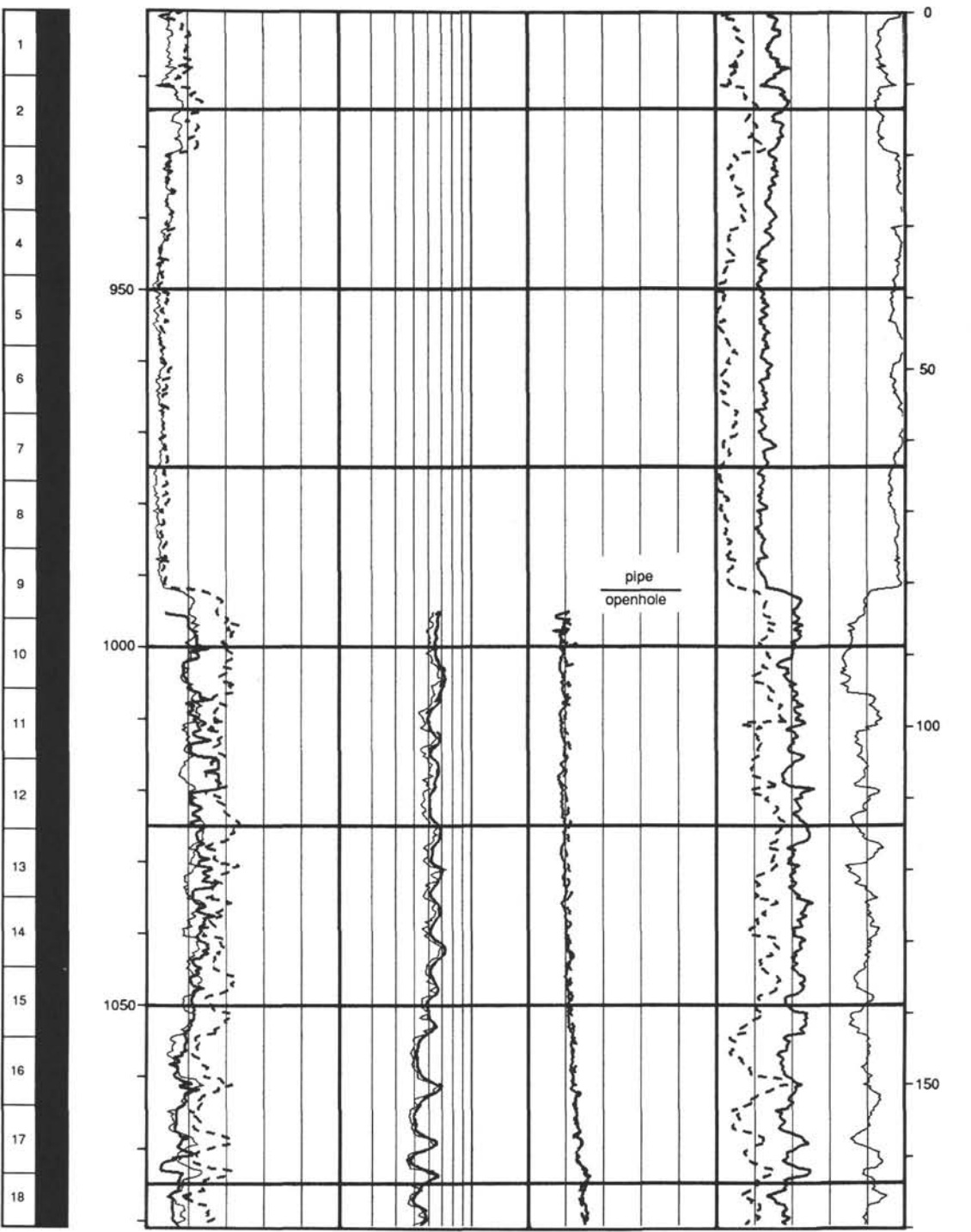


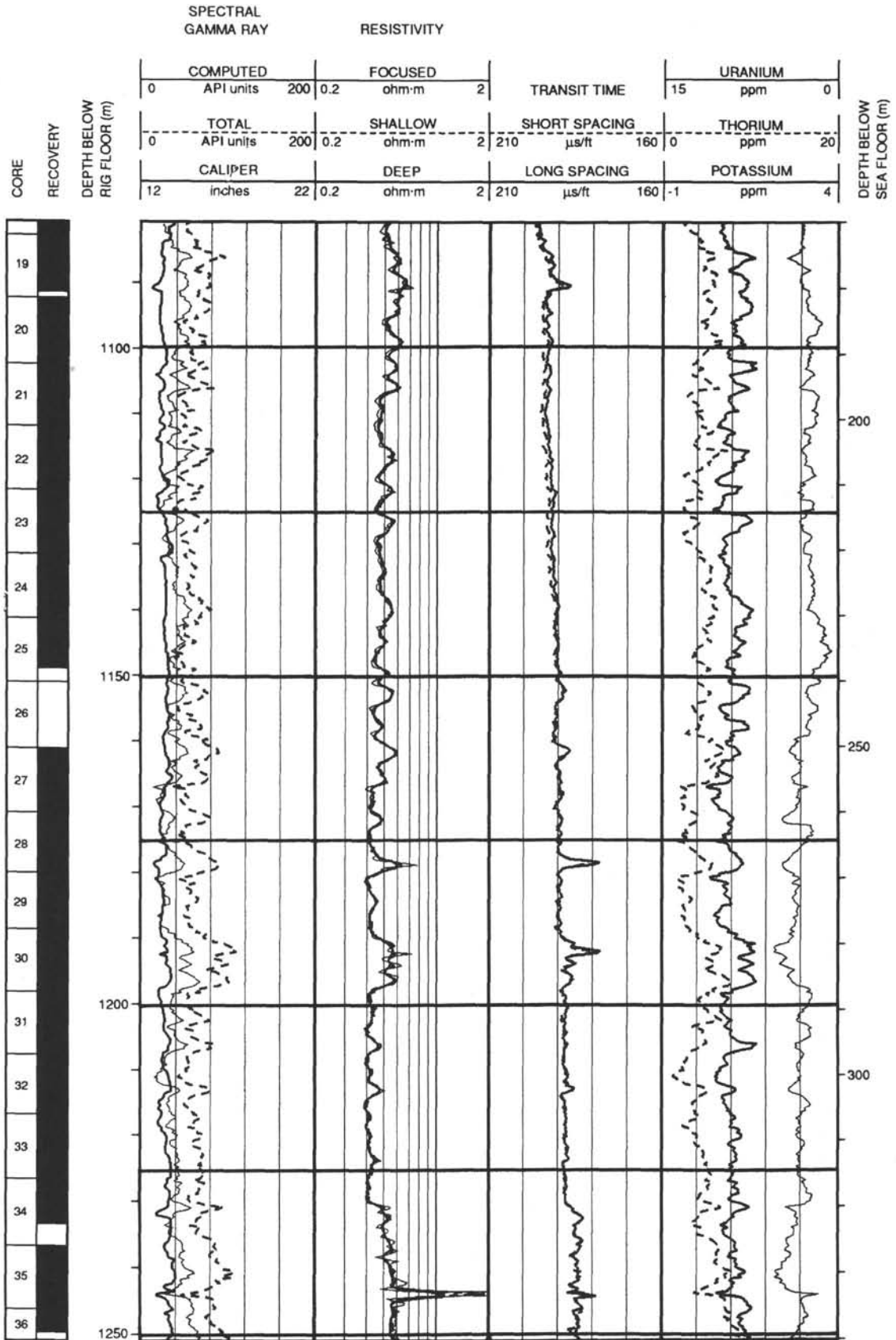
Figure 101. Summary of seismic stratigraphy and correlations with lithostratigraphy, logging, and physical properties at Site 798.

Hole 798-B: Resistivity-Sonic-Gamma Ray Log Summary

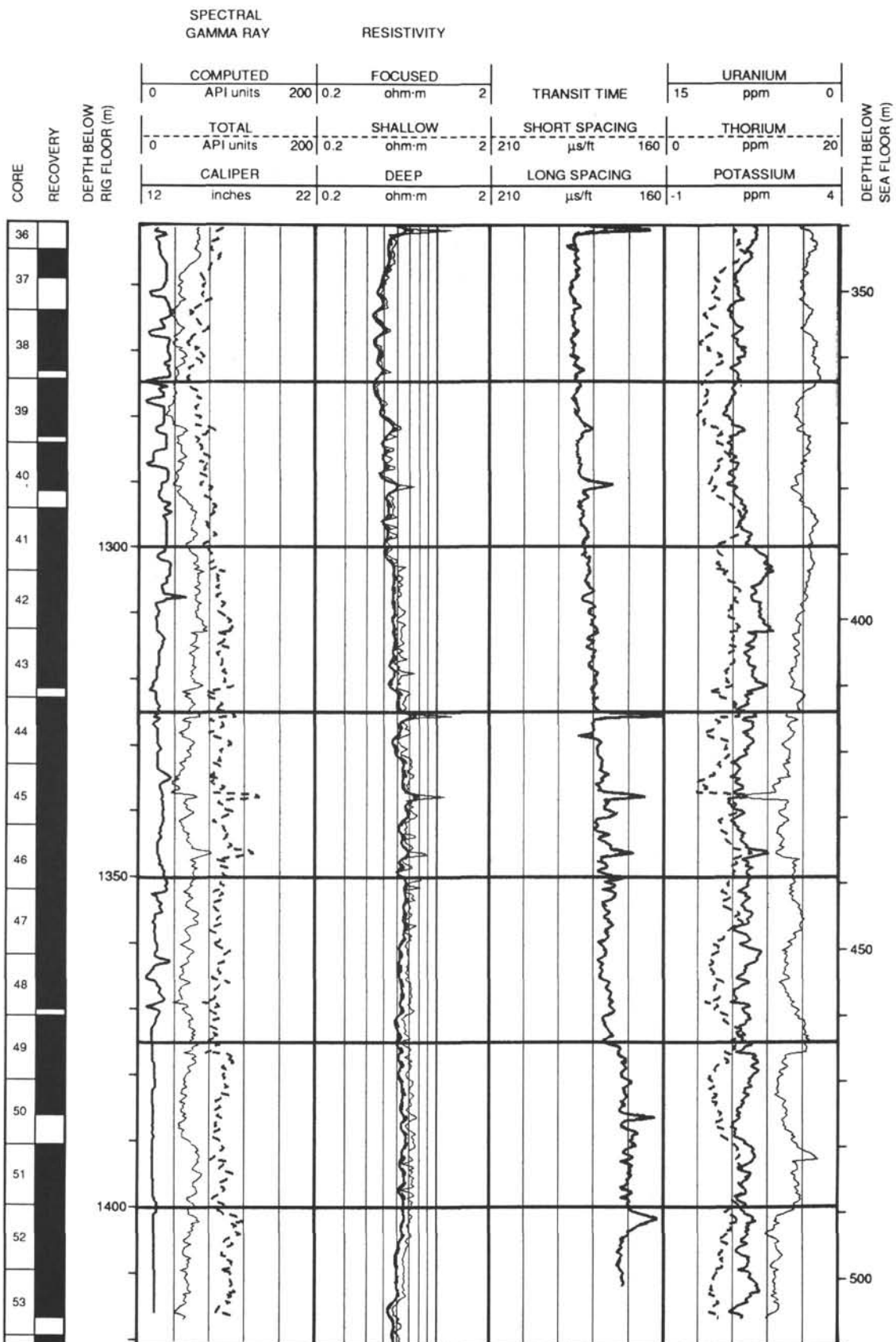
		SPECTRAL GAMMA RAY		RESISTIVITY				TRANSIT TIME		URANIUM				
0	COMPUTED	API units	200	0.2	FOCUSED	ohm-m	2	15	ppm	0				
0	TOTAL	API units	200	0.2	SHALLOW	ohm-m	2	210	μs/ft	160	0	THORIUM	ppm	20
12	CALIPER	inches	22	0.2	DEEP	ohm-m	2	210	μs/ft	160	-1	POTASSIUM	ppm	4



Hole 798-B: Resistivity-Sonic-Gamma Ray Log Summary (continued)



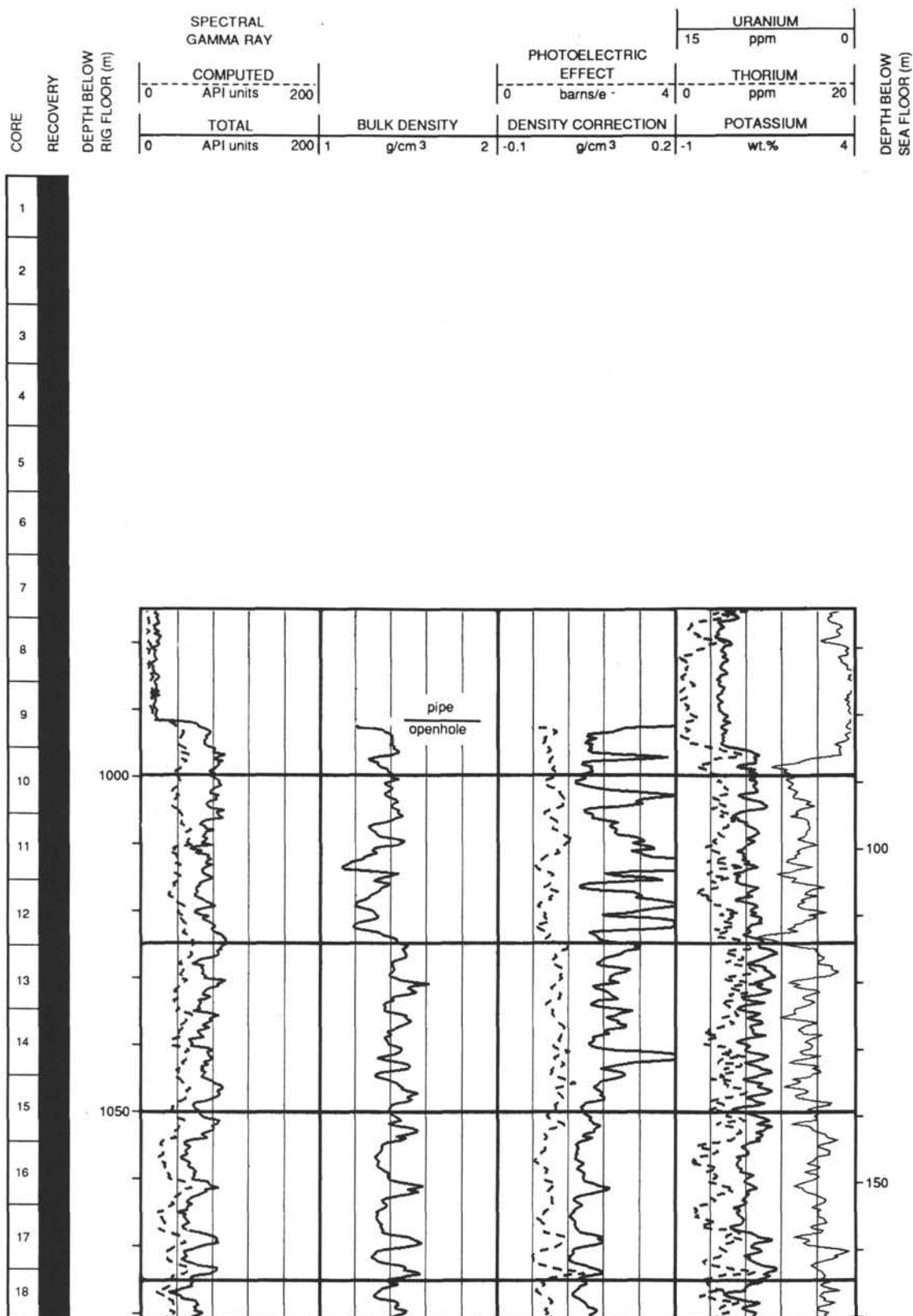
Hole 798-B: Resistivity-Sonic-Gamma Ray Log Summary (continued)



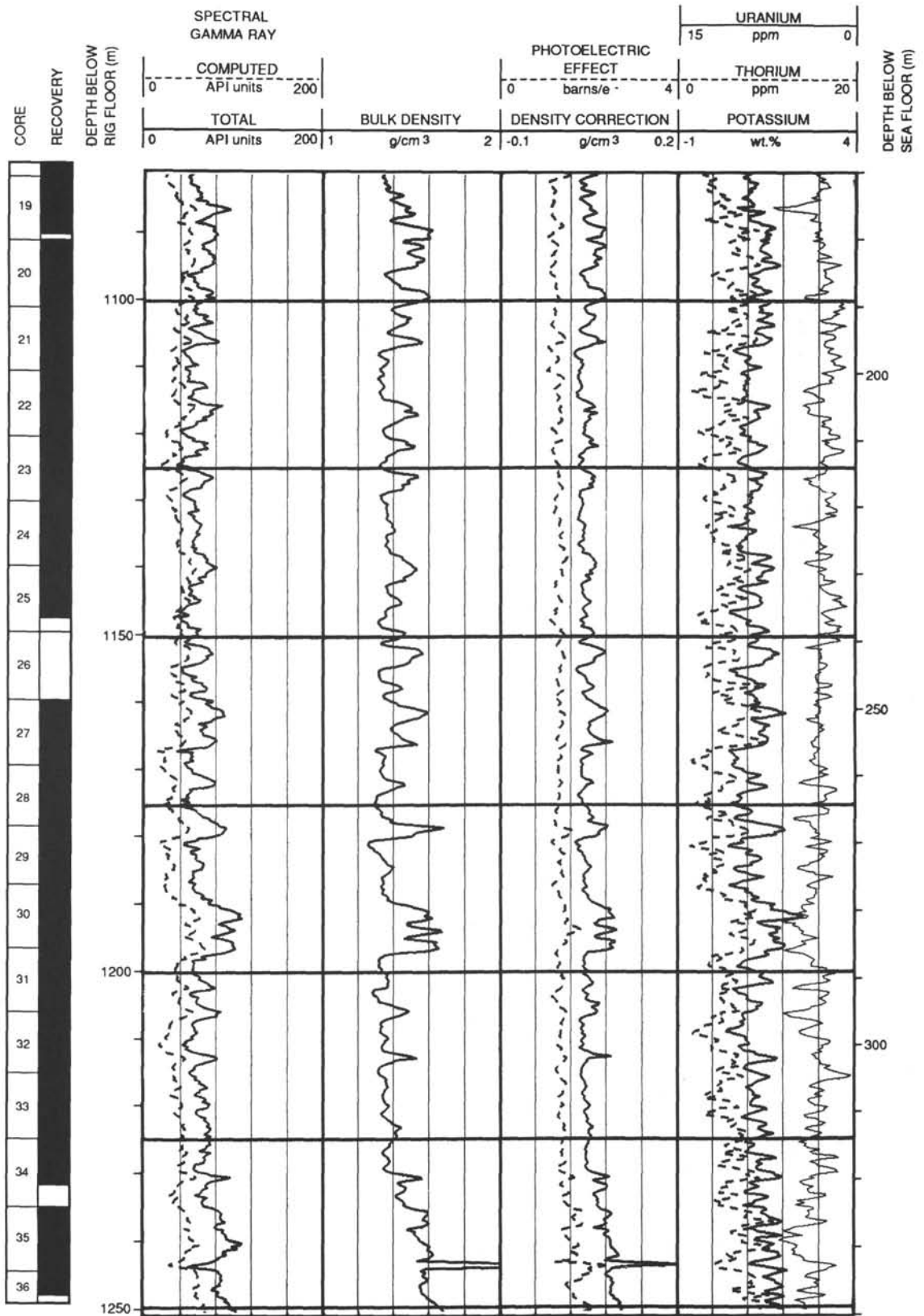
Hole 798-B: Resistivity-Sonic-Gamma Ray Log Summary (continued)

CORE RECOVERY	DEPTH BELOW RIG FLOOR (m)	SPECTRAL GAMMA RAY		RESISTIVITY				TRANSIT TIME		URANIUM		DEPTH BELOW SEA FLOOR (m)										
		COMPUTED	200	FOCUSED	0.2	ohm-m	2	15	ppm	0												
		API units																				
		TOTAL	200	SHALLOW	0.2	ohm-m	2	SHORT SPACING	210	μs/ft	160	THORIUM	0	20								
		API units										ppm										
		CALIPER	22	DEEP	0.2	ohm-m	2	LONG SPACING	210	μs/ft	160	POTASSIUM	-1	4								
		inches										ppm										
54																						

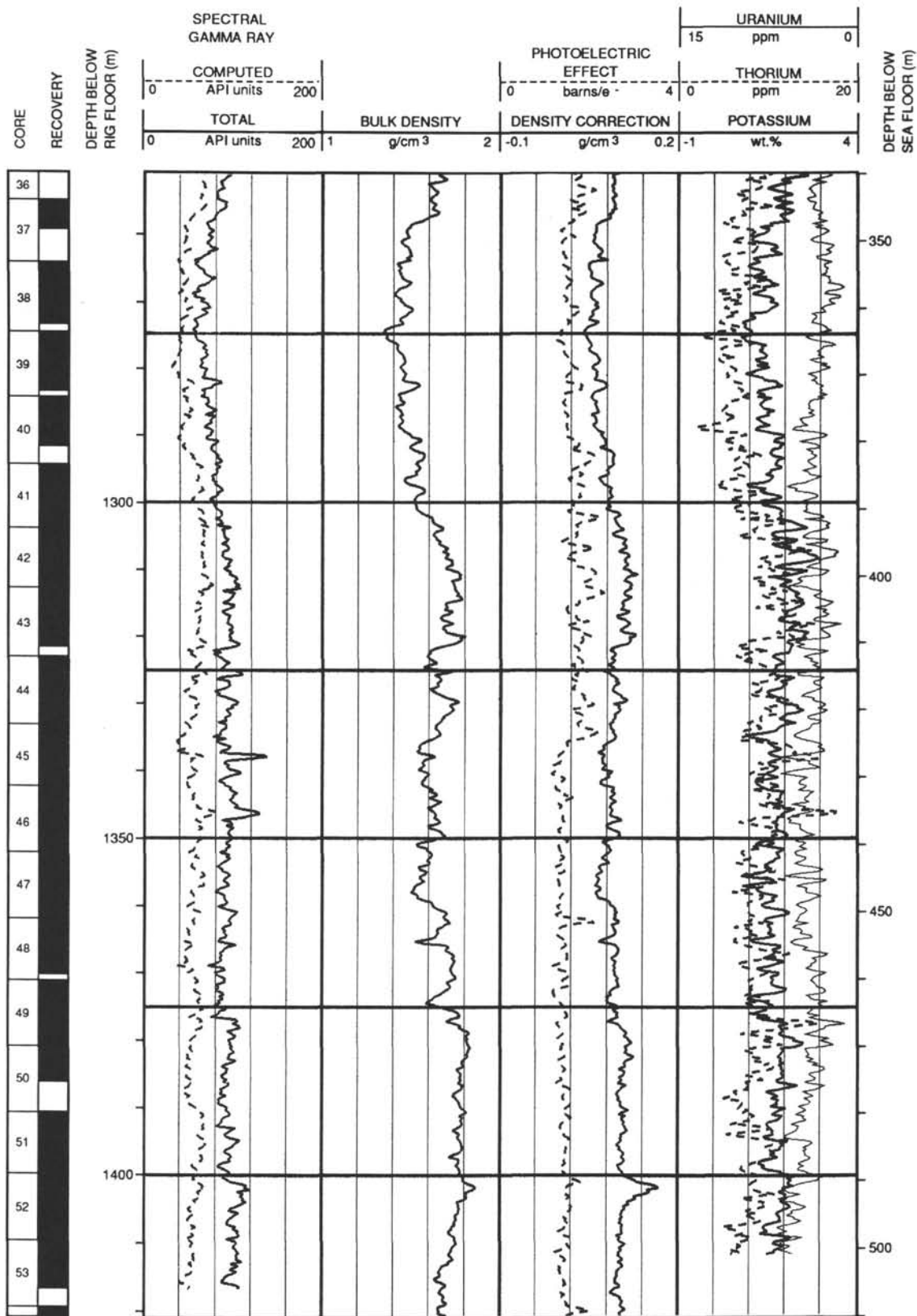
Hole 798-B: Density-Gamma Ray Log Summary



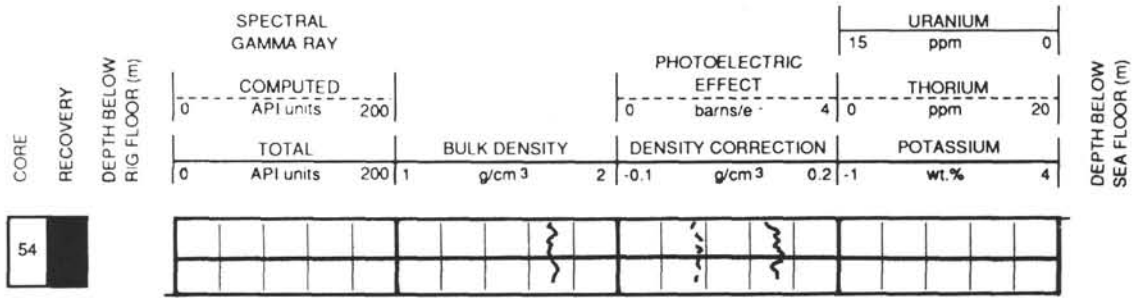
Hole 798-B: Density-Gamma Ray Log Summary (continued)



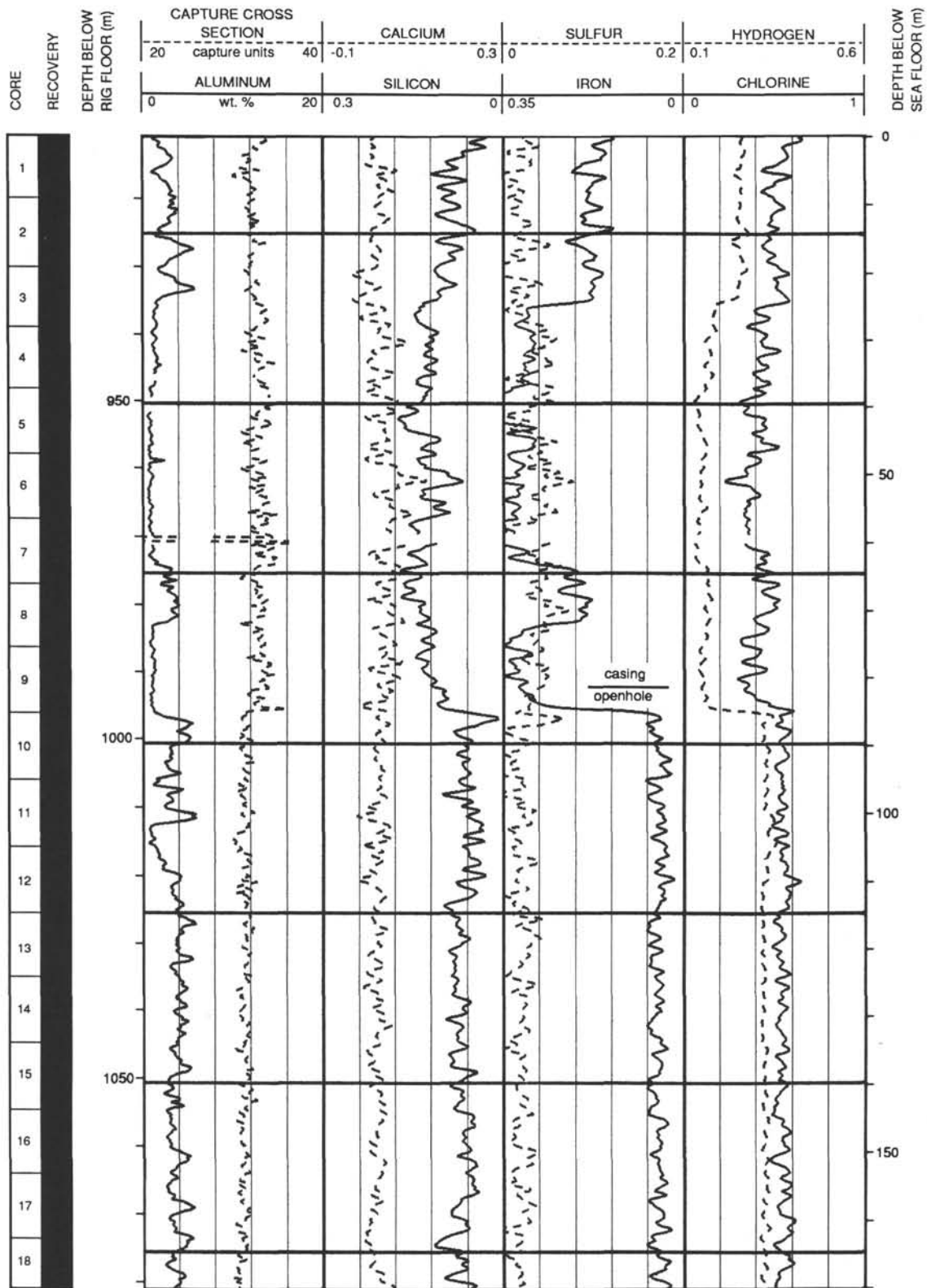
Hole 798-B: Density-Gamma Ray Log Summary (continued)



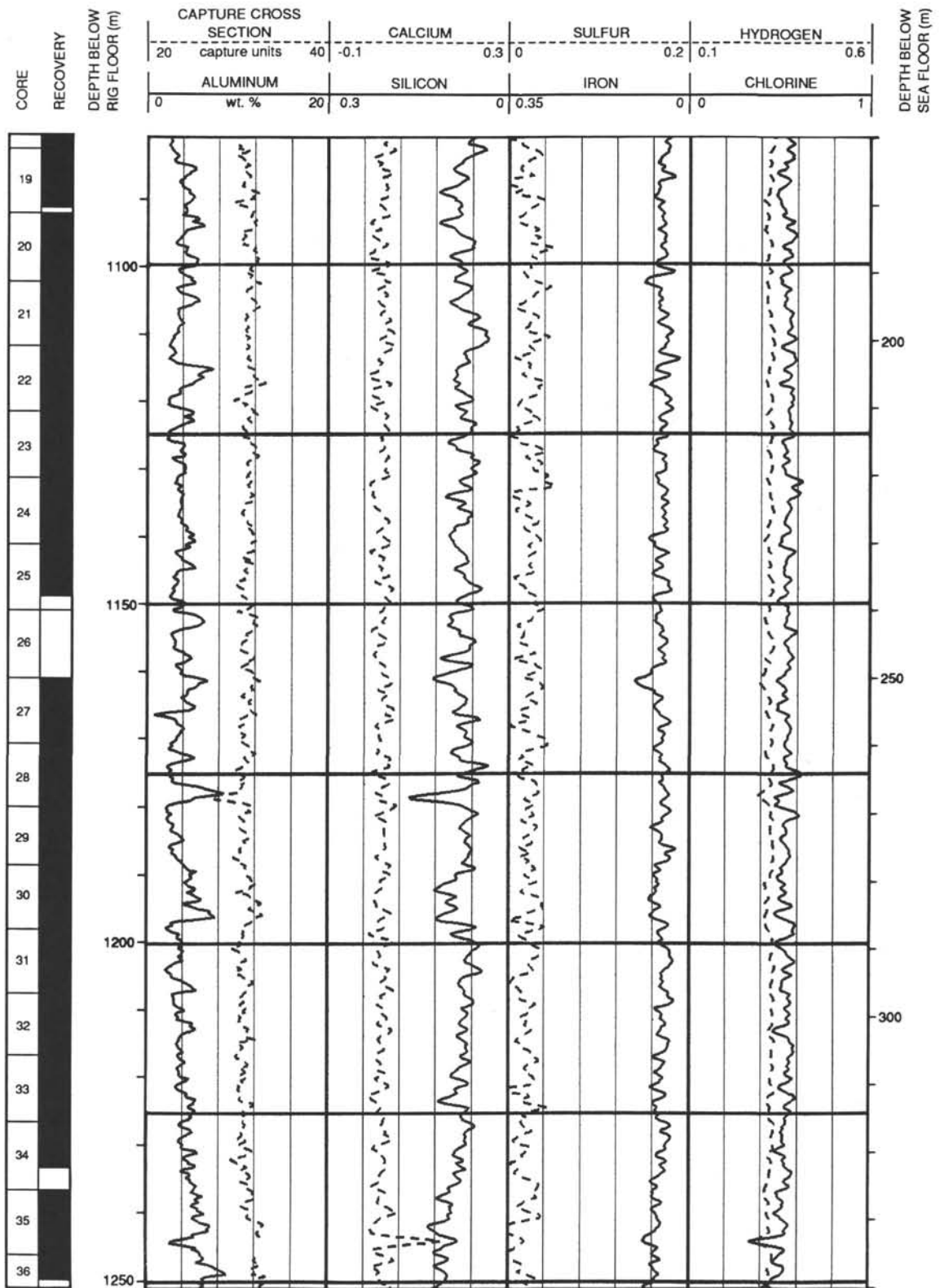
Hole 798-B: Density-Gamma Ray Log Summary (continued)



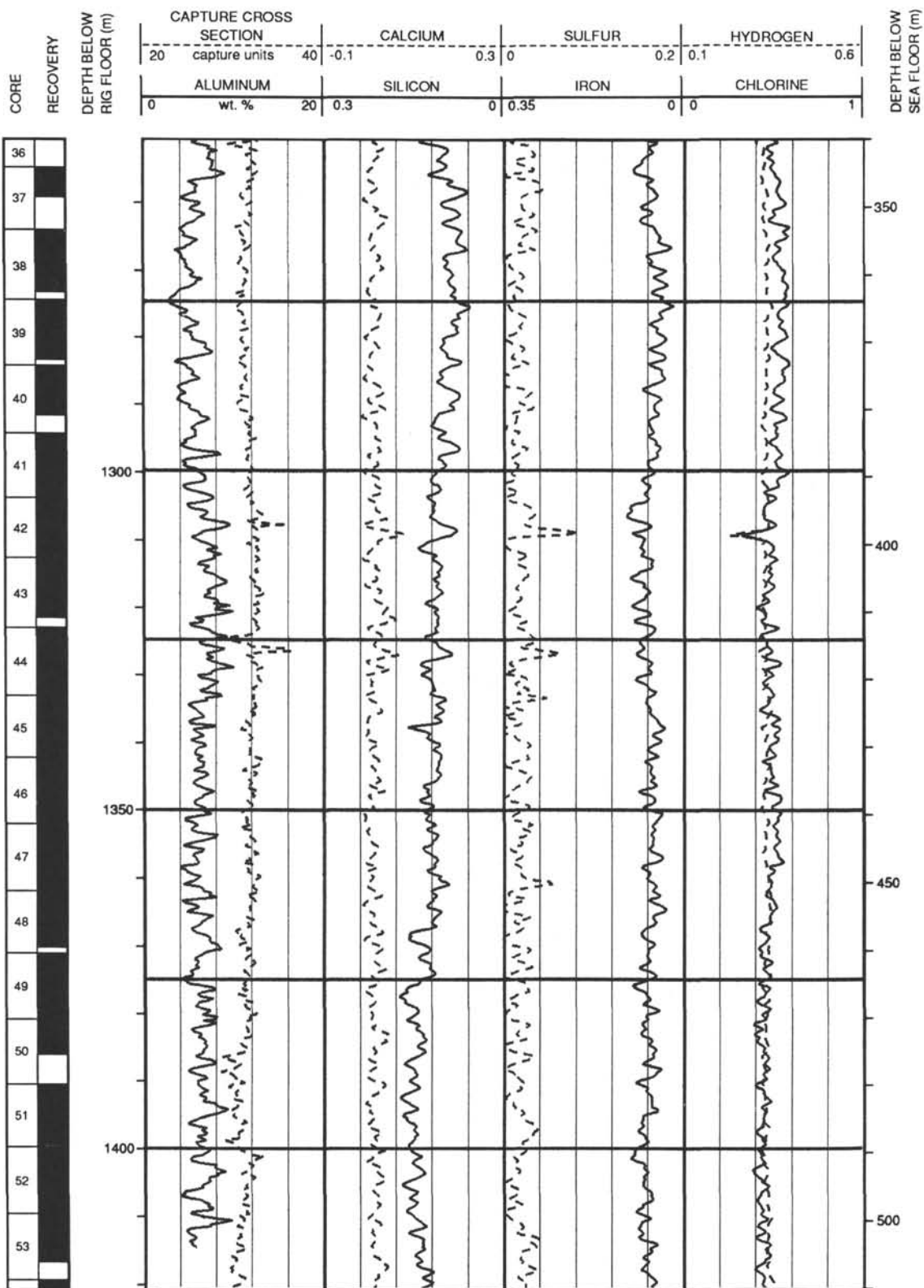
Hole 798-B: Geochemical Log Summary



Hole 798-B: Geochemical Log Summary (continued)



Hole 798-B: Geochemical Log Summary (continued)



Hole 798-B: Geochemical Log Summary (continued)

